ПОЛИТЕХ
Санкт-Петербургский
политехнический университет
Петра Великого

Инженерно-строительный институт
Центр дополнительных профессиональных программ

195251, г. Санкт-Петербург, Политехническая ул., 29,
тел/факс: 552-94-60, www.stroikursi.spbstu.ru,
stroikursi@mail.ru

Приглашает специалистов организаций, вступающих в СРО,
на курсы повышения квалификации (72 часа)

Код	Наименование программы	Виды работ*
Курсы по строительству		
БС-01-04	«Безопасность и качество выполнения общестроительных работ»	п.1,2, 3, 5, 6, 7, 9, 10, 11, 12, 13, 14
БС-01	«Безопасность и качество выполнения геодезических, подготовительных и земляных работ, устройства оснований и фундаментов»	1,2,3,5
БС-02	«Безопасность и качество возведения бетонных и железобетонных конструкций»	6,7
БС-03	«Безопасность и качество возведения металлических, каменных и деревянных конструкций»	9,10,11
БС-04	«Безопасность и качество выполнения фасадных работ, устройства кровель, защиты строительных конструкций, трубопроводов и оборудования»	12,13,14
БС-05	«Безопасность и качество устройства инженерных сетей и систем»	15,16,17,18,19
БС-06	«Безопасность и качество устройства электрических сетей и линий связи»	20,21
БС-08	«Безопасность и качество выполнения монтажных и пусконаладочных работ»	23,24
БС-12	«Безопасность и качество устройства мостов, эстакад и путепроводов»	29
БС-13	«Безопасность и качество выполнения гидротехнических, водолазных работ»	30
БС-14	«Безопасность и качество устройства промышленных печей и дымовых труб»	31
БС-15	«Осуществление строительного контроля»	32
БС-16	«Организация строительства, реконструкции и капитального ремонта. Выполнение функций технического заказчика и генерального подрядчика»	33
Курсы по проектированию		
БП-01	«Разработка схемы планировочной организации земельного участка, архитектурных решений, мероприятий по обеспечению доступа маломобильных групп населения»	1,2,11
БП-02	«Разработка конструктивных и объемно-планировочных решений зданий и сооружений»	3
БП-03	«Проектирование внутренних сетей инженерно-технического обеспечения»	4
БП-04	«Проектирование наружных сетей инженерно-технического обеспечения»	5
БП-05	«Разработка технологических решений при проектировании зданий и сооружений»	6
БП-06	«Разработка специальных разделов проектной документации»	7
БП-07	«Разработка проектов организации строительства»	8
БП-08	«Проектные решения по охране окружающей среды»	9
БП-09	«Проектные решения по обеспечению пожарной безопасности»	10
БП-10	«Обследование строительных конструкций и грунтов основания зданий и сооружений»	12
БП-11	«Организация проектных работ. Выполнение функций генерального проектировщика»	13
Э-01	«Проведение энергетических обследований с целью повышения энергетической эффективности и энергосбережения»	
Курсы по инженерным изысканиям		
И-01	«Инженерно-геодезические изыскания в строительстве»	1
И-02	«Инженерно-геологические изыскания в строительстве»	2,5
И-03	«Инженерно-гидрометеорологические изыскания в строительстве»	3
И-04	«Инженерно-экологические изыскания в строительстве»	4
И-05	«Организация работ по инженерным изысканиям»	7

*(согласно приказам Минрегионразвития РФ N 624 от 30 декабря 2009 г.)

По окончании курса слушателю выдается удостоверение о краткосрочном повышении квалификации установленного образца (72 ак. часа)

Для регистрации на курс необходимо выслать заявку на участие, и копию диплома об образовании по телефону/факсу: 8(812) 552-94-60, 535-79-92, , e-mail: stroikursi@mail.ru.

Contents

Contents

Failure mechanism and slope factors for a footing resting on slopes

R.P. Shukla[a]*, R.S. Jakka[b]
[a] *Department of Civil Engineering, National Institute of Technology Srinagar, Srinagar, India*
[b] *Department of Earthquake Engineering, IIT Roorkee, Roorkee, India*
*E-mail: rpshukla.2013@iitkalumni.org

Keywords: slope, footing, setback, bearing capacity, slope factor, failure mechanism

Abstract. The behaviour of a footing affected significantly with the presence of the slope. The effect of slope on the bearing capacity, slope factor, and failure mechanism has been explored using limit analysis. Both lower and upper bound bearing capacities are determined, and average values are reported. The bearing capacity increases with an increase in the setback, footing depth, and angle of internal friction of soil, but reduces with an increase in slope angle. However, the slope factor decreases with an increase in footing depth, slope angle, and angle of internal friction of soil, but increases with the setback. The failure mechanism as well slope factors change substantially with an increase in the angle of internal friction of soil and slope angle. The failure mechanism of the foundation changes from bearing capacity to combined mode with an increase in the slope. The results of small-scale model testing are compared with numerical study results. Finally, nonlinear regression equations are developed to predict bearing capacity factor, slope factor, and the critical setback for a footing resting on a slope.

1. Introduction

Footings are most often built on the slopes under various circumstances. The footing is subjected to less confining pressure on the sloping side, and soil tends to move toward the slope. It makes the behaviour of footing dissimilar to those resting on the level ground. The bearing capacity on a slope is either less than or equal to the footing resting on the level ground [1]. Footings resting precisely on the slope crest possess the minimum bearing capacity, which improves with an increase in the setback (B') between the footing and slope crest.

A number of studies have analysed the footing resting on the slopes under various loading conditions. Many of the available studies are an extension of bearing capacity methods for level ground. There are two cases possible: (i) footing either resting on a slope or resting precisely on slope crest; (ii) the footing resting adjacent to the slopes with some setback. Most of the studies have considered the case first [2–13]. Some studies have also analysed the footing resting adjacent to the slope crest with some setback [14–29]. Most of the studies were mainly focused on determining the bearing capacity without considering the mechanism of failure and slope factor. Few studies presented the slope factor, which indicates the effects of slope on the bearing capacity. The bearing capacity of footing resting on the slopes can be determined directly by means of slope factor if the bearing capacity for the level ground is known.

The earlier presented slope factors are mostly valid for the footings, resting precisely on the slope crest. The given slope factors are primarily applicable to surface footings. Further, there are discrepancies in the effect of the internal friction angle on the slope factor. Some studies observed the slope factor to be independent of the angle of internal friction [2, 3, 26]. Other studies observed the reduction in slope factor with an increase in the angle of internal friction of soil [1, 15, 19, 24, 28]. However, Castelli and Motta [29] made the contrary observation. Similarly, Shukla and Jakka [18] also observed an increase in the slope factor with an increase in the undrained shear strength of purely cohesive soil. It is also observed that the bearing capacity factors are varying significantly from study to study. The variations are sometimes even up to 100 %. It creates confusion for practicing engineers to decide upon the appropriate bearing capacity

factor. Most of the earlier studies used the limit equilibrium method to determine bearing capacity, which significantly underestimates the bearing capacity. A few studies have also used limit analysis but used either upper bound or lower bound. The present study considers the factors affecting slope factor and bearing capacity using the upper and lower bound limit analyses. The optimised value, which is an average of upper and lower bound, has been reported. Significant importance has been given to the failure mechanism. Few experimental studies have also been performed to support the numerical study results. Finally, predictive models were developed to predict the bearing capacity factor, slope factor, and critical setback.

2. Methods

The strip footing resting on a slope is analysed by considering full-scale numerical modelling and small-scale experimental modelling. Methodology for both methods has been discussed separately in the sections, namely, "2.1 Numerical modelling" and "2.2 Experimental modelling".

2.1. Numerical modelling

A 2D limit analysis finite element analysis was carried out to model the problem. A typical model considered in the study is shown in Fig. 1. The slope (β^0) has been assumed to be uniform throughout the soil slope. The footing width (B) has also been assumed constant throughout the study. Based on the slope geometry and setback, the domain area was selected large enough to reduce the boundary effect. The width and height of the domain were maintained 20 B and 10 B, respectively. Increasing the number of elements to more than 5000 does not affect the results. Mesh was refined through adaptive iterations. Mostly, the results are stable after 3–4 iterations. A total of 7000 elements were used in the first iteration and increased to 10000 in the final iteration. The loading was applied in terms of load multiplier directly on the footing. The problem geometry and numerical modelling are shown in Fig. 1 (a, b).

The soil has been modelled as a drained material, and the Mohr-Coulomb model represents the shear strength. Both upper and lower bound analyses were performed using Optum G2 program to determine the ultimate capacity of footing. The average value has been adopted for further analysis. The detail of formulation for finite element upper bound and lower bound limit analysis is provided in earlier studies [30–33]. Makrodimopoulos and Martin [30] found that six nodes triangular elements are appropriate to determine the strict upper bound provided that sides are straight. Therefore, six node triangular elements have been used in the upper bound analysis to describe the soil elements. However, the lower bound analysis was performed with three-node elements. Second-order conic optimisation has been used to obtain the optimised value of the upper and lower bound loads. Makrodimopoulos and Martin [30–31] developed the formulation of yield criteria, equilibrium, and compatibility equations to second-order cone programming (SOCP). The poor optimisation may result in a low lower and a high upper bound. However, the application of SOCP enables to get the close upper and lower bound solution, which indicates the exact upper and lower bounds. The comparison of upper and lower bound bearing capacity is presented in section "3.1 Results and discussions".

2.2. Experimental modelling and procedure

In the experimental study, the strip footing of 1.15 m length and 0.09 m width has been tested in a tank with dimensions of 2 m × 1.2 m × 1.2 m. The model foundation testing setup is shown in Fig. 1 (c, d). Tank walls were marked with slope geometry to fill the sand in the desired slope. Rainfall technique, wherein sand is dropped from a fixed height, was used to pour the sand into the tank to attain the required density. Researchers had already used this technique to achieve reproducible densities [35]. Several trails were made to find the relation between the height of sand fall and the relative density of sand bed.
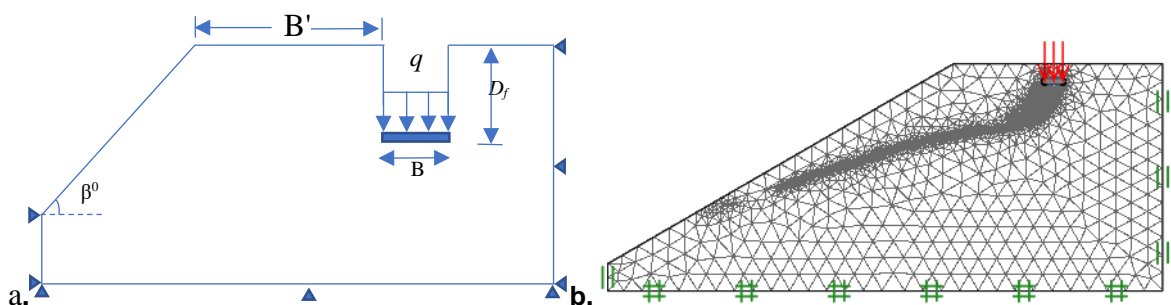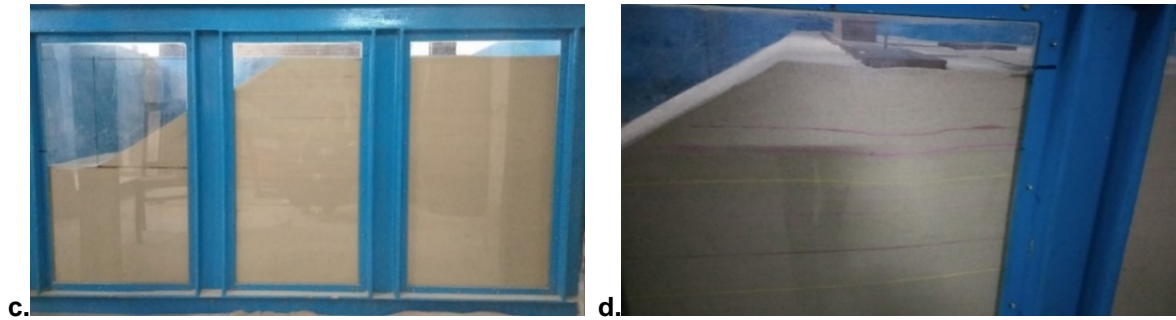
Figure 1. Model testing setup: (a) numerical model before iterations; (b) after three iterations; (c) experimental setup with prepared bed; (d) during loading stage.

Pulley and chain arrangement were used to maintain the required height of sand fall at regular intervals. After filling the tank up to the top level, the surface of the sand bed was levelled to maintain continuous contact between the soil and foundation. It also avoids the inclination of foundation. After this, the model foundation was placed on the top of the sand bed. This step requires high precision to maintain the level of the footing surface. The level of the model footing was checked using a spirit leveller to avoid any tilting. The footing was placed on the sand bed. The dial gauges were placed on the top of the footing to measure the settlement. The loading on the footing surface was applied using a mechanical arrangement. The load cell was connected to a transducer, which shows the magnitude of the applied load. The least count of the used load cell is 100 gms. Similar to plate load testing, load and settlement were measured for every load increment. The loading was applied in 10-15 load intervals. From the obtained load-settlement curves, the ultimate bearing capacity is determined.

2.3. Parameters considered in the analysis

The parameters studied in the present study include slope (β^0), setback (B'), angle of internal friction of soil (ϕ), and footing depth (D). The parameters range used in the study are presented in Table 1. The density of soil is varied based on the angle of shearing resistance of the soil. The unit weights used in the numerical study are 15, 17, and 19 kN/m^3, and similarly, the stiffness of soil is assumed to be 10000 kN/m^2, 12500 kN/m^2, and 14000 kN/m^2, respectively. The setback and embedment depth are normalised with respect to the footing width (B).

Table 1. Parameters considered in the study.

ϕ (^{0})	B'/B	β (^{0})	D/B	No. of analysis
25	0, 1, 3, 5	0, 5, 10, 15, 20	0, 0.5,1.0, 1.5, 2.0	600
30	0, 1, 3, 5	0, 5, 10, 15, 20, 25	0, 0.5,1.0, 1.5, 2.0	720
35	0, 1, 3, 5, 7	0, 5, 10, 15, 20, 25, 30	0, 0.5,1.0, 1.5, 2.0	1225
40	0, 1, 3, 5, 7, 9	0, 5, 10, 15, 20, 25, 30, 35	0, 0.5,1.0, 1.5, 2.0	1680
45	0, 1, 3, 5, 7, 9	0, 5, 10, 15, 20, 25, 30, 35, 40	0, 0.5,1.0, 1.5, 2.0	1890
		Total number of the analysis		6115

For experimental model testing, cohesionless dry sand was used as a foundation bed. Many tests were conducted to determine the properties of the sand, such as sieve analysis, maximum dry density, minimum dry density, and specific gravity. Sieve analysis was performed as per IS: 2720-Part IV (1985) [36]. The description of soil properties and experimental testing program are shown in Table 2 and 3, respectively. The maximum and minimum sizes of sand particles are 1.18 mm and 0.1 mm, respectively.

Table 2. Description of soil.

Soil properties	Values	Soil properties	Values
Coefficient of Uniformity	1.60	Specific gravity	2.67
Coefficient of Curvature	1.00	Maximum density in gm/cm^3	1.67
Effective Size (D_{10}) mm	0.15	Minimum Density in gm/cm^3	1.43
D_{30} mm	0.19	Angle of internal friction of soil (ϕ^0)	37.50
D_{60} mm	0.24	Sand content	> 99 %

Table 3. Description of experimental testing on cohesionless soil slopes.

Relative density (%)	β^0	Setback (B'/B)	No. of tests
50 %	20, 25, 30	0, 1, 3, 6	12
60 %	20, 25, 30	0, 1, 3, 6	12
75 %	20, 25, 30	0, 1, 3, 6	12

3. Results and Discussions

3.1. Numerical study results

The effect of various factors on bearing capacity factor ($N_{\gamma q}$) and slope factor (S_f) is studied for a wide range of considered parameters. Both results are presented together for comparison purposes, as some trends are opposite for bearing capacity factor and slope factor. Error contributed to using the superposition method has been minimised by considering the effect of soil weight and the surcharge together through bearing capacity factor ($N_{\gamma q}$).

Fig. 2 shows the comparison of the upper and lower bound bearing capacity factors for different angles of internal friction of soil. The upper and lower bound bearing capacity factors are almost identical for soils with small internal friction angles (Fig. 2a). The difference between upper bound and lower bound increases with an increase in the angle of internal friction of soil; however, the error always remains trivial (< 3 %). The error is found to be small due to the application of second-order cone programming for optimisation. Therefore, it can be stated that the bearing capacity factors presented in the manuscript are mostly close to exact values.
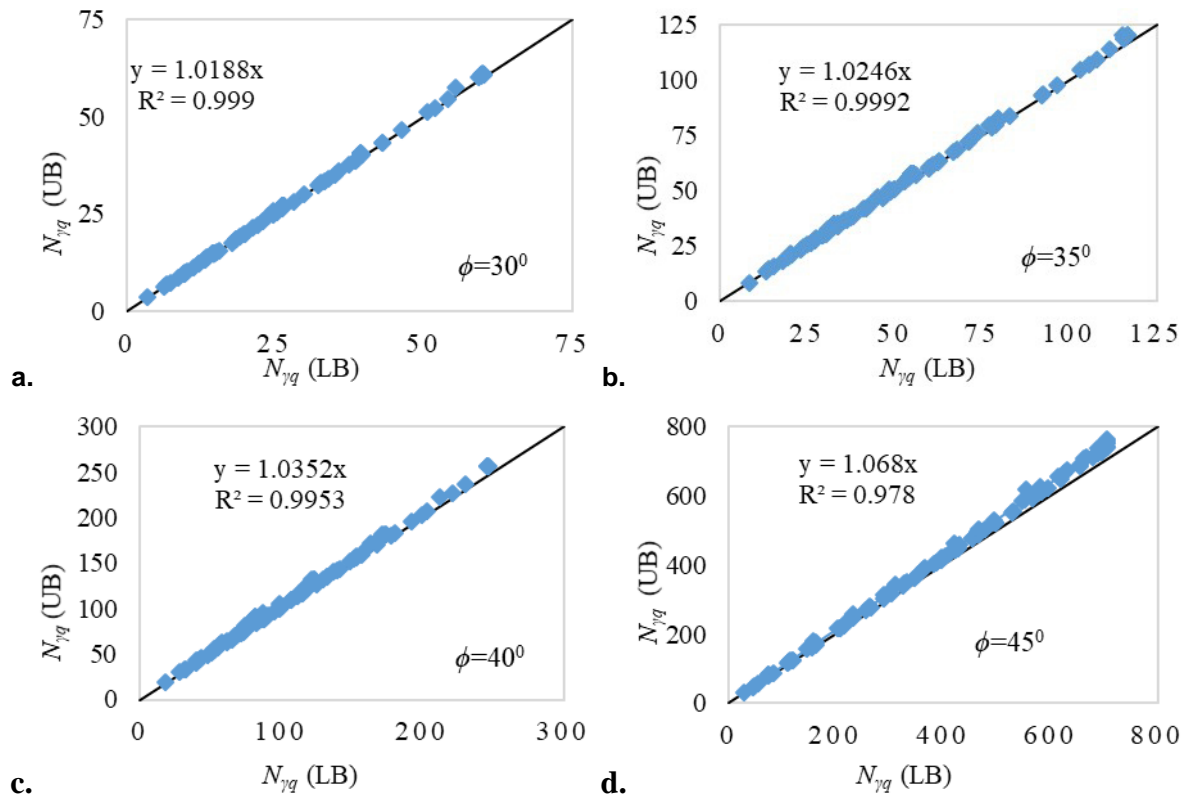
**Figure 2. Comparison of upper and lower bounds bearing capacity factor
for footing resting on slope: (a) ϕ = 30°; (b) ϕ = 35°; (c) ϕ = 40°; (d) ϕ = 45°.**

Fig. 3 shows the typical variation in bearing capacity factor ($N_{\gamma q}$) and slope factor (S_f) with the setback for a soil with a friction angle of 35^0. In all the cases, $N_{\gamma q}$ and S_f improve with an increase in the setback. The soil confinement increases, and the instability caused by the slope reduces with the setback. Also, passive resistance increases with an increase in setback due to an increase in a surcharge. The stiffness of the foundation-soil system enhances with an increase in the setback, which also improves the bearing capacity [12, 24]. These factors contribute to bearing capacity enhancement. The results are comparable to earlier studies of Rostami and Ghazavi [37] and Keskin and Laman [20] for an embedment depth of zero (Fig. 3 a, b). However, both the studies were confined to surface footings with a maximum setback of 5B.

The S_f is higher in the case of gentle slopes and becomes constant at a relatively small setback. The bearing capacity and slope factors become almost constant with a setback ratio (B'/B) of 3, 5, and 7 for foundation depth ratio (D/B) of 0, 0.5, and 1.0, respectively. The rate of increase in S_f and $N_{\gamma q}$ is large in steep slopes compared to gentle slopes. The curves are relatively gentle in case of footing with a higher depth ratio. It means the bearing capacity enhancement with a setback is relatively more in steep slope and footing resting on the ground surface.

Figure 3. Effect of a setback (a) $N_{\gamma q}$, D_f/B = 0; (b) S_f, D_f/B = 0; (c) $N_{\gamma q}$, D_f/B = 0.5; (d) S_f, D_f/B = 0.5; (e) $N_{\gamma q}$, D_f/B = 1.0; (f) S_f, D_f/B = 1.0.

Fig. 4. shows that at a smaller setback, strength is mobilised only on the sloping side. It means that the soil on the sloping side entirely governs the behaviour of footing at a low setback. The strength mobilisation on the level side of the footing axis enhances with the setback. At a particular setback, strength mobilises equally on both sides of the footing axis, and the failure zone becomes almost symmetrical, and the slope factor also becomes close to one. This setback is stated as a critical setback. For the angle of internal friction of 35°, the slope influences the failure zone up to the setback of 7B-8B. The influence of soil surcharge is absent at zero setbacks (Fig. 4a). The surcharge increases with an increase in the setback and reaches a maximum value at level ground. Therefore, bearing capacity increases with an increase in the setback. A similar observation was made in the experimental study carried by Chang *et al.* [38]. The slip surface direction changes from lateral to the upward direction with an increase in the setback (Fig. 4). The area within the failure zone or length of failure surface increases with an increase in the setback; therefore, bearing capacity increases also increases.
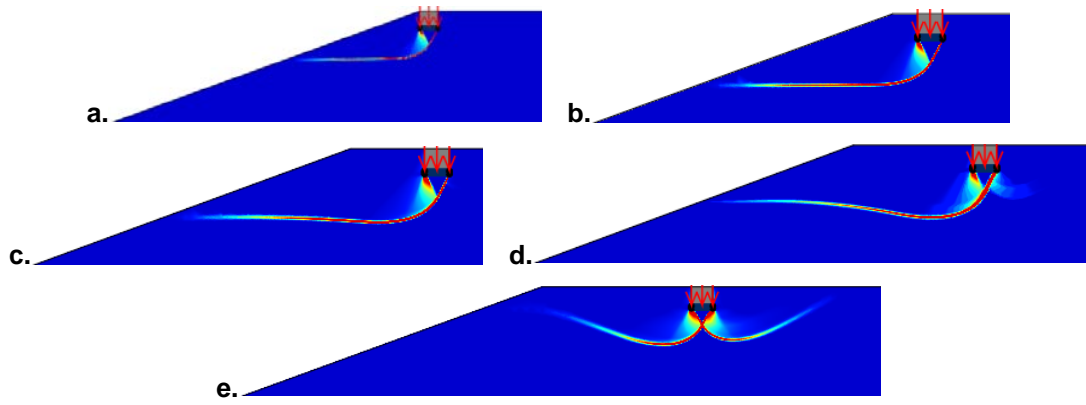
Figure 4. Failure mechanism for various setback for soil of internal friction 35°:
(a) B'/B = 0; (b) B'/B = 1; (c) B'/B = 3; (d) B'/B = 5; (e) B'/B = 7.

The typical variations in $N_{\gamma q}$ and S_f with the slope angle for soil with internal friction of 35° are shown in Fig. 5. The S_f as well $N_{\gamma q}$ reduces with an increase in slope, and the reduction depends on the embedment depth of foundation and setback. The reduction in $N_{\gamma q}$ and S_f with an increase in slope is very significant at zero setbacks. It is also observed that the reduction in bearing capacity factor, as well as slope factor, augments with an increase in the footing depth. In large setbacks, $N_{\gamma q}$ and S_f remain relatively unaffected with the change in slope.
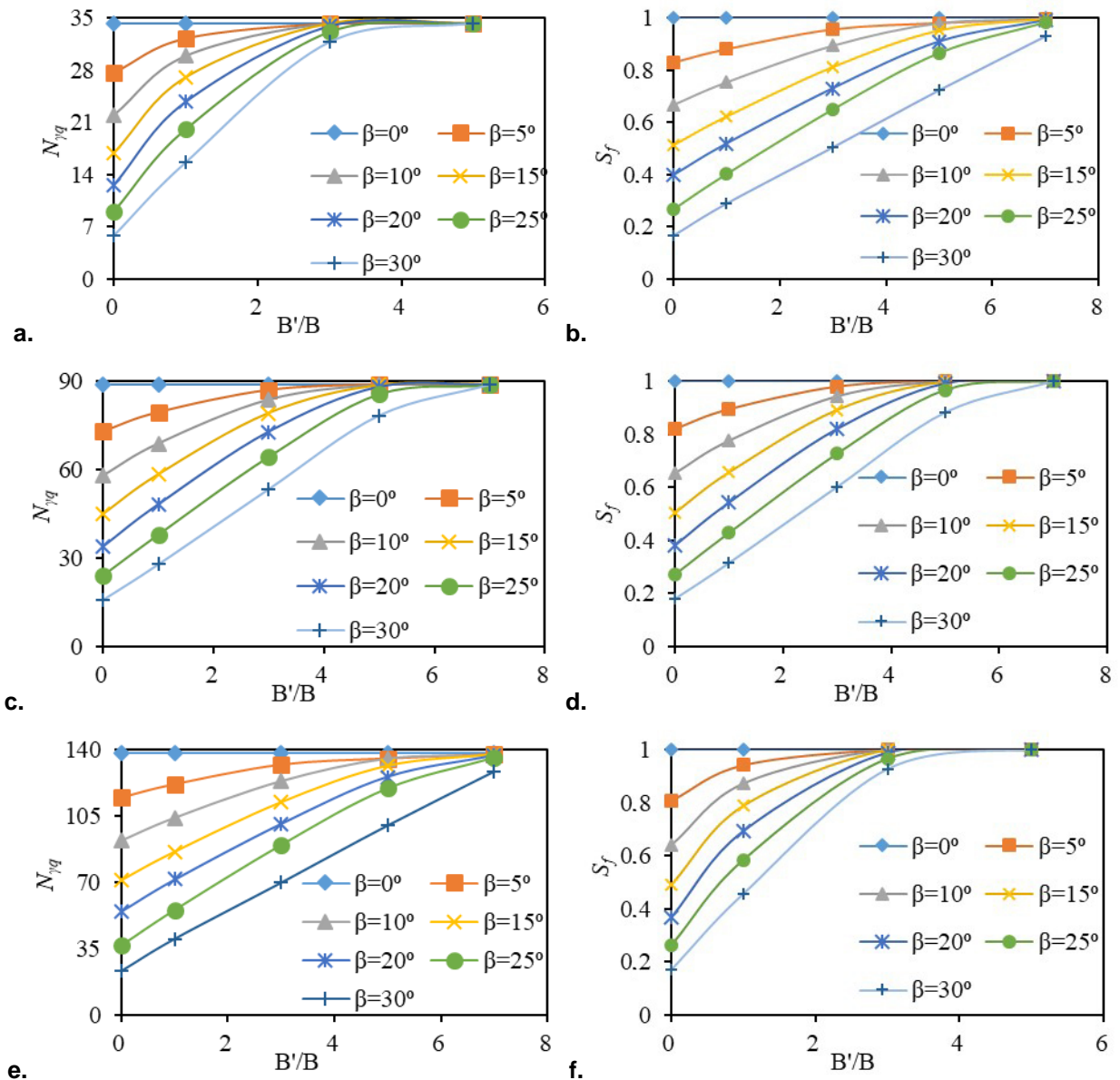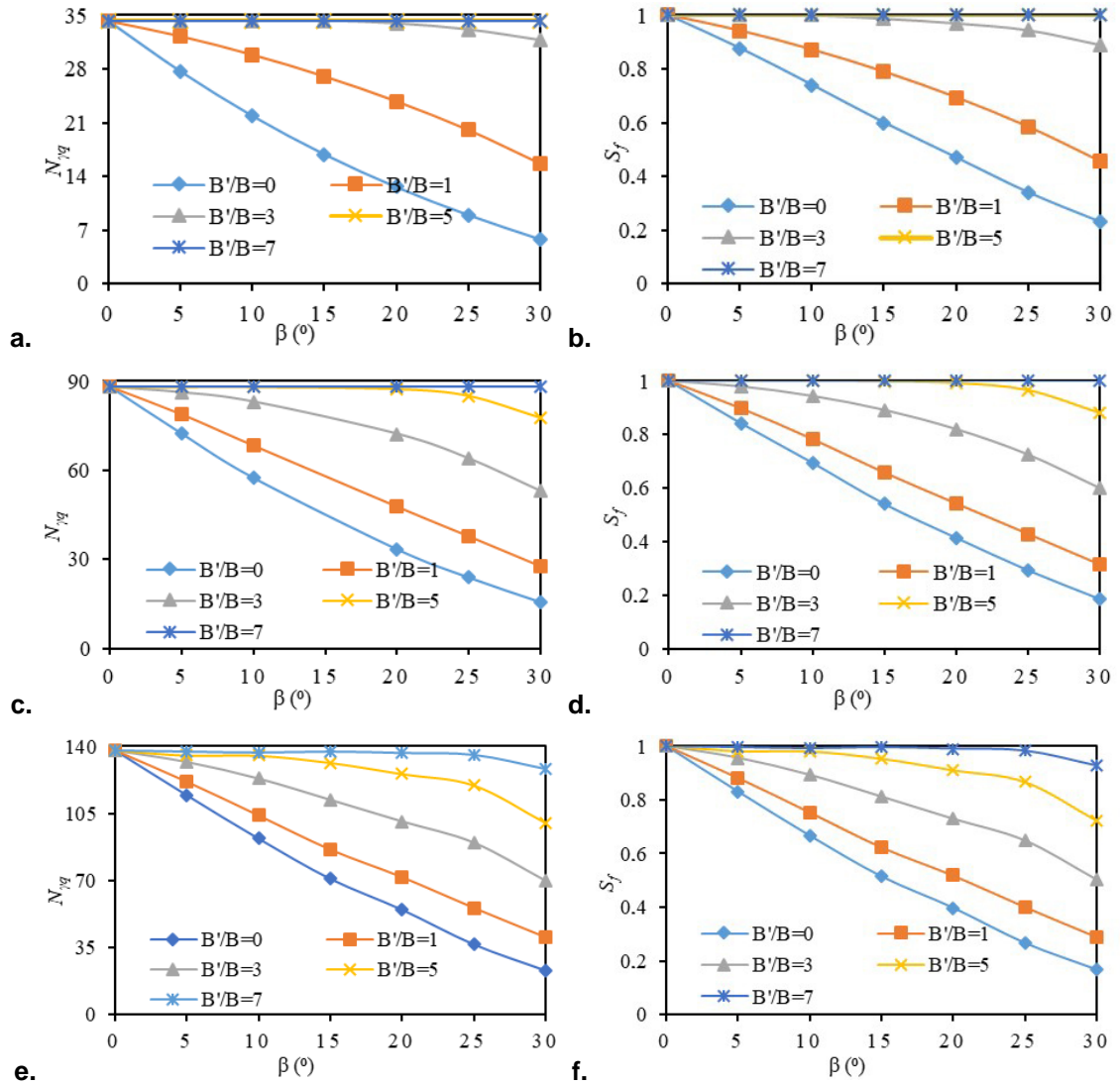

Figure 5. Effect of slope angle: (a) $N_{\gamma q}$, $D_f/B = 0$; (b) S_f, $D_f/B = 0$; (c) $N_{\gamma q}$, $D_f/B = 0.5$;
(d) S_f, $D_f/B = 0.5$; (e) $N_{\gamma q}$, $D_f/B = 1.0$; (f) S_f, $D_f/B = 1.0$.

The effect of slope on the failure mechanism for a footing of depth ratio 1.0 is shown in Fig. 6. The results are shown for a footing resting at a setback of 5B on soil with internal friction of 35°. On level ground, the failure surface is symmetrical and gradually becomes one-sided with an increase in the slope (Fig. 6 a-d). It is due to a decrease in the shear dissipation on the level side of the footing. At steep slopes, the failure mode is a combination of the slope and bearing capacity failures (Fig. 6 d). Further increasing the slope results in an unstable slope. At this stage, the interaction of slope with the footing is maximum, and the failure is entirely a slope failure. This stage depends on the angle of internal friction of soil as well as loading intensity. The failure surface orientation is upward at a smaller slope (general shear failure) and is turning gradually to lateral and finally toward the downward side, i.e., towards the slope base with an increase in the slope (Fig. 6 a-d).
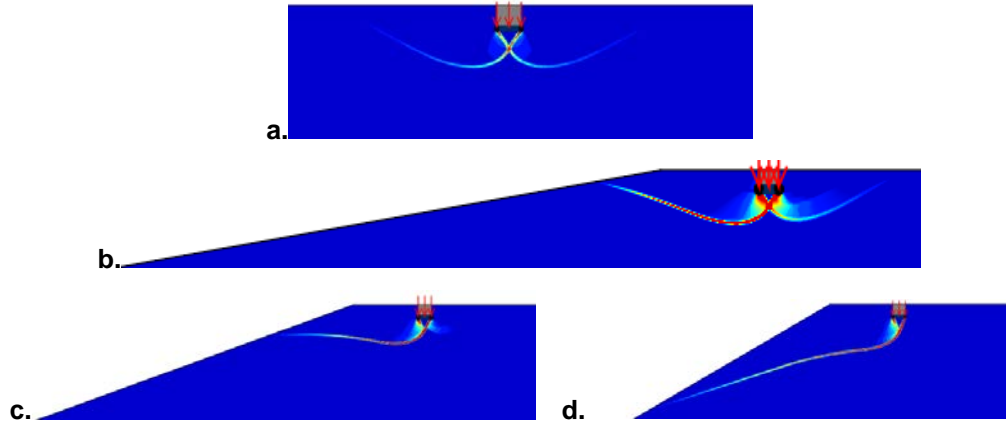
Figure 6. Failure mechanism for various slope gradients:
(a) β = 0°; (b) β = 10°; (c) β = 20°; (d) β = 30°.

Fig. 7 shows that $N_{\gamma q}$ increases and S_f decrease with an increase in embedment depth of footing. The contrary behaviour is observed as increasing the depth increases the bearing capacity relatively by a large amount on the level ground as compared to footings on slopes. The increase in footing depth indirectly increases the setback also (at the base level of footing). Therefore, the bearing capacity increases with the footing depth. The decrease in the slope factor indicates the increase in the adverse effect of the slope. The effect of footing depth is significant at a higher setback. The observation is contrary to Castelli and Motta [29], where the influence of embedment depth on S_f was found to be insignificant. The effect of depth ratio of footing is relatively more significant for soil with a low friction angle, and a similar observation has also been made for the footings resting on sloping ground. Garnier *et al.* [39] found the slope factor is always greater than 0.2 in steep slopes (3V: 2H) for soils with an internal friction angle of 40.5°. However, in the present study, it is found to be 0.14.
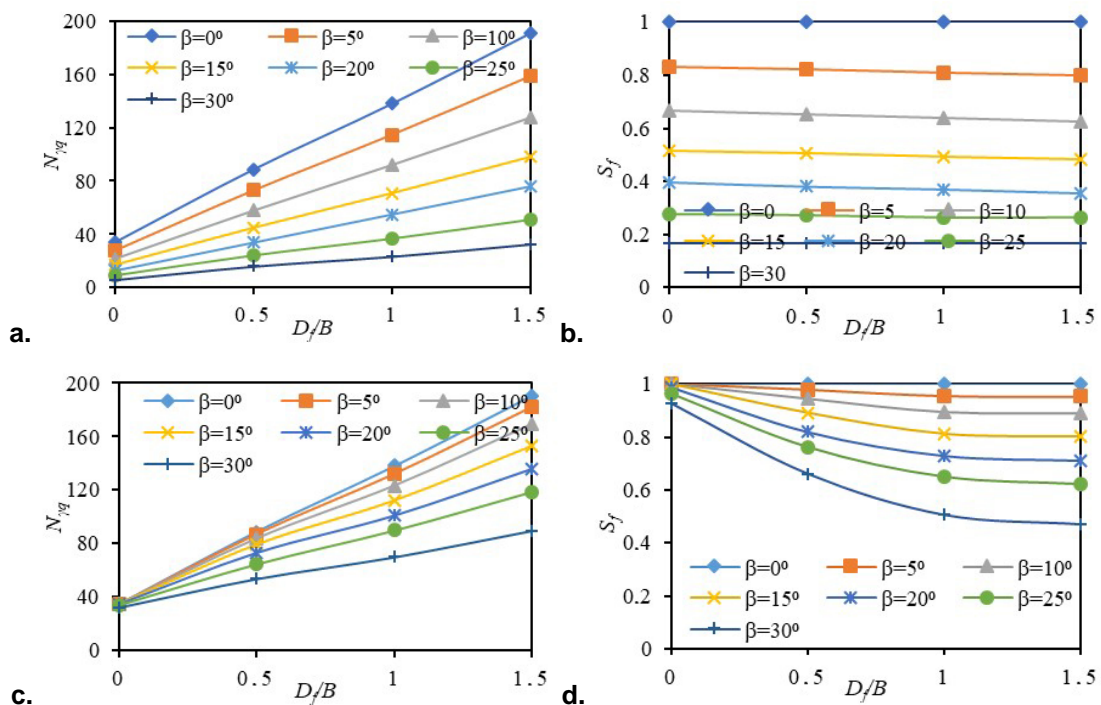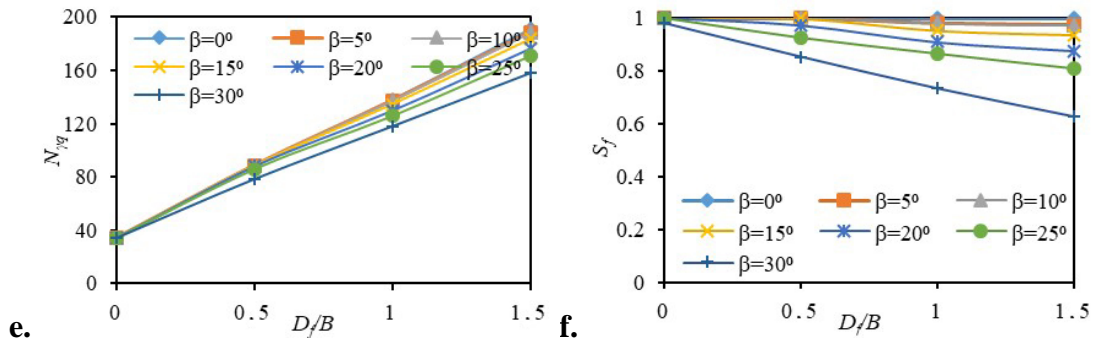
Figure 7. Effect of embedment depth of footing: (a) $N_{\gamma q}$, B'/B = 0; (b) S_f, B'/B = 0; (c) $N_{\gamma q}$, B'/B = 3; (d) S_f, B'/B = 3; (e) $N_{\gamma q}$, B'/B = 5; (f) S_f, B'/B = 5.

Fig. 8 shows that the failure surface is symmetrical about the footing axis, and is independent of the slope effect when a footing is resting on the ground surface. Therefore, the slope factor is either 1 or close to 1 (Fig. 8a). The footing resting on ground surfaces fails due to local shear failure (Fig. 10 a). An increase in the slip surface length and the area is observed with an increase in the footing depth, which increases the bearing capacity (Fig. 8 a, c, e). However, the contribution from the level side of the soil reduced with footing depth. It indicates the increased interaction between slope and footing, which decreases the slope factor. Initially, the failure surface orientation is upward (Fig. 8 a, b), but it changes from upward to lateral direction with an increase in footing depth (Fig. 8 b, c). Increasing the footing depth from 1B to 1.5B increases the failure zone area marginally (Fig. 8 c, d). Therefore, bearing capacity increases only slightly.
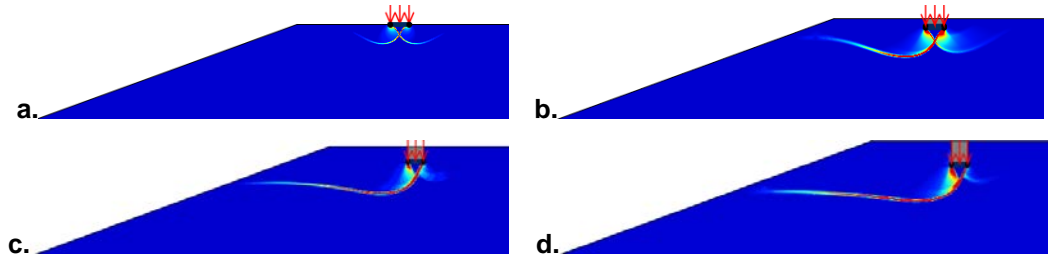
Figure 8. Effect of embedment depth of footing on failure surface:
(a) D_f/B = 0; (b) D_f/B = 0.5; (c) D_f/B = 1.0; (d) D_f/B = 1.5.

3.1.4 Effect of angle of internal friction of soil

For a particular setback, slope, and embedment depth of footing, $N_{\gamma q}$ increases, and the S_f decreases with an increase in the angle of internal friction of soil (Fig. 9). The increase in $N_{\gamma q}$ with an angle of internal friction is relatively substantial in the level ground as compared to slopes. The reduction in S_f is relatively higher for a small setback and a steep slope. The soil with a higher angle of internal friction can be stable even at a higher inclination ($\beta = \phi°$); therefore, the slope factor is relatively less. The relationship between S_f and friction angle of soil is linear for gentle slopes and becomes nonlinear with an increase in the slope. In soils with a higher internal friction angle, the pressure from the external load is dispersed over a relatively large area. Therefore, a large setback needs to be maintained to minimise the slope effects [22, 24]. Therefore, the slope factor reduces with an increase in the angle of internal friction of soil. This observation is contradictory to those made by Hansen [2], Vesic [3], Gemberlin [26], and Castelli and Motta [29].
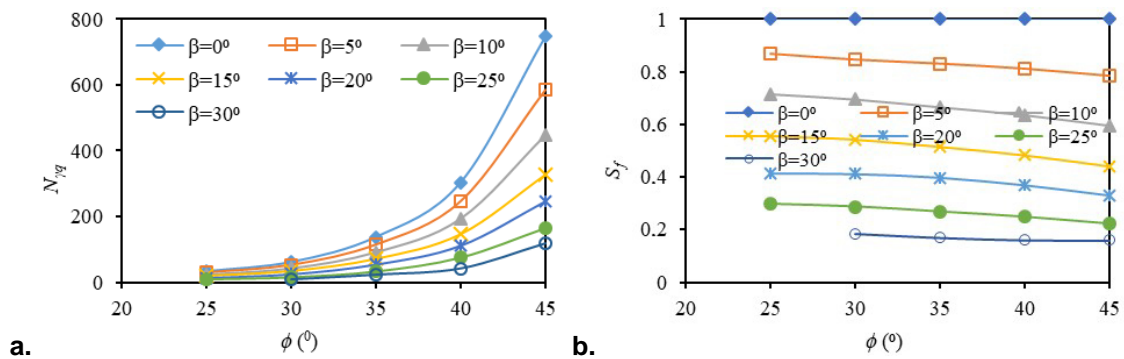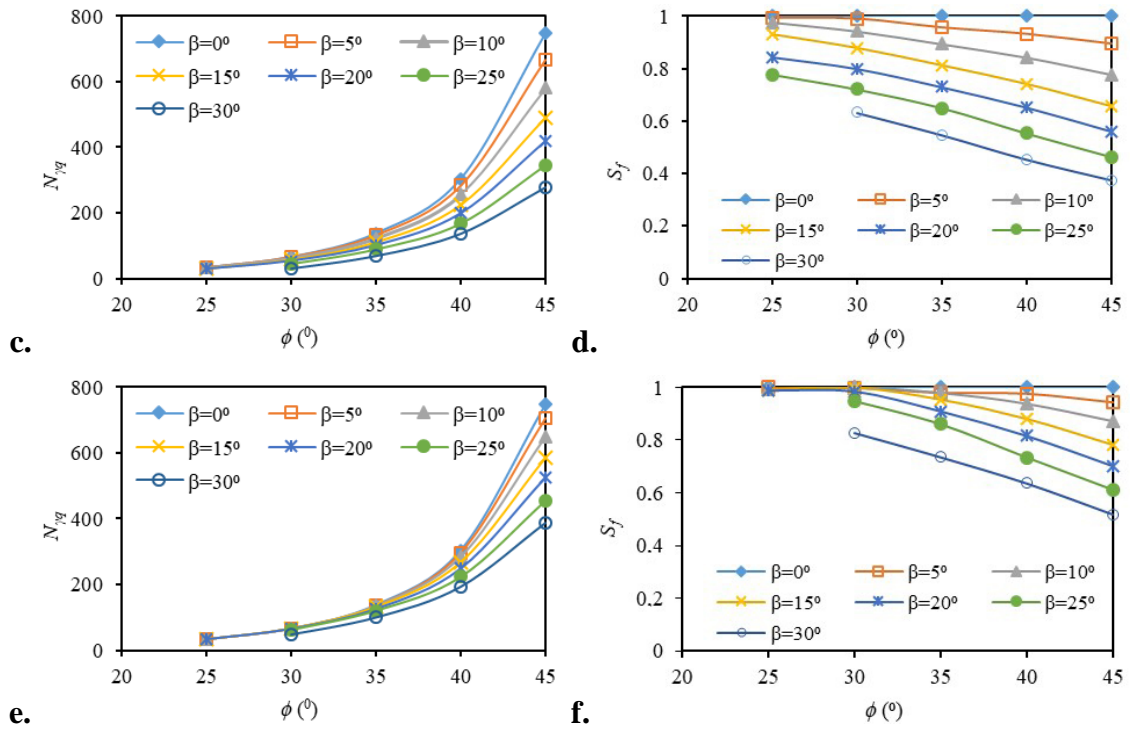
Figure 9. Effect of friction angle for a footing of zero embedment resting over soil of internal friction 35⁰: (a) $N_{\gamma q}$, B'/B = 0; (b) S_f, B'/B = 0; (c) $N_{\gamma q}$, B'/B = 3; (d) S_f, B'/B = 3; (e) $N_{\gamma q}$, B'/B = 5; (f) S_f, B'/B = 5.

The effect of the angle of internal friction of soil on the failure mechanism is shown in Fig. 10. An increase in the angle of internal friction of soil increases the failure zone area, which increases the bearing capacity (Fig. 10 a). Also, the failure is a local shear failure, and the slip surface is not developing clearly in soils with a low angle of internal friction (10 a). The slip surface/fracture surface is small and symmetrical about the footing axis for a soil with a small internal friction angle. Therefore, the slope factor is close to 1. The failure mechanism changes gradually from symmetrical to one-sided, increasing the soil angle of internal friction (Fig. 10 a-d). It indicates the effective transfer of stress (plastic zone) toward the slope-side due to early mobilization of strength. However, stresses are not mobilizing on the level side of the footing axis. Therefore, the slope factor reduces significantly.
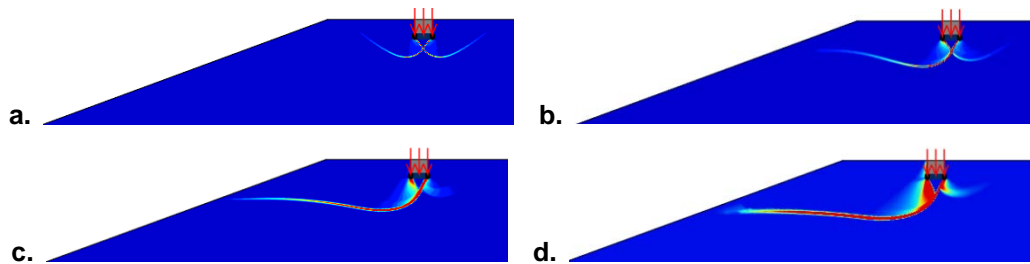
**Figure 10. Effect of angle of internal friction of soil on failure mechanism:
(a) ϕ = 25°; (b) ϕ = 30°; (c) ϕ = 35°; (d) ϕ = 40°.**

Table 4. Slope factor for cohesionless soil slopes.

ϕ^0	β^0	S_f
25	05–20	0.5–1.0
30	5–20	0.45–1.0
	20–30	0.25–0.45
35	0–20	0.4–1.0
	20–30	0.20–0.4
40	0–20	0.35–1
	20–40	0.1–0.35
45	0–20	0.3–1
	20–45	0.05–0.30

3.2. Experimental study results and comparison

The load and settlement of footing were recorded for the various setback, slope, and relative density of soil. The load-settlement characteristic of footing resting on the slope is shown in Fig. 11. Failure points are clearly visible in almost all cases, which indicates general shear failure. General shear failures are observed in the numerical study as well. Fig. 11 (a, b) shows that the failure load increases with an increase in sand and setback density. The slope effect is shown in Fig. 11(c) for a footing resting at $B' = 0$ on soil with a relative density of 50 %. It indicates that load-settlement behaviour changes significantly with the decrease in slope. The effect of slope on load-settlement characteristic is relatively more noticeable as compared to relative density and setback.
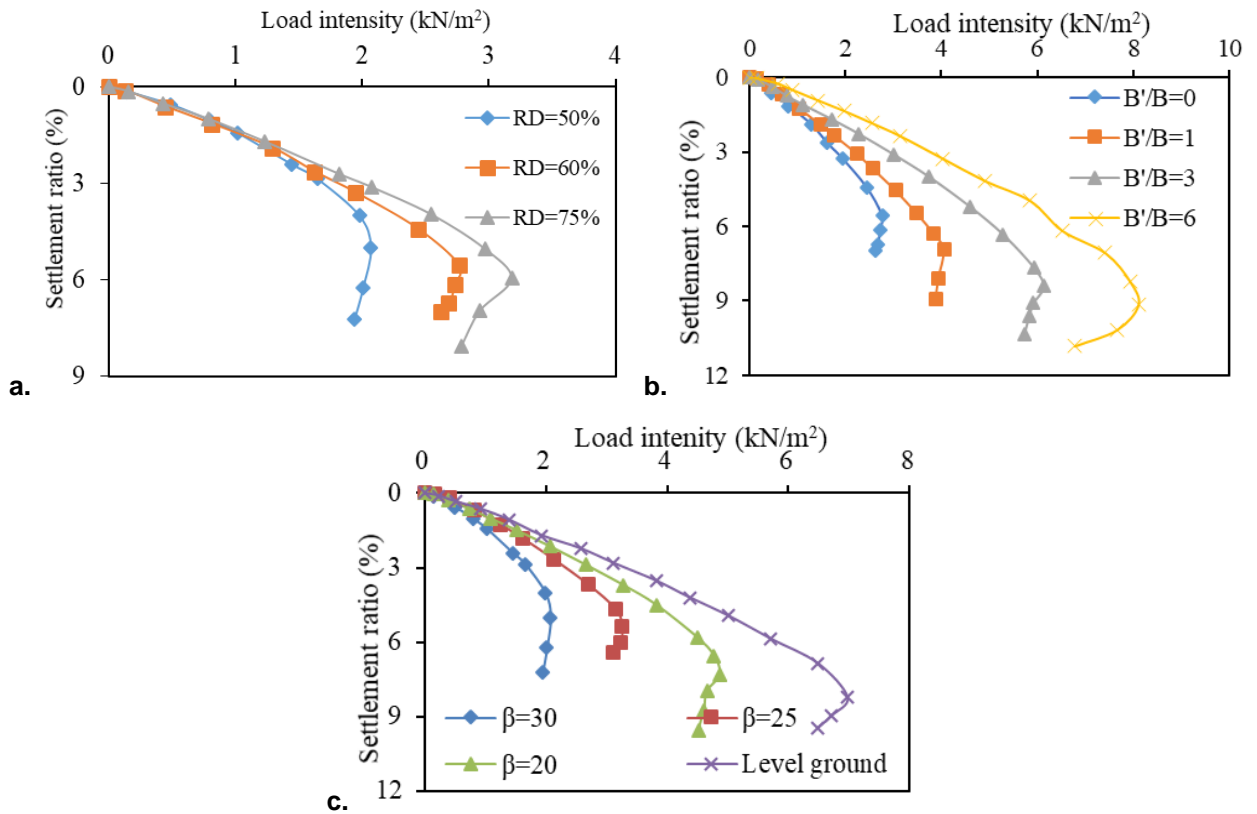
Figure 11. The load-settlement relationship for model footing:
(a) effect of relative density; (b) effect of a setback; (c) effect of slope.

The results of the numerical study are compared with the experimental studies and shown in Fig. 12. The experimental and numerical study results are shown as dashed and continous lines, respectively. The effect of the setback on S_f for a slope of 20^0 is compared in Fig. 12 (a). Similarly, the effect of the slope is compared in Fig. 12 (b). Though there is a small quantitative difference in the experimental and numerical study results, the qualitative similarity (result trends) exists between both cases. The rate of increase in S_f with the setback is more in the numerical study (Fig. 12 a). The difference is maximum for a small setback, which reduces with an increase in the setback. In soils with low friction angle (loose soils), the prevailing confining pressures and mobilised friction angles are almost identical in the experimental and numerical study. Therefore, the experimental results are reasonably close to the full-scale numerical study. The critical value of setback is also remained unaffected by the method of determination (experimental and numerical) for soils with a low angle of internal friction ($\phi < 35^0$). The difference in the results of full and small-scale testing may become noticeable with an increase in the angle of internal friction of soil. The small-scale model underestimates the severity of the slope effect compared to the full-scale study as prevailing confining pressure is higher in actual cases.

a.

b.
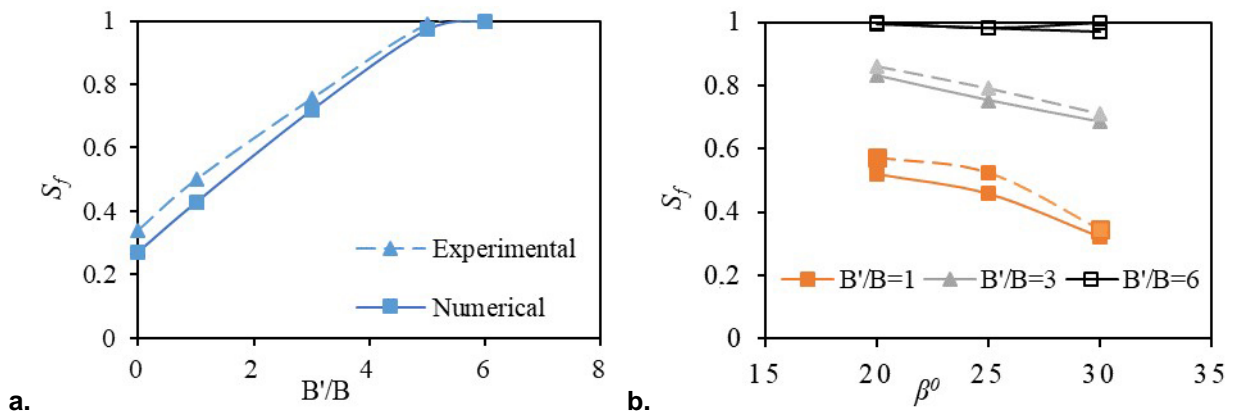
**Figure 12. Comparison of experimental results with numerical results:
(a) effect of a setback; (b) effect of slope.**

Numerical results are also compared with earlier published results for a footing resting precisely on slope crest with zero setbacks and are shown in Fig. 13 [2, 14, 40–45]. It indicates that for the smaller angle of internal friction (ϕ = 20°), the values obtained through the present numerical study are almost of average values proposed by earlier studies (Fig. 13 a). However, for a higher angle of internal friction (ϕ = 40°), the values obtained through the present numerical study are either lower side or close to the average values proposed by earlier studies (Fig. 13 c).

In most of the cases, the bearing capacity factor is found close to Hansen's [2] and Giroud *et al.* [41]. This difference in the values is observed due to the different methodologies adopted by earlier studies. The reduction in bearing capacity with slope is significant in soil with a low internal friction angle (ϕ = 20°), which reduces with an increase in the internal friction angle (ϕ = 30°, 40°). Bearing capacity is less than those presented by Chen and Davidson [43] using upper bound and is more than those given by Absi [40].

a.

b.

c.

- – – ◆ – · Absi [40]
- – – ■ – · Hansen [2]
- – – ▲ – · Giroud et al. [41]
- – – – Mizuno [42]
- – – ✳ – · Chen [43]
- – – ● – · Meyerhof [1]
- —✕— Present study
- – – ● – · Tatsuoka et al. [44]
- – – ● – · Graham et al. [14]
- —+— Lebegue [45]
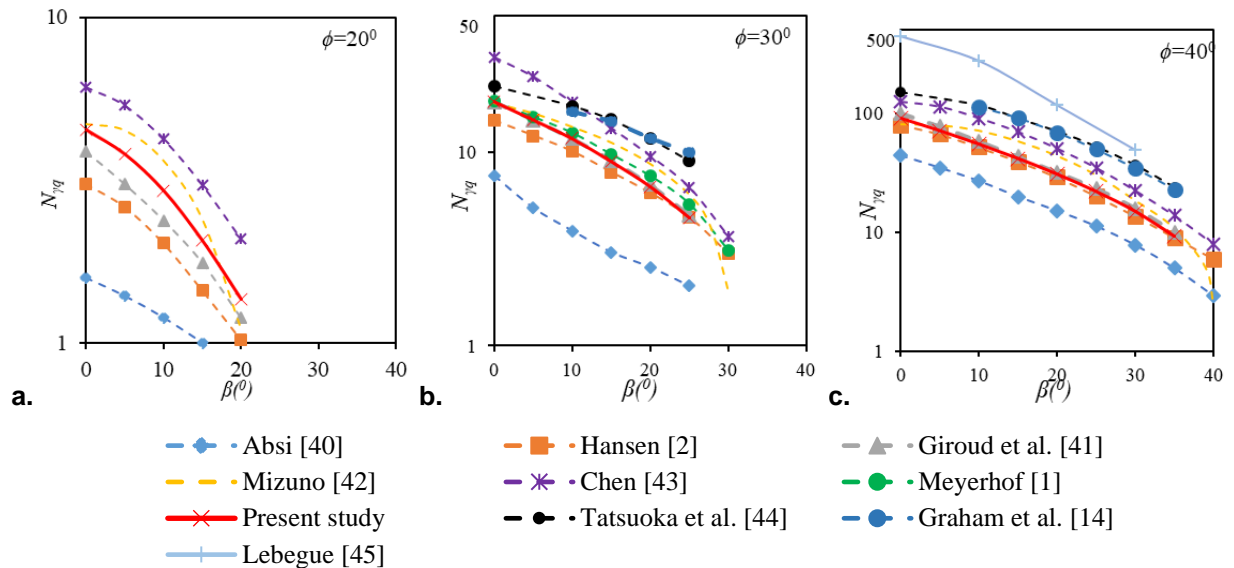
**Figure 13. Comparison of results with earlier results for a footing resting precisely
on slope crest: (a) ϕ = 20⁰, (b) ϕ = 30⁰, (c) ϕ = 40⁰.**

3.3. Statistical analyses and validation of equations

Statistical analyses were also performed to develop nonlinear equations to predict bearing capacity, slope factor, and critical setback. It can be seen from the numerical analysis that setback, slope, soil friction angle, and footing depth influencing the bearing capacity of a footing on the slope. The numerical study results also show that the relationship between the independent parameters and S_f and $N_{\gamma q}$ is nonlinear. Consequently, nonlinearity needs to be considered while developing equations of S_f, $N_{\gamma q}$, and B'. The precise nonlinearity is not known initially. It is presumed that the S_f, $N_{\gamma q}$, and B' depend not only on four parameters but also on derivatives of these factors.

Initially, a total of 96 parameters, which are the function of initially known four independent variables, are considered in the regression analysis. Along with the multicollinearity, the R² was used to remove the

variables, not affecting bearing capacity. It is observed that only 12 parameters, including the four basic parameters, critically affect the slope factor. Later these 12 variables were used to develop the equation. Similarly, for developing the bearing capacity factor ($N_{\gamma q}$) equation, 14 variables and 9 variables have been used for the critical setback. Fig. 14 (a, b, c) compares observed and predicted slope factors and critical setback and bearing capacity factor.
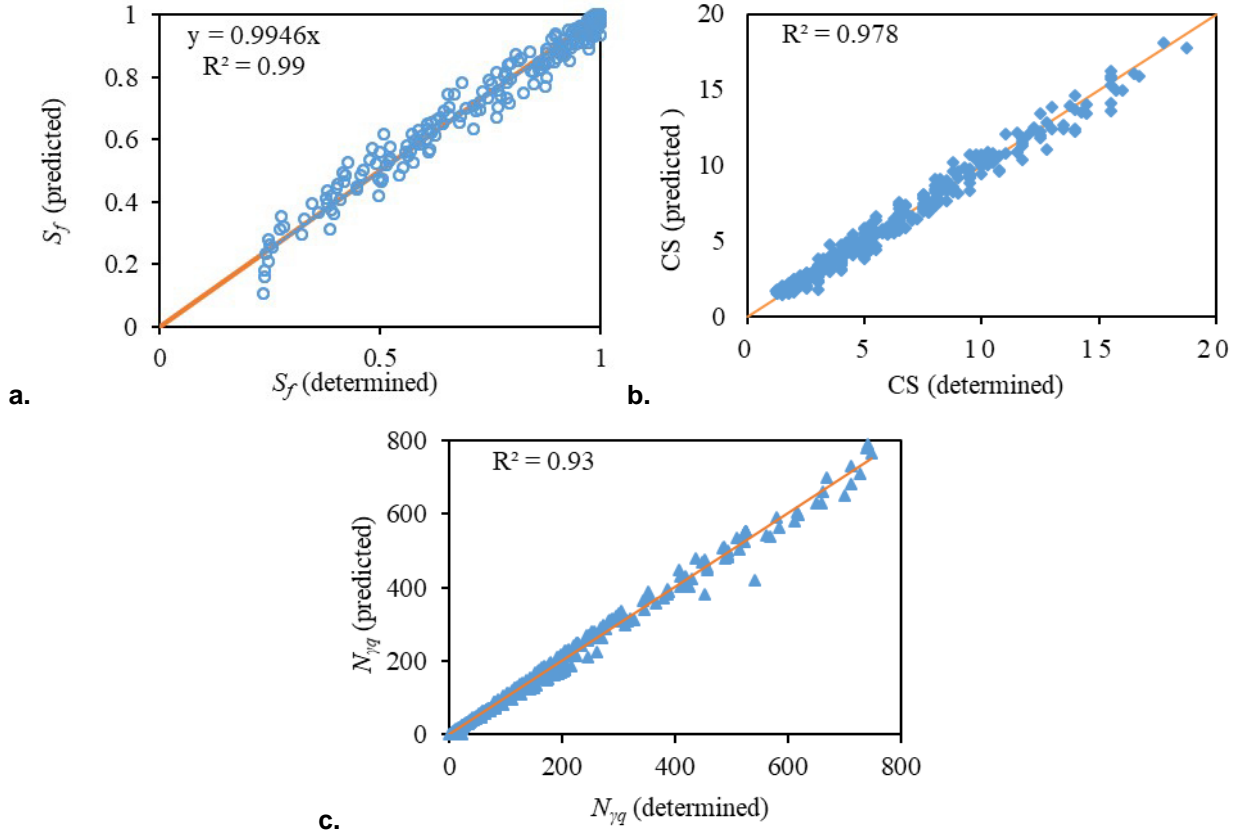
Figure 14. Determined vs. predicted values:
(a) slope factor; (b) critical setback; (c) bearing capacity factor ($N_{\gamma q}$).

$$S_f = 1 + 0.12\left(B'/B\right)\left(1 + 2.1\tan\beta - 0.47\tan\phi\right) - \tan\beta\left(1 - \tan\beta\right) -$$
$$-0.04\left(D/B\right)\left(B'/B + 7.9\tan\beta - D/B\right) - \tag{1}$$
$$-0.015\left(B'/B\right)^2\left(1 - 0.33\,D/B - 0.66\tan\phi\right) - 0.17\tan\beta\tan\phi\left(B'/B + 5.3\right)$$

$$N_{\gamma q} = 400 - 100\,D/B\left(1 - \tan\phi\right) - 60\,B'/B\left[1 + 0.1\left(B'/B\right)^2 - 0.45\left(B'/B\right)\beta\right] -$$
$$-27\,D/B\left(D/B - 0.5\,B'/B + 12\left(D/B\right)\beta\right) + 814\left(1 - 1.5\tan\phi + 0.03\beta^2\right) - \tag{2}$$
$$-1520\tan\phi\left[1 - 0.9\tan^2\phi - 0.05\left(B'/B\right)\tan\phi\right]$$

$$CS = 2.5 - 1.2\,D/B\left[1 - 0.8\left(D/B\right) - 0.4\tan\phi\right] -$$
$$-5.5\tan\phi\left(1 - \tan\phi - 3.2\beta\right) - 8.5\beta\left(1 - 1.3\beta - 0.6\,D/B\right) \tag{3}$$

$$N_{\gamma q(slope)} = N_{\gamma q(level\ ground)}\left(S_f\right) \tag{4}$$

Bearing capacity on slope = Bearing capacity on level ground*Slope factor $\qquad$ (5)

Bearing capacity on slope = $\dfrac{1}{2}B\gamma N_{\gamma q(slope)}$ $\qquad$ (6)

where, S_f = Slope factor, B' = setback, B = width of footing, CS = critical setback, β = slope in degree, and ϕ = angle of internal friction of the soil in degree.

R^2 is reduced from 0.9925 to 0.9807 when the number of the insignificant variables were removed from the analysis. It confirms that the other dependents variables do not affect the bearing capacity, as assumed in the initial phase of the regression analysis. The slope factor (S_f), bearing capacity factor ($N_{\gamma q}$), and critical setback can be determined by Eqns. 1, 2, and 3, respectively. S_f cannot be more than 1, as bearing capacity on slopes may reach the maximum level ground. If equation 1 predicts values more than 1, then it should be corrected to 1. Eqn. 3 can be used to determine the critical location of the footing relative to the slope crest. Critical location means setback at which the effect of the slope is almost negligible. The slope factor can be also be used to assess the effect of slope angle on bearing capacity. Eqn. 4 is beneficial if the bearing capacity factor for the level ground is already known. Alternatively, bearing capacity can be determined by using Eqns. 5 and 6. These equations have developed considering the influence of the slope geometry, footing depth, setback, and the angle of internal friction of the soil.

A few earlier studies have given importance to setback and determined the critical setback, at which the effect of slope becomes negligible [17–18, 22, 24]. However, change in bearing capacity and slope factor is relatively more noticeable with a change in slope inclination and internal friction angle. Therefore, these factors need relatively more attention in design foundations. The foundation can be placed near to slope crest without much compromising bearing capacity if the slope is modified considering the steepness of slope and angle of internal friction of soil. The slope can be modified either by making it relatively gentle or enhancing the angle of internal friction of soil through various available techniques. Both options are feasible from a practical point of view. Therefore, it is suggested to place the footing close to the crest of the modified slope.

4. Conclusions

1. The presence of slope reduces the overall mobilisation of shear strength, particularly on the level side of the footing, which reduces the bearing capacity of footing. The range of slope factors varies from 0.05 to 1, depending on various factors. It indicates 95 % to 0 % reduction in bearing capacity of footing due to the adverse slope effects.

2. The bearing capacity factor increases and the slope factor reduces with an increase in the footing depth and angle of internal friction of soil due to change in failure mechanism.

3. The failure mechanism changes from both sides to one side with an increase in slope inclination, footing depth, and angle of internal friction of soil. Therefore, it is recommended to consider one side failure mechanism for designing the footings resting on slopes.

4. The effect of slope inclination and angle of internal friction of soil on bearing capacity, slope factor, and failure mechanism is relatively more noticeable than the footing depth and setback.

5. The increase in bearing capacity with setback contributes to an increase in strength mobilisation of soil and change in failure mechanism from local shear failure or rotational failure to general shear failure.

6. The load-settlement behaviour of footing improves with an increase in the setback and relative density of soil. However, the behaviour worsens with an increase in slope inclination. The model testing results are found reasonably close to numerical study.

7. Load-settlement plots and failure mechanisms show that the failure is bearing capacity rather than slope failure for the stable slopes. However, in the case of steep slopes or marginally stable slopes, the failure is a combination of slope and bearing failures.

8. The equation is also proposed to determine the critical location of footing relative to slope crest (critical setback). The proposed equations for slope factor, bearing capacity factor, and critical setback considers the possible factors affecting footing behaviour, such as footing depth, slope inclination, and soil strength parameter.

9. It is recommended to either modify the slope geometry or increase the soil strength and place the footing close to the slope crest.

References

1. Meyerhof, G.G. The Ultimate Bearing Capacity of Foundation on Slopes. 4th Int. Conf. on Soil Mech. and Foundation Engineering. 1957. 3. Pp. 384–386.
2. Hansen, J.B. A Revised and Extended Formula for Bearing Capacity. Dan. Geotech. Institute. 1970. Bulletin No. 28.

3. Vesic, A.S. Analysis of ultimate loads of shallow foundations. Journal of the Soil Mechanics and Foundations Division. 1973. 99(1). Pp. 45–73.

4. Bowles, J.E. (1988). Foundation engineering and design. McGraw-Hill, Inc.

5. Kumar, J., Mohan Rao, V.B.K. Seismic bearing capacity of foundations on slopes. Geotechnique. 2003. 53(3). Pp. 347–361.

6. Jahanandish, M., Keshavarz, A. Seismic bearing capacity of foundations on reinforced soil slopes. Geotextiles and Geomembranes. 2005. 23(1). Pp. 1–25.

7. Choudhury, D., Subba Rao, K.S. Seismic bearing capacity of shallow strip footings embedded in slope. International Journal of Geomechanics. 2006. 6(3). 176–184.

8. Kumar, J., Ghosh, P. Seismic bearing capacity for embedded footings on sloping ground. Geotechnique. 2006. 56(2). Pp. 133–140.

9. Huang, C.C., Kang, W.W. Seismic bearing capacity of a rigid footing adjacent to a cohesionless slope. Soils and Foundations. 2008. 48(5). Pp. 641–651.

10. Huang, C.C. Effects of horizontal and vertical seismic loads on the bearing capacity of a surface footing adjacent to a slope. Soils and Foundations. 2009. 49(2). Pp. 249–258.

11. Kumar, J., Chakraborty, D. Seismic bearing capacity of foundations on cohesionless slopes. Journal of Geotechnical and Geo-Environmental Engineering. 2013. 139(11). Pp. 1986–1993.

12. Varzaghani, I.M., Ghanbari, A. A new analytical model to determine dynamic displacement of foundations adjacent to slope. Geomechanics and Geoengineering. 2014. 6(6). Pp. 561–575.

13. Chakraborty, D., Kumar, J. Seismic bearing capacity of shallow embedded foundations on a sloping ground surface. International Journal of Geomechanics. 2014. 15(1), 04014035.

14. Graham, J., Andrews, M., Shields, D.H. Stress characteristics for shallow footings in cohesionless slopes. Canadian Geotechnical Journal. 1988. 25(2). Pp. 238–249.

15. Saran, S., Sud, V.K., Handa, S.C. Bearing Capacity of Footings Adjacent to Slopes. Journal of Geotechnical Engineering, ASCE. 1989. 115(4). Pp. 553–573.

16. Lee, K.M., Manjunath, V.R. Experimental and numerical studies of geosynthetic-reinforced sand slopes loaded with a footing. Canadian Geotechnical Journal. 2000. 37(4). Pp. 828–842.

17. Huang, C.C., Kang, W.W. The effects of a setback on the bearing capacity of a surface footing near a slope. Journal of Geo-Engineering. 2008. 3(1). Pp. 25–32.

18. Shukla, R.P., Jakka, R.S. Determination and prediction of bearing capacity on clayey slopes. Acta Geotechnica Slovanica. 2019. 16(2). Pp. 50–65.

19. Krabbenhoft, S., Damkilde, L., Krabbenhøft, K. Upper and Lower Bound Calculations of the Bearing Capacity of Strip Footings near Slopes in Cohesionless Soil. In the International Conference on Structural Engineering. Mechanics and Computation. 2013. Pp. 2479–2484.

20. Keskin, M.S., Laman, M. Model studies of bearing capacity of strip footing on sand slope. KSCE Journal of Civil Engineering. 2013. 17(4). Pp. 699–711.

21. Acharyya, R., Dey, A. Finite element investigation of the bearing capacity of square footings resting on sloping ground. INAE Letters. 2017. 2(3). Pp. 97–105.

22. Shukla, R.P., Jakka, R.S. Critical setback distance for a footing resting on slopes. Acta Geotechnica Slovenica. 2017. 14(2). Pp. 19–31.

23. Zhou, H., Zheng, G., Yin, X., Jia, R., Yang, X. The bearing capacity and failure mechanism of a vertically loaded strip footing placed on the top of slopes. Computers and Geotechnics. 2017. 94. Pp. 12–21.

24. Shukla, R.P., Jakka, R.S. Critical setback distance for a footing resting on slopes under seismic loading. Geomechanics and Engineering. 2018. 15(6). Pp. 1193–1205.

25. Mansouri, T., Abbeche, K. Experimental bearing capacity of eccentrically loaded foundation near a slope. Studia Geotechnica et Mechanica. 2019. 41(1). Pp. 33–41.

26. Gemberline, M.C. Centrifuge modeling of shallow foundations. Proc., 11th Int. Conf. on Soil Mech. and foundation Engrg., Balkema, Rotterdam, the Netherlands. 1988. 2. Pp. 33–36.

27. Shukla, R.P., Jakka, R.S. Discussion of "Experimental and numerical studies of circular footing resting on confined granular subgrade adjacent to slope." International Journal of Geomechanics, ASCE. 2017. 17(2). Pp. 1–3.

28. Van Baars, S. The inclination and shape factors for the bearing capacity of footings. Soils and Foundations. 2014. 54(5). Pp. 985–992.

29. Castelli, F., Motta, E. Seismic bearing capacity of shallow foundations. In Earthquake-Resistant Structures-Design, Assessment and Rehabilitation. IntechOpen. 2012.

30. Makrodimopoulos, A., Martin, C.M. Upper bound limit analysis using simplex strain elements and second-order cone programming. International journal for numerical and analytical methods in geomechanics. 2007. 31(6). Pp. 835–86.

31. Makrodimopoulos, A., Martin, C.M. Lower bound limit analysis of cohesive frictional materials using second-order cone programming. International Journal of Solids and Structures. 2006. 66(4). Pp. 604–634.

32. Krabbenhøft, K., Lyamin, A.V., Sloan, S.W. Formulation and solution of some plasticity problems as conic programs. International Journal of Solids and Structures. 2007. 44(5). Pp. 1533–1549.

33. Krabbenhøft, K., Lyamin, A.V., Sloan, S.W. Three-dimensional Mohr-Coulomb limit analysis using semidefinite programming. Communications in Numerical Methods in Engineering. 2008. 24(11). Pp. 1107–1119.

34. Alencar, A.S., Galindo, R.A., Melentijevic, S. Bearing capacity of foundation on rock mass depending on footing shape and interface roughness. Geomechanics and Engineering. 2019. 18(4). Pp. 391–406.

35. Shukla, R.P. Pile groups subjected to abrupt collapse of retaining structure. Građevinar. 2018. 70(11). Pp. 953–964.

36. Indian Standard, IS: 2720 (Part IV)-1975. Methods of test for soils: Part 4 Grain size analysis. India: Bureau of Indian Standards. 2006.

37. Rostami, V., Ghazavi, M. Analytical solution for calculation of bearing capacity of shallow foundations on geogrid-reinforced sand slope. Iranian Journal of Science and Technology: Transactions of Civil Engineering. 2015. 39(C1). Pp. 167–182.

Shukla, R.P., Jakka, R.S.

38. Chang, J.C., Liao, J.J., Pan, Y.W. Bearing behavior and failure mechanism of a shallow foundation located on/behind the crest of a poorly cemented artificial sandstone. International Journal of Rock Mechanics and Mining Sciences. 2008. 45(8). Pp. 1508–1518.

39. Gamier, J., Canepa, Y., Corte, J.F., Bakir, N.E. Etude delaPortance de Foundations enBorddeTalus. 13th Int. Conf. on Soil Mechanics and Foundation Engineering. 1994. 2. Pp. 705–708.

40. Absi, E. La théorie des équivalences et son application à l'étude des ouvrages d'art. In Annales de ITBTP. 1972. 295. Pp. 61–90.

41. Giroud, J.P. et Tran-Vo-Nhiem. Force portante d'une fondation sur une pente,: A.I.T.B.T.P. No. 283–284 juillet-août, Série: théorie et méthodes de calcul. 1971. 142.

42. Mizuno, T., Takumitsu, Y., Kavakami, H. On the bearing capacity of a slope of cohesionless soil. Soils and Foundations. 1060. 1(20). Pp. 30–37.

43. Chen, W.F., Davidson, H.L. Bearing capacity determination by limit analysis. Journal of the Soil Mechanics and Foundations Division. 1973. 99(6). Pp. 433–449.

44. Tatsuoka, F., Huang, C.C., Morimoto, T., Okahara, M. Discussion of stress characteristics for shallow footing in cohesionless slopes. Canadian Geotech. J. 1989b. 26. Pp. 748–755.

45. Lebegue, Y. Essais de fondations superficielles sur talus. 8th International Conference on Soil Mechanics and Foundation Engineering, Moscow. 1973. 4(3). 313 p.

Contact:

Rajesh Prasad Shukla, rpshukla.2013@iitkalumni.org

Ravi S. Jakka, rsjakka@iitr.ac.in

Modeling of international roughness index in seasonal frozen area

L.N. Zhang[a], D.P. He[a*], Q.Q. Zhao[b]
[a] *Northeast Forestry University, Harbin, Heilongjiang Province, China*
[b] *Northeast Agricultural University, Harbin, Heilongjiang Province, China*
* E-mail: hdp@nefu.edu.cn

Keywords: pavements, deterioration, pavement maintenance

Abstract. In order to solve the international roughness index problem of asphalt concrete pavement in seasonal frozen area, this article takes four typical highways from China's seasonally frozen regions as examples to organize and analyze the geographic location, climatic conditions, structural layer materials and traffic volume of the four roads. Based on the mechanistic-empirical pavement design guide, and by the statistical product and service solutions software for regression analysis, propose IRI correction prediction model of asphalt concrete pavement in the seasonal frozen area and choose IRI measuring values of other highways and the predicted values of IRI prediction model to verify. The result shows that there is a linear relationship between international roughness index, environmental factor, fatigue crack area, transverse crack length and average rut depth. The coefficient of determination R^2 is 0.999, the adjusted R^2 is 0.999, the significance level is 0, and the regression model is effective. The values corresponding to modified model, environmental factor, fatigue crack area, transverse crack length and average rut depth indicators are 0.004, 0.074, 0.143 and 51.563 respectively; The IRI predicted value of the modified model is closer to the measured value than that of the traditional prediction model. The research results are of great significance for the international roughness index prediction of an asphalt concrete pavement in a seasonal frozen area.

1. Introduction

In order to reduce the impact of road surface roughness on driving comfort and safety in the seasonal frozen area, and to solve the impact of road surface on driving safety and road life, the international roughness index needs to be modeled. Since the international roughness index is an important indicator reflecting the road function and evaluating the road performance, the international roughness index prediction model of the asphalt pavement in the seasonal frozen area is established based on the parameters of the asphalt pavement structure, climatic conditions and traffic conditions in the seasonal frozen area. This model is of significant importance for the evaluation of asphalt pavement maintenance in the seasonal frozen area.

At present, the research time of international roughness index prediction at home and abroad is still short, and all of them are research biases to analyze the trend and detection methods of international roughness index. M. Mubaraki [1] establishes the relationship between the International Roughness Index (IRI) and road damage (including cracking, rutting and scattering), but the study is based on the climatic characteristics of Saudi Arabia; S.A. Arhin et al. [2] is based on 2-year IRI-PCI data. The model was developed to predict the relationship between IRI and PCI by functional classification for the pavement type in the Colombian region, but the relationship between IRI and PCI has no guiding significance for the prediction of the IRI model; P. Múčka [3] addresses the main problems in developing countries and some common problems that usually exist on secondary road networks, but there is no distinction between the degree of serious damage; J.P. Bilodeau et al. [4] uses the simulated heavy-duty wheel load response to calculate the dynamic load factor, and establishes the relationship between vehicle axle load and IRI, but the study did not consider the impact of climate and other factors on IRI. S.A. Arhin et al. [5] compares only

the methods of using IRI in US states with those used in non-US countries. M.I. Hossain et al. [6] is based on the neural network-based flexible pavement international flatness index. The analysis is only aimed at wet, frozen, wet, non-frozen and dry non-frozen climate zones. In addition, the neural network has the disadvantages of easy convergence and so on. The model has limitations. M.J. Khattak et al. [7] studied the international flatness index model of flexible base and pavement HMA overlays. The research section is based on Louisiana. The model itself is subject to environmental factors and it is notfurther aimed at the climate characteristics of the seasonal frozen zone. Note that the model is only for flexible base and pavement HMA overlays. In summary, the domestic and international research still lacks the establishment of the international roughness index model for the seasonal frozen area. Therefore, we establish an international roughness index prediction model for asphalt pavement that is suitable for the climate characteristics of the seasonal frozen area, which can fill the blank of the international roughness index prediction of the asphalt pavement in the seasonal frozen area.

2. Methods

The National Cooperative Highway Research Project (NCHRP) and the American National Association of Highway Transportation Administrators (AASHTO) have conducted several years of investigation and collated the observation results of long-term pavement performance distributed in more than 2,200 test sections in various states in the United States, which published Mechanistic-Empirical Pavement Design Guide in 2004, abbreviated as MEPDG [8–11]. It calculates stress and strain [12–13] of pavement structures by means of mechanical methods, based on climatic conditions and material properties of each structural layer, and bridges the gap between laboratory tests and actual road performance [14], based on empirical method and design. The prediction model is shown in formula 1. IRI is affected by the comprehensive influence of fatigue crack area, lateral crack length, rut depth, and environmental factors on the asphalt pavement. These four factors form a linear relationship [15]. The following content of the International Roughness Index is abbreviated as IRI for short.

After years of research, AASHTO in the United States has derived the IRI prediction formula 1 for asphalt pavements in the local MEPDG in the United States:

$$IRI = IRI_0 + 0.015(SF) + 0.400\left(FC_{Total}\right) + 0.0080(TC) + 40.0(RD) \qquad (1)$$

where IRI_0 is Initial IRI after construction (in/mile);

SF is Environmental factor;

FC_{Total} is Fatigue crack area, a percentage of total lane area;

TC is Transverse crack length (including reflection of lateral cracks in existing HMA pavement) (ft/mile);

RD is Average rut depth (in).

$$SF = Age\left[0.02003(PI+1) + 0.007947(Precip+1) + 0.000636(FI+1)\right] \qquad (2)$$

where Age is Pavement age (year);

PI is Percentage plasticity index of soil;

$Precip$ is Average annual rainfall or snowfall (in);

FI is Annual average freezing index (d).

According to the research in the existing literature [16], IRI is significantly affected by FCTotal, TC, and RD, and the linear relationship is obvious. In order to further verify, in the IRI prediction model of asphalt pavement in MEPDG, whether there is a linear relationship between IRI and SF in the seasonal frozen area, and the climate characteristics of the seasonal frozen area are fully covered. In the area of the seasonal frozen area, four typical highwaysare selected, namely the Jian-Ji Highway (Yanggang to Mishan Section) in Hulin City, Heilongjiang Province, China, hereinafter abbreviated as the Jian-Ji Highway; Zhang-Shi Highway (Zhangjiakou Section), Zhangjiakou City, Hebei Province, China, hereinafter abbreviated as Zhang-Shi Highway; Lian-Huo National Highway (Kuitun-Wusu Section) in Wusu City, Xinjiang Uygur Autonomous Region, China, hereinafter abbreviated asLian-Huo National Highway; 110 National Highway (Hubao section), Hohhot City, Inner Mongolia, China, hereinafter abbreviated as 110 National Highway, as shown in Fig. 1.

In Fig. 1, the four roads selected in the article are evenly distributed in China's seasonal frozen soil regions, and the latitude and longitude differences are large, which can reflect the climatic characteristics

of China's seasonal frozen soil regions more comprehensively. The seasonal freezing area in China is characterized by severe freezing in winter and warm and thawing in summer. The freezing and thawing cycle of asphalt concrete pavement in seasonal freezing area is very significant.

Figure 1. Geographical location of a typical highway.

To further verify the impact of SF on IRI, relevant statistical data for four typical highways in 2015 are collected, as shown in Table 1. From Table 1, it can be seen that the difference between the maximum temperature and the minimum temperature of the city where the Jian-Ji Highway among the four typical highways is 67 °C, and the minimum temperature difference between the Jian-Ji Highway and the Zhang-Shi Highway is 16 °C. There are significant differences in temperature characteristics among the four highways. In Table 1, the road age is within 7 years, and the difference in service life is small; the type of subgrade soil is sandy soil or gravel soil (According to China's Highway Subgrade Design Code JTG D30-2004, the subgrade can be divided into four categories: dry, medium wet, wet, and excessively wet, based on the dry and wet states. The maximum particle size of sandy soil and gravel soil is less than 150 mm). The number of maximum freezing-thawing cycles and the number of minimum freezing-thawing cycles are significantly different, reaching 51 times. The winter humidity of the subgrade soil is mainly concentrated between 8-11 %. Because the Lian-Huo National Highway is located in northwestern China, with drought and little rain all the year round, and the total rainfall is only 185 mm, the winter humidity of the subgrade soil is only 8 %.

Table 1. Basic information of typical roads.

Highway name	Highway age	Latitude and longitude	Winter humidity of subgrade soil	Subgrade soil type	Freezing-thawing cycles	Total annual precipitation (including snowfall) (mm)	Maximum temperature (°C)	Minimum temperature (°C)
Jian-ji Highway	5	North latitude 45.23 East longitude 132.11	10 %	Dry,Sandy soil	112	312	34	-33
Zhang-shiHighway	6	North latitude 40.82 East longitude 114.88	11 %	Dry,Gravelly soil	61	460	36	-17
Lian-huo National Highway	7	North latitude 44.45 East longitude 84.62	8 %	Dry,Gravelly soil	87	185	40	-24
110 National Highway	7	North latitude 40.48 East longitude 111.41	10 %	Dry,Sandy soil	103	344	32	-17

Zhang, L.N., He, D.P., Zhao, Q.Q.

In order to analyze the differences in temperature, average annual freezing index, and average annual precipitation of the four highways, monthly average temperature curves, freezing depth curves, and precipitation distribution curves corresponding to the highways are drawn, as shown in Fig. 2 – 4. Because the temperatures below 0 °C from October of each year to March of the following year appear in seasonal frozen soil regions, a complete freezing-thawing process is selected from October of each year to October of the following year. It can be seen from Fig. 2 that the month with the largest monthly average temperature difference among the four highway cities is January 2017. The monthly average temperature difference between the Jian-Ji Highway and the Zhang-Shi Highway is 9.5 °C, and the temperature difference is 2.46 times. The month with the lowest monthly average temperature difference among the four highway cities appeared in October 2017. The monthly average temperature difference between the Lian-Huo National Highway and the Jian-Ji Highway was 3 °C, and the temperature difference is 1.47 times.
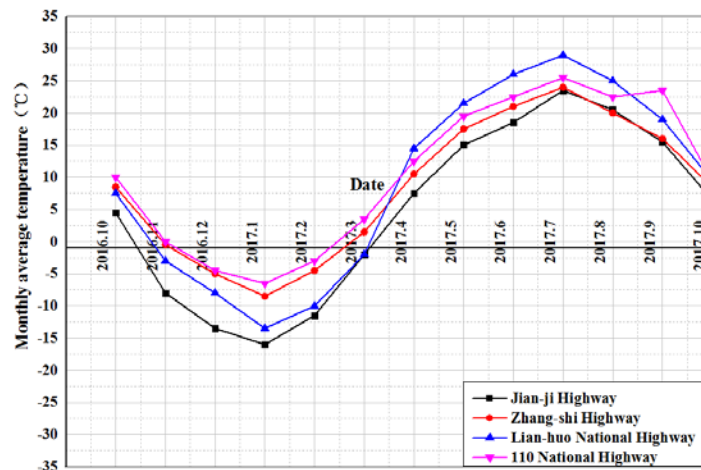
Figure 2. Monthly mean temperature curve of a typical highway.

Fig. 3 is the freezing-thawing depth curve of four typical roads. Since the freezing-thawing time of the highway in the seasonal frozen area is from October of each year to April of the following year, from May 2007 to September 2007, the freezing-thawing depth of the four curves is basically 0 cm. The maximum freezing depth of all four typical highways appeared in February 2017. The largest freezing depth is the Jian-Ji Highway in northeastern China, with a maximum freezing depth of 216 cm, which is followed by Lian-Huo National Highwayin northwestern China, with maximum freezing depth of 161 cm. The third is the 110 National Highway in northern China, with maximum freezing depth of 149 cm, and the smallest freezing depth is the Zhang-Shi Highway in northern China, with the maximum freezing depth of 109 cm. The difference between the maximum freezing depth and the minimum freezing depth is 105 cm. Through analyzing the reason, because in February 2017, the temperature difference between Jian-Ji Highway and Zhang-Shi Highway was 3.83 times, and the difference in precipitation was 2.5 times, under the the coupling of precipitation and temperature, there is a significant difference in freezing depth.
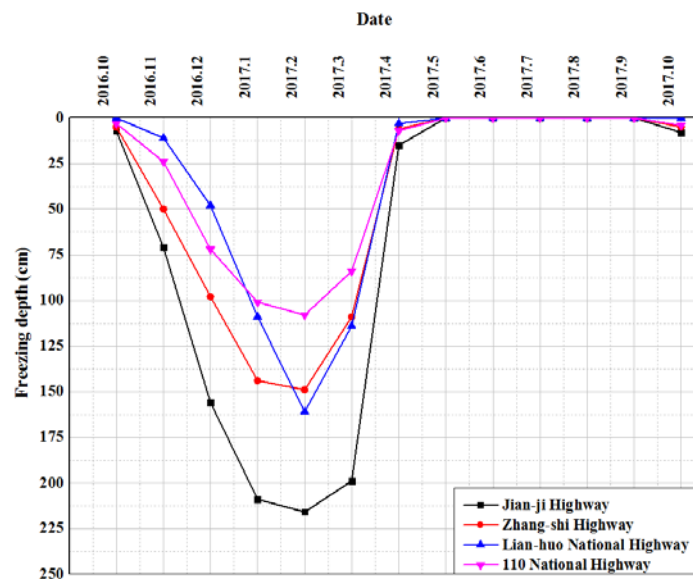
Figure 3. Freezing depth curve of a typical highway.

Fig. 4 shows the precipitation distribution curves of four typical highways from January to December 2017. All four highways have the highest rainfall season of the year in July, among which Jian-Ji Highway is the largest and Lian-Huo National Highway is the smallest. The month when the maximum precipitation occurred also accorded with the actual characteristics of climate precipitation in the seasonal frozen area. The highway with the largest precipitation in the year was Jian-Ji Highway, whose annual precipitation is 393 mm. It accounted for 4.84 %, 80.5 %, 10.43 %, and 4.58 % of the annual precipitation, respectively in spring, summer, autumn and winter. The precipitation of the Zhang-Shi Highway is 388.8 mm, and it accounted for 16.25 %, 62.53 %, 19.11 %, and 2.11 % of the annual precipitation, in spring, summer, autumn and winterrespectively. The precipitation of the Lian-Huo National Highway was 161.9 mm, and it accounted for 32.06 %, 33.23 %, 23.16 %, and 11.55 % of the annual precipitation, in spring, summer, autumn and winterrespectively. The precipitation of the 110 National Highway was 380.8 mm, and it accounted for 13.6 %, 63.2 %, 20.7 %, and 2.5 % of the annual precipitation, in spring, summer, autumn and winterrespectively. It can be seen from Fig. 4 that January-March 2017 and October-December 2017 were periods when the rainfall of four typical highways was relatively small. The reason was that the four highways had successively entered winter.
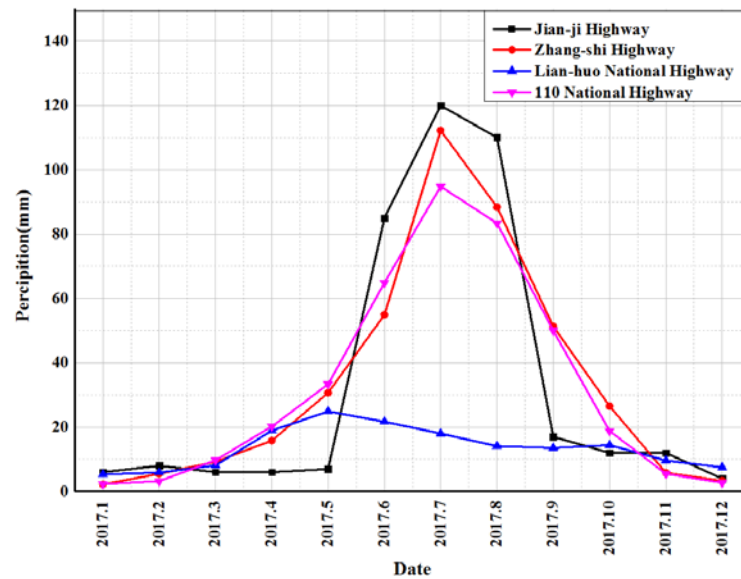
Figure 4. Distribution curve of precipitation of typical roads.

In order to further analyze the impact of temperature, average annual freezing index, and average annual rainfall on IRI, the IRI curve corresponding to four typical highways is established, as shown in Fig. 5. In Fig. 5, the IRI values of the four expressways change with time, and the change law is a linear increase. The three stages of rapid IRI slope change were November-December 2016, June-July 2017, and November-December 2017. The stage maximum appeared first in December 2016, July 2017, and December 2017. From the analysis of the reasons, it can be seen from Fig. 3 that in December 2017, the freezing depth of the four highways reached the maximum, and the soil thawing rate corresponding to the four highways was more than 93.5 %, and the number of freezing-thawing cycles reaches a peak. Under the repeated action of external loads, the smoothness index of the road surface decreases; as shown in Fig. 4, it was the highest rainfall of the four highways in July 2017. At the time of concentration, under the effect of external load, abundant rainwater was poured from the gaps in the road surface, which caused the flatness index of the road surface to decrease. From December 2016 to June 2017, and from August to November 2017, the changes in IRI values were relatively flat. The change slope of the Jian-Ji Highway is significantly higher than that of the other three highways. The reasons were that the annual average temperature of the area where the Jian-Ji Highway was located can vary up to 39.5 °C, the freezing depth can reach 216 cm, and the number of freeze-thaw cycles can be 116 times. According to the above analysis, it can be known that the temperature, average annual freezing index, and average annual rainfall and other factors that constitute SF have positive and linear effects on IRI.
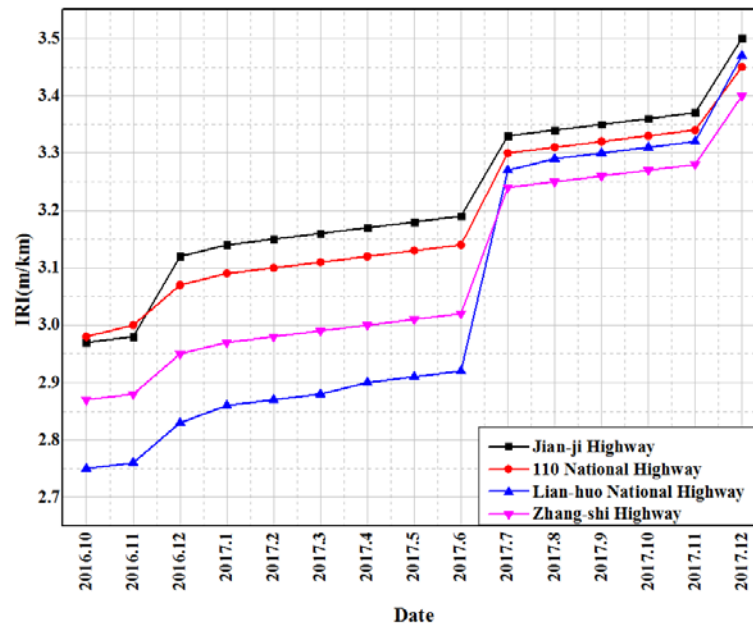
Figure 5. IRI curve of typical highway.

3. *Results and Discussion*

According to the analysis above, there is a linear relationship among IRI, SF, FCTotal, TC, and RD, and linear regression is performed in combination with field measured data to solve the correlation coefficient R^2. The measured data of the regression are from measured data of road surface IRI, 600 in total, of Jian-Ji Highway (Yanggang to Mishan Section) in Heilongjiang Province, China, Zhang-Shi Highway (Zhangjiakou Section) in Hebei Province, China, and Lian-Huo National Highway (Quitun-Wusu section), Xinjiang Uygur Autonomous Region, China and 110 National Highway (Hubao section), Inner Mongolia Autonomous Region, the four typical roads during 5 years from 2014 to 2018, which were used as the dependent variables of the regression model; combined with the above content, the measured values of SF, FCTotal, TC, and RD of four roads including Jian-Ji Highway (Yanggang to Mishan Section) in Heilongjiang Province, China, Zhang-Shi Highway (Zhangjiakou Section) in Hebei Province, China, and Lian-Huo National Highway (Quitun-Wusu section), Xinjiang Uygur Autonomous Region, China and 110 National Highway (Hubao section), Inner Mongolia Autonomous Region are used as the independent variables of the regression model.

The regression method uses "Statistical Product and Service Solutions" software for linear regression [17–22]. The steps of regression are as follows. First, observe the statistical relationship between the variables through the scatter plot. Through the above analysis, determine the linear relationship of the shape of the regression curve, and get a linear function that reflects the fit, which is shown in Table 2. R^2 is obtained before and after adjustment. Secondly, due to the existence of sampling randomness, the estimated regression equation may not be a true reflection of the quantitative relationship between the population of things. Therefore, it is necessary to perform various tests on the regression equation and display the relevant characteristics between the parameters data to determine whether the equation truly reflects the statistical relationship between the population of things, and get the Anovab of the regression model, as shown in Table 3. Then, by using the sample data under certain statistical fitting criteria, each parameter in the regression model is estimated, and a definitive regression equation is obtained, as shown in Table 4; finally, a colinear diagnosis is performed by the regression equation, as shown in Table 5. In the regression model, V1 represents IRI, V2 represents SF, V3 represents FC Total, V4 represents TC, and V5 represents RD.

In Table 2, the value of R^2 is 0.999. R^2 represents the determinant coefficients of the dependent variable IRI and the independent variables SF, FC Total, TC, and RD. The more the value of R^2 approaches 1, the higher the fit degree of the linear regression equation is. The number of independent variables will affect the value of R^2. In order to prevent the goodness of fit from being affected by the number of independent variables, R^2 needs to be adjusted. The adjusted R^2 is the ratio of the mean square error, and the adjusted R^2 is 0.999. The more the result is close to 1, the more the value is closer to 1, the better the fit degree of the regression equation is. Among them, the standard estimation error of the regression equation is only 0.10885, so it is concluded that the regression equation has a higher degree of good fit, and the part that the model can express IRI accounts for 99.9 %.

Table 2. Summary of regression models.

R^2	Adjusted R^2	Standard estimated error
0.999	0.999	0.10885

Table 3 is used to test the multiple linear regression equation by using the analysis of variance method. The table is used to test the significance of the regression equation. Table 3 shows that the data with relevant characteristics are F, significance, and sum of regression squares. The statistic F is the ratio of the square of the average regression to the sum of the squares of the average residuals. If the value of F is larger, it means that the influence of SF, FC Total, TC, and RD on IRI is much greater than that of random factors on IRI; if the significance value, Sig, is smaller, indicate that the linear equation regression is obvious, the goodness of fit is good, and the significance level should be less than 0.05. If the F value is too small, it means that the influence of the above four variables on IRI is very poor, and the fitted regression line is meaningless. The F value must obey the statistical distribution in degrees of freedom. The total IRI of the linear regression model is 19.544, the regression square is 18.893, the regression mean square is 4.723, the residual square is 0.652, and the residual mean square is 0.012. The F value in the table is very large, whose value is 398.632, and the significance value Sig. is 0, which is less than 0.05. It indicates that the four variables have a great impact on IRI, which is much greater than the impact of random factors on IRI;so the straight line is meaningful. There is a significant linear relationship between the IRI of the F test and SF, FCTotal, TC, and RD, and a linear model can be established. Through the above analysis, it can be determined that the linear regression of IRI as the dependent variable and SF, and FC Total, TC, and RD as independent variables is still valid in the seasonal frozen area [23]. In order to further solve the weights corresponding to SF, FC Total, TC, and RD, the regression model coefficients are solved by using SPSS.

Table 3. Anova[b] of the regression model.

	Model	Sum of square	Degree of freedom	Mean square	F	Significance
	Return	18.893	4	4.723	398.632	0
1	Residual	0.652	55	0.012		
	Total	19.544	59			

In Table 4, the non-standardized coefficient B represents the coefficient of each variable, and the corresponding coefficients of SF, FC Total, TC, and RD are 0.04, 0.074, 0.143, and 51.563. The value 0.408 corresponding to IRI0 represents the initial constant corresponding to the regression equation. In Table 4, the confidence intervals of the four variables in the linear equation do not include 0, which proves that the four variables are statistically significant. It can be seen that the linear relationship between the four variables and the IRI is obvious, so these four variables must be retained in the equation which can not be excluded. The magnitude of the absolute value of the standardized partial regression coefficient represents the impact of the four variables on the IRI. The standardized partial regression coefficients are all positive numbers, indicating that the variables are positively correlated with the IRI.

Table 4. Regression model coefficients[a].

Parameter	Partial regression coefficient	Partial regression coefficient standard error	Standardized partial regression coefficient	t	Significance	B's 95.0 % confidence interval	
						Lower limit	Upper limit
IRI_0	0.408	0.133		3.061	0.003	0.141	0.676
SF	0.004	0.015	0.008	3.286	0.076	0.027	0.035
FC_{Total}	0.074	0.011	1.853	7.055	0	0.053	0.095
TC	0.143	0.021	1.652	6.837	0	0.184	0.101
RD	51.563	30.132	0.759	8.349	0	0.045	0.096

To avoid the problem of collinearity among the four variables, it is necessary to use SPSS software to diagnose the collinearity of the model. In order to fully consider the four independent variables and conduct a comprehensive analysis by using stepwise regression method, the order by which the diagnostics are entered in sequence are SF, FCTotal, TC, and RD. All variables are not excluded. Table 5 shows the analysis results of collinear diagnosis.

In Model 1, IRI is the dependent variable, and SF, FCTotal, TC, and RD are independent variables to form a quaternary linear function. According to the model, all variables and constant terms are positive numbers and passed the variable test, which is consistent with the actual situation. From the analysis results in Table 5, it can be concluded that more than 90 % of the variance contribution comes from itself. If the eigenvalues in the table are similar and close to 0, it indicates that the commonality between the four independent variables is serious. In Table 5, the maximum eigenvalue is 4.180 and the minimum is 0.002, and these eigenvalues are different. Therefore, it can be concluded that there is no colinearity problem among the four variables. If the value of the condition index in the table is greater than 15, it means that there may be collinearity. If the value of the condition index is greater than 30, it indicates that the problem of collinearity is serious. In Table 5, the value of the maximum condition index is 8.424, which is far less than 15. From the above analysis, it can be concluded that there is no problem of multicollinearity in the international flatness index model of seasonally frozen regions.

Table 5. Collinear diagnosis.

Model	Dimension	Eigenvalues	Conditional index	Constant	V_2	V_3	V_4	V_5
	1	4.180	1.000	0	0.02	0	0	0
	2	0.501	2.888	0	0.86	0	0	0
1	3	0.314	3.650	0.01	0.08	0	0	0
	4	0.004	2.882	0.69	0	0.01	0.19	0.73
	5	0.002	8.424	0.29	0.04	0.81	0.81	0.27

Based on the above analysis, the international roughness index model in the seasonalfrozen area is proposed as:

$$IRI = 0.408IRI_0 + 0.004(SF) + 0.074(FC_{Total}) + 0.143(TC) + 51.563(RD) \qquad (3)$$

In order to test the accuracy of the prediction results of the prediction model, the test sections of the other five highways in the seasonal frozen area are selected as the verification sections, as shown in Fig. 6. The following 5 roads in December 2018 are verified by the predicted and measured IRI values, as shown in Fig. 7-11, which are 20 test sections of Sui-Man Highway (K550+750~K569+750) in Heilongjiang Province, China, and the 20 test sections of Qinggang-Zhenxiang Highway (K013 + 110 ~ K032 + 110) in Heilongjiang Province, China, 21 test sections of Shen-Da Highway (K183 + 300 ~ K203 + 300) in Liaoning Province, China, 16 test sections of S201 Highway (K223 + 000 ~ K238 + 000) in Xinjiang Uygur Autonomous Region, China, and 15 test sections of 110 National Highway (K574 + 000 ~ K588 + 000) in Inner Mongolia Autonomous Region, China, as shown in 7-11. In Fig. 7–11, the curve change table is drawn based on the field measured IRI value, the predicted IRI value of the international flatness index model of the seasonal frozen area, and the predicted value of the traditional IRI model. The abscissa is the station number of the site section, and the ordinate is IRI value. Compared with the traditional IRI prediction model, the IRI value predicted by the international flatness index model of the seasonal frozen area is closer to the IRI value measured in the field, and the error rate is within 3 %. The above analysis verifies the validity of the IRI results predicted by the international flatness index model of the seasonal frozen area.

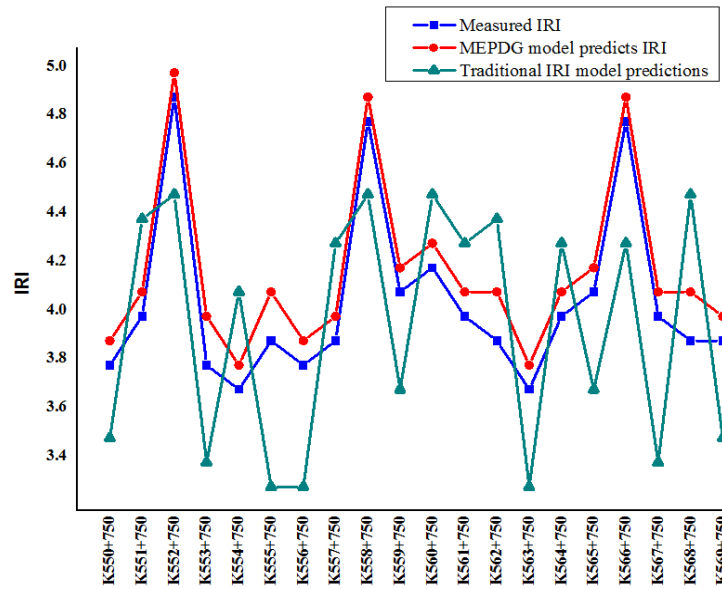**Figure 6. Verify the geographic location of the road.**

Figure 7. IRI comparison of the Sui-Man Highway.
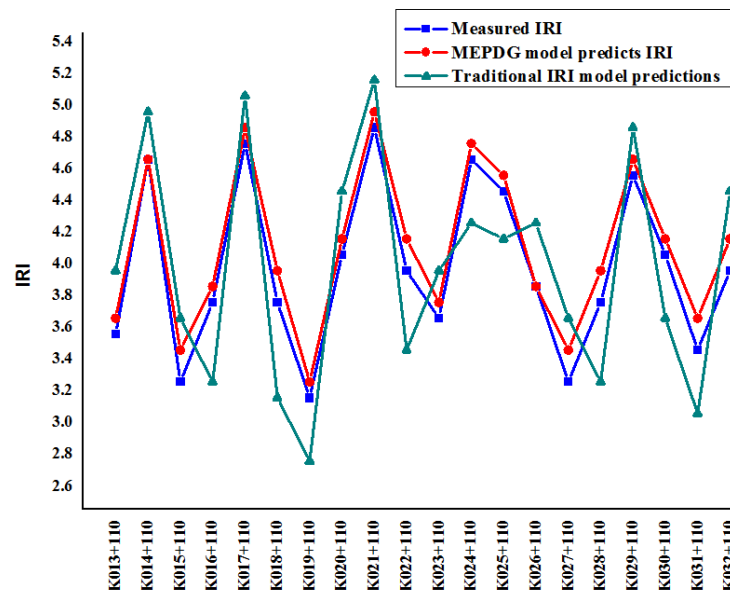

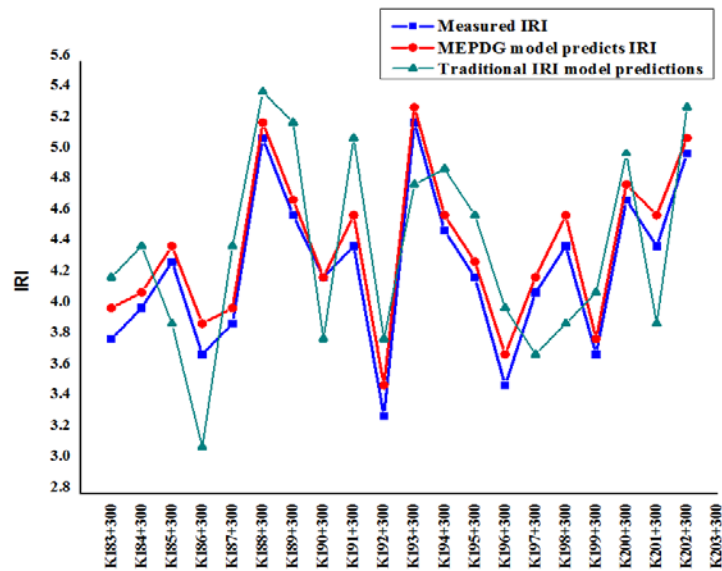**Figure 8. IRI comparison of Qinggang-Zhenxiang Highway.**

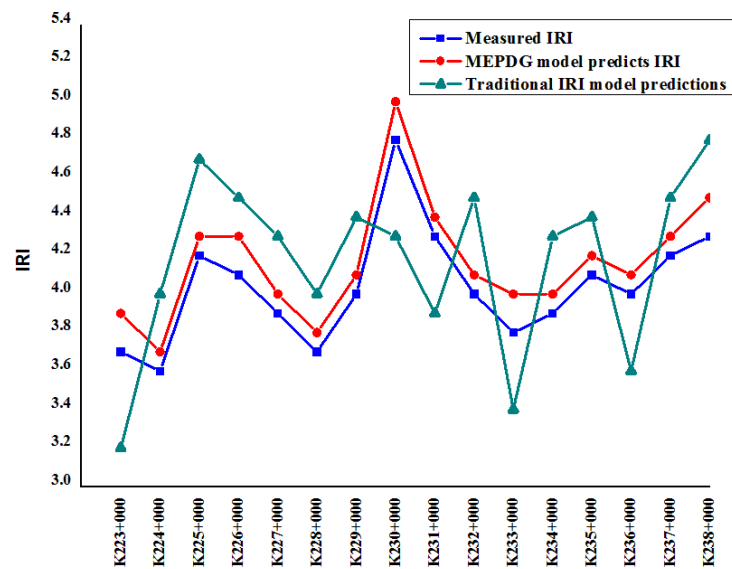**Figure 9. IRI comparison of the Shen-Da Highway.**

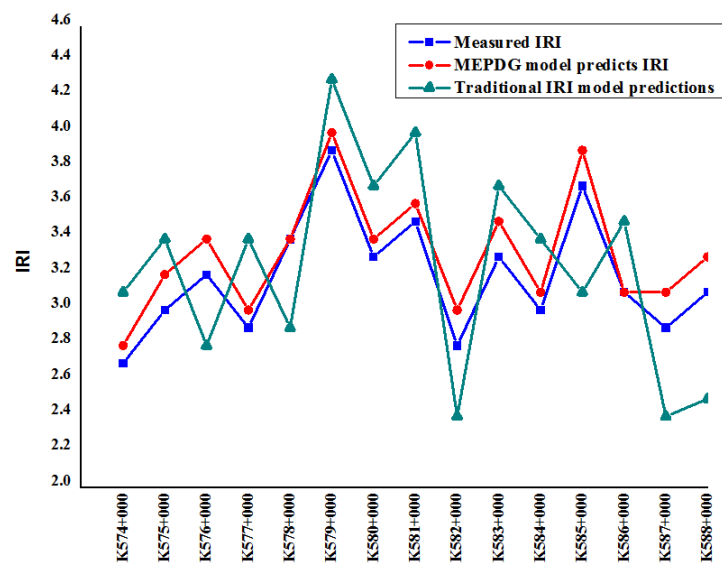**Figure 10. IRI comparison of the S201 Highway.**

Figure 11. IRI comparison of the 110 National Highway.

4. Conclusion

1. By using SPSS linear regression, the prediction coefficient R^2 is 0.999, the adjusted R^2 is 0.999, the F value is 398.632, and the significance level is 0, which is less than 0.05. It indicates that the regression model has a significant effect.

2. The IRI prediction model of asphalt concrete pavement in the seasonal frozen area is proposed. There is a linear relationship between IRI and the environmental factor, fatigue crack area, transverse crack length and average rut depth, and the values of the four variables are 0.004, 0.074, 0.143 and 51.563 respectively.

3. There is no multicollinearity in the model of the international roughness index of the seasonal frozen area. In the SPSS analysis, the maximum eigenvalues of the four variables are 4.180, the minimum one is 0.002, and the eigenvalues are different. The maximum condition index is 8.424, which is much less than 15.

4. The prediction accuracy of the international roughness index model in the seasonal frozen area is high. In the same time period, choose five highways to compare the predicted value of IRI, the measured IRI value and the traditional predicted IRI value. The results show that the IRI prediction accuracy of the seasonal frozen area international roughness index model is higher than that of other models.

References

1. Mubaraki, M. Highway subsurface assessment using pavement surface distress and roughness data. 8th International Conference on Maintenance and Rehabilitation of Pavements, MAIREPAV 2016. 9(5). Pp. 393–402. DOI: 10.3850/978-981-11-0449-7-329-cd

2. Arhin, S.A., Williams, L.N., Ribbiso, A., Anderson, M.F. Predicting Pavement Condition Index Using International Roughness Index in a Dense Urban Area. Journal of Civil Engineering Research. 2015.5(1). Pp. 10–17. DOI: 10.5923/j.jce.20150501.02

3. Sandra, A.K., Sarkar, A.K. Development of a model for estimating International Roughness Index from pavement distresses. International Journal of Pavement Engineering. 2013. 14(8). Pp. 715–724. DOI: 10.1080/10298436.2012.703322

4. Bilodeau, J.P., Gagnon, L., Doré, G. Assessment of the relationship between the international roughness index and dynamic loading of heavy vehicles. International Journal of Pavement Engineering. 2017. 18(8). Pp. 693–701. DOI: 10.1080/10298436.2015.1121780

5. Múčka, P. International Roughness Index specifications around the world. Road Materials and Pavement Design. 2017. 18(4). Pp. 929–965. DOI: 10.1080/14680629.2016.1197144

6. Hossain, M.I., Gopisetti, L.S.P., Miah, M.S. International roughness index prediction of flexible pavements using neural networks. Journal of Stomatology. 2019. 145(1). DOI: 10.1061/JPEODX.0000088

7. Khattak, M.J., Nur, M.A., Bhuyan, M.R.U.K., Gaspard, K. International roughness index models for HMA overlay treatment of flexible and composite pavements. International Journal of Pavement Engineering. 2014. 15(4). Pp. 334–344. DOI: 10.1080/10298436.2013.842237

8. Mogawer, W.S., Austerman, A.J., Daniel, J.S., Zhou, F., Bennert, T. Evaluation of the effects of hot mix asphalt density on mixture fatigue performance, rutting performance and MEPDG distress predictions. International Journal of Pavement Engineering. 2011. 12(2). Pp. 161–175. DOI: 10.1080/10298436.2010.546857

9. Li, Q., Xiao, D.X., Wang, K.C.P., Hall, K.D., Qiu, Y. Mechanistic-empirical pavement design guide (MEPDG): A bird's-eye view. Journal of Modern Transportation. 2011. 19(2). Pp. 114–133. DOI: 10.3969/j.issn.2095-087X.2011.02.007

10. Caliendo, C. Local calibration and implementation of the mechanistic-empirical pavement design guide for flexible pavement design. Journal of Transportation Engineering. 2012. 138(3). Pp. 348–360. DOI: 10.1061/(ASCE)TE.1943-5436.0000328

11. Tarefder, R., Rodriguez-Ruiz, J.I. Local calibration of MEPDG for flexible pavements in New Mexico. Journal of Transportation Engineering. 2013. 139(10). Pp. 981–991. DOI: 10.1061/(ASCE)TE.1943-5436.0000576

12. Zhang, C., Wang, H., You, Z., Ma, B. Sensitivity analysis of longitudinal cracking on asphalt pavement using MEPDG in permafrost region. Journal of Traffic and Transportation Engineering (English Edition). 2015. 2(1). Pp. 40–47. DOI: 10.1016/j.jtte.2015.01.004

13. Saha, J., Nassiri, S., Bayat, A., Soleymani, H. Evaluation of the effects of Canadian climate conditions on the MEPDG predictions for flexible pavement performance. International Journal of Pavement Engineering. 2014. 15(5). Pp. 392–401. DOI: 10.1080/10298436.2012.752488

14. Allan Reese, R. R for SAS and SPSS Users. Journal of the Royal Statistical Society: Series A (Statistics in Society). 2009. 172(3). Pp. 697–698. DOI: 10.1111/j.1467-985x.2009.00595_7.x

15. Hayes, A.F., Matthes, J. Computational procedures for probing interactions in OLS and logistic regression: SPSS and SAS implementations. Behavior Research Methods. 2009. 41(3). Pp. 924–936. DOI: 10.3758/BRM.41.3.924

16. Gulfam-E-Jannat, Yuan, X.X., Shehata, M. Development of regression equations for local calibration of rutting and IRI as predicted by the MEPDG models for flexible pavements using Ontario's long-term PMS data. International Journal of Pavement Engineering. 2016. 17(2). Pp. 166–175. DOI: 10.1080/10298436.2014.973024

17. Wang, H., Rosner, G.L., Goodman, S.N. Multiple Regression Using SPSS. Clinical Trials. 2016. 13(6). Pp. 621–631. DOI: 10.1177/1740774516649595

18. SPSS survival manual: a step by step guide to data analysis using IBM SPSS. Australian and New Zealand Journal of Public Health. 2013. 37(6). Pp. 597–598. DOI: 10.1111/1753-6405.12166

19. McCormick, K., Salcedo, J. IBM SPSS Data Preparation. SPSS reg Statistics for Data Analysis and Visualization. 2017. Pp. 303–324. DOI: 10.1002/9781119183426.ch12

Zhang, L.N., He, D.P., Zhao, Q.Q.

20. Pallant, J. SPSS survival manual: a step by step guide to data analysis using IBM SPSS. 2011. Pp. 597–598. DOI: 10.1046/j.1365-2648.2001.2027c.x
21. Field, A. Factor Analysis Using SPSS. Scientific Research and Essays. 2013. 22(6). Pp. 1–26. DOI: 10.1016/B978-0-444-52272-6.00519-5
22. Preacher, K.J., Hayes, A.F. SPSS and SAS procedures for estimating indirect effects in simple mediation models. Behavior Research Methods, Instruments, and Computers. 2004. 36(4). Pp. 717–731. DOI: 10.3758/BF03206553
23. Karpov, V.V., Semenov, A.A. Mathematical model of deformation of orthotropic reinforced shells of revolution. Magazine of Civil Engineering. 2013. 40(5). Pp. 100–106. DOI: 10.5862/MCE.40.11

Contacts:

Lina Zhang, 53860470@qq.com
Dongpo He, hdp@nefu.edu.cn
Qianqian Zhao, 492954791@qq.com

Deflection of a cladding panel of fully tempered glass in curtain wall system

E. Gerasimova*[a], A. Galyamichev[b], G. Schwind[c], J. Schneider[c]
[a] *NIUPC «Mezhregional'nyj institut okonnyh i fasadnyh konstrukcij», St. Petersburg, Russia*
[b] *Peter the Great St. Petersburg Polytechnic University, St. Petersburg, Russia*
[c] *Technical University of Darmstadt, Darmstadt, Germany*
*E-mail: katyageras17@gmail.com

Keywords: facade, cladding, glass, aluminum, substructure, sealant

Abstract. The article presents a study on the mechanical behavior of facade cladding panel consisting of aluminum frame and fully tempered sheet glass under the action of uniformly distributed load. The study involved tests of full-size samples of two structural solutions of the cladding panel in a curtain wall system for two different geometrical configurations of the panel. Experimental data showed a high similarity with the results of a static calculation in the zone of linear elastic deformation. Therefore, the use of SJ Mepla finite element software package for the calculation of described structures was verified. The influence of the boundary conditions on determination of deflections in numerical model as well as the character of seal deformation was described. The criteria of the loss of bearing capacity of a system was defined. Empirical formulas for calculating the panel deflection for specific geometrical configurations of a panel were proposed.

1. Introduction

Nowadays glass is widely used as a main translucent material of the building enclosing structures due to its structural and aesthetical advantages and unique properties [1, 2]. Besides the mullion-transom and structural glass facades, curtain wall systems with glass panels as a cladding material are actively used in modern construction practice. These systems are characterized by faster installation in comparison with other glazing systems and offer aesthetical benefits.
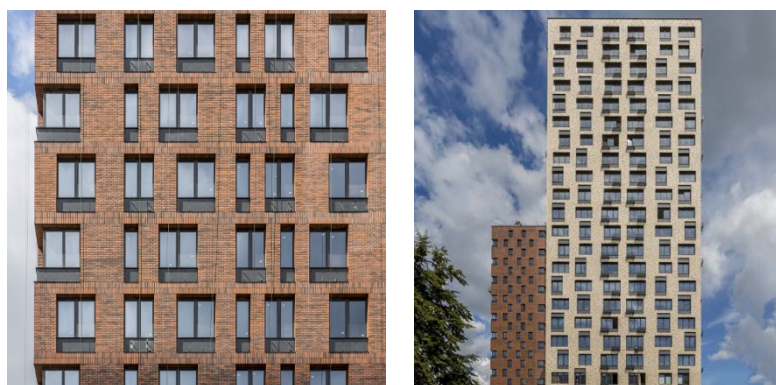
Figure 1. Example of glass cladding in curtain wall systems – residential complex "Petrovsky" (source: Official website of the manufacturer of facade system www.nordfox.ru).

The choice of facade structure directly affects the safety and comfort of people inside the building [3, 4]. In [5] a study on the influence of the glass fixing type on the fire resistance of structure is presented. Article [6] is devoted to an analysis of the stress-strain state of curtain wall systems under extreme loads

---

such as natural exposures and man-made threats. The correlation between characteristics of the glass and performance of double-glazed facades is described in [7].

Modern glazing systems can be classified on the base of different criteria [8]. One of the factors which determines the overall performance of a system is method of fixing of a glass panel to the substructure [9–11]. The dependence of the fixing method on the strength of glass is studied in [12]. In [13] an analysis of existing design guidelines and methods intended for calculation of glass fencing, which is fixed in an aluminum profile, is presented. Application and experimental verification of glass fencing system are also presented. According to [13], the stiffness of the clamping profile and the choice of approach among different methods proposed in regulatory documents (e.g. national building codes) have the greatest impact on the calculation result. At the same time, the calculation procedures need to be improved, since they are not adapted for the fence fixed in the curtain wall system. A study on the aluminum-and-glass facades is presented in [14]. The study in [14] contains investigation on various systems in order to verify their economic viability and possibility of use in modern construction.

Due to increased requirements for the heat transfer through building envelope [15, 16], parameters of curtain wall systems are actively reconsidered [17]. Modeling approach for climatic simulation of curtain facades is described in [18]. The study on the influence of orientation of buildings with glass facades on its energy consumption is presented in [19].

In [20] simulations were performed in order to assess the mechanical behavior of panels with direct glass-aluminum connection. The numerical study in [20] is particularly focused on the influence of elastic layer (rubber spacers or glue layers) on improvement of working conditions of the glass-aluminum connections. The study in [21] is devoted to the determination of partial material safety factor for structural silicone adhesives. Obtained on the base of experimental data, this value can be applied in finite element calculation programs, leading to the optimization of structural sealant design.

The use of glass beads in facade systems raises the issues related with tightness of the joint. Experimental study on the tightness of glazing bead butt joints of aluminum windows was performed in [22].

Experimental and numerical investigation of the properties and possibilities of application of structural sealants in glazing systems is described in [23]. Issues related to the modeling and fracture analysis of sealants are observed in [22–25].

Facade structures face various exposures during its operational lifetime, however in absence of thermal loading the wind load represents the highest contribution to the stress-strain state of the members of facade system. Lateral loads (e.g. wind) are prevalent and require detailed consideration in accordance with local climate conditions during the process of design and calculation of such structures [28].

In this research, the object of the study was a fully tempered sheet glass in a specific aluminum frame as the cladding of curtain facade system. Within the study both experimental and numerical analysis of the cladding of a curtain wall system were performed.

The purpose of the study was determination of the deflection of a cladding panel within the fixing system of a curtain wall.

The following tasks were carried out:

- Experimental determination of deflection of a cladding panel of fully tempered sheet glass, fixed to a curtain wall system, under the action of a uniformly distributed load;

- Determination of the influence of the geometric dimensions on the deflection of a panel;

- Determination the criteria characterizing loss of bearing capacity of the system;

- Comparison of results of the panel's stress-strain state obtained through numerical methods and laboratory tests.

2. Methods

The study contains experimental and numerical investigation of a full-size fragment of a considered curtain wall system. A glass cladding panel was continuously fixed to the aluminum frame through a glass bead what represents a particular case of clamped solution. Furthermore, two different fixation schemes were performed:

- Test setup 1: Cladding panel of fully tempered sheet glass is 2-side simply supported (Navier's support) by glazing beads and frame through the EPDM profiles. Glazing bead and a frame thus form a compound profile. This profile is supported on its edges by self-tapping screws which attach it to the transom.
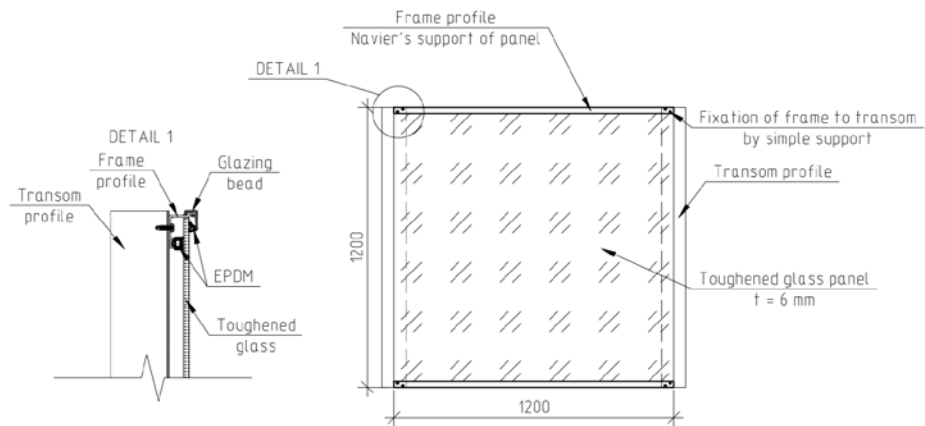
Figure 2. Scheme of system type 1 (test setup 1).

- Test setup 2: Cladding panel of fully tempered sheet glass is 2-side simply supported (Navier's support) by glazing beads and frame through the EPDM profiles. Frame profile is discretely supported along its entire length by self-tapping screws which attach it to the transom. Glazing bead, a frame and transom thus form a compound profile of a higher stiffness than test setup 1.
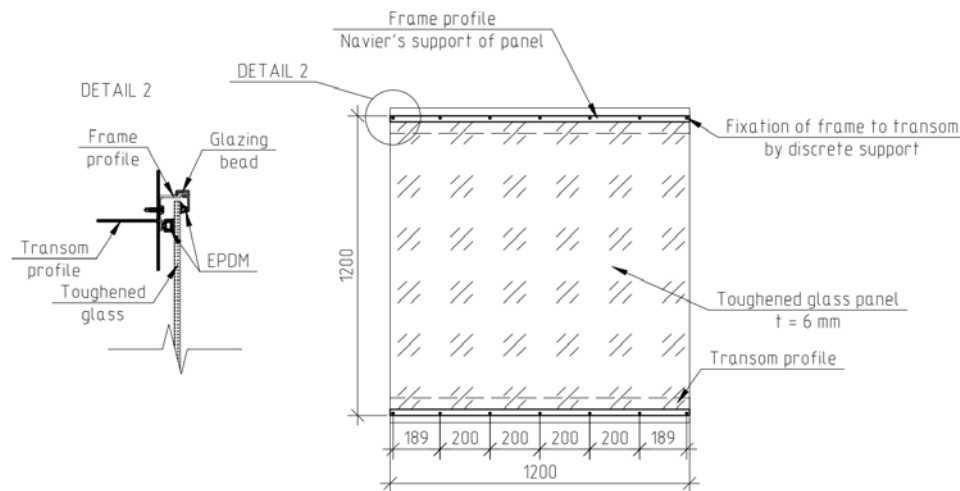
Figure 3. Scheme of system type 2 (test setup 2).
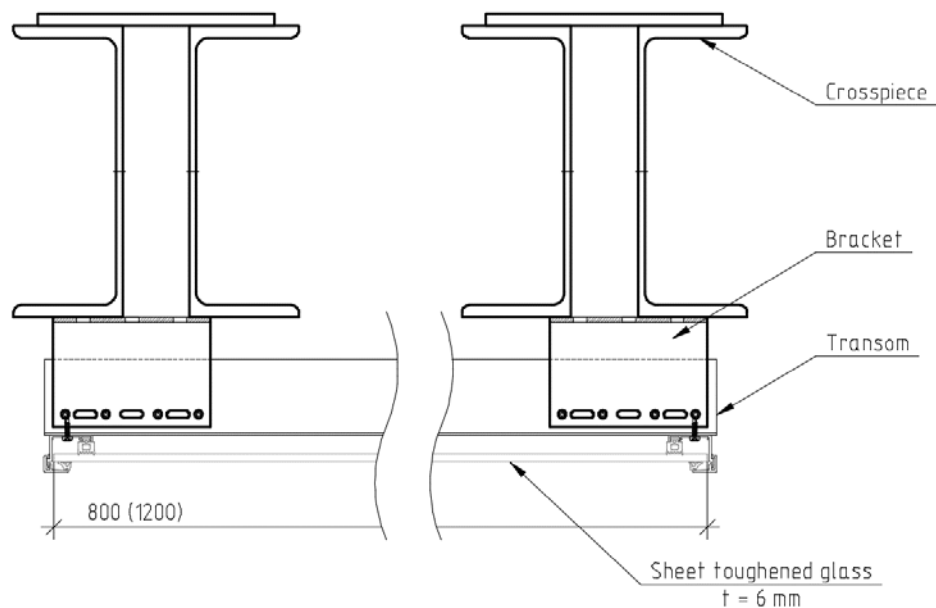
Figure 4. Cross-section of the test setup 2.

Gerasimova, E., Galyamichev, A., Schwind, G., Schneider, J.

The experiments were performed for two different configurations of cladding panels: 1200x1200 mm and 1200×800 mm.

Fully tempered glass for all considered schemes had a thickness of 6 mm. According to Russian State Standard GOST 30698-2014 «Tempered glass. Specifications», fully tempered glass has a bending strength of 120 MPa.

All the aforementioned geometrical values were measured during the test.

Therefore, following schemes were considered:

- Test setup 1a: 1200×800×6 mm;
- Test setup 1b: 1200×1200×6 mm;
- Test setup 2a: 1200×800×6 mm;
- Test setup 2a: 1200×1200×6 mm.

2.1. Experimental approach

The purpose of the testing was an experimental determination of the deflections of the curtain wall system in characteristic points: in the center of the panel, center of the free edge and center of the frame profile. The obtained results were subsequently compared to the results of numerical calculation.

Determination of the cladding panel's deflection was carried out by means of a full-size simulation of a frame fragment of the curtain wall system and its subsequent loading with a uniformly distributed load. Special high rigidity crosspieces with brackets mounted to them in the horizontal plane were used as a bearing base in test setup.

The use of horizontal arrangement of the panels was justified by the convenience of testing, as well as by the small influence of loads in the plane of the facade on the stress-strain state of the system [29]. The uniformly distributed load on the cladding panels was applied by means of concrete cores with a diameter of 150 mm, height of 150 mm and an average weight of 6.22 kg each. The cores were distributed on the surface of the panel evenly and symmetrically with respect to the center of the glass plate. The order of applying the load is chosen with the purpose to achieve a load value of approximately 1 kN/m^2 with subsequent unloading for the purpose of detecting backlash and crumples in the areas where the bracket is fixed through rivet connection. The assumption of value of 1 kN/m^2 for the purpose of detecting backlash is based on previous preliminary studies made by authors which were performed for various facade structures. Furthermore, loading with concurrent deflection control was continued until the loss of the bearing capacity of the system.
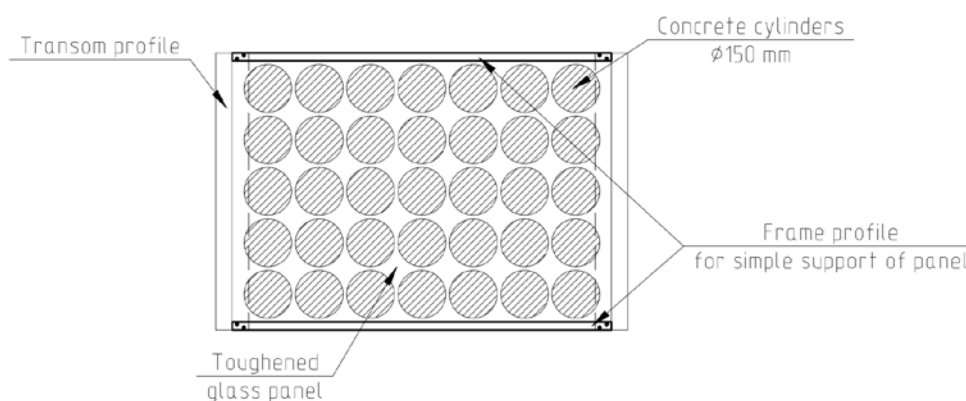
Figure 5. Principal loading scheme (test setup 1a).

The values of deflection in the center of the panel, center of the free edge and center of the frame profile were measured by dial indicators 6-PAO with following characteristics:

- Graduation: 0.01 mm;
- Maximum value of measurement: 100 ± 0.5 mm;
- Accuracy in the interval [0...1 mm]: ± 0.03;
- Accuracy in the interval [0...10 mm]: ± 0.3.

Location of dial indicators (DI) is shown in Fig. 6.
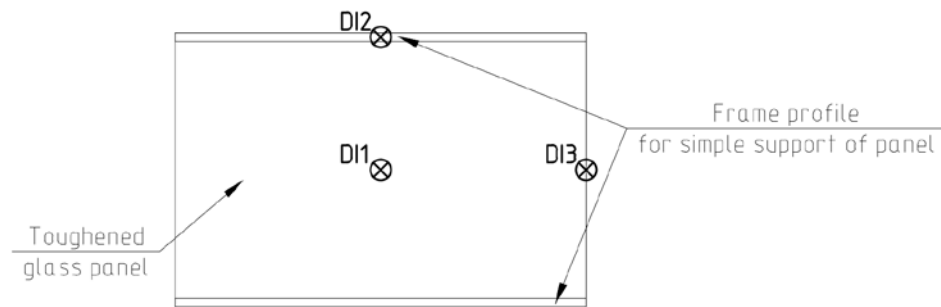
Figure 6. Location of dial indicators for measurement of the deflections for test setup 1 and 2.

Values obtained from dial indicators were processed in Excel and resulting deflections for each step of loading were obtained.

Tests were carried out on the two identical samples of each structural scheme.

Figure 7. Experimental setup – test setup 1.
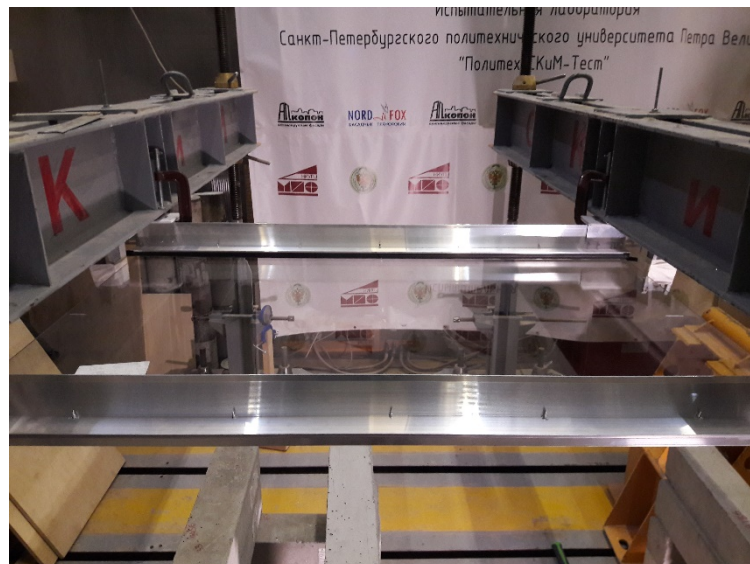
Figure 8. Experimental setup – test setup 2.

2.2. Numerical approach

The fragment of considered curtain wall system was modeled in finite element software package in accordance with schemes shown in Fig. 2 and 3 and experimental setup. Values of deflection in the same characteristic points of curtain wall system were obtained for the further analysis.

The considered elements were rectangular homogeneous isotropic flexible plates of a large deflection, where two parallel sides are simply supported with a stiffness defined by configuration of the aluminum profiles. The other two sides of glass plates are free.

Flexible plates of a large deflection are the plates, which are thin to that extend that the membrane stresses arising in them can have a noticeable effect on the deflections under an action of a transverse load. At the same time, these plates bend so significantly that the influence of their deflection on the value of the efforts striving to cause deformation of their middle layer cannot be neglected. The calculation of flexible plates of large deflection is based on the use of the system of differential equations describing bending and tensile deformations. In this study, the Finite Element Method (FEM) based on the theory of thin plates and realized in software SJ Mepla version 4.0.6 was used for the calculation of the plates fixed in aluminum profiles. Basic isoparametric finite element included 9 nodes and was created by means of interpolation functions in Lagrange form.
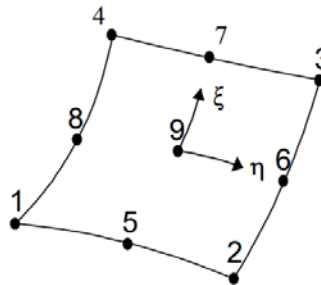
Figure 9. 9-nodes finite element.
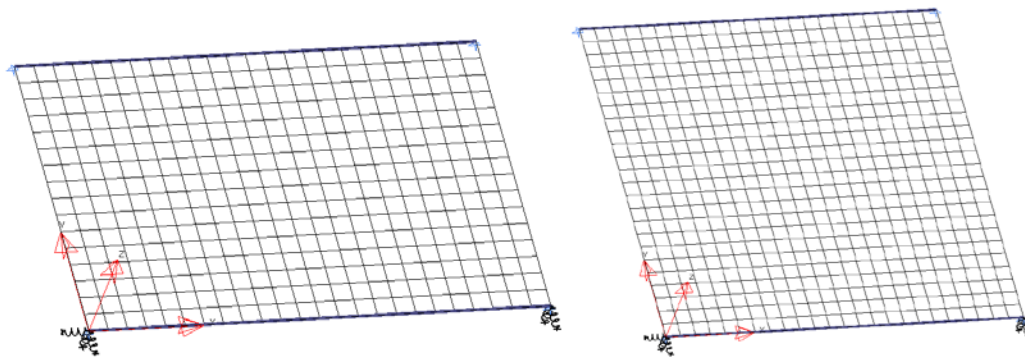
Figure 10. Finite element models of panels (maximum size of mesh element is 50 mm).

Curtain wall system of test setup 1 can be interpreted as follows:
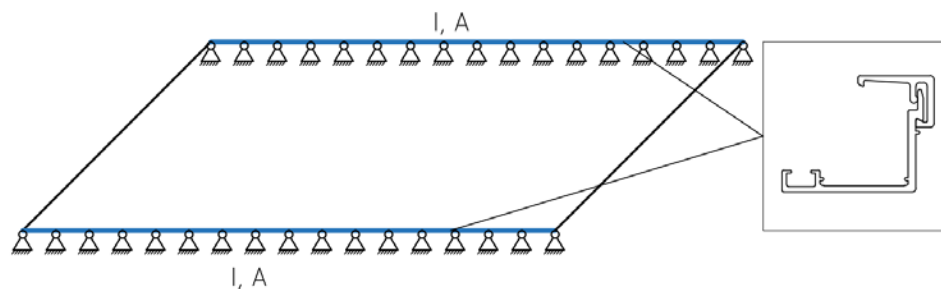
**Figure 11. Principal structural scheme of test setup 1
(simple supports refer to the fixation of glass).**

Curtain wall system of test setup 2 can be interpreted as follows:
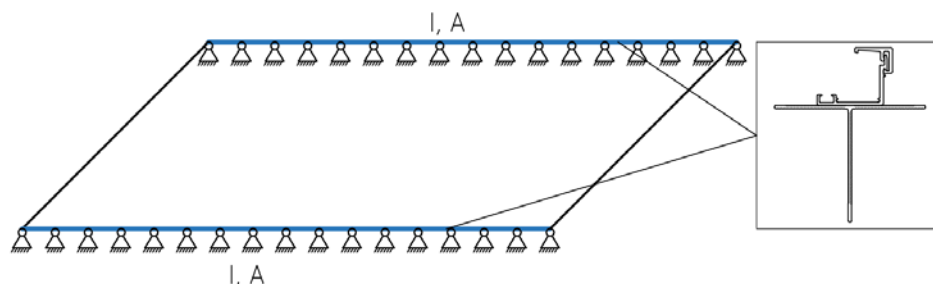
**Figure 12. Principal structural scheme of test setup 2
(simple supports refer to the fixation of glass).**

Gerasimova, E., Galyamichev, A., Schwind, G., Schneider, J.

The finite element model assumed the direct interaction between aluminum profiles and glass panel.

For ease of calculation the mechanical behavior of EPDM was not accounted in numerical model at this stage of research.

Correct static calculation required considering the stiffness of aluminum transoms installed along two parallel sides of the panel:
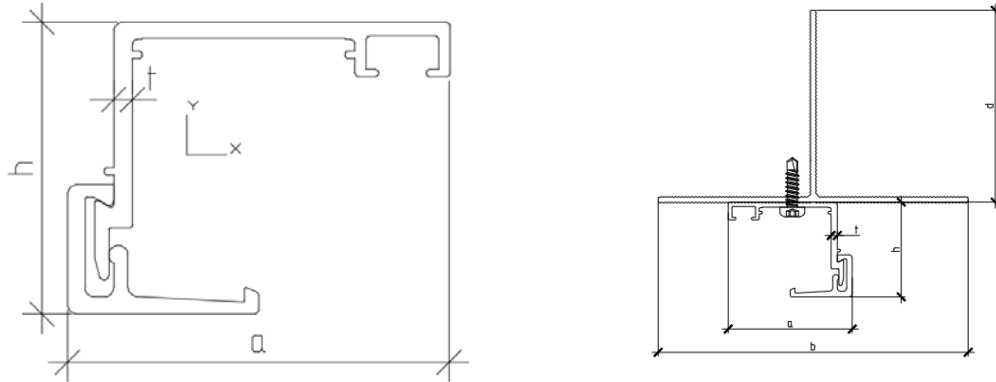
Figure 13. Left – transom profile of test setup 1; right – transom profile of test setup 2.

Stiffness characteristics of aluminum used in the study are presented below. The values were obtained in Consul, a satellite of SCAD Office software.

Modulus of elasticity:

$$E_{\text{aluminum}} = 70\,GPa\,.$$

Poisson's ratio:

$$\upsilon_{\text{aluminum}} = 0.3\,.$$

Table 1. Geometric characteristics of transom profile of test setup 1.

A	Area of cross-section	1.912	cm^2
I_x	Moment of inertia about the central axis X1 parallel to the axis X	2.542	cm^4
I_y	Moment of inertia about the central axis Y1 parallel to the axis Y	2.501	cm^4
I_t	Free torsion moment of inertia	0.019	cm^4
I_p	Polar moment of inertia	5.043	cm^4

Table 2. Geometric characteristics of transom profile of test setup 2.

A	Area of cross-section	4.75	cm^2
I_y	Moment of inertia about the central axis Y1 parallel to the axis Y	20.208	cm^4
I_y	Moment of inertia about the central axis Y1 parallel to the axis Y	20.941	cm^4
I_t	Free torsion moment of inertia	0.064	cm^4
I_p	Polar moment of inertia	40.63	cm^4

3. Results and Discussion

Results obtained during numerical calculations and experiments demonstrate that curtain wall system of test setup 2 has a higher overall stiffness in comparison with test setup 1. The profiles in test setup 1 turn as the panel bends under the action of uniformly distributed load on the panel. The angle of inclination of clamped edge of a glass panel is proportional to the load value, profile's stiffness and size of the panel. The profiles in test setup 2 resist turning due to the fact of discrete connection to the transom. Fig. 14 shows the results determined with SJ Mepla of the rotation at the support due to the load.
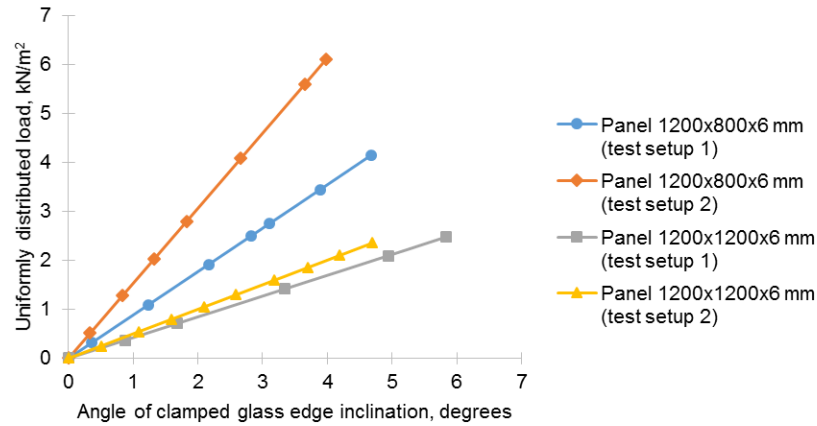
Figure 14. Dependence between inclination of clamped glad edge and value of uniformly distributed load.

Rotation of profiles impacts its geometrical characteristics. Fig. 15 shows how the moment of inertia of the profiles changes as a function of rotation. Therefore two types of numerical models were considered during static calculation: in the first option the moment of inertia as a characteristic of support conditions is set constant while in the second option the moment of inertia is variable and refers to the value of face load.
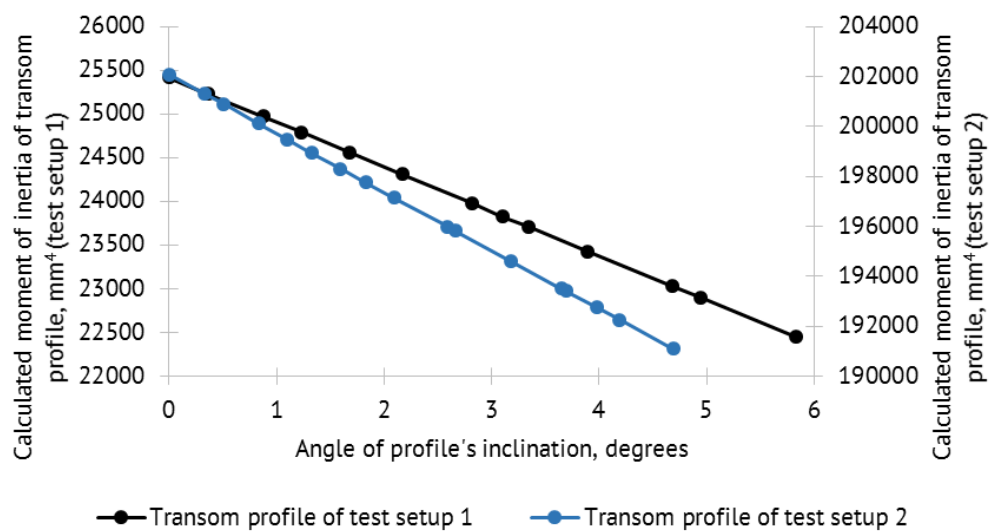
Figure 15. Dependence between inclination of the profile and profile's moment of inertia.

The results of tests performed on two samples of each structural scheme were compared to the results of static calculation in SJ Mepla. Two types of models were calculated: with constant and variable moment of inertia of profiles.

Test setup 1a: Comparison between experimental and numerical determined results
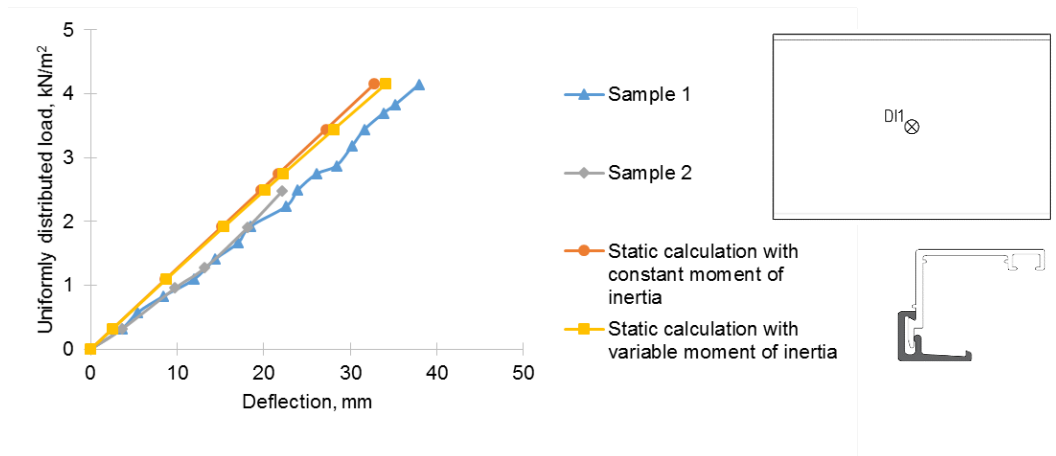
Figure 16. Deflection of the center of the panel (DI1).
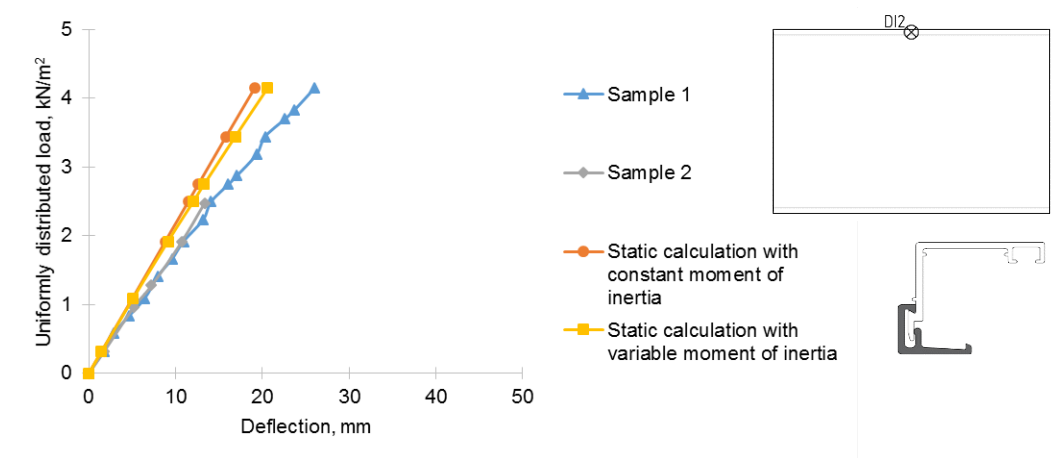
Figure 17. Deflection of the center of the frame (DI2).
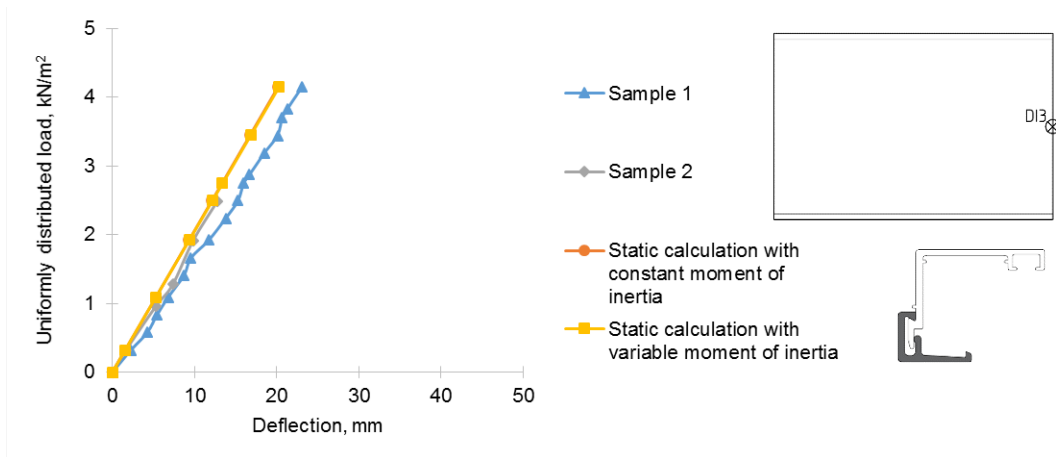
Figure 18. Deflection of the panel edge (DI3).

Gerasimova, E., Galyamichev, A., Schwind, G., Schneider, J.

Test setup 2a: Comparison between experimental and numerical determined results
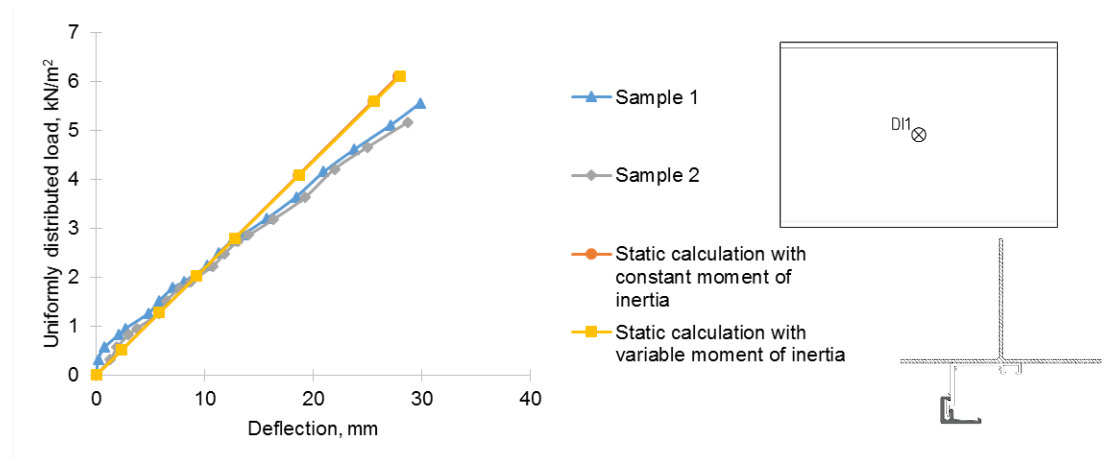
Figure 19. Deflection of the center of the panel (DI1).
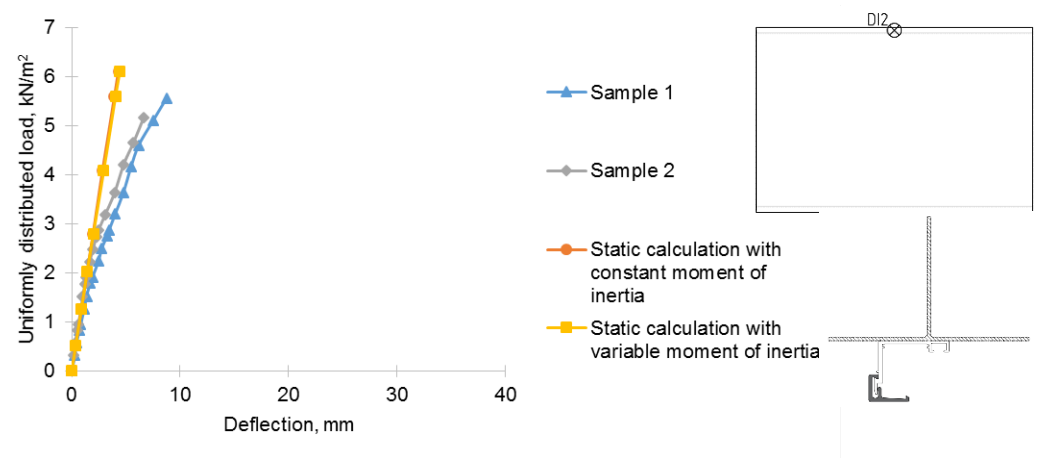
Figure 20. Deflection of the center of the frame (DI2), position of DI, section of edge beam.
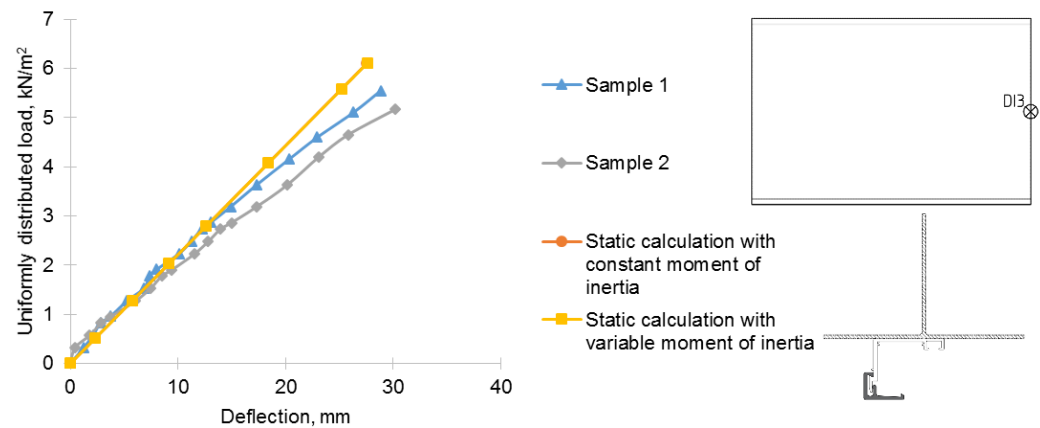
Figure 21. Deflection of the panel edge (DI3).

Gerasimova, E., Galyamichev, A., Schwind, G., Schneider, J.

Test setup 1b: Comparison between experimental and numerical deter4mined results
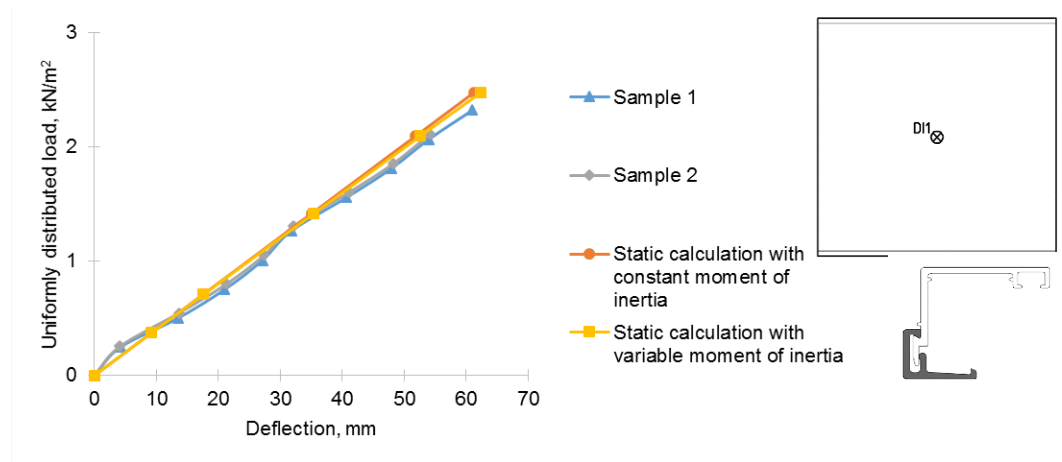
Figure 22. Deflection of the center of the panel (DI1).
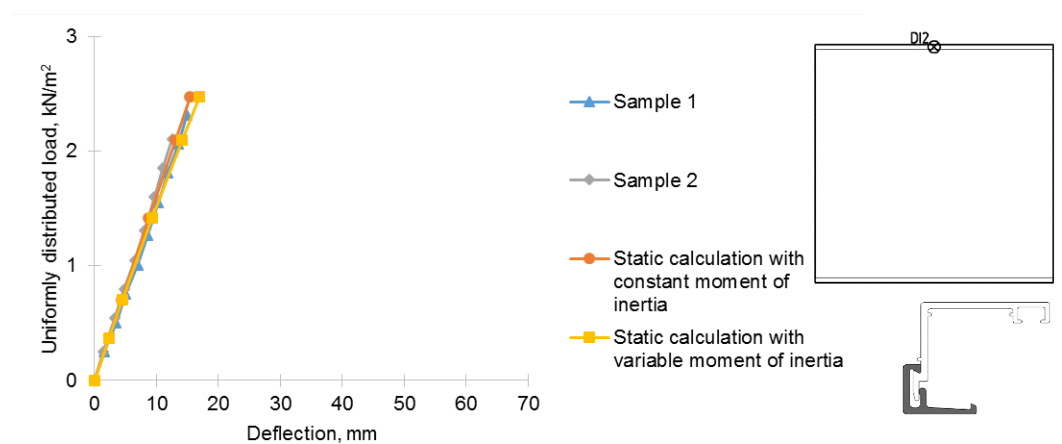
Figure 23. Deflection of the center of the frame (DI2).
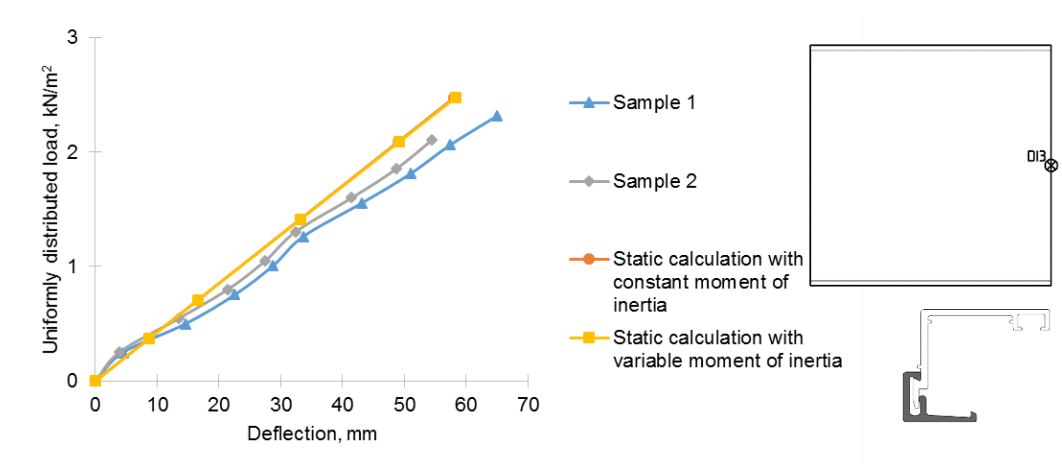
Figure 24. Deflection of the panel edge (DI3).

Test setup 2b: Comparison between experimental and numerical determined results
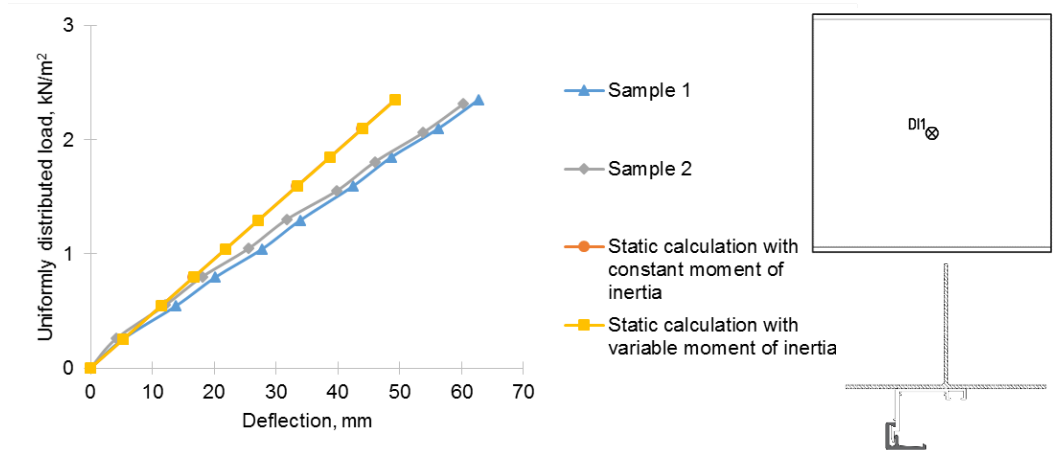
Figure 25. Deflection of the center of the panel (DI1).
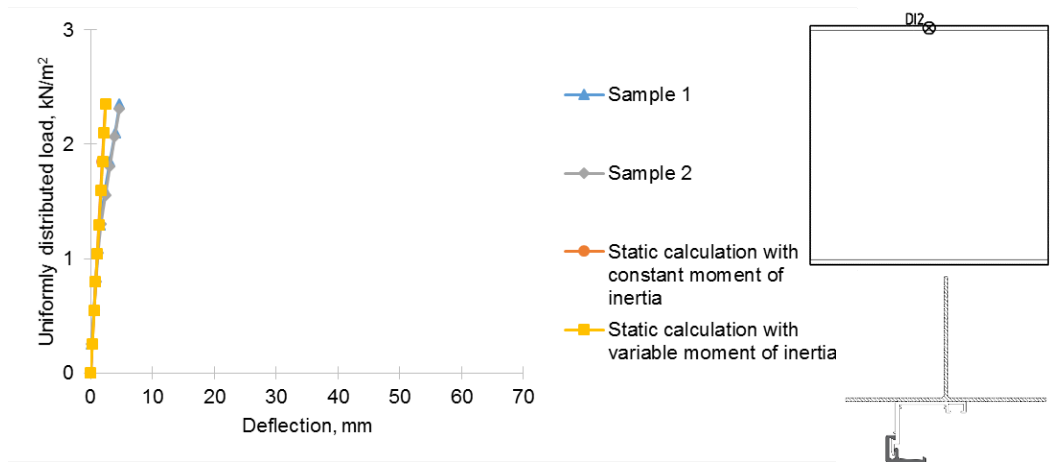
Figure 26. Deflection of the center of the frame (DI2).
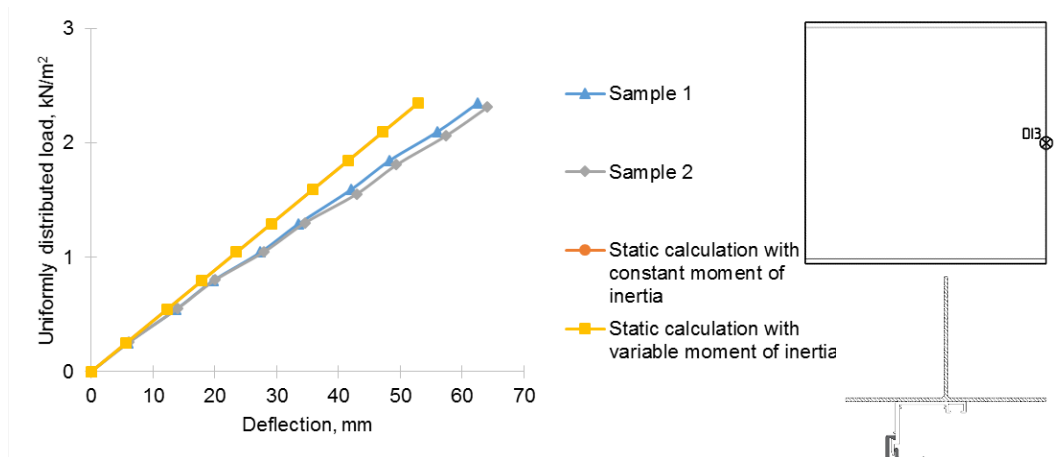
Figure 27. Deflection of the panel edge (DI3).

Graphs shown in Fig. 17, 20, 23 and 26 demonstrate that the results of static calculation are close to the experimental data until a certain value of uniformly distributed load, which depends on the stiffness of profile used in system. After exceeding this value mechanical behavior of the profile changes from linear to nonlinear. Additional discrepancy between experimental and numerical values is consequence of EPDM seal contribution to the overall performance of all investigated types of panels. In test setup 1 EPDM seal is subjected to crumpling in areas of point supports while it keeps its shape in the span. The EPDM seal remains elastic and recovers original shape after unloading. On the other hand, in test setup 2 crumpling occurs along the entire length of high-stiffness profile what leads to the displacement of starting point and increasing of experimental values. Since the national design codes set maximum allowable deflection for a structural element and not a system of elements (except the technological limitations), deflections of a glass panel can be preliminary estimated by static calculation in SJ Mepla.

Gerasimova, E., Galyamichev, A., Schwind, G., Schneider, J.

During the design stage additional actions should be taken against the situation, in which the angle between the tangent to the curved axis of the panel and its initial position would exceed 10 degrees (see Fig. 28).
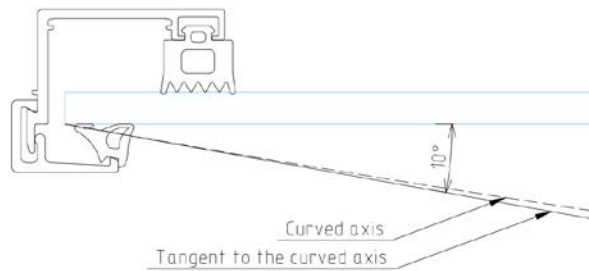
Figure 28. Curved axis of the panel and its tangent.

Figure 29. Deformation of sealant (test setup 1).

The total deflection of the system is supplemented by the deformation value of the rubber sealing profile. This phenomenon is observed in test setup 1 for parts of the system close to points of attachment to the bearing base, and, in the case of high rigidity frame profile (test setup 2), for the entire length of profile. Attention should be paid to the possible use of the system on the sections of facade where leakage may occur due to the deformation of the sealant.

Figure 30. Residual deformation of profile after unloading (test setup 1).

Aluminum profiles showed mechanical behavior in elastic zone at the stresses which did not exceed the yield strength of material. Example of residual deformation is shown in Fig. 29.

The solution of differential equation for the determination of deflection in case of plates with two parallel sides simply supported and the other two sides free is given in [30]. The adapted formula for the deflection of the center of the panel can be read as:

$$\omega = k \cdot 12\left(1 - v^2\right) \cdot \frac{q \cdot b^4}{E \cdot \delta^3}$$

where ω is a deflection of the panel, mm;

k is coefficient which characterizes the inclination of the graphs;

q is a value of uniformly distributed load, kN/m²;

b is a longer side of the panel, mm;

δ is a panel's thickness, mm;

E is a modulus of elasticity, GPa;

v is a Poisson's ratio.

On the base of graphs in Fig. 16, 19, 22 and 25 (presenting the deflection in the center of the glass obtained from the calculation), following coefficients k were obtained:

Table 3. Coefficients k for determination of deflection in the center of the panel.

Scheme type	k
Test setup 1a	$5.064 \cdot 10^{-9}$
Test setup 2a	$2.927 \cdot 10^{-9}$
Test setup 1b	$1.589 \cdot 10^{-8}$
Test setup 2b	$1.344 \cdot 10^{-8}$

Thus, for preliminary determination of the deflection of the panels with configuration and dimensions close to the ones mentioned in this study, following formulas can be used:

$$\text{Test setup 1a: } \omega = 5.064 \cdot 10^{-9} \cdot \frac{q \cdot b^4}{D}$$

$$\text{Test setup 2a: } \omega = 2.927 \cdot 10^{-9} \cdot \frac{q \cdot b^4}{D}$$

$$\text{Test setup 1b: } \omega = 1.589 \cdot 10^{-8} \cdot \frac{q \cdot b^4}{D}$$

$$\text{Test setup 2b: } \omega = 1.344 \cdot 10^{-8} \cdot \frac{q \cdot b^4}{D}$$

where D is a cylindrical rigidity of the panel, N/m.

4. Conclusions

Experimental investigation and numerical modeling performed on the fragment of considered curtain wall system led to the following conclusions:

1. The values of deflection of the panels obtained during experimental study and numerical calculation in finite element software package show high similarity in the zone of linear elastic reaction of a system if specific boundary conditions emerging from the way of fixation of a panel to the system, such as rigidity of the compound aluminum frame, are accounted while calculating the glass panels.

2. Test results demonstrated that the loss of the bearing capacity of the system was caused by excessive deflection of the panel resulting in appearance of longitudinal forces, which led to displacement and subsequent fall of the rubber seal.

3. Empirical formulas for the analytical calculation of the panels with configuration and dimensions close to the ones mentioned in this study were proposed. They can be used in preliminary stages of design for estimation of the deflection in the center of the panel.

References

1. Roginska-Niesluchowska, M. Use of Daylight and Aesthetic Image of Glass Facades in Contemporary Buildings. Proceedings of IOP Conference Series: Materials Science and Engineering. Prague, 2017. 245(8). DOI: 10.1088/1757-899X/245/8/082035

2. Slaton, D. Challenges of modern materials: Assessment and repair. Journal of Architectural Conservation. 2017. 23(1–2). Pp. 47–61. DOI: 10.1080/13556207.2017.1312759

3. Pariafsai, F. A review of design considerations in glass buildings. Frontiers of Architectural Research. 2016. 5(2). Pp. 171–193. DOI: 10.1016/j.foar.2016.01.006

4. Jin, Q., Overend, M. A comparative study on high-performance glazing for office buildings. Intelligent Buildings International. 2017. 9(4). Pp. 181–203. DOI: 10.1080/17508975.2015.1130681

5. Kinowski, J., Sędłak, B., Sulik, P. Large glazing in curtain walls – Study on impact of fixing methods on fire resistance. MATEC Web of Conferences. 2016. No. 46. Article Number 05004. DOI: 10.1051/matecconf/20164605004

Gerasimova, E., Galyamichev, A., Schwind, G., Schneider, J.

6. Bedon, C., Zhang, X., Santos, F., Honfi, D., Kozłowski, M., Arrigoni, M., Figuli, L., Lange, D. Performance of structural glass facades under extreme loads – Design methods, existing research, current issues and trends. Construction and Building Materials. 2018. No. 163. Pp. 921–937. DOI: 10.1016/j.conbuildmat.2017.12.153

7. Pérez-Grande, I., Meseguer, J., Alonso, G. Influence of glass properties on the performance of double-glazed facades. Applied Thermal Engineering. 2005. 25(17–18). Pp. 3163–3175. DOI: 10.1016/j.applthermaleng.2005.04.004

8. Atkins, C. Sustainability of glass in construction. Chapter of book: Sustainability of Construction Materials. 2009. Pp. 171–183. DOI: 10.1533/9781845695842.171

9. Wang, Y., Wang, Q., Sun, J., He, L., Liew, K.M. Effects of fixing point positions on thermal response of four point-supported glass façades. Construction and Building Materials. 2014. No. 73. Pp. 235–246. DOI: 10.1016/j.conbuildmat.2014.09.085

10. Bedon, C., Amadio, C. Buckling analysis and design proposal for 2-side supported double Insulated Glass Units (IGUs) in compression. Engineering Structures. 2018. No. 168. Pp. 23–34. DOI: 10.1016/j.engstruct.2018.04.055

11. Bernard, F., Daudeville, L. Point fixings in annealed and tempered glass structures: Modeling and optimization of bolted connections. Engineering Structures. 2009. 31(4). Pp. 946–955. DOI: 10.1016/J.ENGSTRUCT.2008.12.004

12. Chesnokov, A.G., Chesnokov, S.A., Krasnopolskij, B.I. Vliyanie sposoba zakrepleniya steklopaketov na prochnost stekol [Influence of the method of fixing double-glazed windows on the strength of glasses]. Strojprofil. 2006. 5(51). Pp. 110–114. (rus)

13. Baidjoe, Y., Van Lancker, B., Belis, J. Calculation methods of glass parapets in aluminium clamping profiles. Glass Structures and Engineering. 2018. 3(2). Pp. 321–334. DOI: 10.1007/s40940-018-0075-8

14. Leśniak, A., Górka, M. Analysis of the cost structure of aluminum and glass facades. Proceedings of the 3rd International Conference on Engineering Sciences and Technologies: Advances and Trends in Engineering Sciences and Technologies. Tatranské Matliare, 2018. Pp. 445–450.

15. Petritchenko, M.R., Kotov, E.V., Nemova, D.V., Tarasova, D.S., Sergeev, V.V. Numerical simulation of ventilated facades under extreme climate conditions. Magazine of Civil Engineering. 2018. 77(1). Pp. 130–140. DOI: 10.18720/MCE.77.12

16. Baiburin, A.Kh., Rybakov, M.M., Vatin, N.I. Heat loss through the window frames of buildings. Magazine of Civil Engineering. 2019. 85(1). Pp. 3–14. DOI: 10.18720/MCE.85.1

17. Rusanov, A.E., Baiburin, A. Kh., Baiburin, D.A., Bianco, V. Heat loss from defects of hinged facade systems of buildings. Magazine of Civil Engineering. 2020. 95(3). Pp. 57–65. DOI: 10.18720/MCE.95.6

18. Samarin, O.D. Temperature in linear elements of enclosing structures. Magazine of Civil Engineering. 2017. 70(2). Pp. 3–10. DOI: 10.5862/MCE.70.1

19. Samarin, O.D., Zaycev, N.N. Influencing of orientation of glazed facades on general energy consumption of residential buildings. Magazine of Civil Engineering. 2010. 18(8). Pp. 16–20. DOI: 10.18720/MCE.18.2. (rus)

20. Cwyl, M., Michalczyk, R., Grzegorzewska, N., Garbacz, A. Predicting performance of aluminum – Glass composite facade systems based on mechanical properties of the connection. Periodica Polytechnica Civil Engineering. 2018. 62(1). Pp. 259–266. DOI: 10.3311/PPci.9988

21. Drass, M., Kraus, M.A. Dimensioning of silicone adhesive joints: Eurocode-compliant, mesh-independent approach using the FEM. Glass Structures and Engineering. 2020. DOI: 10.1007/s40940-020-00128-4

22. Bäumler, A., Müller, P. Experimental study on the tightness of glazing bead butt joints of aluminium windows considering comfort aspects. Bauphysik. 2014. 36(2). Pp. 74–79. DOI: 10.1002/bapi.201410020

23. Hagl, A. Experimental and numerical analysis of edge seal spacers of insulated glass units for structural sealant glazing applications. Proceedings of Challenging Glass 3: Conference on Architectural and Structural Applications of Glass. Delft, 2012. Pp. 221–234. DOI: 10.3233/978-1-61499-061-1-221

24. Rosendahl, P.L., Staudt, Y., Schneider, A.P., Schneider, J., Becker, W. Nonlinear elastic finite fracture mechanics: Modeling mixed-mode crack nucleation in structural glazing silicone sealants. Materials and Design. 2019. No. 182. DOI: 10.1016/j.matdes.2019.108057

25. Silvestru, V.A., Englhardt, O., Schneider, J. Linear adhesive connections at the edge of laminated glass panes: an experimental study under tensile, compressive and shear loading. Glass Structures and Engineering. 2019. 4(1). Pp. 45–68. DOI: 10.1007/s40940-018-0080-y

26. Machalická, K., Vokáč, M., Kostelecká, M., Eliášová, M. Structural behavior of double-lap shear adhesive joints with metal substrates under humid conditions. International Journal of Mechanics and Materials in Design. 2019. 15(1). Pp. 61–76. DOI: 10.1007/s10999-018-9404-y

27. Wallau, W., Recknagel, C. Test methodology for performance assessment of structural sealant glazing systems at superimposed mechanical and climatic loading. Polymer Testing. 2019. No. 79. DOI: 10.1016/j.polymertesting.2019.106030

28. Galyamichev, A.V. Vetrovaja nagruzka i ejo dejstvie na fasadnye konstrukci [Wind load and its action on facade structures]. Construction of Unique Buildings and Structures. 2017. 60(9). Pp. 44–57. DOI: 10.18720/CUBS.60.4. (rus)

29. Galyamichev, A.V., Alkhimenko, A.I. Design features of facade cassettes from thin ceramics. Magazine of Civil Engineering. 2017. 69(1). Pp. 64–76. DOI: 10.18720/MCE.69.6

30. Vainberg, D.V., Vainberg, E.D. Raschet plastin [Design of plates]. Budivelnik. Kiev, 1970. 436 p. (rus)

Contacts:

Ekaterina Gerasimova, katyageras17@gmail.com

Alexander Galyamichev, gav@spbstu.ru

Gregor Schwind, schwind@ismd.tu-darmstadt.de

Jens Schneider, schneider@ismd.tu-darmstadt.de

The location of supports under
the monolithic reinforced concrete slabs optimization

A. Chepurnenko*, E. Efimenko, D. Mailyan, B. Yazyev
Don State Technical University, Rostov-on-Don, Russia
*E-mail: anton_chepurnenk@mail.ru

Abstract. We consider the problem of finding the optimal location of point supports under a monolithic reinforced concrete floor slab, which provides the minimum of the objective function. The maximum deflection, potential strain energy, and reinforcement consumption are selected as the objective function. The load and plate configuration can be arbitrary. A restriction on the number of supports is introduced. The solution is performed using stochastic and deterministic optimization methods in combination with the finite element method to determine the objective functions An assessment of the proposed methods for a different number of supports n is made. Particular solutions are presented for n = 3, 4, 5. The optimal relations between the marginal and middle spans are established for buildings with a rectangular grid of columns with large n. It is shown that only the pitch of the columns of the marginal rows can act as a variable parameter, and the steps of the middle rows at the optimal arrangement are equal to each other. The developed methods were tested for the real object. It is established that of the three criteria used, the criterion of the minimum potential strain energy is preferable. It was also revealed that in most of the considered problems, the selected criteria give very close results. The plate thickness and material characteristics do not affect the optimal arrangement of columns.

1. Introduction

The issues of reinforced concrete structures optimal design, including reinforced concrete floor slabs of buildings for various purposes, are the subject of a large number of papers including [1–12]. The inverse method is widely used for optimization, the essence of which is to find such laws of changing the characteristics of a material within a structure in which its stress-strain state is given [1–5]. In some publications, for example [13], models of equal-strength plates of variable thickness are constructed, however, the practical implementation of this model is associated with great difficulties, as well as the creation of artificial heterogeneity of the structure. As a method of optimizing reinforced concrete slabs, the most common one is the selection of rational reinforcement [6–12].

Optimization problems by varying the location of the supports are solved mainly for beams [14–16]. There are relatively few publications on determining the optimal arrangement of supports for slabs [17–26]. The criterion of optimization in these publications is deflection, the frequency of natural vibrations, and the value of the breaking load. They are distinguished by a simple statement of the problem, for example, in [17] a round axisymmetrically loaded plate is considered, in [18–24] the problem for a rectangular plate on four point supports is solved. The presented solutions are not applicable for real objects. The publications [27–28] optimize the real object, but not by changing the position of the supports, but by partially replacing the existing columns with modernized ones.

The goal of this work is the development and testing of the methods for determining the optimal location of point supports under the reinforced concrete slabs with arbitrary configuration and load.

In the framework of the goal, the following tasks are solved:

1. Development of the methodology for determining the optimal arrangement of supports based on a stochastic approach.

2. Development of optimization methodology using the deterministic approach.

3. Comparative evaluation of the effectiveness of stochastic and deterministic methods with a different number of supports.

4. Testing optimization techniques at a real construction object.

2. Methods

Let us first consider the application of the stochastic method to this problem. The following values will be selected as the objective function f:

1. The maximum value of the deflection of the slab $w_{\max}$, mm;

2. The value of the potential strain energy W, kJ;

3. Reinforcement consumption m_s, t.

The choice of the potential strain energy (PSE) as the objective function is explained by the fact that it is an integral measure that determines the level of the stress-strain state. The smaller the value of W, the better the system resists external influences.

While using the values of w_{max} and W as target values, we assume that the rigidity of the slab does not depend on reinforcement. The calculation will be based on the theory of elastic thin plates. Supports are considered as restraints in nodes along the z axis. The reinforcement consists of rods located near the upper and lower surfaces of the slab along the x and y axis. As a result of the selection of reinforcement for each finite element, the values of cross-sectional areas in m^2 per linear meter for tensile reinforcement $A_{sx,i}$, $A_{sy,i}$ and compressed reinforcement $A'_{sx,i}$, $A'_{sy,i}$ are determined.

To determine the optimal arrangement of the columns, we will use the Monte Carlo method in combination with the finite element method. At the first stage, the slab, depending on its geometry, is meshed by triangular or rectangular finite elements of plate with three degrees of freedom at the node: deflection along the z axis and two angles of rotation relative to the x and y axis. The load on the slab, as well as the number of point supports n are considered to be given and constant. The structural stiffness matrix and the load vector are calculated taking into account stationary supports, but excluding columns, the position of which can vary. Then, using a random number generator, n uniformly distributed random values are generated that determine the numbers of the nodes in which the columns are installed. A check is made for the absence of duplicate node numbers, and it is also controlled so that the minimum distance between the supports is greater than the specified value. Otherwise, random numbers are generated repeatedly.

Then, boundary conditions are imposed on the stiffness matrix and the load vector, taking into account the selected arrangement of columns, the system of equations of FEM is solved:

$$[K]\{U\} = \{P\},\tag{1}$$

where $[K]$ is stiffness matrix, $\{U\}$ is nodal displacement vector, $\{P\}$ is load vector.

The implementation of the FEM calculation was carried out by the authors personally in the Matlab software package.

The potential strain energy is determined by the formula:

$$W = \frac{1}{2}\{U\}^T[K]\{U\}.\tag{2}$$

The selection of reinforcement in the slab is based on Russian standards for the design of reinforced concrete structures from the conditions:

$$\left(M_{x,ult} - M_x\right)\left(M_{y,ult} - M_y\right) - M_{xy}^2 \geq 0;$$
$$M_{x,ult} \geq M_x;$$
$$M_{y,ult} \geq M_y;$$
$$M_{xy,ult} \geq M_{xy},$$

(3)

where M_x, M_y are bending moments acting on a flat selected element; M_{xy} is torque; $M_{x,ult}$, $M_{y,ult}$, $M_{xy,ult}$ are ultimate bending moments and torques perceived by a flat selected element.

The total consumption of reinforcement in tons for the slab can be determined by the formula:

$$m_s = \rho \sum_{i=1}^{k} \left(A_{sx,i} + A_{sy,i} + A'_{sx,i} + A'_{sy,i}\right) A_i,$$

(4)

where ρ = 7.8 t/m^3 is the density of steel, A_i is the area of the i-th finite element, k is total number of finite elements.

The value of the objective function f is compared with the value f_0, for which a very large number is initially taken. If $f < f_0$, then f_0 is assigned the value f. The calculation with a random arrangement of columns is repeated a large number of times (by us, the number of tests k was taken equal to 10^6 or more). The block-scheme of the calculation is shown in the Fig. 1.

Due to the large number of possible combinations of the arrangement of columns, the variant obtained as a result of the calculation may not be the most optimal. However, for large k, it will be rational and can be further implemented in practice.
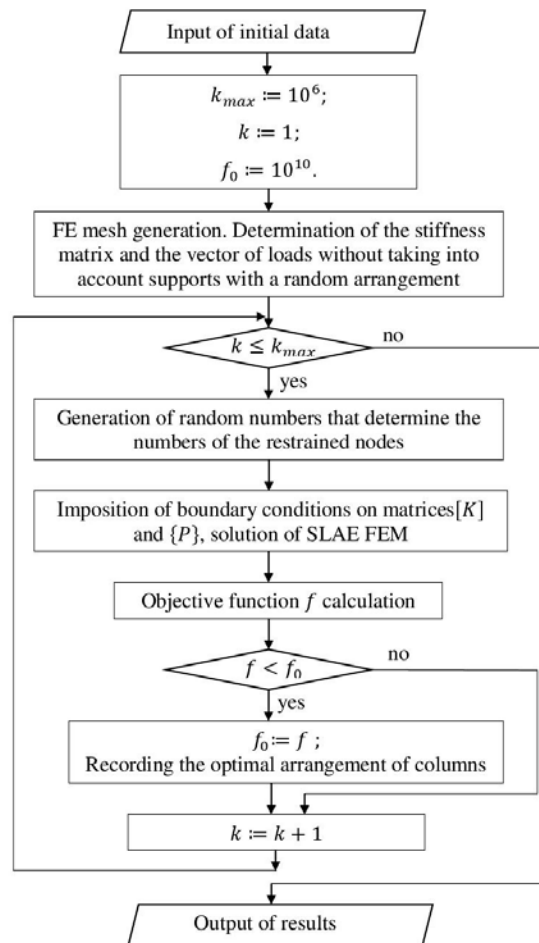
Figure 1. The block-scheme of the calculation using the stochastic method.

The presence of reinforcement leads to the change in the rigidity of the structure and a redistribution of internal forces, therefore, the task of selecting reinforcement taking into account changes in the rigidity of the slab is nonlinear. This non-linearity is called "engineering", and it is implemented in some software systems, for example, LIRA-SAPR. When using the Monte Carlo method, the calculation is repeated many times, so taking non-linearity into account is impractical because of sharp increase in the calculation time.

Also, the proposed algorithm can be slightly modified. In the modified algorithm, the initial arrangement of the columns is set regularly with a given step. Then, for each column, two random values are generated that determine their offset relative to the initial position in x and y so that the new position of the column coincides with some node of the finite element mesh. The maximum offset should be less than the half of the initial column pitch. The calculation is also performed 10^6 times and the most optimal variant is selected.

When using the deterministic method to achieve the best result, the number of varied parameters must be minimized. To do this, optimization is performed on a regular grid of columns with varying steps. We perform calculations in the *Matlab* environment using the *fmincon* function of the *Optimization Toolbox* non-linear optimization package. As an optimization method, the internal point method is chosen. The calculation of objective functions is based on the subprogram developed by the authors based on the finite element method.

3. Results and Discussion

Using the Monte Carlo method, a series of test problems for a square slab was solved for various values of n. The calculation was performed on the action of a uniformly distributed over the area load with a rectangular grid of finite elements 10×10. The optimal location of the three point supports is shown in Fig. 2. According to the criteria of minimum consumption of reinforcement and minimum potential strain energy, the same result is obtained.
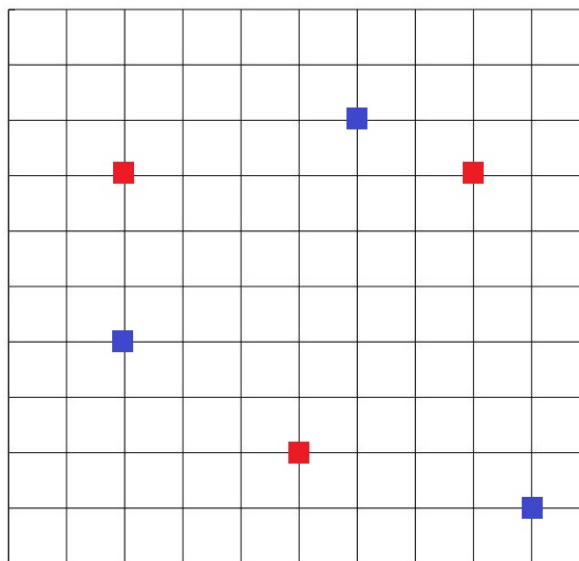
Figure 2. The optimal location of the three supports:
■ **– from the condition of minimum reinforcement consumption and potential strain energy,**
■ **– from the condition of minimum deflection.**

The optimal arrangement of four supports is shown in Fig. 3. From the symmetry of the problem for $n = 4$ it follows that the optimal arrangement of columns should be symmetrical with respect to the center of the slab. However, in the variants shown in Fig. 3, symmetry is not observed due to restrictions on the location of the supports (columns can only be located at the nodes of the finite element mesh). In the practical realization of the obtained supports arrangement, it is advisable to place them symmetrically relative to the center of the slab (see below Fig. 6).

Note that the arrangement of the supports corresponding to the minimum deflection is similar to the arrangement of supports obtained in the paper [20] from the condition of maximum fundamental frequency of the plate (Fig. 4).
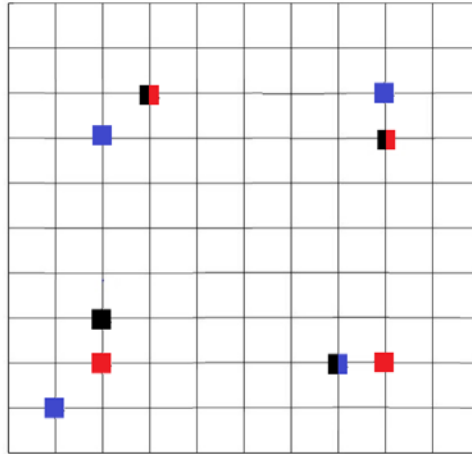
Figure 3. The optimal location of four supports:
■ – from the condition of minimum potential strain energy,
■ – from the condition of minimum deflection,
■ – from the condition of minimum reinforcement consumption.
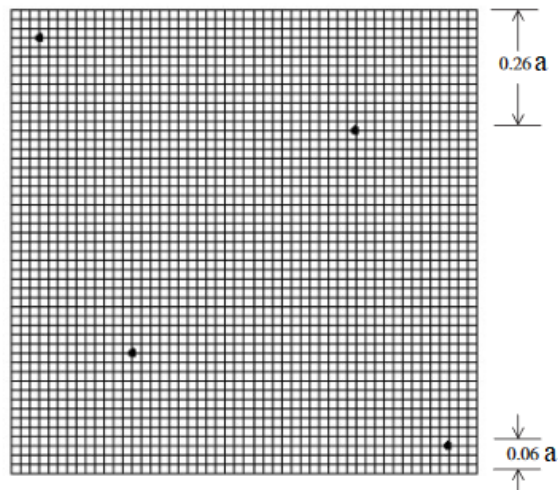
Figure 4. The optimal arrangement of four supports from the condition
of maximum natural frequency obtained in [20].

At $n = 5$, the location of the supports was found, satisfying both the minimum of displacements, potential strain energy, and the reinforcement consumption (Fig. 5).
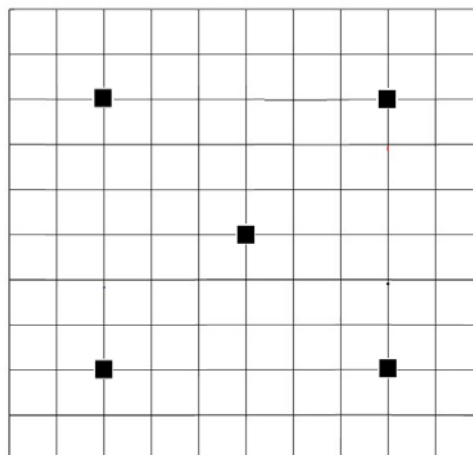
Figure 5. The optimal location of the five columns.

For $n = 4$ and $n = 5$, the problem was also solved by the deterministic method. Four columns were located symmetrically relative to the center of the plate, and the ratio a_1/a was used as a variable parameter (Fig. 6). The restriction on size a_1 was $0 \leq a_1 < a/2$. The calculation of the objective functions was performed by the finite element method. For each iteration, the FE grid was automatically regenerated taking into account the size a_1. Because of symmetry, a quarter of the structure was considered. At $n = 5$, the fifth column was placed in the center. The optimal a_1/a ratios for $n = 4$ were 0.224 from the condition of minimum deflection, 0.228 from the condition of minimum potential strain energy, and 0.233 from the condition of minimum reinforcement consumption. At $n = 5$, these ratios turned out to be 0.2028, 0.1989, and 0.2034, respectively. The obtained values are consistent with the results based on the Monte Carlo method.
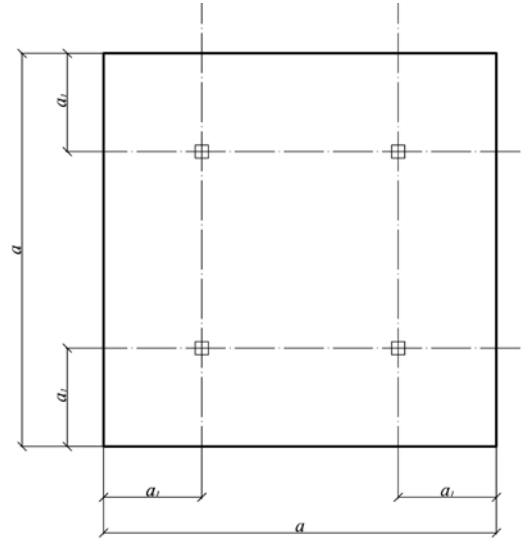
Figure 6. To optimization of the slab by deterministic method.

The presented solutions for $n = 3, 4, 5$ are mainly illustrative and are unlikely to be encountered in the design of real objects. If the position of most of the supports is predetermined and it is required to find how to optimally place the small number of the remaining supports, the task can be easily solved using proposed approach.

We pass on to a large number of supports n. Fig. 7 shows the arrangement of 25 columns obtained using the Monte Carlo method and basic algorithm as a result of 10^6 tests for a 24×24 m slab. The maximum deflection at $E_b = 3 \times 10^4$ MPa, $q = 50$ kPa, and $h = 20$ cm was 58.4 mm. For the same slab with a uniform column pitch of 6 m: $w_{max} = 43.6$ mm. Thus, with such a number of columns, the proposed algorithm was ineffective. The result of the search for the optimal support location using a modified algorithm is shown in Fig. 8. For the supports location presented on Fig. 8, the maximum deflection was 25.4 mm, which is lower by 42 % in comparison with the result for a regular step of the columns. However, in comparison with the regular arrangement of columns, inconveniences may arise with the arrangement of premises in the building.

A stochastic calculation was also performed for a 36×36 m building with an initial column pitch of 6 m. In this case, the efficiency of the modified algorithm turned out to be relatively low, the maximum deflection decreased by only 5.7 %.

With an increase in the number of supports, the effectiveness of the Monte Carlo method decreases due to the large number of possible combinations. We proceed further to the optimization of the grid of columns using deterministic methods. Consider a slab 48×36 m with a column pitch of 6 m (Fig. 9). By virtue of symmetry, a quarter of the structure is calculated. The following initial data are used: concrete B25, reinforcement A400, load $q = 50$ kPa, plate thickness $h = 20$ cm. Column steps a_1, a_2, a_3, b_1, b_2 are used as variable parameters.
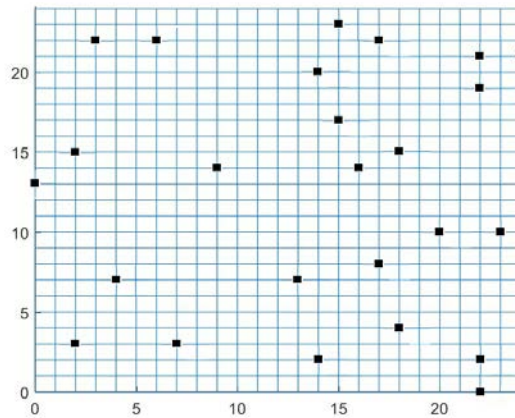
Figure 7. The result of the search for the optimal supports location using a basic algorithm.
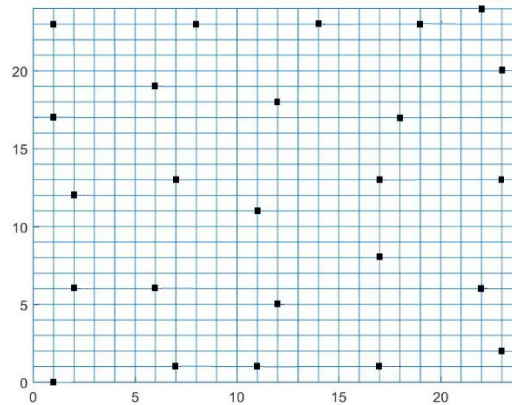
Figure 8. The result of the search for the optimal supports location using a modified algorithm.
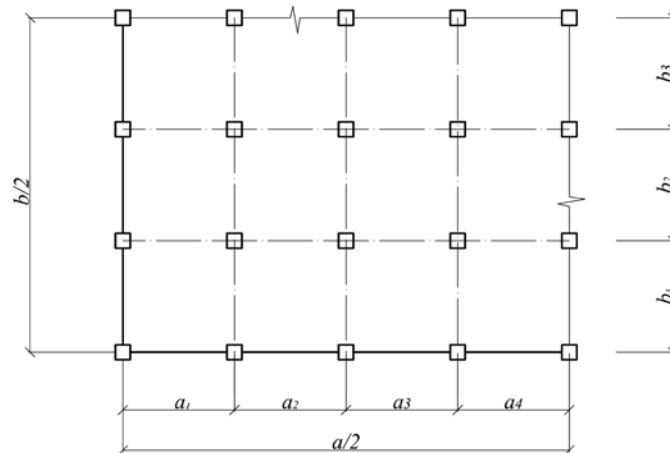
Figure 9. A quarter of the optimized slab 48×36 m.

With regular column pitch, maximum deflections and forces occur in marginal spans. Contour plot of vertical displacements is shown in Fig. 10. The values of the objective functions are w_{max} = 43.8 mm, W = 233.36 kJ, m_s = 17.01 t. The results of optimization of the slab based on three criteria are presented in Table 1. The effect of optimization was 48 % for deflection, 29 % for potential strain energy and 27 % for reinforcement consumption. When optimizing for deflection, alignment of displacements in the middle of the marginal and middle spans occurs, as can be seen from Fig. 11. Table 1 shows that for alignment of displacements and internal forces in all spans, it is possible to take only the steps of the marginal rows as a variable parameter, and put the remaining steps equal among themselves. In addition to the slab 48×36 m, the calculation of slabs 48×48 m, 36×36 m and 24×24 m was carried out. It was found that the optimal column steps along the x axis do not depend on the steps along the y axis, and the ratio between the steps of the columns of the marginal and middle row is determined by the number of spans.
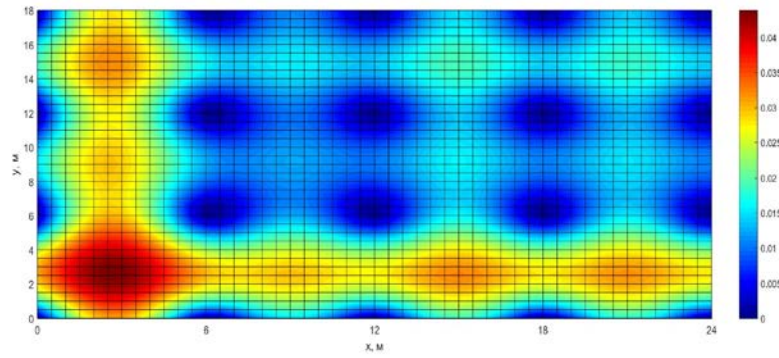
**Figure 10. Contour plot of vertical displacements (m) for a 48×36 slab
with a basic arrangement of columns.**
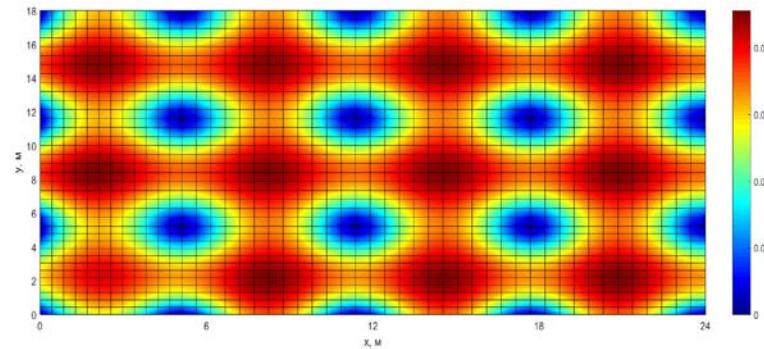
**Figure 11. Contour plot of vertical displacements (m) for a 48×36 slab
with an optimal arrangement of columns.**

Table 1. Optimization results for the 48×36 m slab.

	a_1, m	a_2, m	a_3, m	a_4, m	b_1, m	b_2, m	b_3, m	w_{max}, mm	W, kJ	m_s, t
From a minimum of a deflection	5.11	6.27	6.3	6.32	5.22	6.39	6.39	22.8	164.99	12.389
From a minimum of PSE	5.16	6.28	6.28	6.28	5.24	6.38	6.38	23.2	164.97	12.392
From the minimum consumption of reinforcement	5.06	6.3	6.32	6.32	5.14	6.42	6.44	23.5	165.19	12.385

Our program allows to optimize floor slabs with more complex configurations. With its use, we performed the optimization of the project of the scientific and laboratory complex of the Maritime State Academy named after Admiral F.F. Ushakov in the city of Rostov-on-Don. In the original design, the building consisted of two parts, separated by an expansion joint. Optimization of each part was carried out separately. The offsets a_1 and a_2 of the middle row columns were used as variable parameters. The position of some columns, as well as stiffness diaphragms, was left unchanged. Performed optimization allowed to preserve the initial dimensions of the premises. A schematic representation of the part of the floor slab located to the right of the expansion joint is shown in Fig. 12.
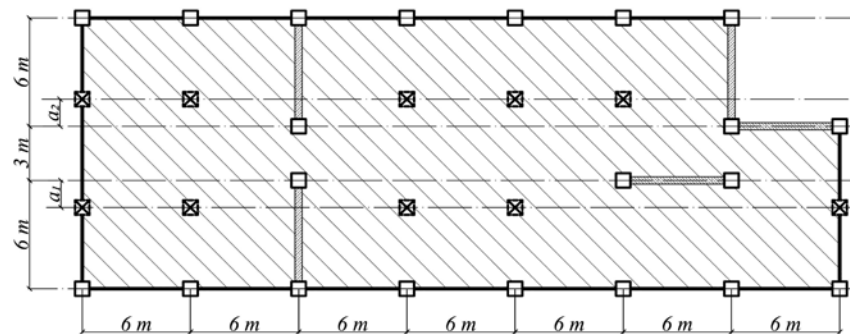
Figure 12. Schematic representation of part of the floor slab:
□ – columns whose position does not change, ⊠ – displaceable columns.

As before, the maximum deflection, the potential strain energy, and the reinforcement consumption were used as optimization criteria. The calculation was performed with the following initial data: concrete class B25, reinforcement class A400, plate thickness h = 20 cm, load uniformly distributed over an area with intensity q = 20 kPa. Fig. 13 shows the contour plot of vertical displacements for the right part of the slab with the basic arrangement of columns ($a_1 = a_2 = 0$). The values {w_{max}, W, m_s} were {1.96 mm, 4.37 kJ, 6.57 t}.
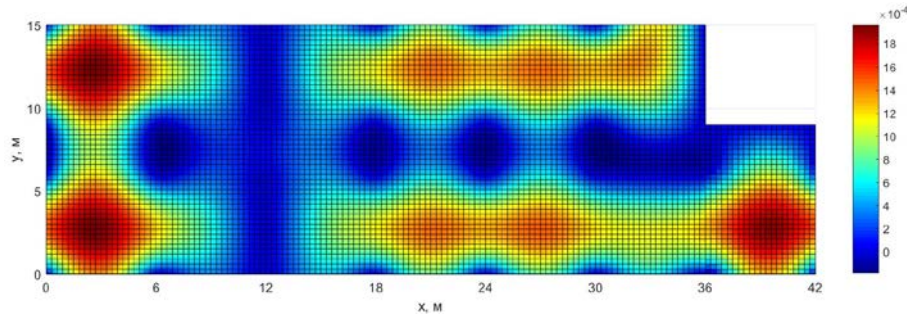
Figure 13. Deflections contour plot (m) at the basic arrangement of columns.

The optimal values of the parameters a_1 and a_2 obtained using three criteria, as well as the corresponding values {w_{max}, W, m_s} are given in Table 2.

Table 2. Building optimization results.

Criterion	a_1, m	a_2, m	w_{max}, mm	W, kJ	m_S, t
Minimum deflection	2.34	0.848	1.52	3.19	5.41
Minimum PSE	1.35	1.51	1.61	3	5.18
Minimum reinforcement consumption	1.38	1.65	1.61	3.01	5.18

From the Table 2 it can be seen that the results based on the criteria of minimum PSE and minimum consumption of reinforcement are quite close. Finally, we accepted the variant corresponding to the minimum PSE, since it also provides a minimum reinforcement consumption. The reinforcement consumption has reduced by 21.1 %, the potential strain energy by 31.4 %, and the maximum deflection by 17.9 %. The contour plot of vertical displacements corresponding to this arrangement of columns is shown in Fig. 14.

Note that optimization based on the criterion of minimum PSE requires less machine time, since there is no need to determine internal forces and perform the calculation of reinforcement.

When using the criterion of the minimum deflection, it is also not necessary to calculate the internal forces, but the deflection, unlike the PSE and the total reinforcement consumption, is not an integral characteristic of the structure efficiency.
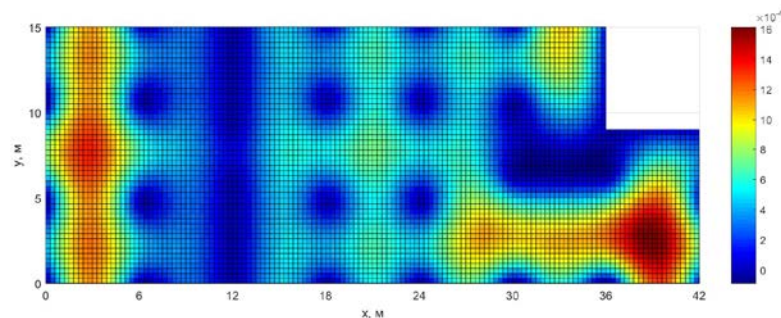
Figure 14. Deflections contour plot (m) at the optimal arrangement of columns.

4. Conclusions

1. The methodology has been developed for determining the optimal arrangement of supports for a given number of them using stochastic approach based on three optimization criteria: minimum deflection, minimum potential strain energy and minimum reinforcement consumption. In most of the problems considered, these criteria give very close results. In all the examples considered, the calculation was carried out for a uniformly distributed load. Since the optimization methodology is based on the finite element method, the load can be arbitrary.

2. The methodology for optimizing columns location by deterministic approach is proposed. For buildings with a rectangular grid of columns, it was found that only the pitch of the columns of the marginal rows can act as a variable parameter.

3. It is shown that the stochastic method is effective with a small number of columns, and with an increase in their number, the efficiency decreases due to a large number of possible combinations. With a large number of columns, deterministic method should be used and the number of variable parameters should be minimized.

4. The solution of the optimization problem for a real object is presented. During the optimization process, compared to the initial project, the reinforcement consumption was reduced by 21.1 %, the potential strain energy by 31.4 %, and the maximum deflection by 17.9 %. It is shown that of the three optimization criteria used, the criterion of the minimum potential strain energy is the most preferable, since its calculation requires less machine time and at the same time, potential energy is an integral characteristic of the design efficiency in contrast to the maximum deflection. It was also found that plate thickness and material characteristics do not affect the optimal arrangement of columns. This is because these parameters, if they are constant within the structure, do not affect the character of the internal forces distribution in the slab.

References

1. Andreev, V.I., Barmenkova, E.V., Potekhin, I.A. Way of optimization of stress state of elements of concrete structures. Procedia Engineering. 2016. 153. Pp. 37–44. DOI: 10.1016/j.proeng.2016.08.077

2. Yazyev, S., Bekkiev, M., Peresypkin, E., Turko, M. Task for a Prestressed Reinforced Concrete Cylinder with External Reinforcement and Cylinder Optimization by Varying the Modulus of Elasticity. Energy Management of Municipal Transportation Facilities and Transport. Springer, Cham, 2017. Pp. 869–876. DOI: 10.1007/978-3-319-70987-1_93

3. Andreev, V.I. About one way of optimization of the thick-walled shells. Applied mechanics and materials. Trans Tech Publications, 2012. 166. Pp. 354–358. DOI: 10.4028/www.scientific.net/AMM.166-169.354

4. Andreev, V.I. Optimization of thick-walled shells based on solutions of inverse problems of the elastic theory for inhomogeneous bodies. Computer Aided Optimum Design in Engineering. 2012. Pp. 189–202. DOI: 10.2495/OP120171

5. Andreev, V.I., Chepurnenko, A.S., Yazyev, B.M. Model of equal-stressed cylinder based on the Mohr failure criterion. Advanced Materials Research. 2014. 887–888. Pp. 869–872. DOI: 10.4028/www.scientific.net/AMR.887-888.869

6. Alcalá, J. et al. Embodied energy optimization of prestressed concrete slab bridge decks // Technologies. 2018. 6(2). DOI: 10.3390/technologies6020043

7. Aldwaik, M., Adeli, H. Cost optimization of reinforced concrete flat slabs of arbitrary configuration in irregular highrise building structures. Structural and Multidisciplinary Optimization. 2016. 54(1). Pp. 151–164. DOI: 10.1007/s00158-016-1483-5

8. Ahmadi-Nedushan, F., Hojjatli, A. Optimum cost design of reinforced concrete slabs using neural dynamics model. Engineering Applications of Artificial Intelligence. 2005. 18 (1). Pp. 65–72. DOI: 10.1016/j.engappai.2004.08.025

9. Fraile-Garcia, E. et al. Optimization based on life cycle analysis for reinforced concrete structures with one-way slabs. Engineering Structures. 2016. 109. Pp. 126–138. DOI: 10.1016/j.engstruct.2015.12.001

10. Mohammed, A.H. et al. Finite element analysis and optimization of bonded post-tensioned concrete slabs. Cogent Engineering. 2017. 4(1). DOI: 10.1080/23311916.2017.1341288

11. Yepes, V., Albiñana, M., García-Segura, T. Design optimization of precast-prestressed concrete road bridges with steel fiber-reinforcement by a hybrid evolutionary algorithm. International Journal of Computational Methods and Experimental Measurements. 2017. 5(2). Pp. 179–189. DOI: 10.2495/CMEM-V5-N2-179-189

12. Vatin, N.I., Ivanov, A.Yu., Rutman, Y.L., Chernogorskiy, S.A., Shvetsov, K.V. Earthquake engineering optimization of structures by economic criterion. Magazine of Civil Engineering. 2017. 76(8). Pp. 67–83. DOI: 10.18720/MCE.76.7

13. Moita, J.S. et al. Material distribution and sizing optimization of functionally graded plate-shell structures. Composites Part B: Engineering. 2018. 142. Pp. 263–272. DOI: 10.1016/j.compositesb.2018.01.023

14. Hauser, B.R., Wang, B.P. Optimal design of a parallel beam system with elastic supports to minimize flexural response to harmonic loading using a combined optimization algorithm. Structural and Multidisciplinary Optimization. 2018. 58(4). Pp. 1453–1465. DOI: 10.1007/s00158-018-1973-8

15. Aydin, E. et al. Optimization of elastic spring supports for cantilever beams. Structural and Multidisciplinary Optimization. 2020. Pp. 1–27. DOI: 10.1007/s00158-019-02469-3

16. Kozikowska, A. Multi-objective topology and geometry optimization of statically determinate beams. Structural Engineering and Mechanics. 2019. 70(3). Pp. 367–380. DOI: 10.12989/sem.2019.70.3.367

17. Xie, C.N., Li, X.F. Optimal location of ring support for heavy Mindlin plates under axisymmetric loading. Proceedings of the Institution of Mechanical Engineers, Part C: Journal of Mechanical Engineering Science. 2018. 232(7). Pp. 1270–1279. DOI: 10.1177/0954406217700182

18. Won, K.M., Park, Y.S. Optimal support positions for a structure to maximize its fundamental natural frequency. Journal of Sound and Vibration. 1998. 213(5). Pp. 801–812. DOI: 10.1006/jsvi.1997.1493

19. Park, Y.H., Park, Y. Optimal Support Positions to Enhance Structure Natural Frequency. Proceedings of the KSME Dynamics and Control Division Summer Annual Meeting. KSME Dynamics and Control Division, 1999. DOI: 10.1006/jsvi.1997.1493

20. Wang, D., Jiang, J.S., Zhang, W.H. Optimization of support positions to maximize the fundamental frequency of structures. International journal for numerical methods in engineering. 2004. 61(10). Pp. 1584–1602. DOI: doi.org/10.1002/nme.1124

21. Wang, D. Optimization of support positions to minimize the maximal deflection of structures. International Journal of solids and structures. 2004. 41(26). Pp. 7445–7458. DOI: 10.1016/j.ijsolstr.2004.05.035

22. Wang, D. Optimal design of structural support positions for minimizing maximal bending moment. Finite Elements in Analysis and Design. 2006. 43(2). Pp. 95–102. DOI: 10.1016/j.finel.2006.07.004

23. Wang, C.M. et al. Optimization of internal line support positions for plates against vibration. Journal of Structural Mechanics. 1993. 21(4). Pp. 429–454. DOI: 10.1080/08905459308905196

24. Son, J.H. Kwak, B.M. Optimization of boundary conditions for maximum fundamental frequency of vibrating structures. AIAA journal. 1993. 31(12). Pp. 2351–2357. DOI: 10.2514/3.11935

25. Wang, B.P. Chen, J.L. Application of genetic algorithm for the support location optimization of beams. Computers & structures. 1996. 58(4). Pp. 797–800. DOI: 10.1016/0045-7949(95)00184-I

26. Kwon, Y.D. et al. Convergence enhanced genetic algorithm with successive zooming method for solving continuous optimization problems. Computers & Structures. 2003. 81(17). Pp. 1715–1725. DOI: 10.1016/S0045-7949(03)00183-4

27. Seo, H., Kim, J., Kwon, M. Optimal seismic retrofitted RC column distribution for an existing school building. Engineering Structures. 2018. 168. Pp. 399–404. DOI: 10.1016/j.engstruct.2018.04.098

28. Papavasileiou, G.S., Charmpis, D.C. Earthquake-resistant buildings with steel or composite columns: Comparative assessment using structural optimization. Journal of Building Engineering. 2020. 27. Pp. 100988. DOI: 10.1016/j.jobe.2019.100988

Contacts:

Anton Chepurnenko, anton_chepurnenk@mail.ru

Ekaterina Efimenko, ovekaterina90@yandex.ru

Dmitry Mailyan, usp-dr@yandex.ru

Batyr Yazyev, ps62@yandex.ru

Frost cracks formation in permafrost regions

V.A. Stetjukha
Transbaikal state University, Chita, Russia
E-mail: stetjukha_chita@mail.ru

Abstract. The object of the study is the soil susceptible to cryogenic cracking during freezing. The formation of cracks creates the problems in the development of mineral deposits in northern regions with sharply continental climates in Europe, Asia and North America. The destructive effects of cracks on the construction of roads and linear structures require the prediction of cryogenic cracks. The developed mathematical model and the method of its use provide the prediction of the processes of frost cracks formation in harsh climates. The calculation algorithm realizes the procedures for the step-by-step solution of the spatial strength problem for a fragment of a soil mass taking into account changes in temperature fields and physical and mechanical properties of frozen soils over time. The given example demonstrates the results of predicting of cryogenic cracking of the soil in the form of graphs of stress distribution in the freezing massif. The calculation results illustrate the ability to predict the formation of frost cracks, the ability to determine the main parameters and periods of cracking. The research results can be used in the design of objects in the conditions of propagation of soils subjected to cracking.

1. Introduction

The object of research is a massif of frozen soils subjected to cryogenic cracking in cold regions. In articles [1–3] permafrost propagation zones in the Northern Hemisphere were identified. In [4, 5], the studies devoted to modeling changes in the permafrost occurrence area and changes in soil characteristics over time are presented. The consequences of cryogenic soil cracking are observed in the form of special relief forms during the formation of cracks and polygons in natural conditions on the Earth's surface, during the formation of ice wedges. This is confirmed by field observations in Siberia, Alaska, Canada, the European North and several other regions [6–10].

Most often, cracks occur in areas with a sharply continental climate, with a low negative average annual air temperature, with large amplitudes of annual air temperatures, with a small thickness of snow cover, on the slopes [11, 12]. The formation of cryogenic cracks is also noted in territories with seasonally freezing soils. The size of the seasonally thawed layer in such regions can reach 2-3 meters or more. The average monthly temperature of frozen rocks, for example, in the Central Transbaikalia can decrease at a depth of 2 m to –8 °C, at a depth of 6 m – to –4 °C [13, 14]. The listed factors affect the nature and magnitude of temperature stresses and strains. In this case, cracks form at approximately equal distances from each other in mutually perpendicular directions. So-called "polygons" that are similar in shape to rectangles are formed. The dimensions of "polygons" depend on moisture and other properties of soils, on the dynamics of changes in air temperature. With an increase in the strength of the near-surface soil layer, the size of the polygons increases.

The relevance of this study is due to the fact that the northern regions of our planet are distinguished by large reserves of minerals. Development of regions is complicated by a number of problems associated with the natural conditions of the regions [14, 15]. Among the problems, one can distinguish such a phenomenon as cryogenic cracking. The formation of frost cracks in the soil creates serious difficulties in the operation of roads [16], long linear objects (pipes, cables), which are located underground [14]. There is a threat of damage to objects; the appearance of cracks provokes the formation of ground icing [12]. Thus, the relevance of studying the problem is associated with the influence of frost cracking of the soil on

tecnogenic objects. There is a need for reliable forecasting of crack formation and taking these phenomena into account when designing objects in the northern regions.

Prediction of the processes of cryogenic cracks formation is based on previous studies in a number of directions of research reflected in the world literature. Crack formation processes are closely related to the laws of soil temperature changes. As the initial data for modeling cracks, we used the results of a study of the dynamics of soil temperature in the Northern regions during freezing and thawing [15, 17–21]. A number of authors have previously established the properties of frozen soils [22–25], including their strength characteristics [26, 27]. There are known studies of temperature deformations of soils with different properties at negative temperatures, not accompanied by the formation of frost cracks [28–30].

The most important element in predicting the process of fracture of porous materials and cracks formation is mathematical modeling. From publications devoted to modeling cryogenic cracks, we can distinguish works that use simple formulas. One of the first crack modeling schemes proposed by B.N. Dostavalov and S.E. Grechishchev, are given in article [12]. Criteria for the formation and individual parameters of cracks here are determined by approximate empirical formulas. A key factor in such techniques is the magnitude of the decrease in soil temperature in relation to its average annual temperature. As a condition for the formation of a cryogenic crack, the excess of temperature stresses in the massif over the breaking stress is considered. The possibility of cracking and their parameters is established depending on the properties of frozen soils, which vary in each case.

The simple analytical expressions of stresses in the soil are used in a number of modern publications [14, 31, 32]. In [14, 31], the authors propose to consider frozen soil as a linearly deformable material. Based on the solution of the thermoelasticity problem for half-space, in [31, 32] simple expressions are formed to calculate the stresses in soil massif, to determine the conditions for crack formation and their parameters. At the same time, the number of arguments in the applied empirical formulas remains insignificant. The joint solution of the spatial problem of heat and mass transfer and geomechanics makes it possible to use a much larger number of physical-mechanical and geometric parameters, climatic characteristics. This should provide a more objective assessment of the development of processes in the soil, since each of the factors can become decisive when the condition for the formation of a crack is met.

In article [11] a model of frost cracking was presented for a particular problem under conditions of the development of a slope process. Here, one-dimensional simplified heat transfer equations are used. The model is based on ice segregation in a previously formed crack, which can be considered as a secondary phenomenon. The probability of cracking during seasonal freezing in the absence of permafrost is confirmed. The occurrence of horizontal cracks and methods for their mathematical modeling in connection with the formation of lenses during ice segregation are considered in [23, 33]. In relation to the problem being solved, the interest here is the criteria for the rupture of frozen soil during its freezing.

The application of the finite element method to modeling the processes of freezing and thawing in known articles is usually limited to solving one-dimensional or two-dimensional problems [33–35]. In publications [33, 34], vertical displacements of the soil surface are determined when horizontal ice lenses are formed in soil massif. In article [35], channel slope deformations during freezing were studied using the finite element method in the framework of solving a two-dimensional problem. In [13], the purpose of research is to assess the effect of previously formed frost cracks in the soil mass on heat and mass transfer processes in a separate soil block located between the cracks. In this case, the role of external factors of influence on the strength and deformation characteristics of frozen soil used as the foundations of structures is established. When calculating the thermal regime in the soil block, two-dimensional heat conduction equations are used. Deformations and stresses in soil blocks are determined when solving a plain problem for a linearly deformable medium. Thus, the criteria and parameters of the formation of emerging frost cracks in the last presented works are not determined. When predicting frost cracks, preference should be given to solving the spatial problem. This makes it possible to take into account the redistribution of internal stresses (taking into account Poisson's ratio), temperature and moisture flows in the elements of the design scheme along the directions of the three coordinate axes. This approach makes it possible to use the available results of long-term meteorological observations, the traditional and obligatory list of materials obtained as a result of engineering-geological surveys as initial data.

The presented literature review confirms the absence of solutions to the spatial problem for assessing the formation of vertical frost cracks, taking into account the whole complex of external factors and the dynamics of the process under study. The purposes of the work are to estimate the possibility of cryogenic cracking of frozen soil, to develop a method for predicting the formation of cracks for various geological and climatic conditions. Within the framework of the indicated problem, the following tasks are solved. A correct mathematical model of the formation of cryogenic cracks in frozen soil is formed. A methodology for using the model is being developed; an analysis of the results is performed. To implement the tasks, the finite element method and three-dimensional elements of the soil massif are used. The calculation model

includes the solution of the nonlinear problem of heat and mass transfer, the nonlinear problem of deformation of the soil mass taking into account the dynamics of the development of processes in time.

2. Methods

A soil massif with specified physical and mechanical properties during the formation of cryogenic cracks is considered. The process of thermal deformations studying is divided into 2 stages. At the first stage, the dynamics of changes in temperature fields in the soil mass is determined based on the temperature field model. The air temperature forecast is formed on the basis of the results of long-term weather observations. The temperature distribution near the surface of the soil massif is determined by the climatic conditions of the region [20]. The temperature in the near-surface part of the soil half-space is determined by solving the non-stationary problem of heat and mass transfer. The solution of the equations of heat and mass transfer determines the values of temperature drops in the elements of the soil mass. At the second stage the methods of mechanics of a continuous medium are applied. The obtained values of temperature drops are included in the composition of the load vector at the stage of determining deformations and stresses in the soil mass using the software package "Lira". In this case, temperature drops are parameters for loading the soil massif.

The algorithm for solving the problem of thermomechanics is presented in Fig. 1 as a combined mathematical model. The formation of a combined model begins with the establishment of the geometric dimensions and physico-mechanical properties of the studied soil masses. The composition of the model includes the climatic influences model, mathematical models of heat and moisture transfer processes, models of changes in the stress-strain state in rocks. In connection with the increase in the number of factors during the selection of parameters, the significance of factors is estimated by the correlation analysis method.

The most important element of the combined model is the mechanism for adjusting the basic physical and technical parameters of soils at each calculation step at given intervals. Fig. 1 lists the main mutual functional dependencies of the parameters implemented in the model. The dependences of temperature and humidity at individual points of the soil massif on the thermal conductivity and heat capacity of the soil are taken into account at the stage of solving the heat and mass transfer problem. The thermal conductivity and heat capacity at each step are adjusted as a function of humidity of the soil mass. Thermal deformations are determined taking into account the changing of coefficients of linear expansion, soil temperature and deformation modulus. The linear expansion coefficient is adjusted at each step as a function of temperature.

Another important feature of the technique is the use of a spatial model. The use of such a model provides accounting for heat transfer and moisture transfer in the direction of three coordinate axes, redistribution of stresses and deformations in three directions. When solving the spatial problem, the laws of the theory of elasticity and plasticity, the laws of heat and mass transfer in porous media are used. An increase in the total number of arguments in these dependencies in comparison with the use of empirical formulas is intended to ensure greater reliability of the results obtained.

The finite element method is applied. Multiple solution of the problem of continuum mechanics in changing conditions is performed using the modern software package "Lira". A three-dimensional soil model is formed from spatial finite elements into which a soil massif with variable parameters is divided. The use of volumetric finite elements allows to assign different properties to each of the finite elements at different time intervals. A fragment of the section according to the calculation model of the soil massif with a breakdown into finite elements is shown in Fig. 2. The movement of the soil mass at the boundaries of the studied model is limited by the installation of links in nodes at the outer contour of the massif.

The change in temperature fields in the soil mass at the considered time intervals is determined on the basis of the theory of unsteady heat and moisture transfer [36]. The transfer of heat and moisture in the soil is described by differential equations:

$$\frac{\partial T}{\partial \tau} = \nabla \left(a \cdot \nabla T \right) + \frac{c_w \cdot \left(D_w \cdot \nabla W + D_w \cdot \delta \cdot \nabla T \right) \cdot \nabla T}{c} +$$
$$+ \frac{\varepsilon \cdot L}{c \cdot (1-\varepsilon)} \cdot \frac{\partial W}{\partial \tau} + \frac{q_v}{c \cdot \rho_d}; \tag{1}$$

$$\frac{\partial W}{\partial \tau} = D_w \cdot \nabla^2 W + D_w \cdot \delta \cdot \nabla^2 T - \varepsilon / \left(1-\varepsilon \right) \cdot \frac{\partial W}{\partial \tau} + \frac{\partial K_w}{\partial y}, \tag{2}$$

where T is soil temperature, °C;

W is soil humidity, %;

y is vertical coordinate, m;

τ is time, s;

c is specific thermal capacity of a soil, J/(m³·°C);

ε is phase transition criterion;

L is specific heat of ice crystallization, J/kg;

D_w is coefficient of diffusion of moisture, m²/s;

δ is thermogradient coefficient, 1/°C;

$a = \lambda / \left(c \cdot \rho_d \right)$ is coefficient of thermal diffusivity, m²/s;

λ is specific thermal conductivity of a soil, W/(m·°C);

ρ_d is density of a dry soil, kg/m³;

q_v is density of internal thermal sources or heat sinks, J/(m³·h);

c_w is heat capacity of water, J/(m³·°C);

K_w is moisture transfer coefficient, m/s;

ρ_w is density of water, kg/m³.
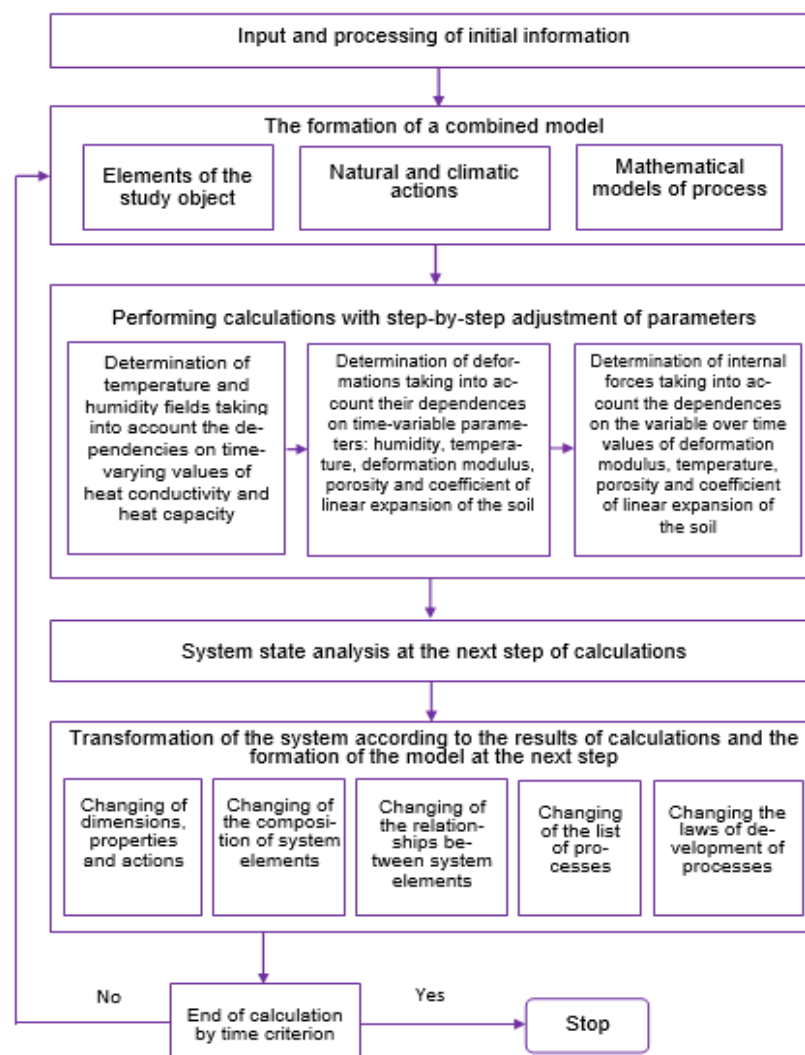
Figure 1. Scheme of dynamic modeling of the development of processes in the soil.

Moisture transfer in the saturation zone, if it presents, is described by the well-known filtration equation.

The heat balance equation is used in the form:

$$\lambda \cdot \frac{\partial T}{\partial y} + (1 - A)\left[q_p^s(\tau) + q_r^s(\tau) \right] - q_1^s(\tau) - q_k(\tau) - q_i(\tau) = 0, \tag{3}$$

where A is surface albedo;

$q_p^s(\tau)$ and $q_r^s(\tau)$ is thermal flow conditioned by direct and scattered solar radiation to the surface, respectively, J/m²·s;

$q_1^s(\tau)$ is effective surface radiation, J/m²·s;

$q_k(\tau)$, $q_i(\tau)$ are thermal flow conditioned by convective transfer and evaporation, respectively, J/m²·s.

The moisture balance equation is formed on the basis of the expressions given in [2, 4]. As a result, the conditions for the movement of moisture into the soil are proposed to be represented in the form:

$$\Delta W_{\text{lay}} = I_{kr} - G, \text{ if } I \geq I_{kr}; \quad \Delta W_{\text{lay}} = X - S - E - G, \text{ if } I < I_{kr}; \tag{4}$$

$$G = -D_w \cdot \left(\frac{\partial W}{\partial y} + \delta \cdot \frac{\partial T}{\partial y} \right) - K_w. \tag{5}$$

In this case, the amount of moisture supplied to the surface I and the limiting amount of moisture that can be absorbed per unit of time I_{kr} are determined from the expressions

$$I = X - S - E, \ \ I_{kr} = \frac{q_w}{\rho_w \cdot \Delta\tau}, \tag{6}$$

where X is moisture inflow from outside, m / s;

G is the intensity of movement of moisture under the influence of gradients of temperature, humidity and gravitational forces, m / s;

S and E are the intensity of runoff and evaporation of moisture, m / s;

q_w is the maximum absorption rate during the time $\Delta\tau$, determined by the formula of I.A. Zolotar, kg/m²;

ΔW_{lay} is change in moisture content in the soil layer, m / s.

The resolving heat and moisture transfer equations take into account: heat transfer due to diffusive moisture transfer, phase transition criteria, moisture transfer caused by a temperature gradient, gravitational component of moisture transfer. The heat balance equation on the surface takes into account effective radiation, direct and scattered solar radiation, and heat fluxes associated with convective transport and evaporation. The moisture balance equation in the model takes into account evaporation, moisture movement associated with runoff and absorption of precipitation on the surface, moisture movement caused by the action of gravitational forces, temperature and humidity gradients. The interrelation of the constituent elements of heat and moisture balances is taken into account. The features of heat and moisture transfer associated with the presence of two fronts of freezing are taken into account. The mathematical model of heat and mass transfer used provides for the correction of parameters such as specific heat, thermal conductivity, moisture transfer coefficient, and others due to changes in soil temperature and humidity. Parameters are adjusted in the nodes and elements of the model over time. As a result, at each time interval, the model adapts to changing boundary conditions and the properties of its elements.

At the stage of determining temperature deformations, the methods of continuum mechanics are applied. Initial information about the model includes the physicomechanical characteristics of the constituent elements of the soil mass, temperature gradients. When determining the internal forces in the soil mass, the dependences of the deformation modulus and the coefficient of linear expansion on temperature are taken into account. Long-period temperature fluctuations at which stresses can reach the

ultimate of long strength are taken into account. In the course of solving the problem of thermoelasticity using the software package «Lira», at lowering the temperature with a given step, the values of tensile stresses in the freezing soil mass are established. At some step, tensile stresses reach the breaking stress. In the soil model, a crack is formed by removing bonds between the finite elements of the soil massif in the near-surface layer. A further decrease in temperature in the algorithm for solving the problem is realized, and the thermoelasticity problem is solved repeatedly within a given time interval. Redistribution of stresses in the soil massif is reevaluated. The end of calculations is determined by the criterion of reaching the boundary of a given period of time.

3. Results and Discussion

During numerical experiments, temperature and stress fields in the soil mass were studied for the Central Transbaikalia region. A part of a half-space with dimensions in plan 50×50 m and a height of 5 m is considered as a design model. Using a larger part of the massif does not change the calculation results. The image of such an object is not informative, therefore it is not given, and further fragments of sections drawn through the half-space are used. The finite elements are prisms with dimensions in plan 1×1 m and heights of 0.25 and 1 m.

The following boundary conditions are used. When solving the problem of heat and mass transfer, the temperature and humidity on the lower edge of the considered massif are taken constant. On the lateral faces, the conditions of symmetry of these parameters with respect to the faces are used. At the second stage, when solving the problem of geomechanics, at the boundaries of the massif, at the nodes of the finite element grid, links are established that are perpendicular to the planes that bound the soil massif.

The time step for the problem of heat and mass transfer is taken equal to 4 hours, for the problem of geomechanics – 24 hours. A freezing soil massif composed of clay loam with a density of γ = 1.8 g/cm³ a Poisson's ratio of 0.3 and humidity W = 20 % is considered. The specific thermal capacity and the thermal conductivity of the soil in the thawed state are, respectively, c = 2.48·10-6 J/(m³·°C), λ = 1.1 W/(m·°C). Density of a dry soil ρ_d = 1400 kg/m³; coefficient of diffusion of moisture D_w = 2.8 ·10⁻⁸ m²/s; moisture transfer coefficient K_w = 0 m/s. Climatic characteristics are taken according to SP 131.13330.2018 Construction climatology and the meteo.ru website. Variable characteristics of the frozen soil were taken as a function of temperature in each finite element of the model using the materials presented in SP 25.13330.2012 Bases and foundations on permafrost and in works [22, 24, 25, 27, 29, 37, 38].

The mechanism of cracking is due to a decrease in the volume of the soil as a result of its temperature reduction during cooling. The stresses caused by the temperature drop in the frozen soil massif are determined when solving the geomechanics problem using the software package "Lira". Researchers of this problem traditionally consider the ultimate of long-term tensile strength as a criterion for the formation of cracks. The calculated stresses in each soil layer are compared with the ultimate of long-term tensile strength. If these stresses in the layer exceed the long-term strength limit, a crack is formed in the layer. For the soil considered in the example, the long-term strength limit is 259 kPa. When the stress reaches this value in the layer, a rupture occurs.

Based on the results of the first stage of solving the problem, the fields of temperature and humidity are formed in the half-space and the physical and mechanical properties depending on them are corrected. The tables 1 and 2 shows the average parameters for each of the layers into which the soil massif is divided in the vertical direction at key stages in the development of processes associated with the formation of cracks. These parameters are included in the equilibrium equations solved by the finite element method using the software package "Lira" and are the initial data for determining the stresses and deformations in the considered soil mass by this software package.

As a result of the calculations, the displacements of all nodes of the finite element network and the internal forces in the elements of the soil model are determined. In the process of lowering the temperature of the air and the upper layers of the soil massif, on November 5, tensile stresses reach 259 kPa in the near-surface layer of the soil. Fig. 2 shows a mosaic of stress distribution on the eve of cracking. The corresponding characteristics of soil elements are given in Table 1. The distance between the horizontal lines in all figures is 0.25 m in the near-surface layer and 1 m in the layers lying below, between the vertical lines – 1 m. As can be seen from the table and graphs, tensile stresses reach the breaking stress in the upper zone of the soil mass, taken in the calculations equal to 259 kPa [22, 27]. In the second layer from the surface, tensile stresses remain insignificant and reach 112 kPa. This is due to the small temperature difference in the indicated area. For this reason, at a depth of more than 0.25 meters, soil rupture for a given period of time is not predicted according to the results of calculations. Cracks are formed in the upper layer.

The distance between cracks depends on the modulus of deformation, Poisson's ratio, density, moisture content, coefficient of linear expansion of the soil, temperature gradient. The criterion for determining the distance between cracks is the absence in the upper soil layer of areas with tensile stresses exceeding the ultimate tensile strength of the soil after cracking. For soil with the physical and mechanical parameters considered in the work, this distance is 3 meters. With a larger distance between the cracks, this condition will not be met. The achievement of this condition is checked at the stages of lowering the temperature of the massif in the course of calculations.

After the formation of cracks in the near-surface layer of the soil, the nature of the stress distribution in the massif changes, and the characteristics of the soil are preserved. Fig. 3 shows a mosaic of stress distribution in the soil after the formation of cracks. For better demonstration of the results, only typical fragments of the model in the area of crack formation are highlighted in the figures. As can be seen from the graphs, the magnitude of tensile stresses after the formation of cracks in the near-surface layer decreases and amounts to 253 kPa. Redistribution of stresses in the layers of the soil massif located below is noted. In the second row of finite elements from the top, the average stresses are 126 kPa. In the third row, the influence of location of cracks on the nature of stress distribution is noted. Directly under the cracks, the stresses are 63 kPa; in the zones remote from the cracks, they approach zero. Here, a decrease in stresses occurs as a result of a redistribution of the load on the layers lying above. The crack opening width is about 1 cm. The tensile stresses at the surface after the formation of cracks remain below the ultimate strength of the soil.

With a further decrease in soil temperature on November 26, tensile stresses in some areas of the massif again reach the limit of long-term strength of the soil. Such areas are highlighted in Fig. 4 with a dark tone and are located in the second row of finite elements from the surface. Average stresses in the upper and third layers from the surface do not exceed 129 kPa. The characteristics of the soil are presented in Table 2.

In weakened sections, the cracks continue to deepen, and already the second row of finite elements in the model is subject to rupture. The nature of stress distribution in the elements is shown in Fig. 5. After the development of cracks in depth, unloading zones with stresses up to 48 kPa are observed near the cracks in the upper row of soil elements. At the same time, stresses of about 96 kPa remain in the middle part of the polygons. In the second layer weakened by cracks, the stresses decrease to 192 kPa. Under the cracks, due to the weakening of the section, the load is taken by the elements of the third row, where the stresses reach 168 kPa. In the elements at some distance from the cracks, the stresses in the third layer decrease to 120 kPa. In a soil massif that does not experience large temperature drops, tensile stresses remain small.
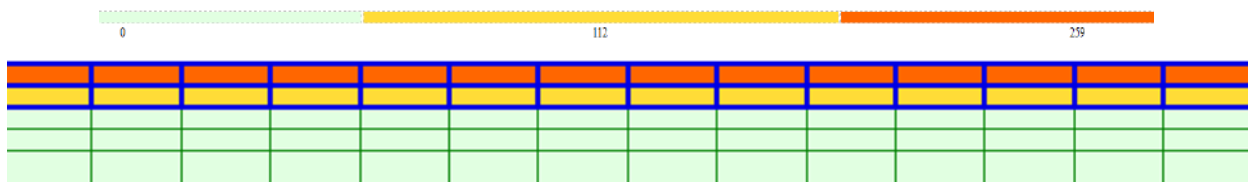
Figure 2. Distribution of stresses in the soil massif as of November 5 before crack formation (The numerical values on the color scale are given in kPa).
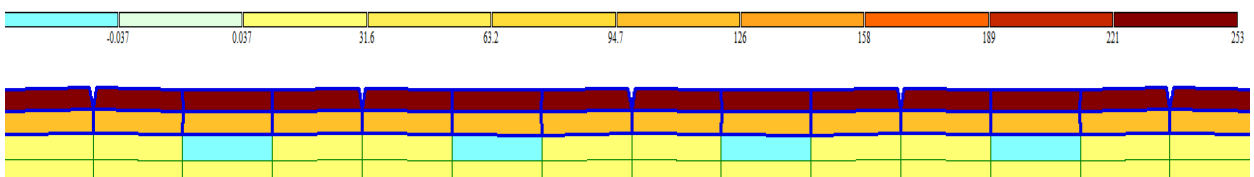
Figure 3. Distribution of stresses in the soil massif after the formation of cracks (The numerical values on the color scale are given in kPa).
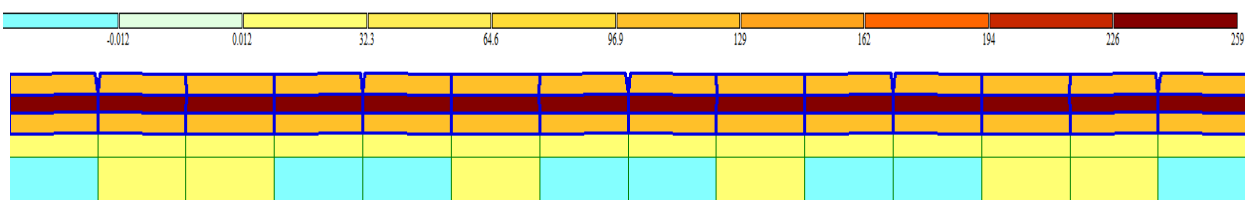
Figure 4. Distribution of stresses in the soil massif after the formation of cracks and with a further decrease in temperature as of November 26 (The numerical values on the color scale are given in kPa).

Table 1. Soil characteristics at different depths of the massif as of November 5.

Layer number	Layer thickness, m	Depth of the bottom of the layer, m	Average temperature in the layer, °C	Temperature difference in the layer, °C	Deformation modulus, MPa	Coefficient of thermal expansion, 10^{-6} $(°C)^{-1}$	Maximum stress in the soil massif, kPa	
							Before cracking	After the formation of cracks
1	0.25	0.25	-8.2	-7.7	160	150	259	253
2	0.25	0.5	-3.3	-2.8	150	190	112	126
3	0.25	0.75	-0.5	0	25	380	0	63
4	0.25	1	-0.5	0	25	380	0	63
5	1	2	-0.5	0	25	380	0	0
6	1	3	-0.6	-0.1	25	380	0	0
7	1	4	-1	-0.5	25	380	0	0
8	1	5	-1.1	-0.6	25	380	0	0
9	1	6	-1.2	-0.7	25	380	0	0

Table 2. Soil characteristics at different depths of the massif as of November 26.

Layer number	Layer thickness, m	Depth of the bottom of the layer, m	Average temperature in the layer, °C	Temperature difference in the layer, °C	Deformation modulus, MPa	Coefficient of thermal expansion, 10^{-6} $(°C)^{-1}$	Maximum stress in the soil massif, kPa	
							Before cracking	After the formation of cracks
1	0.25	0.25	−17.6	−17.1	170	30	129	96
2	0.25	0.5	−8.4	−7.9	160	150	259	192
3	0.25	0.75	−3.5	−3	150	190	129	168
4	0.25	1	−2.4	−1.9	150	190	65	48
5	1	2	−1	−0.5	25	380	0	0
6	1	3	−0.5	0	25	380	0	0
7	1	4	−0.7	−0.2	25	380	0	0
8	1	5	−1	−0.5	25	380	0	0
9	1	6	−1.2	−0.7	25	380	0	0
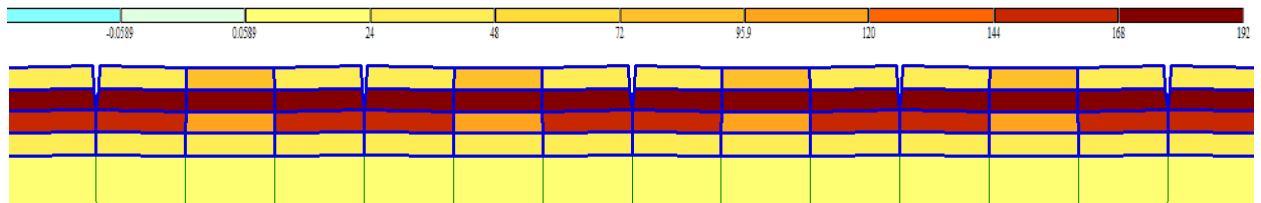
Figure 5. Distribution of stresses in the soil massif after deepening cracks up to 0.5 m (The numerical values on the color scale are given in kPa).

To evaluate the effectiveness of the used model of cryogenic cracking, the author compared the results obtained with the results obtained previously for similar conditions by the methods of Grechishchev and Dostalov and with the observations of these authors [12]. In both cases, the results establish the likely formation of cracks in November with an opening width of about 1 cm. The obtained parameters of crack formation correspond to the results of observations in the region in open areas without snow cover [12]. The advantage of the proposed method lies in the fact that in addition to determining individual parameters of cracks formation (opening width, distance between cracks); time factors are taken into account. There is an opportunity to track the dynamics of the processes of deformation of the soil massif over a given period of time under various variants of climatic influences.

The models of frost cracking under consideration have a wide range of uses. They can be applied in practice when predicting their possible development in regions with sharply continental climate, where this phenomenon is common. Such estimates are of great importance in the construction of roads, airfields, hydraulic structures, pipelines and other engineering facilities. Crack formation models can also be used to predict the ground icing formation.

4. Conclusions

1. A mathematical model of the formation of cryogenic cracks in the soil mass has been formed, It reflects the thermomechanical and geomechanical processes in the freezing soil, taking into account the dynamics of their development. The mathematical model is distinguished by the use of the finite element method and three-dimensional elements of the soil massif, periodic adjustment of the model parameters in conditions changing with time.

2. A methodology to assess the likelihood of cryogenic cracks formation in the conditions of continuously changing soil parameters and external influences over time has been developed. In contrast to the known techniques, the joint solution of the problems of geomechanics and heat and mass transfer as part of the spatial problem allows one to take into account the redistribution of internal forces, temperature and moisture flows in the soil mass along the directions of three coordinate axes. The advantages of the methodology are the adjustment of parameters, the use of a large number of parameters in comparison with other known methods, the use of soil characteristics in the model, traditionally obtained during engineering and geological surveys.

3. Based on the results of calculations, the nature of the distribution of stresses in the massif at different stages of the formation and development of frost cracks at the soil surface was established within the selected dimensions of the soil layers and the time step. The resulting displacements of nodes and internal forces in the elements presented in sections drawn through the middle of the polygons take into account the dynamics of the formation of cracks in the soil mass within a given period of time. The analysis of the obtained results confirms the possibility of predicting the formation of cryogenic cracks and determining their parameters in the northern regions by the proposed method. The obtained results of predicting the cryogenic soil cracking in November are consistent with observations in the region.

4. Since the formation of cracks poses a threat of damage to objects, the values of temperature deformations and stresses arising from this, of course, should be taken into account in the design calculations as a temporary load in the conditions of permafrost propagation in regions with low temperatures. The proposed technique allows to prevent the threat of damage to objects.

References

1. Obu, J., Westermann, S., Bartsch, A., Berdnikov, N., Christiansen, H., Dashtseren, A., Delaloye, R., Elberling, B., Etzelmuller, B., Kholodov, A., Khomutov, A., Kaab, A., Leibman, M., Lewkowicz, A., Panda, S., Romanovsky, V., Way, R., Westergaard-Nielsen, A., Wu, T., Yamkhin, J., Zou, D. Northern Hemisphere permafrost map based on TTOP modelling for 2000–2016 at 1 km2 scale. Earth-Science Reviews. 2019. No. 193. Pp. 299–316. DOI: 10.1016/j.earscirev.2019.04.023

2. Czekirda, J., Westermann, S., Etzelmuller, B., Johannesson, T. Transient Modelling of Permafrost Distribution in Iceland. Frontiers in Earth Science. 2019. No. 7. Article 130. DOI: 10.3389/feart.2019.00130

3. Magnin, F., Etzelmuller, B., Westermann, S., Isaksen, K., Hilger, P., Hermanns, R. Permafrost distribution in steep rock slopes in Norway: measurements, statistical modelling and implications for geomorphological processes. Earth Surface Dynamics. 2019. No. 7. Pp. 1019–1040. DOI: 10.5194/esurf-7-1019-2019

4. Luo, J., Yin, G., Niu, F., Lin, Z., Liu, M. High Spatial Resolution Modeling of Climate Change Impacts on Permafrost Thermal Conditions for the Beiluhe Basin, Qinghai-Tibet Plateau. Remote Sensing. 2019. 11(11). P. 1294. DOI: 10.3390/rs11111294

5. Tao, J., Koster, R., Reichle, R., Forman, B., Xue, Y., Chen, R., Moghaddam, M. Permafrost variability over the Northern Hemisphere based on the MERRA-2 reanalysis. The Cryosphere. 2019. No. 13. Pp. 2087–2110. DOI: 10.5194/tc-13-2087-2019

6. Alekseev, V.R. Indicator geometry of cryogenic landscapes. Advances in Biology and Earth Sciences. 2017. 2(1). Pp. 73–84. http://jomardpublishing.com/UploadFiles/Files/journals/ABES/V2N1/AlekseevV.pdf

7. Khimenkov, A.N., Sergeev, D.O., Vlasov, A.N., Kozireva, E.A., Rybchenko, A.A., Svetlakov, A.A. Contemporary and paleo-cryogenic formations on Olkhon island. Earth's Cryosphere. 2015. 19(4). Pp. 48–57.

8. Kade, A., Walker, D. Experimental Alteration of Vegetation on Nonsorted Circles: Effects on Cryogenic Activity and Implications for Climate Change in The Arctic. Arctic, Antarctic, and Alpine Research. 2008. 40(1). Pp. 96–103. DOI: 10.1657/1523-0430(06-029)[KADE]2.0.CO;2

9. Streletskaya, I.D. Soil wedge structures in the southern coast of the Finland Gulf. Kriosfera Zemli. 2017. 21(1). Pp. 3–10. DOI: 10.21782/EC2541-9994-2017-1(3-10)

10. Matsuoka, N, Christiansen, H., Watanabe, T. Ice-wedge polygon dynamics in Svalbard: Lessons from a decade of automated multi-sensor monitoring. Permafrost and Periglac Process. 2018. No. 29. Pp. 210–227. DOI: 10.1002/ppp.1985

11. Andersen, J.L., Egholm, D.L., Knudsen, M.F., Jansen, J.D., Nielsen, S.B. The periglacial engine of mountain erosion – Part 1: Rates of frost cracking and frost creep. Earth Surf. Dynam. 2015. No. 3. Pp. 447–462. DOI: 10.5194/esurf-3-447-2015 www.earth-surf-dynam.net/3/447/2015/

12. Stetyukha, V.A. Prognozirovaniye obrazovaniya naledey pri vozdeystviyakh fizicheskikh protsessov gornogo proizvodstva na okruzhayushchuyu sredu [Prediction of ice formation during environmental impacts of mining processes]. Gornyj informasionno-analiticheskij byulleten. 2006. No. 8. Pp. 43–46. (rus)

13. Khudyakova, A.A., Gubaydullin, M.G., Konyukhov, A.V. Model deyatelnogo sloya mnogoletnemerzlykh porod s morozoboynymi treshchinami i usovershenstvovaniye metodiki rascheta napryazhenno-deformirovannogo sostoyaniya gruntovykh osnovaniy [A model of the permafrost active layer with frost cracks and improvement of the methodology for calculating the stress-strain state of soil bases]. Vestnik MGTU. 2010. Vol. 13. 4(1). Pp. 810–815. (rus)

14. Burgonutdinov, A.M., Yushkov, B.S. Uchet morozoboynykh treshchin pri stroitelstve truboprovodov [Accounting for frost cracks in the construction of pipelines]. Zashchita okruzhayushchey sredy v neftegazovom komplekse. 2011. No 7. Pp. 39–43. (rus)

15. Frolov, V. Some problems of buildings and structures service within permafrost area. Procedia Engineering. 2016. No. 165. Pp. 385–393. DOI: 10.1016/j.proeng.2016.11.714 https://www.sciencedirect.com/science/article/pii/S1877705816-340759

16. Burmistrova, O.N., Burgonutdinov, A.M., Pilnik, Yu.N. Mekhanizm obrazovaniya morozoboynykh treshchin na avtomobilnykh dorogakh, ekspluatiruyemykh v umerenno-kontinentalnom klimate [The mechanism of formation of frost cracks on roads operated in temperate continental climate]. Lesotekhnicheskiy zhurnal. 2016. No 4. Pp. 133–138. DOI: 10.12737/23446 http://lestehjournal.ru/journal/2016/no-4/ (rus)

17. Tran, A.P., Dafflon, B., Hubbard, S.S. Coupled land surface-subsurface hydrogeophysical inverse modeling to estimate soil organic carbon content and explore associated hydrological and thermal dynamics in the Arctic tundra. The Cryosphere. 2017. 11(5). Pp. 2089-2109.

18. Westermann, S., Peter, M., Langer, M., Schwamborn, G., Schirrmeister, L., Etzelmuller, B., Boike, J. Transient modeling of the ground thermal conditions using satellite data in the Lena River delta, Siberia. The Cryosphere. 2017. 11(3). Pp. 1441–1463. DOI: 10.5194/tc-11-1441-2017

19. Wang, C., Wu, D., Kong, Y., Li, R., Shi, H. Changes of soil thermal and hydraulic regimes in northern hemisphere permafrost regions over the 21st century. Arctic Antarctic and Alpine Research. 2017. 49(2). Pp. 305–319.

20. Li, A., Xia, C., Bao, C., Yin, G. Using MODIS Land Surface Temperatures for Permafrost Thermal Modeling in Beiluhe Basin on the Qinghai-Tibet Plateau. Sensors. 2019. No. 19. P. 4200. DOI: 10.3390/s19194200.

21. Westermann, S., Ostby, T.I., Gisnas, K., Schuler, T.V., Etzelmuller B. A ground temperature map of the North Atlantic permafrost region based on remote sensing and reanalysis data. The Cryosphere. 2015. No. 9. Pp. 1303–1319. DOI: 10.5194/tc-9-1303-2015

22. Akagawa, S., Nishisato, K. Tensile strength of frozen soil in the temperature range of the frozen fringe. Cold Regions Science and Technology. 2009. No. 57(1). Pp. 13–22. DOI: 10.1016/j.coldregions.2009.01.002

23. Kang, Y., Liu, Q., Huang, S., Liu, X. Theoretical and numerical studies of crack initiation and propagation in rock masses under freezing pressure and far-field stress. Journal of Rock Mechanics and Geotechnical Engineering. 2014. 6(5). Pp. 466–476. DOI: 10.1016/j.jrmge.2014.05.004

24. Zhang, B., Han, C., Yu, X. A non-destructive method to measure the thermal properties of frozen soils du ring phase transition. Journal of Rock Mechanics and Geotechnical Engineering. 2015. No. 7. Pp. 155–162. DOI: 10.1016/j.jrmge.20-15.03.005.

25. Rasmussen, L., Zhang, W., Hollesen, J., Cable, S., Christiansen, H., Jansson, P-E., Elberling, B. Modelling present and future permafrost thermal regimes in Northeast Greenland Cold Regions. Science and Technology. 2018. No. 146. Pp. 199–213. www.elsevier.com/locate/coldregions

26. Wang, P., Zhou, G. Frost-heaving pressure in geotechnical engineering materials during freezing process. International Journal of Mining Science and Technology. 2018. 28(2). Pp. 287–296. https://www.sciencedirect.com/science/article/pii/S20-95268617300034

27. Zhang, Z., Ma, W., Feng, W., Zhao, S., Roman, L.T. The freeze-thaw cycles-time analogy method for forecasting long-term frozen soil strength. Measurement. 2016. No. 92. Pp. 483–488. DOI: 10.1016/j.measurement.2016.06.044 https://www.researchgate.net/publication/304401244

28. Luo, L., Zhuang, Y., Zhang, Y., Ma, W., Zhang, Z., Mu, Y., Yang, J., Cao, X., Liang, S. Freeze/thaw-induced deformation monitoring and assessment of the slope in permafrost based on terrestrial laser scanner and GNSS. Remote Sensing. 2017. 9(3). P. 198.

29. Roman, L.T., Merzlyakov, V.P., Maleeva, A.N. Thermal deformation of frozen soils: role of water and gas saturation. Kriosfera Zemli. 2017. 21(3). Pp. 23–29.

30. Marmy, A., Salzmann, N., Scherler, M., Hauck, C. Permafrost model sensitivity to seasonal climatic changes and extreme events in mountainous regions. Environmental Research Letters. 2013. 8(3). Pp. 35–48.

31. Merzlyakov, V.P., Sergeyev, D.O. Otsenka opasnosti vozniknoveniya morozoboynykh treshchin dlya oblastey s rezko kontinentalnym klimatom [Frost crack risk assessment for areas with sharply continental climate] Analiz, prognoz i upravleniye prirodnymi riskami v sovremennom mire: materialy 9-y Mezhdunarodnoy nauchno-prakticheskoy konferentsii «GEORISK–2015» [Analysis, forecast and management of natural risks in the modern world: materials of the 9th International Scientific and Practical Conference "GEORISK-2015"]. M.: RUDN, 2015. No. 2. Pp. 486–492. http://geoenv.ru/conferences/georisk-2015/georisk-2.pdf (rus)

32. Burgonutdinov, A.M., Yushkov, B.S., Burmistrova, O.N. Metodika obrazovaniya morozoboynykh treshchin na avtomobilnykh dorogakh i sposoby borby s etim yavleniyem [Methodology for the formation of frost cracks on roads and methods of dealing with this phenomenon]. Fundamentalnyye issledovaniya. 2014. 8(2). Pp. 285–289. (rus)

33. Thomas, H.R., Cleall, P., Li, Y.-C., Harris, C., Kern-Luetschg, M. Modelling of cryogenic processes in permafrost and seasonally frozen soils. Geotechnique. 2009. 59(3). Pp. 173–184. DOI: 10.1680/geot.2009.59.3.173

34. Haxairea, A., Aukenthalera, M., Brinkgreve, R.B.J. Application of a Thermo-Hydro-Mechanical Model for Freezing and Thawing. Procedia Engineering. 2017. No. 191. Pp. 74–81. DOI: 10.1016/j.proeng.2017.05.156. http://pure.tudelft.nl/ws/files/227-87927/1_s2.0_S1877705817322968_main.pdf

35. Wang, E.L., Fu, Q., Liu, X.C., Li, T.X, Li, J.L. Simulating and validating the effects of slope frost heaving on canal bed saturated soil using coupled heat-moisture-deformation model. International Journal of Agricultural and Biological Engineering. 2017. 10(2). Pp. 184–193. DOI: 10.3965/j.ijabe.20171002.2551

36. Stetyukha, V.A. Sovershenstvovaniye modeley perenosa tepla i vlagi pri otsenke vozdeystviy gornogo proizvodstva na porody v usloviyakh yuzhnogo Zabaykalya [Improving models of heat and moisture transfer in assessing the impacts of mining on rocks in southern Transbaikalia]. Gornyy informatsionno-analiticheskiy byulleten. 2004. № 10. Pp. 71–74. (rus)

37. Merzlyakov, V.P. Koeffitsiyent teplovogo rasshireniya kak kharakteristika merzlykh gruntov [Thermal expansion coefficient as a characteristic of frozen soils]. Geoekologiya. 2012. No. 2. Pp. 159–167. (rus)

38. Roman, L.T., Kotov, P.I., Tsarapov, M.N. Deformation Modulus of Frozen Ground in Compression Tests. Soil Mechanics and Foundation Engineering. 2016. 53(5). Pp. 357–363.

Contacts:

Vladimir Stetjukha, stetjukha_chita@mail.ru

Freeze-thaw damage model
for cement pavements in seasonal frost regions

Q.Q. Zhao[a], H.T. Zhang[b], R.S. Fediuk[c], J.W. Wang[d], Q. Fu[a]*
[a] *Northeast Agricultural University, Harbin Heilongjiang, China*
[b] *China Communications First Public Bureau Highway Survey and Design Institute Co., Ltd., Urumqi City, China,*
[c] *Far Eastern Federal University, Vladivostok, Russia*
[d] *Harbin Dongan Automobile Engine Manufacturing Co., Harbin Heilongjiang, China*
*E-mail: fuqiang @neau.edu.cn

Abstract. In order to evaluate the damage of cement concrete pavement after the freeze-thaw cycle in the seasonal frozen area, it is determined that the dynamic elastic modulus and flexural tensile strength by analyzing the influence of the freeze-thaw on the concrete performance. The two indexes are most sensitive to the evaluation of the freeze-thaw damage of the pavement. Based on regression analysis method, two freeze-thaw damage models based on two indexes are established, and the goodness of fit and significance state of the model are tested. The applicable conditions of the two models are determined by response surface test method. The validity of the model is verified by comparing the prediction results of the existing model. The results show that when the water cement ratio is 0.450.48, the gas content is 1 % – 4 %, and the freezing temperature is – 15 °C – 25 °C. The model based on dynamic elastic modulus index has the best evaluation effect. When the water cement ratio is 0.4–0.46, the gas content is 1–3.5, and the freezing temperature is below – 5 °C, the model based on the flexural tensile strength index has the best evaluation effect. The explainable parts of the two models are 99.1 % and 99.2 % respectively, and the fitting degree of the damage evaluation value and the measured damage value is 0.997 and 0.998 respectively. The model has a good fitting degree. The evaluation effect of the model is better than that of the existing model. The determination of the model is of great significance to the future pavement maintenance work.

1. Introduction

Freeze-thaw damage has a significant influence on the mechanical properties of concrete. It is a representative index to evaluate the durability of concrete. After freezing-thawing damage, the surface of cement concrete pavement will produce peeling, pockmarked surface, exposed surface and other phenomena, and internal diseases such as strength decline, frost resistance and permeability reduction will occur, which will seriously affect the driving safety and service life of cement concrete pavement [1]. Therefore, reasonable evaluation of freezing-thawing damage of cement concrete pavement is of great significance to improve traffic safety and extend the service life of pavement [2–4].

The research on freeze-thaw damage of concrete started earlier at home and abroad, and the research results focus on studying the influence of freezing-thawing cycle on different types of concrete or the attenuation law of mechanical properties of concrete under freezing-thawing action. Alsaif [5] designed the rapid freeze-thaw test, compared the damage degree of three kinds of freeze-thaw media to concrete, and established the relative residual compressive strength and flexural strength attenuation equations based on the relative dynamic elastic modulus, which can be used to calculate the compressive strength and flexural strength, but cannot directly calculate the damage degree of concrete. Smith et al [6–8] analyzed the difference of frost resistance between recycled concrete and ordinary concrete, and concluded that the strength grade has a greater impact on recycled concrete, but the strength is only a part of the mechanical properties of concrete, which is not enough to be the only index reflecting the state of

freeze-thaw failure. Nayak [9] analyzed the characteristics of freeze-thaw damage of concrete, and confirmed that the freeze-thaw damage of concrete is similar to fatigue. The number of freeze-thaw cycles is random under certain damage, but it is only qualitative analysis, and no calculation method of damage is proposed. Grubesa et al [10, 11] used the dynamic triaxial repeated loading method to test the dynamic elastic modulus of subgrade soil, and determined that the dynamic elastic modulus is significantly affected by freeze-thaw, but there is no comparative analysis with other mechanical performance indexes. Fursa et al [12–15] established the concrete freeze-thaw compression failure model based on the improved kupfer-gerstle criterion, which can obtain the compressive strength loss of concrete under different freeze-thaw cycles. However, the freeze-thaw action can damage both the flexural strength and the tensile strength, so the concrete damage model established only based on the compressive strength is not practical. Tianjun et al [16–20] studied the damage mechanism of concrete holes structure under the coupling environment of fatigue load and freeze-thaw cycle, but did not establish the relationship between damage amount, load and freeze-thaw times.

Although the above research deeply analyzes the influence of freeze-thaw damage on various performance indexes of concrete, most of them are based on indoor tests, and do not take into account the actual damage condition of cement concrete road affected by freeze-thaw under the effect of climate in the seasonal freezing area. Moreover, most of them only use one model to evaluate the index, and the damage model established is low accuracy. Therefore, the freeze-thaw damage model of cement concrete pavement suitable for the seasonal freezing area needs to be further improved.

In this study, the freeze-thaw damage index is determined by comparing the influence degree of the concrete performance index affected by the freeze-thaw action. Based on the actual investigation data of the typical roads in the seasonal frost regions, the freeze-thaw damage model is established, and the applicable conditions of the model are determined through the test, to achieve the purpose of establishing the freeze-thaw damage model of the cement concrete pavement suitable for the seasonal frost regions.

2. Methods

2.1. Parameter determination of freeze-thaw damage evaluation model

The indexes for evaluating freezing-thawing damage of cement concrete pavement include dynamic elastic modulus, mass change rate, water absorption rate, flexural strength, compressive strength and crimp-compression ratio [21–25], among them, the mass change rate is the ratio of the mass change value before and after freezing and thawing to the mass before freezing and thawing, from which model parameters for evaluating freezing-thawing damage of cement concrete pavement in seasonal frost regions are selected. According to the test of Sun ming et al [26–29], the binder is CEM I 42.5 N; the coarse aggregate is gravel and pebble with the nominal particle size is 5-20 mm, the apparent density is 2808 kg/m³; the fine aggregate is natural river sand with the nominal diameter is less than 4.75 mm. Water is a common life in Harbin, Heilongjiang Province, China. The concrete strength grade is C30; the concrete mix ratio is shown in Table 1. Analyze the concrete performance attenuation data obtained through the test, and compare the changes of the above six indexes under the condition of gradually increasing freeze-thaw cycles, as shown in Fig. 1 and Fig. 2.

Table 1. Mix proportion of concrete.

Code	W/C	Mix proportion of concrete (kg/m³)			
		Cement	Coarse aggregate	Fine aggregate	Water
NC	0.48	358.34	1096.75	598.42	183

In Fig. 1, with the increasing number of freeze-thaw cycles, the relative dynamic modulus of elasticity and relative compressive strength are reduced, and the loss of relative dynamic modulus of elasticity is more serious, reaching a loss rate of 40 % before 150 cycles. The reason is that the freeze-thaw action makes the pores of concrete larger, the compactness worse and the strength loss increased. After the pores of concrete are damaged, the cracks expand greatly, which makes the dynamic elastic modulus drop sharply. Because the compression failure of concrete belongs to the whole failure and the dynamic elastic the weakest plane controls modulus, the loss of dynamic elastic modulus will be more significant than the loss of compressive strength. The curve of bending tensile strength is observed. During the increase of freeze-thaw cycles, the bending tensile strength decreased sharply until it was completely lost. Compared with the curve of relative dynamic modulus of elasticity, when the decrease of relative dynamic modulus is less than 10 %, the flexural strength is reduced by 23 %, which shows that the flexural strength is very sensitive to freeze-thaw cycle. The compression ratio is basically the same before 100 times of freeze-thaw and increases gradually in the later stage of freeze-thaw, because the reduction of flexural strength of

concrete after multiple times of freeze-thaw is greater than the reduction of compressive strength, and the compression ratio will increase.

In Fig. 2, the mass change rate does not change significantly before the number of freeze-thaw cycles reaches 125, and it tends to increase after more than 125 cycles. The reason is that in the early stage of freeze-thaw cycle, although the concrete test block absorbs water, the amount of surface debris peeling is less, and the mass will increase. In the later stage of freeze-thaw, the internal cohesion of concrete will decrease, and the mass of water absorbed is less than that of peeling debris. The rate of change in this mass has increased. The water absorption has no significant change in the freeze-thaw test of concrete, because the water absorption can help to reflect the degree of internal water saturation of concrete structure. After the number of freeze-thaw cycles reaches 100, the concrete does not appear serious peeling and fracture phenomenon, and the water absorption will reach a balance state.

Therefore, in the process of freeze-thaw cycle times increasing from 0 to 200, there is no significant difference between the two node values of mass change rate, water absorption rate and compression fold ratio. In the process of freeze-thaw cycle times increasing, the curve fluctuates up and down, the trend of change is uncertain, and the three indexes do not reflect the clear law affected by freeze-thaw cycle.
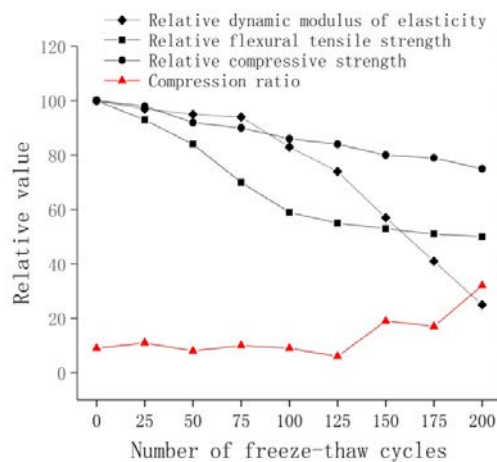
Figure 1. Changes of relative value and compression ratio.
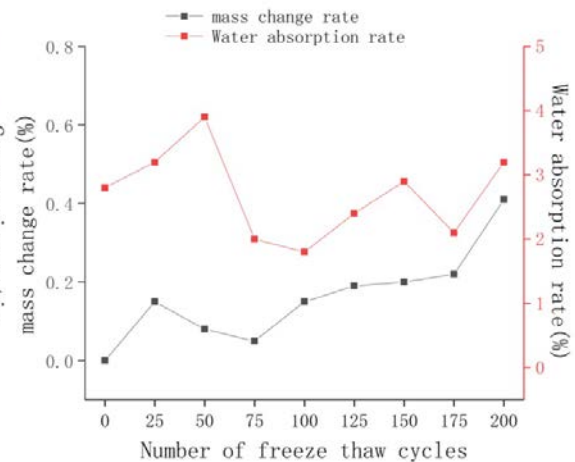
Figure 2. Change of mass change rate and water absorption rate.

Based on the above analysis, among the six indexes of freeze-thaw damage evaluation, the change level of mass change rate, water absorption rate, compression ratio and compressive strength affected by freeze-thaw cycle is relatively low, so the freeze-thaw damage cannot be accurately evaluated, while the dynamic elastic modulus and bending tensile strength are relatively affected by freeze-thaw cycle.

In order to select the most suitable freeze-thaw damage model parameters, the dynamic elastic modulus and flexural tensile strength were further compared. In order to avoid misleading the test results by a single concrete grade, under the freeze-thaw test conditions such as Sunming [26–29], take C40 concrete as an example, the dynamic modulus of elasticity and flexural strength are compared with each other in the case of increasing freeze-thaw cycles, as shown in Fig. 3.
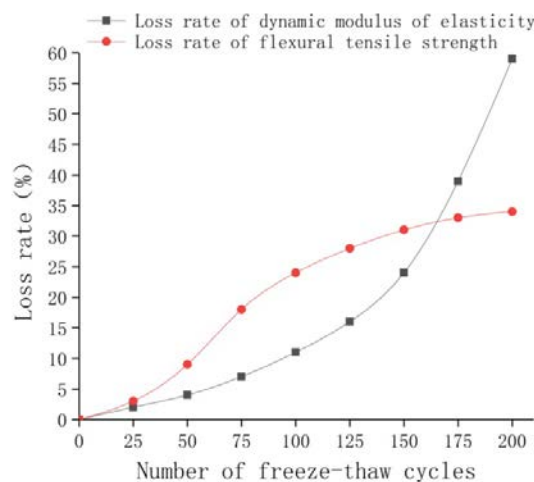
Figure 3. Comparison of dynamic modulus loss rate and flexural strength loss rate.

Zhao, Q.Q., Zhang, H.T., Fediuk, R.S., Wang, J.W., Fu, Q.

In Fig. 3, with the increase of freeze-thaw cycles, the loss rate of dynamic modulus of elasticity and the loss rate of flexural strength increase gradually. Before 150 freeze-thaw cycles, the loss rate of flexural strength is greater than the loss rate of dynamic modulus of elasticity. After 150 freeze-thaw cycles, the loss rate of dynamic modulus begins to lead, and the growth trend of the loss rate of flexural strength slows down gradually. The reason is that the increase of the number of freeze-thaw cycles makes the number of cracks in concrete accumulates and the width of cracks expand gradually. The dynamic modulus loss rate in the later stage of freeze-thaw has the most rapid growth trend, so the dynamic modulus loss rate curve shows a quadratic function trend. However, the internal cohesive force of concrete declines rapidly in the early stage of freeze-thaw, at this time, the loss rate of flexural tensile strength has the most significant growth trend. When the cohesive force drops to a certain extent, the loss rate of flexural tensile strength has a gradual growth trend.

Based on the above analysis, the flexural strength and dynamic modulus of elasticity can reflect the damage state of concrete in the early stage and the later stage respectively. Therefore, in order to evaluate the freeze-thaw damage state reasonably, the dynamic elastic modulus and flexural strength should be taken as parameters to establish the freeze-thaw damage model respectively.

2.2. Establishment of freeze-thaw damage model

According to the above analysis results, the dynamic elastic modulus and flexural strength can reasonably reflect the damage state of concrete structures, and they are easy to detect. Therefore, dynamic elastic modulus index and flexural tensile strength index are taken as damage variables, and regression analysis is carried out through statistical package for Social Sciences (SPSS) software to determine the coefficient of parameters, and freeze-thaw damage models of cement concrete pavement in seasonal frost regions are established respectively. From the typical sections in the seasonal frost regions, 18 sections of three highways, including A, B and C, are selected for core sampling, and the dynamic elastic modulus and flexural strength data of the samples were measured. 120 sets of measurement data of 12 sections were applied to establish the model, and 60 sets of measurement data of the remaining 6 sections were used for model verification.

2.2.1. Dynamic elastic modulus damage model

According to the definition of damage mechanics of concrete [22], the damage variable of concrete is defined as:

$$D = 1 - \frac{E_N}{E_0} = 1 - E_r \tag{1}$$

Where: E_N is the dynamic elastic modulus of concrete when the number of freezing-thawing cycles is N, E_0 is the dynamic elastic modulus of concrete when the number of freezing-thawing cycles is 0, and E_r is the relative dynamic elastic modulus.

Due to the cement concrete pavement in the climate environment of the seasonal frost regions is more sensitive to the freeze-thaw effect than the concrete specimens in the laboratory, the accuracy of the model in equation (1) to evaluate the freeze-thaw damage is insufficient. In Fig. 3, the change curve of the loss rate of dynamic modulus of elasticity is in the form of quadratic function. Therefore, the damage model in the form of primary function in equation (1) is improved to the damage model in the form of quadratic function, and the freeze-thaw damage model based on relative dynamic elastic modulus is established as follows:

$$D = a E_r^2 + b E_r + c \tag{2}$$

where: a, b and c are coefficients, and E_r is relative dynamic elastic modulus.

According to the above data, using SPSS (Statistical Product and Service Solutions) analysis method, take E_r as the independent variable and D as the dependent variable to carry out nonlinear regression analysis of the model. The significance test results of the model are shown in Table 2. The regression mean square value is 279 times of the residual mean square value; F value is 404.766, which indicates that the change of dependent variable is caused by the change of independent variable rather than the test error. The explanation of independent variable to dependent variable is high, Sig. value value is 0.002, less than 0.05, which indicates that the secondary regression of model is significant, and regression model can be established between independent variable and dependent variable.

Table 2. Regression model of ANOVA.

	Sum of Squares	df	Mean Square	F	Sig.
Regression	0.558	2	0.279	404.766	0.002
Residual	0.003	5	0.001		
Total	0.561	7			

After the F-test shows that the linear model can be established, it is necessary to determine whether the influence of independent variables on the dependent variables is significant, so the significance test should be carried out on the regression coefficient. The significance test of the regression coefficient is shown in Table 3. The absolute value of the critical value t of the bilateral test is all greater than the significance level, and the Sig. value is less than 0.05, indicating that the independent variable has significant influence on the dependent variable, so both coefficients are retained in the model.

Table 3. Coefficient of regression model.

Parameter	Partial regression coefficient	Partial regression coefficient standard error	Standardized partial regression coefficient	t	Sig.
a	1.023	0.167	1.192	6.116	0.002
b	-2.280	0.207	-2.146	-11.013	0.015
Constant	1.257	0.057		21.994	0.007

The results of goodness of fit test are shown in Table 4. R^2 is the decisive coefficient of dependent variable and independent variable, and R^2 is adjusted to the ratio of mean square deviation to eliminate the influence of the number of independent variables. The closer R^2 and R^2 are to 1, the better the fitting effect of regression equation is. The adjusted R^2 of the model is 0.991, close to 1, and the error of standard estimation is only 0.026, which indicates that the goodness of fit of the model is high, and the dependent variable can be accounted for 99.1 % of the model interpretation.

Table 4. Summary of regression models.

R^2	Adjust R^2	Standard estimated error
0.994	0.991	0.026

The model can be obtained by substituting the coefficient value into equation (2):

$$D = 1.023E_r{}^2 - 2.28E_r + 1.257 \tag{3}$$

2.2.2. Bending tensile strength damage model

According to the research results of ShenYin [30] on the loss state of flexural tensile strength under different freeze-thaw cycles, the number of freezing-thawing cycles is in direct proportion to the loss rate of flexural strength. Therefore, if the number of freezing-thawing cycles is N times, the flexural strength is a differentiable function (f_N), and the constant is λ_1, then the expression for the loss rate of flexural strength when the number of freezing-thawing cycles is N to $N + \triangle N$ is:

$$\frac{f(N + \Delta N) - f(N)}{f(N)} = \lambda_1 \Delta N \tag{4}$$

Deformation can be obtained:

$$f(N + \Delta N) - f(N) = \lambda_1 \Delta N f(N) \tag{5}$$

Can become:

$$\frac{df(N)}{dN} = \lambda_1 f(N) \tag{6}$$

By integrating equation (6), we can obtain:

Zhao, Q.Q., Zhang, H.T., Fediuk, R.S., Wang, J.W., Fu, Q.

$$\frac{f(N)}{f_0} = e^{\lambda_1 N} \tag{7}$$

Similarly, by repeating the above steps, the loss rate of dynamic elastic modulus can be expressed as:

$$E_r = e^{\lambda_2 N} \tag{8}$$

According to equations (1), (7) and (8), the freeze-thaw damage model based on the loss rate of flexural tensile strength can be obtained as follows:

$$D = d\left(1 - \frac{f_N}{f_0}\right)^e \tag{9}$$

where: d and e are the coefficients, and f_0 is the flexural tensile strength when the number of freezing-thawing cycles is 0.

Since equation (9) is a nonlinear equation, in order to simplify the method and steps of nonlinear equation in regression analysis, logarithmic function method is used to transform the equation linearly.

To find the natural logarithm of both sides of the equation at the same time, we can get:

$$\ln D = \ln d + e \ln(1 - \frac{f_N}{f_0}) \tag{10}$$

Let $\ln D = y$, $\ln d = \lambda_3$, $\ln(1 - \frac{f_N}{f_0}) = x$, equation (10) can be converted into:

$$y = \lambda_3 + ex \tag{11}$$

Thus, the original nonlinear equation can be transformed into a linear equation for solution. Therefore, according to the above data, the SPSS method is extended to analyze the bending strength damage model with X as the independent variable and y as the dependent variable. Table 5 shows the significance test of the model. The regression square sum of the dependent variable is 76.839, and the ratio (mean square) of the regression square sum to the degree of freedom is 32.279, which is much higher than the mean square of the residual error by 0.054. The ratio (F) of the mean regression square sum to the mean residual square sum is 253.56, which is relatively large, and the Sig. value is 0.008, which is less than 0.05, indicating that the linear regression of the model is significant, and the ratio between the dependent variable and the independent variable can be establish a linear model.

Table 5. Regression model of ANOVA.

	Sum of Squares	df	Mean Square	F	Sig.
Regression	76.839	2	32.279	253.56	0.008
Residual	0.114	10	0.054		
Total	0.561	12			

Table 6 shows the significance test of the coefficient. The sig. values of the parameters are 0.009 and 0.012, respectively, which are less than 0.05. The absolute value of the critical value t of the bilateral test is all greater than the significance level, indicating that the dependent variable is greatly affected by the independent variable, and the independent variable and constant should be retained in the model.

Table 6. Coefficient of regression model.

Parameter	Partial regression coefficient	Partial regression coefficient standard error	Standardized partial regression coefficient	t	Sig.
x	4.720	0.144	5.167	16.575	0.009
Constant	-0.968	0.078		-8.301	0.012

Zhao, Q.Q., Zhang, H.T., Fediuk, R.S., Wang, J.W., Fu, Q.

Table 7 shows the goodness of fit test of the model. The adjusted R^2 of the model is 0.992, close to 1, and the standard estimation error is only 0.078, indicating that the goodness of fit of the modified model is high, and the explanatory part of the dependent variable can be accounted for 99.2 %.

Table 7. Summary of regression models.

R^2	Adjust R^2	Standard estimated error
0.995	0.992	0.078

The model can be obtained by substituting the coefficient values in Table 6 into equation (11):

$$y = -0.968 + 4.72x \tag{12}$$

The nonlinear equation is transformed into:

$$D = 0.38 \left(1 - \frac{f_N}{f_0} \right)^{4.72} \tag{13}$$

2.3. Analysis of applicable conditions of the model

In the climate environment of seasonal frost regions, the dynamic elastic modulus and flexural strength of cement concrete pavement are affected by water cement ratio, gas content and freezing temperature. Therefore, in order to make the model have higher evaluation accuracy, it is necessary to determine the respective applicable conditions of the dynamic elastic modulus damage model and flexural strength damage model constructed.

The range of water cement ratio is 0.4~0.48, and the range of gas content is 1 %~5 %. The range of freezing temperature is from − 5 °C to ~25 °C in the climate of seasonal frost regions. Under the condition of 200 freeze-thaw cycles, the response surface test was designed to observe the change of dynamic elastic modulus and relative bending tensile strength under different water cement ratio, gas content and freezing temperature, so as to determine the applicable conditions of the model. In the test, the water cement ratio, gas content and freezing temperature are used as abscissa, expressed as WCR, GC and FT in sequence; the relative dynamic elastic modulus and relative bending tensile strength are used as ordinate, expressed as ER and FR in sequence. According to the number and range of parameters, the response surface test with 3 factors and 3 levels is selected. The coding level and value are shown in Table 8.

Table 8. 3 factors coding level and value.

Coding level	A(WCR)	B(GC)	C(FT/°C)
-1	0.4	1 %	-5
0	0.44	3 %	-15
1	0.48	5 %	-25

2.3.1 Determine the applicable conditions of the dynamic elastic modulus damage model

When the encoding level of FT is 0, the response surfaces of WCR and GC to ER are designed as shown in Fig. 4. When the WCR value is between 0.45 and 0.48, the GC value is within 1 to 4, the color of the corresponding region is blue, indicating that within this range, ER is significantly affected by WCR and GC, and ER value is in a low horizontal state. The reason is that the larger the water cement ratio of concrete is the more water molecules in the capillary pores are. In the process of freezing-thawing cycle, the volume of water molecules increases when it is frozen, and decreases when it is melted. GC has a great influence on ER. Properly raising the GC value can reduce freeze-thaw damage, and the density of concrete will be reduced if the GC value exceeds 4 %.When the coding level of WCR is 0, the response surface of the designed FT to ER is shown in Figure 5. It can be observed that the corresponding area is blue when the FT value is in the range of -15 °C to -25 °C. The reason is that the lower the FT value is, the faster the freezing speed is, accelerating the concrete damage process. Moreover, the blue color is lighter in this range, indicating that the effect of FT on ER is normal.

Therefore, for the freeze-thaw damage model based on dynamic modulus of elasticity, when the response surface color is close to blue, the corresponding range of water cement ratio, gas content and freezing temperature are the most suitable conditions for the model. When the water cement ratio is 0.45–0.48, the gas content is 1 % − 4 %, and the freezing temperature is − 15 °C − 25 °C, the evaluation effect of the model is the best.
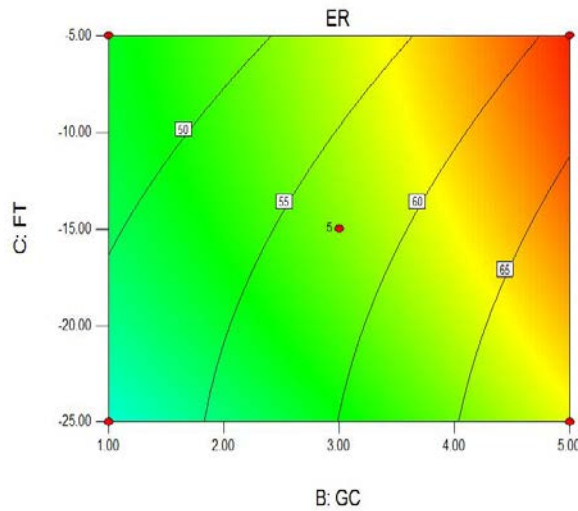
Figure 4. WCR and GC response surface to ER.   **Figure 5. GC and FT response surface to ER.**
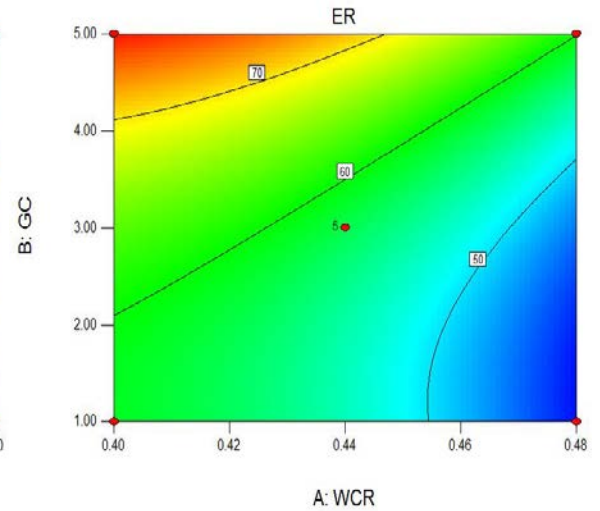
2.3.2. Determine the applicable conditions of the damage model for flexural tensile strength

When the encoding level of FT is 0, the response surfaces of WCR and GC to ER are designed as shown in Fig. 6. When WCR value is between 0.4 and 0.46, GC value is within 1 to 3.5, the color of corresponding region is blue, indicating that within this range, FR is significantly affected by WCR and GC, while ER value is in a low state. The reason is that when the WCR value is small, there is less moisture in the concrete, which increases the brittleness of the concrete to some extent. The flexural tensile strength is more sensitive to freezing-thawing than the dynamic elastic modulus, and the relative flexural tensile strength does not change significantly when the gas content is more than 3.5 %.When the coding level of WCR is 0, the response surface of the designed FT to ER is shown in Fig. 7. The corresponding areas within the range of -5 °C to -25 °C are all blue, indicating that the change of FT value has no significant effect on FR. If the FT value is less than -5 °C, the flexural tensile strength will be damaged. At the same time, the width of the blue region corresponding to -5 °C is less than that of the blue region corresponding to -25 °C, indicating that at a lower freezing temperature, the flexural tensile strength loss is relatively large.

Therefore, when the water cement ratio is between 0.4 and 0.46, the gas content is between 1 and 3.5, and the freezing temperature is below -5 °C, the above range is the most suitable condition for the model of freezing-thawing damage of cement concrete pavement in seasonal frost regions. It established based on flexural tensile strength index, and the model has the best evaluation effect.
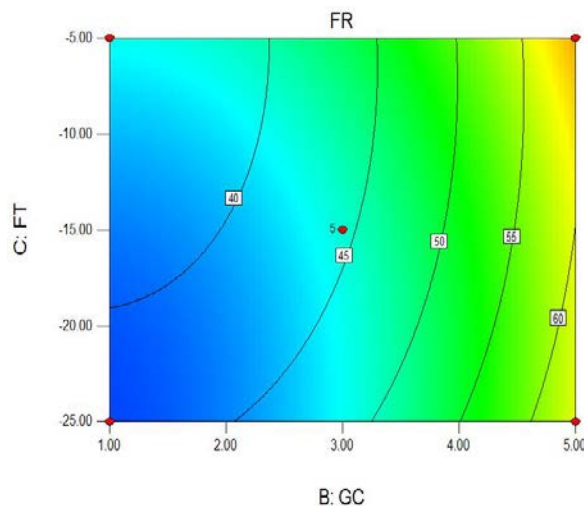
Figure 6. WCR and GC response surface to FR.   **Figure 7. GC and FT response surface to FR.**
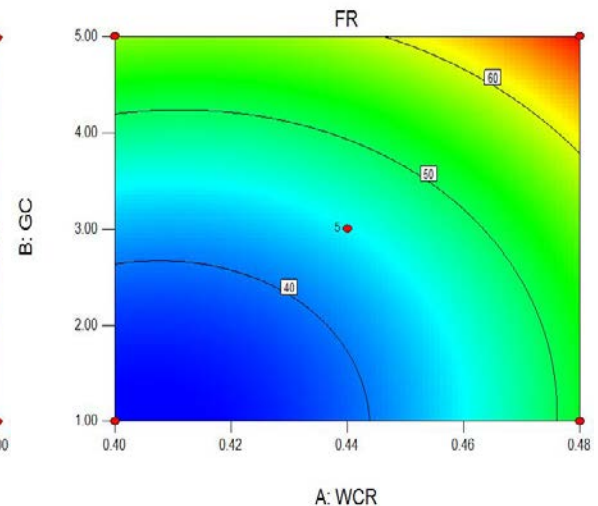
3. Results and Discussion

3.1. Verification of the same section in different periods

In order to verify the practicability and superiority of the freeze-thaw damage model based on dynamic modulus of elasticity and flexural tensile strength of the cement concrete pavement in the seasonal frost regions, the measured damage value of a road section in the past 8 years and the evaluation value of each model are selected for fitting. The model includes damage mechanics model, dynamic elastic modulus damage model, bending strength damage model, dynamic elastic modulus attenuation model established by Sun Ming [26] and bending strength attenuation model established by Shen Yin [30].

In Fig. 8, the abscissa is the measured value D_m of the damage degree, the ordinate is the evaluation value D_P of the damage degree. The decisive coefficient R^2 of the fitting between the evaluation value of the damage mechanics model and the measured value is 0.980. The decisive coefficient R^2 of the fitting between the evaluation value of the dynamic modulus of elasticity attenuation model established by Sun Ming and the measured value is 0.983, and the decisive coefficient of the fitting between the evaluation value of the dynamic modulus of elasticity damage model and the measured value is 0.983; R^2 is 0.997. This proves that the fitting degree of freeze-thaw damage model with dynamic modulus of elasticity is higher.

In Fig. 9, the decisive coefficient R^2 of the fitting between the evaluation value of the damage mechanics model and the measured value is 0.950, the decisive coefficient R^2 of the fitting between the evaluation value of the bending strength attenuation model established by Shen Yin and the measured value is 0.994. The decisive coefficient R^2 of the fitting between the evaluation value of the bending strength damage model and the measured value is 0.998, indicating that the fitting effect of the freeze-thaw damage model with the bending strength as the parameter is better.

The results show that the dynamic elastic modulus damage model and bending tensile strength damage model are more suitable to evaluate the freeze-thaw damage of cement concrete pavement in the seasonal frost regions.
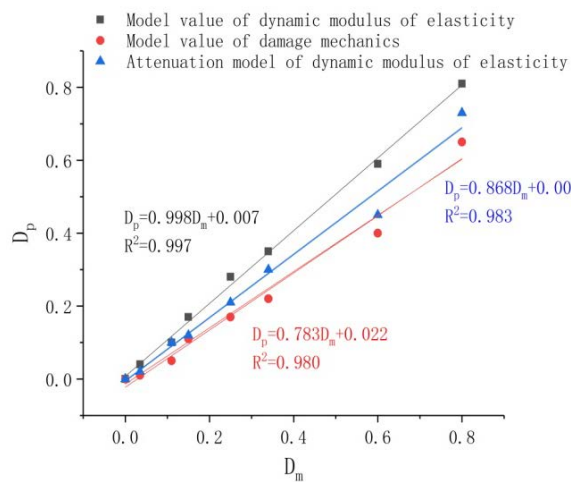
Figure 8. Fitting of ER value.   **Figure 9. Fitting of FR value.**
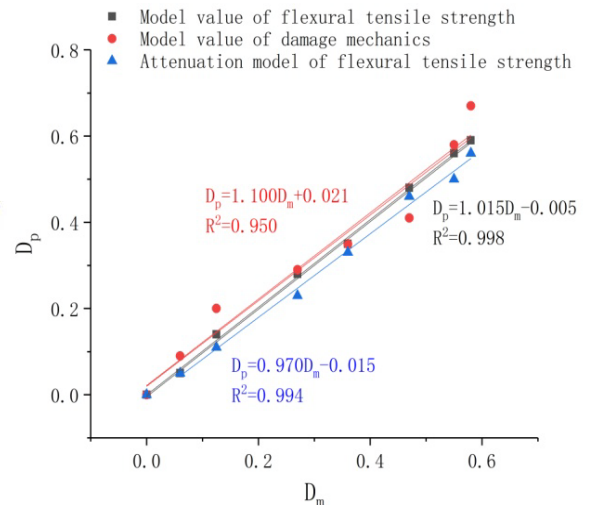
3.2. Verification of different road sections in the same period

Using only samples from the same section for model verification will make the test lack randomness, and the test results may have large errors. Therefore, the measured damage degree of 6 sections of highways A, B and C in the same year is again selected for verification. In Fig. 10, the abscissa is the numerical number of six road sections in turn, and the ordinate is the damage value. The damage value histogram of different road sections is drawn. Each road section corresponds to eight columnar graphs, four columnar graphs with striation correspond to the dynamic elastic modulus damage value, and the other four columnar graphs correspond to the bending tensile strength damage value.

As shown in Fig. 10, the difference between the damage evaluation value of the damage mechanics model and the damage measured value is the largest. The difference between the evaluation value of the attenuation model established by Sun Ming [26] and Shen Yin [30] and the difference between the measured value and the evaluation value of the dynamic elastic modulus damage model and the bending

tensile strength damage model is the closest. The reason is that the damage mechanics model is based on the concrete freeze-thaw test. In the test, one freeze-thaw cycle in the laboratory is equivalent to 14 freeze-thaw cycles in the outdoor, which can only simulate the approximate damage state. However, there are many factors that can damage the field pavement, such as rain, snow, load, other natural and human factors, which damage the cement concrete pavement together with the freeze-thaw effect. The attenuation model established by Sun Ming and Shen Yin also does not take into account the influence of climate factors in the seasonal frost regions on the performance of the cement concrete pavement. Therefore, the damage value calculated by the damage mechanics model and the attenuation model is smaller than the damage degree of the model established based on the field measured data, which proves that the evaluation level of the dynamic modulus damage model and the bending tensile strength damage model is high and has good practicability.
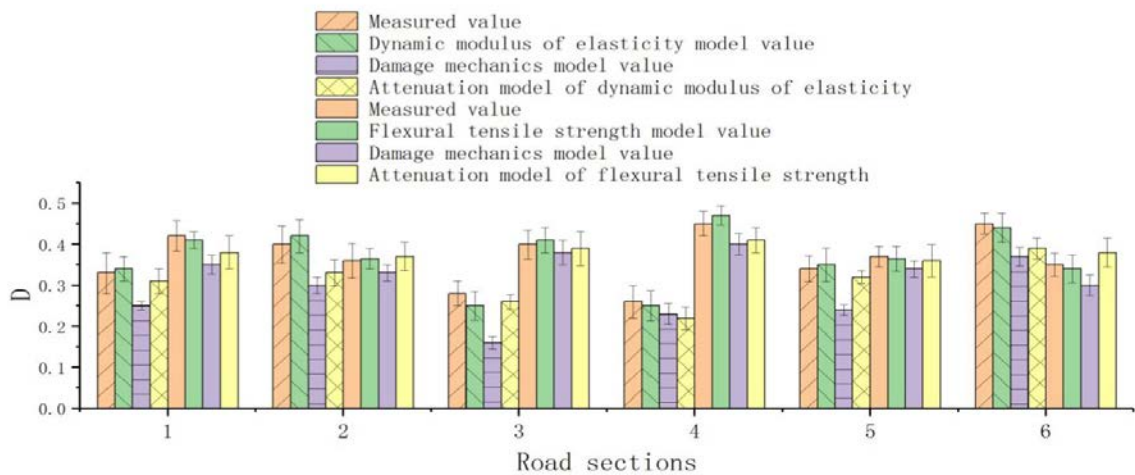
Figure 10. Histogram of ER and FR damage values.

4. Conclusions

1. The dynamic modulus of elasticity and flexural strength can be used as the parameters to establish the freeze-thaw damage model of the cement concrete pavement in the seasonal frozen area. Among the indexes that can reflect the damage state of concrete during freeze-thaw, the four indexes of mass change rate, water absorption rate, compressive strength and compression bending ratio do not show the obvious law of being affected by freeze-thaw cycle. In the other hand ,the the relative dynamic modulus of elasticity reaches 40 % loss rate before 150 freeze-thaw cycles, and the rate of flexural strength loss in the initial stage of freeze-thaw is 2.3 times that of dynamic modulus of elasticity.

2. Two models of freeze-thaw damage of cement concrete pavement in two seasonal frozen areas are established. Based on the dynamic modulus of elasticity index, the decisive coefficient R^2 of the model is 0.991, based on the flexural tensile strength index, the decisive coefficient R^2 of the model is 0.992, and the sig. value is less than 0.05, which shows that the two models have high goodness of fit, significant regression effect and statistical applicability.

3. The applicable conditions of the freeze-thaw damage model of the cement concrete pavement in the seasonal frost regions are put forward. Based on the dynamic modulus of elasticity index, the model of the freeze-thaw damage of the cement concrete pavement in the seasonal frost regions is established. When the water cement ratio is 0.45~0.48, the gas content is 1 %~4 %, and the freezing temperature is –15 ℃~25 ℃, the evaluation effect of the model is the best. The freeze-thaw damage model of the cement concrete pavement in the seasonal frost regions based on the bending tensile strength index is established. When the water cement ratio is 0.4~0.46, the gas content is 1 %~3.5 %, and the freezing temperature is below -5℃, the above range is the most suitable condition for the model, and the model has the best evaluation effect.

4. The evaluation effect of the freeze-thaw damage model is better and more practical than the previous model. In different periods of the same road section and the same period of different road sections, the freeze-thaw damage models of dynamic elastic modulus and flexural tensile strength are compared with the damage mechanics model and the existing model respectively. There verified that the decisive coefficient R^2 of the freeze-thaw damage model of dynamic elastic modulus is 0.997, and the decisive coefficient R^2 of the freeze-thaw damage model of flexural tensile strength is 0.998, which is higher than the damage mechanics model and the existing model respectively. Compared with the evaluation value of

damage mechanics model and the evaluation value of existing model, the evaluation value of freeze-thaw damage of dynamic modulus of elasticity and flexural strength model is closer to the measured value of field damage degree.

5. Acknowledgements

References

1. Chen, S., Ren, J., Song, Y., Li, Q., Sun, J., Che, Y., Chen, J. Salt freeze-thaw damage characteristics of concrete based on computed tomography. Tehnicki Vjesnik. 2019. 26(6). Pp. 1753–1763. DOI: 10.17559/TV-20190819080524
2. Fu, Y., Cai, L., Yonggen, W. Freeze-thaw cycle test and damage mechanics models of alkali-activated slag concrete. Construction and Building Materials. 2011. 25(7). Pp. 3144–3148. DOI: 10.1016/j.conbuildmat.2010.12.006.
3. Li, J., Wang, F., Yi, F., Ma, J., Lin, Z. Fractal analysis of the fracture evolution of freeze-thaw damage to asphalt concrete. Materials. 2019. 12(14). DOI: 10.3390/ma12142288
4. Klyuev, S.V., Klyuev, A.V., Vatin, N.I. Fiber concrete for the construction industry. Magazine of Civil Engineering. 2018. 84(8). Pp. 41–47. DOI: 10.18720/MCE.84.4.
5. Alsaif, A., Bernal, S.A., Guadagnini, M., Pilakoutas, K. Freeze-thaw resistance of steel fibre reinforced rubberised concrete. Construction and Building Materials. 2019. 195. Pp. 450–458. DOI: 10.1016/j.conbuildmat.2018.11.103.
6. Smith, S.H., Qiao, C., Suraneni, P., Kurtis, K.E., Weiss, W.J. Service-life of concrete in freeze-thaw environments: Critical degree of saturation and calcium oxychloride formation. Cement and Concrete Research. 2019. 122. Pp. 93–106. DOI: 10.1016/j.cemconres.2019.04.014.
7. Fediuk, R.S., Lesovik, V.S., Mochalov, A.V., Otsokov, K.A., Lashina, I.V., Timokhin, R.A. Composite binders for concrete of protective structures. Magazine of Civil Engineering. 2018. 82(6). Pp. 208–218. DOI: 10.18720/MCE.82.19
8. Zhao, Q., Cheng, P., Wang, J., Wei, Y. Damage prediction model for concrete pavements in seasonally frozen regions. Magazine of Civil Engineering. 2018. 84(8). Pp. 57–66. DOI: 10.18720/MCE.84.6
9. Nayak, S., Lyngdoh, G.A., Das, S. Influence of microencapsulated phase change materials (PCMs) on the chloride ion diffusivity of concretes exposed to Freeze-thaw cycles: Insights from multiscale numerical simulations. Construction and Building Materials. 2019. 212. Pp. 317–328. DOI: 10.1016/j.conbuildmat.2019.04.003.
10. Grubeša, I.N., Markovic, B., Vracevic, M., Tunkiewicz, M., Szenti, I., Kukovecz, Á. Pore structure as a response to the freeze/thaw resistance of mortars. Materials. 2019. 12(19). Pp. 1–16. DOI: 10.3390/ma12193196
11. Liu, K., Yan, J., Alam, M.S., Zou, C. Seismic fragility analysis of deteriorating recycled aggregate concrete bridge columns subjected to freeze-thaw cycles. Engineering Structures. 2019. 187. Pp. 1–15. DOI: 10.1016/j.engstruct.2019.01.134.
12. Fursa, T.V., Petrov, M., Dann, D.D., Reutov, Y.A. Evaluating damage of reinforced concrete structures subjected to bending using the parameters of electric response to mechanical impact. Composites Part B: Engineering. 2019. 158(June 2018). Pp. 34–45. DOI: 10.1016/j.compositesb.2018.09.042.
13. Xiao, Q.H., Cao, Z.Y., Guan, X., Li, Q., Liu, X.L. Damage to recycled concrete with different aggregate substitution rates from the coupled action of freeze-thaw cycles and sulfate attack. Construction and Building Materials. 2019. 221. Pp. 74–83. DOI: 10.1016/j.conbuildmat.2019.06.060. URL: https://doi.org/10.1016/j.conbuildmat.2019.06.060
14. Hezhev, T.A., Zhurtov, A.V., Tsipinov, A.S., Klyuev, S.V. Fire resistant fibre reinforced vermiculite concrete with volcanic application. Magazine of Civil Engineering. 2018. No. 80(4). Pp. 181–194. DOI: 10.18720/MCE.80.16
15. Song, Z., Lu, Z., Lai, Z. Influence of Hydrophobic Coating on Freeze-Thaw Cycle Resistance of Cement Mortar. Advances in Materials Science and Engineering. 2019. 2019(1). DOI: 10.1155/2019/8979864
16. Tian, J., Wu, X., Zheng, Y., Hu, S., Ren, W., Du, Y., Wang, W., Sun, C., Ma, J., Ye, Y. Investigation of damage behaviors of ECC-to-concrete interface and damage prediction model under salt freeze-thaw cycles. Construction and Building Materials. 2019. 226. Pp. 238–249. DOI: 10.1016/j.conbuildmat.2019.07.237.
17. Fediuk, R.S., Mochalov, A.V., Bituev, A.V., Zayakhanov, M.E. Structuring Behavior of Composite Materials Based on Cement, Limestone, and Acidic Ash. Inorganic Materials. 2019. 55(10). Pp. 1079–1085. DOI: 10.1134/S0020168519100042
18. Ismail, M.K., Hassan, A.A.A. Abrasion and impact resistance of concrete before and after exposure to freezing and thawing cycles. Construction and Building Materials. 2019. 215. Pp. 849–861. DOI: 10.1016/j.conbuildmat.2019.04.206.
19. Kim, J.H., Lee, H.S. Reliability assessment of reinforced concrete rectangular columns subjected to biaxial bending using the load contour method. Engineering Structures. 2017. 150. Pp. 636–645. DOI: 10.1016/j.engstruct.2017.07.061.
20. Tian, W., Han, N. Evaluation of damage in concrete suffered freeze-thaw cycles by CT technique. Journal of Advanced Concrete Technology. 2016. 14(11). Pp. 679–690. DOI: 10.3151/jact.14.679
21. Tsang, C., Shehata, M.H., Lotfy, A. Optimizing a test method to evaluate resistance of pervious concrete to cycles of freezing and thawing in the presence of different deicing salts. Materials. 2016. 9(11). Pp. 1–20. DOI: 10.3390/ma9110878
22. Wang, B., Wang, F., Wang, Q. Damage constitutive models of concrete under the coupling action of freeze–thaw cycles and load based on Lemaitre assumption. Construction and Building Materials. 2018. 173. Pp. 332–341. DOI: 10.1016/j.conbuildmat.2018.04.054.
23. Yu, H., Ma, H., Yan, K. An equation for determining freeze-thaw fatigue damage in concrete and a model for predicting the service life. Construction and Building Materials. 2017. 137. Pp. 104–116. DOI: 10.1016/j.conbuildmat.2017.01.042.
24. Wang, Z.H., Li, L., Zhang, Y.X., Wang, W.T. Bond-slip model considering freeze-thaw damage effect of concrete and its application. Engineering Structures. 2019. 201. Pp. 109831. DOI: 10.1016/j.engstruct.2019.109831.
25. Bharadwaj, K., Glosser, D., Moradllo, M.K., Isgor, O.B., Weiss, W.J. Toward the prediction of pore volumes and freeze-thaw performance of concrete using thermodynamic modelling. Cement and Concrete Research. 2019. 124. Pp. 105820. DOI: 10.1016/j.cemconres.2019.105820.

Zhao, Q.Q., Zhang, H.T., Fediuk, R.S., Wang, J.W., Fu, Q.

26. Sun, M., Xin, D., Zou, C. Damage evolution and plasticity development of concrete materials subjected to freeze-thaw during the load process. Mechanics of Materials. 2019. 139. DOI: 10.1016/j.mechmat.2019.103192

27. Mak, K., Fam, A. Freeze-thaw cycling effect on tensile properties of unidirectional flax fiber reinforced polymers. Composites Part B: Engineering. 2019. 174. Pp. 106960. DOI: 10.1016/j.compositesb.2019.106960.

28. Wei, J., Zhang, L., Li, B., Wen, Z. Non-uniformity of coal damage caused by liquid nitrogen freeze-thaw. Journal of Natural Gas Science and Engineering. 2019. 69. DOI: 10.1016/j.jngse.2019.102946

29. Klyuev, S.V., Khezhev, T.A., Pukharenko, Y.V., Klyuev, A.V. Experimental study of fiber-reinforced concrete structures. Materials Science Forum. 2018. 945. Pp. 115–119. DOI: 10.4028/www.scientific.net/MSF.945.115

30. Shen, Y., Liu, J., Zhou, S., Li, G. Experimental investigation on the freeze–thaw durability of concrete under compressive load and with joints. Construction and Building Materials. 2019. 229. Pp. 116893. DOI: 10.1016/j.conbuildmat.2019.116893.

Contacts:

Qianqian Zhao, 492954791@qq.com
Hetong Zhang, 2586762756@qq.com
Roman Fediuk, roman44@yandex.ru
Jianwu Wang, nihaone@163.com
Qiang Fu, fuqiang0629@126.com

Interaction of drill-injection piles with the surrounding soil

I.S. Salnyi[*a], Ya.A. Pronozin[a], A.M. Karaulov[b]*
[a] Tyumen Industrial University, Tyumen, Russia
[b] Siberian State University of Railways, Novosibirsk, Russia
*E-mail: salnyy2493@mail.ru

Abstract. Nowadays, drill-injection technologies are actively used to create pile foundations in both civil and industrial construction. There are many drill-injection piles technologies which application depends on geotechnical conditions, loads, buildings and constructions purpose, technical and resources sufficiency and other points. Drill-injection piles producing occurs stress-strain state modification and physical and mechanical properties modifications in surrounding soil massive. Detection of features of soil properties modifications in drill-injection pile surrounding region allows to improve drill-injection piles bearing capacity calculations methods and to get more exact results. The article contains the analysis of physical and mechanical properties modifications in the South of Tyumen region (Russia) soils which surround drill-injection piles "Normal". The definition of soil properties was done by experimental investigations during the excavation of the piles to the depth of about 3.5 m in the site investigation with known engineering and geological conditions. There was detected a 6–10 % increase of soil density in 60 mm distance from the pile wellbores which depends on the soil type and increase of soil humidity in the waterless zone due to the high cement mixing-water ratio of the cement mortar. Also, it was found the increase of soil deformation characteristics up to 17.4 % and soil strength characteristics up to 27.3 % with reference to the original values. To the results of the excavation of the piles, it was discovered the wellbores expansion up to 4.4 % and local wellbores expansions in relative to the original values. During the inspection of the drill-injection piles there was discovered some piles defects such as massive soil penetration into the pile shaft near its wellhead and soil and mortar mixing along the perimeter of the piles owing to the insufficient mortar density and its high shrinkage. According to the results of the experimental researches, further investigations problems were defined.

1.   Introduction

The application of drill-injection piles took place from the middle of the last century in Italy [1]. Further development of drill-injection piles technologies helped to extend the region of pile foundations implementation: it allowed to use them for the monuments of architecture strengthening, to create these piles in most soil and climate conditions, near the existing buildings and in the restricted conditions without requirement of organization of protective measures due to the lack of dynamic impact on the soil. Nowadays, drill-injection technologies are actively used to create pile foundations in both civil and industrial construction. Drill-injection piles producing occurs stress-strain state modification and physical and mechanical properties modifications in surrounding soil massive. Authors of the article believe that drill-injection pile technology "Normal", which based on the repeated use of high-strength core-injector due to its extraction after wellbore crimping and subsequent immersion into the pile body a reinforcement frame or a single rod, is promising [2]. Due to the above-mentioned, the object of the investigation is drill-injection pile "Normal" which was created in the soil conditions of South of Tyumen region, and also physical and mechanical soil properties after drill-injection pile creation.

In spite of the high variety of drill-injection piles technologies [3–9], they all have the same technologies operations during their creations which are: wellbore drilling to the required depth with its simultaneous flushing and finished wellbore crimping by cement mortar. Drill-injection piles crimping

produces wellbore expansion and/or local wellbore expansion along with the pile (often intentional) regarding the original values which contribute to the surrounding soil compression and increase the friction forces along with the pile and it, as a result, increases drill-injection piles bearing capacity. It is known that ground anchors technologies gave a start to the drill-injection pile technologies. The main difference between the above-mentioned technologies is that during the ground anchors creation of crimping takes place only in the requirement zone by using a plugging holder and subsequent mortar injection under high pressure into the cut-off area. Nowadays, many researches about examination of interaction of drill-injection anchors with variety of soil bases both in laboratory and field conditions are made. The results of these researches which in different times were done in many European countries as England, Austria, Slovakia, Belarus, Germany, Czech Republic, Bulgaria etc., are summarized and presented in [10] and others publications [11–16]. There are fewer data about the interaction of drill-injection piles with the surrounding soil [17–24]. In the scientific paper [10] this fact is also underlined.

The definition of dependences and character of physical and mechanical properties modifications in surrounding drill-injection piles soil during them creation is a very important problem for drill-injection piles bearing capacity calculation because there are many tests which show that real drill-injection pile bearing capacity is higher up to 2 and more times in comparison with bearing capacity which was calculated for the same piles according to the normative documents [1, 25–26]. This is too relevant owing to the intensive drill-injection piles usage in new construction and also in the strengthening of existing buildings and constructions.

The purpose of the study is an identification of the character of physical and mechanical soil properties modifications in the surrounding drill-injection pile zone after its creation, and an evaluation of the pile shaft geometric parameters for its later usage for drill-injection pile bearing capacity calculation method improving. For the purpose achievement the next tasks are defined: the physical and mechanical soil properties in the surrounding drill-injection pile zone determining before and after its creation; zones of physical and mechanical soil properties modifications definition; pile shafts geometric parameters measurement.

These tasks were solved after drill-injection piles "Normal" static load tests, which were done in the soils conditions of the South of Tyumen region (Russia).

2. Methods

The field experimental researches took place in the site investigation, which is located in Tyumen city centre on the territory of the reconstructing kindergarten on the Murmanskaya, 183 street (Fig. 1).

Figure 1. The site investigation location scheme.

The site investigation within the piles depth is composed by silty-clay soils with stiff and free-flowing consistency (Fig. 2). All the tested drill-injection piles were hanging and for this reason they did not especially lean on the sand layer during the drilling process.
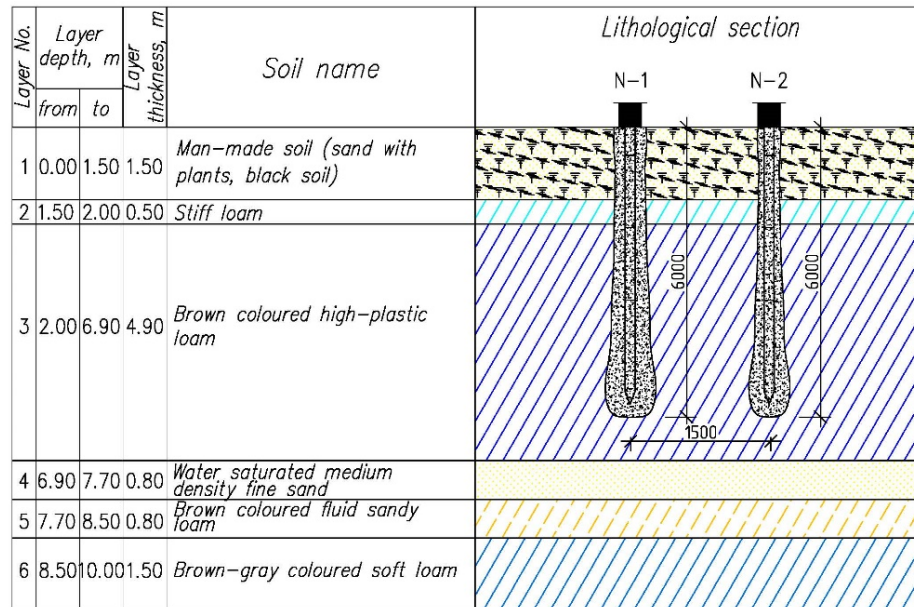
Figure 2. Piles location on the engineering and geological section.

The site investigation physical and mechanical soil properties are shown in Table 1. It's important to say that during the geotechnical surveys in August 2018 all soil samples have taken every 1 m, so soil characteristics in Table 1 are presented for all these samples.

Table 1. Physical and mechanical soil properties based on the results of the geotechnical surveys.

Soil sampling depth, m	W, %	ρ, g/cm³	e	C, kPa	ϕ, degree	$E_{comp.}$, MPa
0.5	–	–	–	–	–	–
1.5	18	1.97	0.62	17	15	4.9
2.5	21	1.92	0.70	9	11	2.3
3.5	21	1.97	0.66	12	22	4.4
4.5	24	1.95	0.72	16	20	3.8
5.5	28	1.90	0.82	7	23	3.7
6.5	28	1.92	0.83	2	22	4.6
7.5	24	2.02	0.64	0	37	17.9
8.5	23	2.01	0.63	1	27	5.5
9.5	26	1.90	0.79	3	20	5.4

In the situ during the 15.09 – 25.09.2018 range drill-injection piles according to the "Atlant" technology [6] and by author's drill-injection piles technology which is called "Normal" for their next static tests were done. Below stages during drill-injection piles "Normal" creation were done:

1. wellbore drilling with required diameter and depth with the protection by the water-cement mortar with 1 to 1 proportion;

2. wellbore crimping by the water-cement mortar with 0.4–0.45 ratio under the pressure up to 0.7 MPa after the required depth have been achieved;

3. gradually high-strength core-injector extraction from the pile body with concurrently extra crimping each meters;

4. reinforcement frame immersion into the pile body. The reinforcement frame consists of 3 bars with 14 mm diameter.

There was used "Figaro" drilling machine and "MINI" injection complex [27] to create drill-injection piles.

After drill-injection piles "Normal" static load tests piles "N-1" and "N-2", which are shown in Fig. 2, were excavated. Drill-injection pile "N-1" had 340 mm diameter during its creation and drill-injection pile "N-2" had 200 mm diameter. Both piles had 6 m in length and reinforced with a 5.5 m triangular frame. During the pile excavation, there was defined physical and mechanical properties of the surrounding soil and piles sizes.

Soil sampling and its further density and humidity definitions were done according to the [28] by the method of cutting rings. Three cutting rings with 56 mm diameter have been located in two perpendicular planes near the "N-1" pile and one plane near the "N-2" pile. After extraction of the rings filled with soil samples, extra soil had been removed away and then the definition of its density and humidity had been started. The location scheme of cutting rings along the piles bores is presented in Fig. 3. Soil samples were taken layer by layer from 0.35 m, 0.55 m, 0.75 m, 0.85 m, 1.0 m, 1.3 m, 1.6 m, 1.9 m, 2.2 m, 2.5 m, 2.8 m, 3.1 m and 3.4 m depth regarding the ground surface. Additionally, soil samples were taken for its deformation and strength characteristics definition in according to the [29].
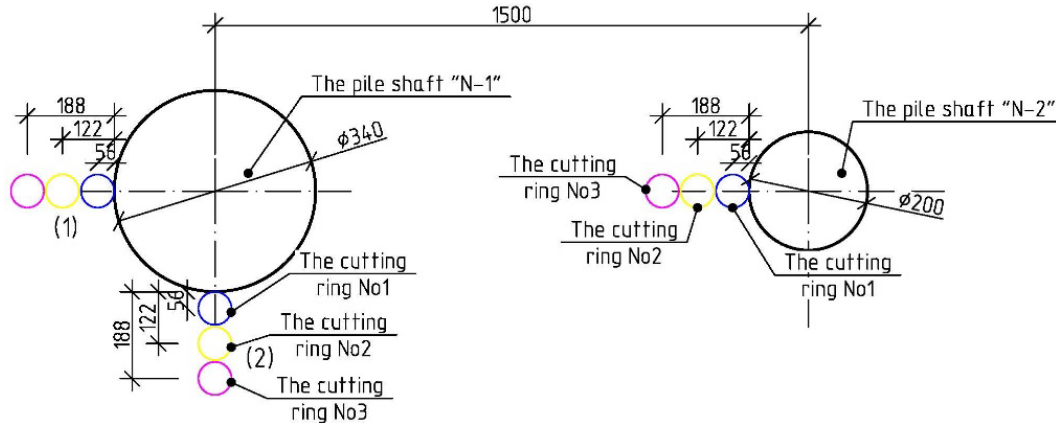
Figure 3. The location scheme of cutting rings along the piles during the excavation.

It was impossible to take continuous soil samples until the 1.5 m depth because of the fill-up soil in this zone that was discovered during the geotechnical surveys. The pile excavation depth where it was possible to do soil sampling was only 3.5 m owing to the found groundwater level below. For this reason, it was important to find the physical and mechanical properties of the fill-up soil that it had before drill-injection piles creation. So, along with the piles there was dug a prospect pit with 1.8 m width to take soil samples in natural content on the opposite side of the piles (Fig. 4).
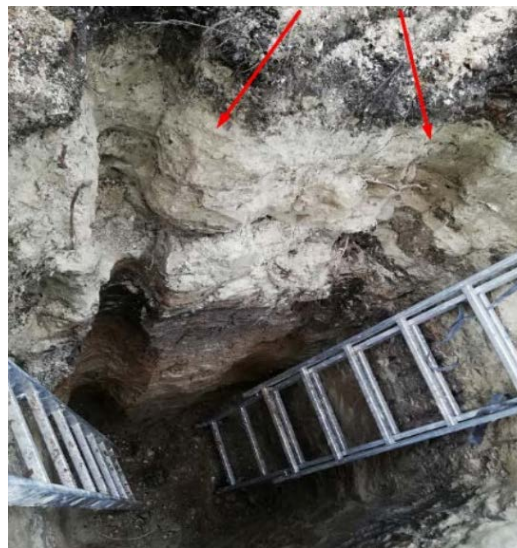
Figure 4. The scheme of layer-by-layer soil sampling in natural content.

Therefore, till the 2.1 m depth there were additionally classified some geotechnical elements such as:

- 30 cm – dark-colored black soil;
- 70 cm – fill-up sand layer;
- 10 cm – clay layer;
- 40 cm – man-made soil layer with black soil incorporations;
- 60 cm – stiff brown colored loam layer.

Soil sampling for density and humidity extra definition was taken with 30 cm gradation in the prospect pit area. Thus, extra soil sampling was taken from the –0.6 m, –0.9 m, –1.2 m, –1.5 m, –1.8 m and –2.1 m depth relative to the ground surface and its physical properties are presented in the Table 2.

Table 2. Soil base physical properties before piles creation.

Soil sampling depth, m	W, %	ρ, g/cm³	e
0.6	10	1.67	0.78
0.9	13	1.65	0.85
1.2	23	1.67	0.99
1.5	16	1.96	0.59
1.8	16	1.97	0.59
2.1	25	1.90	0.78

3. Results and Discussion

The results of soil density definition in the nearby area of the piles are shown in the Fig. 5.
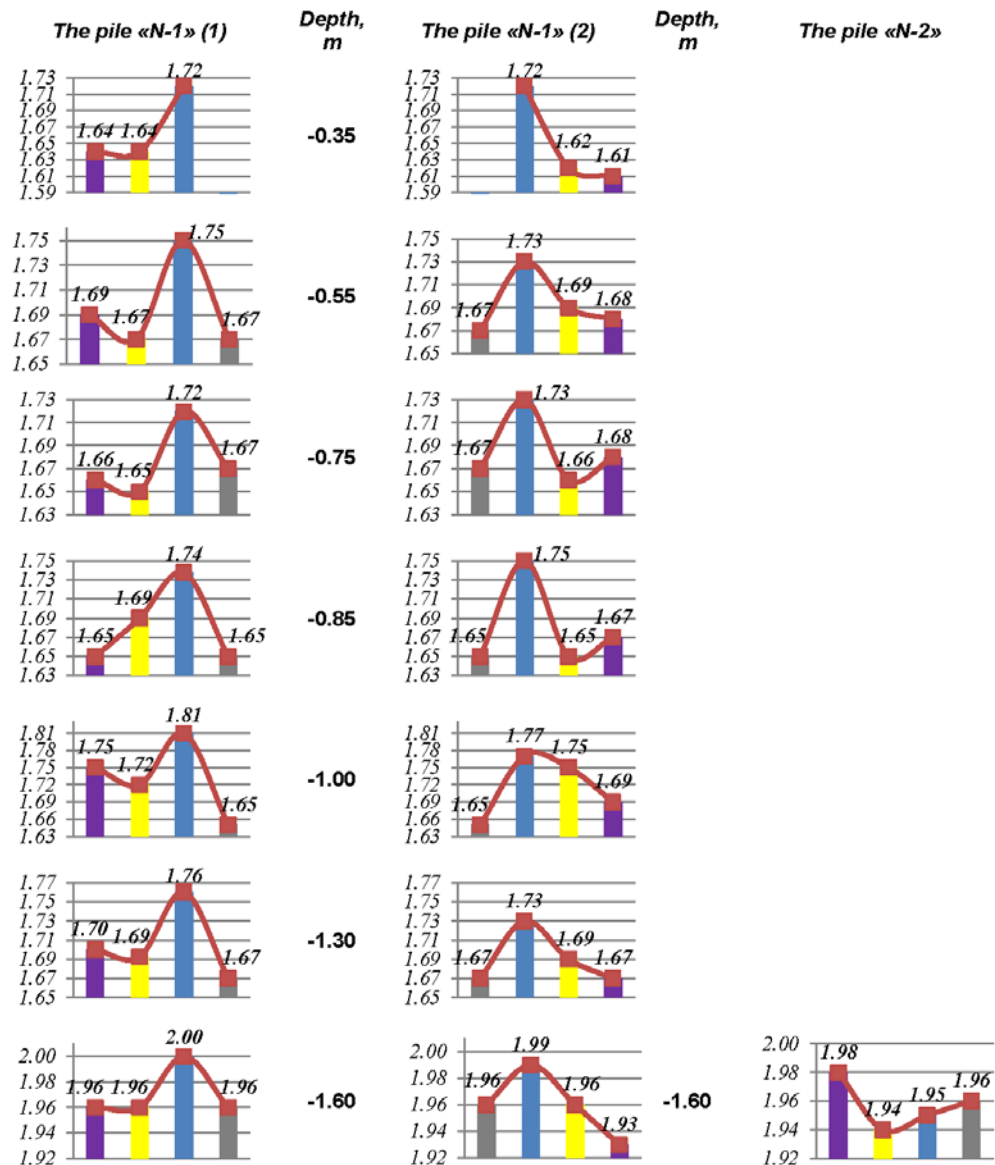
Figure 5. Soil density (g/cm³) modifications graphs along the piles depth (beginning).
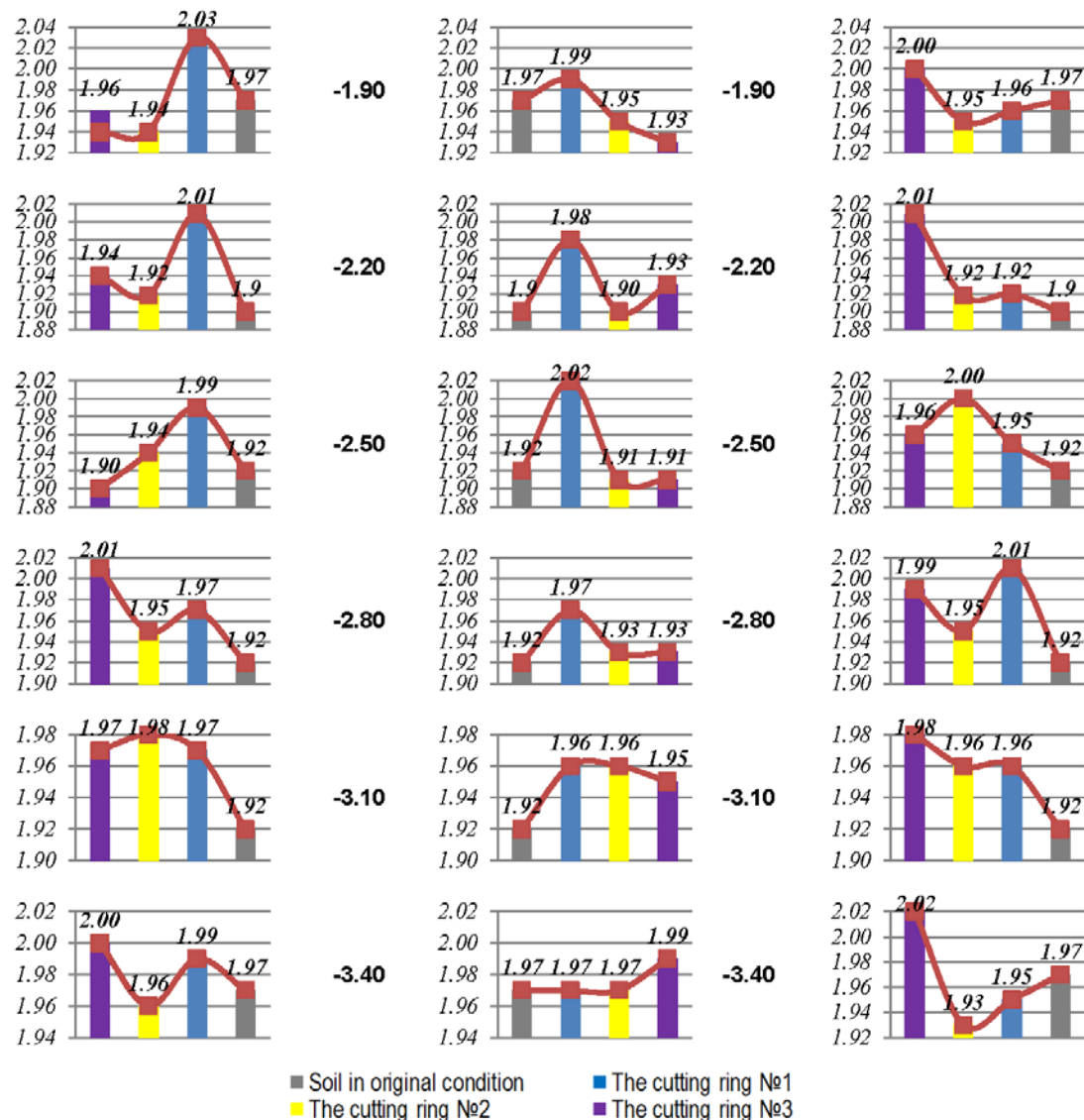
Figure 5. Soil density (g/cm³) modifications graphs along with the piles depth (ending).

These graphs show that for the pile "N-2" there was detected an increase of soil density in the depth range of –2.2 – 3.1 m. At the other depths for the pile "N-2" there is no change in the soil density. These graphs also show the stable trend of soil density increment in the range of the cutting ring No. 1 (in the area up to 60 mm near the piles) for the drill-injection pile "N-1". And, to the –1.3 m depth occurs an extensive density increment for the surrounding pile soils with a maximum 10 % increment value at –1 m depth (from 1.65 g/cm³ to 1.81 g/cm³). Below this level the density increment in the range of the cutting ring No. 1 is only about 1 – 6 %. This occurs because till the –1.5 m depth man-made soils with low density (1.65 – 1.67 g/cm³) and high porosity ratio (0.78 – 0.99) lay (look at Table 2), and under this layer are clay soils with higher density and lower porosity ratio is situated. It should also be noted that for the drill-injection pile «N-1» with a larger diameter takes place more density increment concerning the drill-injection pile "N-2" with a less diameter: the relation of the soil compaction radius to the pile "N-1" wellbore radius is 0.74, and this value for the pile "N-2" is only 0.63. Soil density in the cutting rings No. 2 – 3 range (in the area up to 190 mm near the piles) little changes for both drill-injection piles regarding the original density despite the small jumps in the envelope graph because in according to the [28] the permissible difference in the results of determining the density of clay soil is up to 0.03 g/cm³. Thus, after drill-injection piles creation the soil density increment up to the 60 mm distance near the piles takes place. This occurs because the cement particles incorporated into the nearby area of the piles (Fig. 6) during wellbores crimping and it allows increasing soil specific gravity.

This too short soil density modification distance is connected with free cement mixture flow near piles wellhead during its crimping. On the other hand, during ground anchors crimping there uses plugging holders which allow to create higher pressure in this zone and modify surrounding soil density up to 3.5 – 4 wellbore radiuses distance [10, 11]. A larger soil compaction zone occurs during the formation of drill-injection piles with controlled broadening at the pile end due to the use of a membrane cup: the average

radius of the soil compacted zone is 0.15 – 0.6 m which is depending on the injected volume of the mortar [18]. In addition, in [18], it is noted that during constant pressure on the walls of the drill-injection pile shaft, the density of the surrounding soil increases to an average of 17 %.

Figure 6. Cement particles incorporation into the range of the cutting ring No. 1.

The results of soil humidity definition in the nearby area of the piles are shown in the Fig. 7.
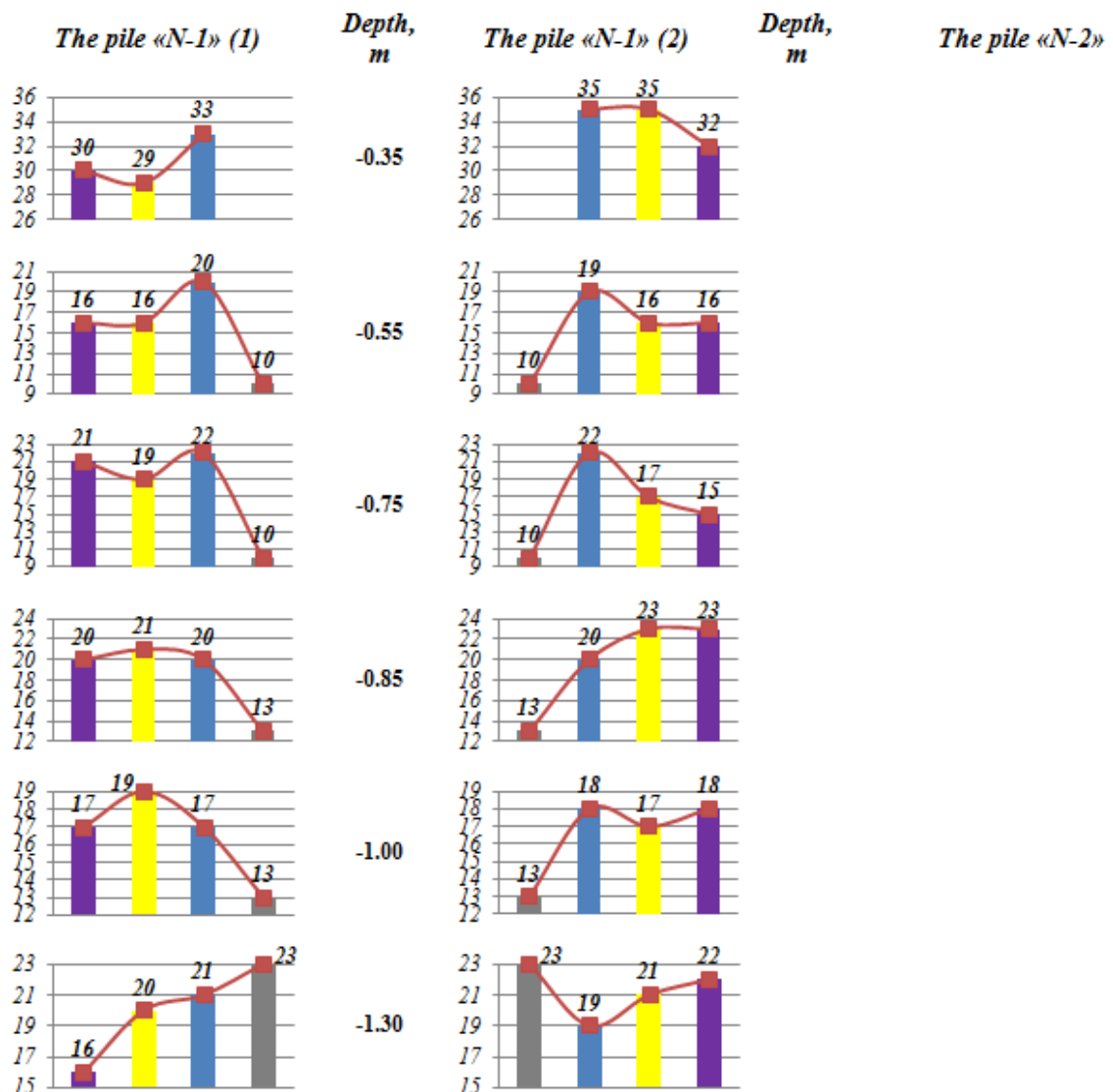
Figure 7. Soil humidity (%) modifications graphs along with the pile depth (beginning).
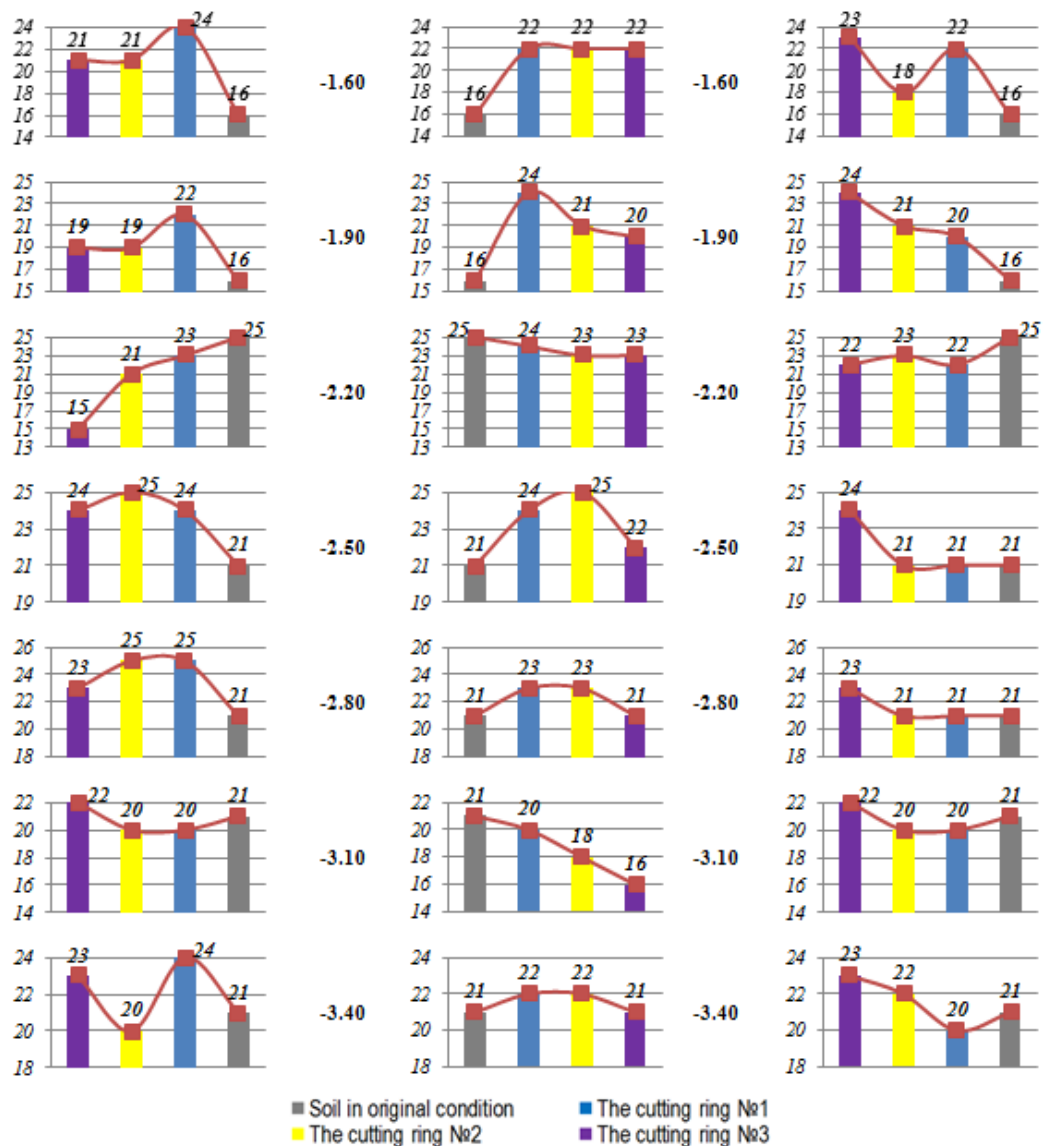
Figure 7. Soil humidity (%) modifications graphs along with the pile depth (ending).

According to the diagrams, which are shown in the Fig. 7, soil humidity modifications in the nearby area of the drill-injection pile "N-1" with 340 mm diameter are characterized by mostly increment concerning its original values. Moreover, within the range of the man-made soil location humidity increment is up to 120 % at the 0.75 m depth. This high humidity increment occurs because of the surfaces water permeation into the soils with a high permeability ratio. Further, after -1.6 m depth (clay soils level) soil humidity increment is up to 50 % with its minimum value 10 %. From the -3.0 m depth, there is mostly no humidity modifications due to the found underground water level.

For the drill-injection pile "N-2" with 200 mm diameter at the 1.5 – 2.0 m depth the soil humidity increase with a maximum value of up to 38 % also takes place. Further, at the investigation depth, there is mostly no soil humidity modification nearby the pile.

Soil humidity modification nearby the piles in the range of all cutting rings is constant (Fig. 7) concerning its original values despite the small jumps in the envelope graph because in according to the [26] the permissible difference in the results of determining the humidity of clay soil with $W < 50$ % is up to 2 %.

Soil humidity increment in clay soils takes place owing high enough cement mixing-water ratio of about 0.4 – 0.45 during drill-injection piles crimping when the process of cement hydration needs about 0.20 – 0.25 value of cement mixing-water ratio [10]. This way, it promotes to appear extra water in the wellbore that later drain into the surrounding soil. Because of the low permeability ratio in clay soils and soil porosity decrement owing to the cement mud injection a consolidation process in the surrounding soil near drill-injection piles needs a lot of time. During the wellbore crimping in accordance to the "Atlant" or «Norma» technology, due to the free release of the mortar from the wellbore top, no extra pressure takes place, otherwise, there is a decrease of soil humidity up to 28 % [16, 18].

Additionally, after soil sampling for its density and humidity definition, there were taken another soil samples by inserting into the soil base a cylinder with 100 mm diameter and 300 mm height close to the drill-injection pile "N-1" (about 5 – 10 mm distance from pile shaft) at the –2.5 m and –3.0 m depth for soil deformation and strength properties definition. Due to the done compressive tests it was detected that soil Young's modulus E, MPa, is 2.4 MPa at the –2.5 m depth and 2.7 MPa at the –3.0 m depth. Soil Young's modulus increment is 4.3 % and 17.4 % respectively in relations to the original value (2.3 MPa). In [10, 18, 22], an increase of Young's modulus in the compacted zone up to 35 % concerning the initial values is noted due to the creation of extra pressure along the pile shaft during its crimping.

An angle of internal friction ϕ, degree, is 13° and 14° at the –2.5 m and –3.0 m depths respectively that higher than its initial value in 18.2 % and 27.3 %. Soil specific cohesion values, c, kPa, have grown up to 11 % in relation to its original value and is 10 kPa for both soil samples.

In addition, during the pile excavation its diameter modifications along with the depth and its defects were inspected. So, due to the pile "N-1" with an initial 340 mm diameter inspection within the excavated depth (about 4 m), there was detected its diameter increment in the man-made soil layer (till the 1.5 m depth) regarding the pile diameter in clay soils, which is shown in Fig. 8. For the drill-injection pile "N-2" there was no emphasized diameter expansions or modifications.

Figure 8. Drill-injection piles inspecting.

Pile shafts for both drill-injection piles within the investigation depth are straight without any seeing defects. Along the pile perimeter, there is a "ground shell", which represents geotechnical elements order in accordance to the geotechnical surveys (Fig. 8–9).

Figure 9. A "soil shell" along the pile perimeter.

After inspection both drill-injection piles were extracted for further investigations. Due to the pile shafts cutting it was detected that pile "N-1" diameter after its creation was 355 mm concerning the initial 340 mm wellbore diameter (Fig. 10). The diameter increment owing to the pile crimping was 4.4 %.

Figure 10. Diameter of drill-injection pile "N-1" after extraction.

During the pile "N-2" shaft inspection after its extraction there were discovered some zones with local wellbore expansions about 150 mm length at the –2.0 m depth on the "man-made soil – clay soil" border and at the –3.5 m depth on the underground water level. These diameters are 280 mm and 300 mm that higher on 40 % and 50 % respectively in relations to the initial 200 mm wellbore diameter. Drill-injection pile "N-2" diameter is constant on the other length and the same with the wellbore diameter (Fig. 11). An extensive increase of the initial diameter (up to 2 or more times) is achieved by creating an extra pressure (about 0.2 MPa or more) in the wellbore during its crimping, as noted in [10, 17, 18].
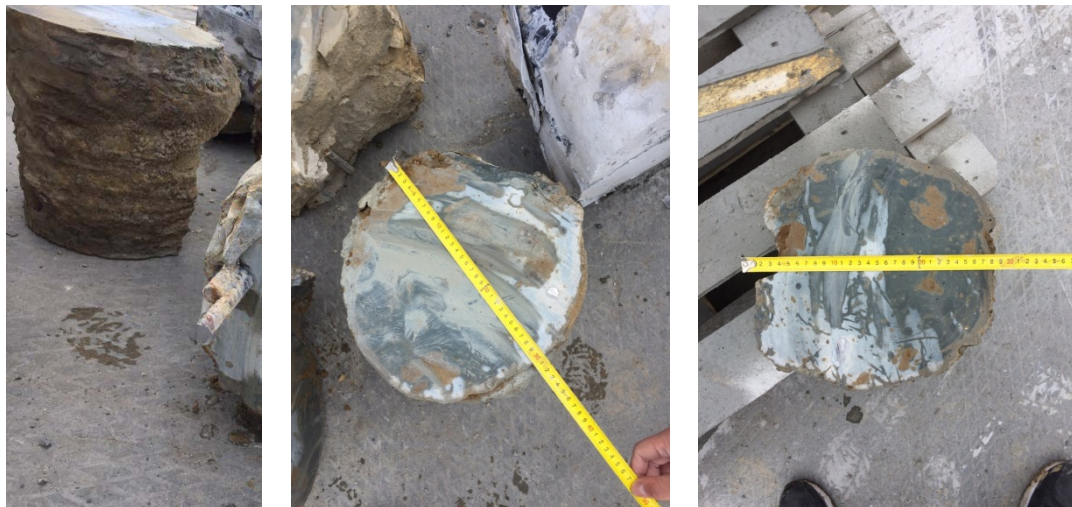
Figure 11. Expansions of drill-injection pile "N-2" shafts.

Moreover, due to the drill-injection piles cutting and its inspection there were noticed some pile shafts defects, which are presented in the Fig. 12:

- soil and mortar mixing along the perimeter of the piles;
- massive soil penetration into the pile shaft near its wellhead.

| a | b | c |
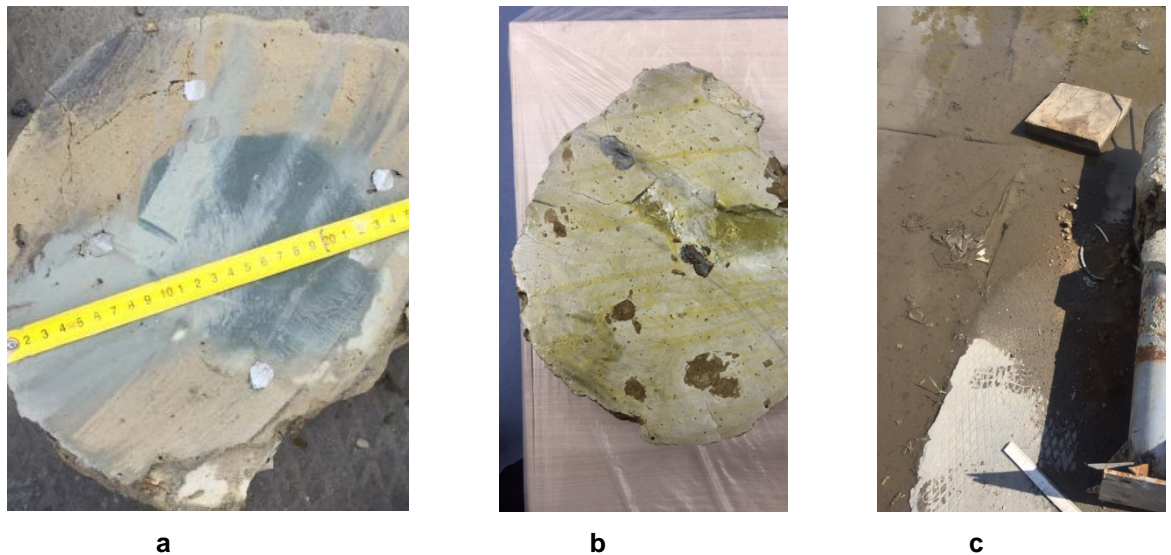
Figure 12. Drill-injection piles defects due to its creations.
a – soil and mortar mixing along the perimeter of the piles;
b – soil incorporations into the pile shaft;
c – massive soil penetration into the pile shaft near its wellhead.

These defects occurred owing to the use of cement/water/water-glass mixtures during wellbore crimping which has low mixture density (about 1.5 – 1.7 g/cm³), too much shrinkage and low strength of about 10–15 MPa.

4.   Conclusion

There are some main conclusions, due to the tests of soil physical and mechanical properties near drill-injection piles "N-1" and "N-2" with 340 mm and 200 mm diameters respectively and due to the pile geometry properties measuring, which are:

1. During drill-injection pile crimping under pressure of about 0.7 MPa there occurs surrounding soil density increment up to 10 % in the range of man-made soil layers and up to 6 % in the range of clay soils owing to the soil particles packing and cement mixture incorporations into the soil pores. Soil density modification in relation to its initial value is noticed up to 60 mm distance from pile shafts regardless of drill-injection pile diameter. This too-short soil density modification distance is connected with free cement mixture flow near piles wellhead during its crimping.

2. For both drill-injection piles was detected surrounding soil humidity increment up to 190 mm distance from pile shafts around 120 % at the range of man-made soil layers with high permeability ratio. At the range of clay soil layers around drill-injection pile with 340 mm diameter soil humidity increment up to 50 % takes place, for the pile with 200 mm diameter within the clay soil layers there is no soil humidity modification. From the depth, where the underground water level starts, soil humidity modifications for both piles do not happen. Soil humidity increment at the range of clay soil layers occurs because of high enough cement mixing-water ratio about 0.4–0.45 during drill-injection piles crimping, when the process of cement hydration needs about 0.20–0.25 value of cement mixing-water ratio.

3. Due to the pile shafts injection crimping there is observed the increment of clay soil Young's modulus up to 17.4 % in relations to its value before drill-injection piles creation and the increment of an angle of internal friction and specific cohesion values up to 27.3 % and 11 % respectively in the contact region.

4. Wellbore crimping under pressure up to 0.7 MPa allowed to increase drill-injection pile "N-1" diameter by 4.4 % within clay soil layers in relation to its 340 mm initial value. Moreover, there was noticed more extensive diameter increment at the range of man-made soil layers in relations to the clay soil layers.

There are some zones with local wellbore expansions within the drill-injection pile "N-2" shaft at the "man-made soil – clay soil" border and at the underground water level. These expansions zones are 40 % and 50 % respectively bigger than the initial 200 mm wellbore diameter. Drill-injection pile "N-2" diameter is constant on the other length and the same with the wellbore diameter

This small wellbore expansion ratio is connected with free cement mixture flow near piles wellhead during its crimping and it does not allow creating a stable extra pressure into the wellbore.

Salnyi, I.S., Pronozin, Ya.A., Karaulov, A.M.

5. There were discovered some piles defects such as massive soil penetration into the pile shaft near its wellhead and soil and mortar mixing along the perimeter of the piles owing to the insufficient mortar density and its high shrinkage. The most vulnerable for ensuring the quality of the continua cement body structure drill-injection pile zone is the top of the pile shaft up to 2–3 its diameters.

Due to obtained results of interaction of drill-injection piles with the surrounding soil authors of the article defined the issues for further investigations, such as:

- laboratory explorations to definition soil physical and mechanical properties modifications and residue stress state owing to the wellbore expansion which occurs during drill-injection piles creation in clay soil with various consistency in relations to the South of Tyumen region soils conditions;

- engineering of an inventory, quick-disassembly plugging holder analogue, which prevents free cement mixture flow near piles wellhead during its crimping. This tool will contribute to bigger wellbore expansion, surrounding soil packing and its physical and mechanical characteristics increment;

- selection of mixture parameters with high density (about 1.90–2.20 g/cm^3), fluidity of mixture, resistibility and low shrinkage based on the existing resources and drill-injection equipment;

- creation of an improved calculation method of drill-injection piles bearing capacity due to surrounding soil physical and mechanical properties modifications and residue stress state.

References

1. Samokhvalov, M.A., Geydt, A.V., Paronko, A.A. Review of existing designs of drill-and-injection anchor piles. Vestnik MGSU. 2019. No. 12. Pp. 1530–1554. DOI: 10.22227/1997-0935.2019.12.1530-1554

2. Pronozin, Y.A., Salnyi, I.S., Volosyuk, D.V. «Normal» bored injection pile with increased bearing capacity. Proceedings of the International Conference on Geotechnics Fundamentals and Applications in Construction: New Materials, Structures, Technologies and Calculations. GFAC. S.-Petersburg, 2019. Pp. 296–300. DOI: 10.1201/9780429058882-58

3. Armour, P.E., Groneck, P.E., Keeley, P.E., Sunil Sharma, P.E. Micropile Design and Construction Guidelines Implementation Manual, 2000. 376 p.

4. Windle, J., Suckling, T. CFA piling: A cheap solution or a problem waiting to happen. Proceedings of the Congress of Forensic Engineering. 2009. Pp. 335–342. DOI: 10.1680/fefftu.36130.0034

5. Müller, W. Slope securing with TITAN injection piles in the railroad area as used in the project «Renovation of the supporting wall near Nittendorf». Felsbau Magazin. 2010. No. 3. Pp. 194–199.

6. Malinin, A.G., Malinin, D.A. Procedure for installation of «Atlant» anchor piles. Soil Mechanics and Foundation Engineering. 2010. 47(1). Pp. 20–25. DOI: 10.1007/s11204-010-9082-8

7. Pronozin, Ya.A., Zazulya, Yu.V., Samokhvalov, M.A. Sposob izgotovleniya buroinyektsionnoy svai s kontroliruyemym ushireniyem [Creation method of drill-injection pile with controlled broadening]. Patent Russia no. 2522358, 2014. (rus)

8. Herrmann, H., Bucksch, H. Titan pile. Dictionary Geotechnical Engineering/Wörterbuch GeoTechnik. 2014. Pp. 1406–1406. DOI: 10.1007/978-3-642-41714-6

9. Jakub, S. The design of drilled displacement system piles using the cavity expansion theory. Acta Geotechnica Slovenica. 2018. 15(2). Pp. 81–91. DOI: 10.18690/actageotechslov.15.2.81-91.2018

10. Nikitenko, M.I. Buroinyektsionnyye ankery i svai pri stroitelstve i rekonstruktsii zdaniy i sooruzheniy [Drill-injection anchors and piles in the construction and reconstruction of buildings and structures]. Minsk: BNTU, 2007. 580 p. (rus)

11. Ostermayer, H.I., Scheele F. Research on ground anchors in non-cohesive soils. Proceedings of 9th International Conference. Tokyo, 1977. Pp. 92–97.

12. Nikitenko, M.I., Sobolevskii, D.Y. Effect of grout injection in holes on the properties of surrounding sandy soil. Soil Mechanics and Foundation Engineering. 1986. 23(3). Pp. 97–102. DOI: 10.1007/BF01717840

13. Mokhkhamad, Kh.M. Buroinyektsionnoye uprochneniye osnovaniy zdaniy i sooruzheniy pri rekonstruktsiyakh: dis. … kand. tekhn. nauk [Drilling and injection hardening of the foundations of buildings and structures during reconstruction: dissertation … candidate of technical sciences]: 05.23.02. Minsk, 1998. (rus)

14. Park, D.W., Jeong, J.K., Seo, J.H., Kim, J.R., Yang, T.S. Study of ground anchor performance analysis by on-site test. Proceedings of 14th Asian Regional Conference on Soil Mechanics and Geotechnical Engineering. Hong Kong, 2011. 6 p.

15. Ter-Martirosyan, A.Z., Ter-Martirosyan, Z.G., Avanesov, V.S. Estimation of residual stresses at the interface between ground anchor and surrounding soil under pressure grouting. Procedia Engineering. 2016. No 153. Pp. 754–760. DOI: 10.10-16/j.proeng.2016.08.238

16. Sawamatsu, T., Nitta, T., Miyatake, H., Otsubo, M. Bearing resistance property of diameter-expanded anchorage in sandy ground. Proceedings of E3S Web of Conferences. Divnomorskoe village, 2019. 92 p. DOI: 10.1051/e3sconf/20199217003

17. Malinin, A.G., Gladkov, I.L. Investigation of the diameter of soil-cement columns under various soil conditions. Soil Mechanics and Foundation Engineering. 2011. 48(3). Pp. 121–126. DOI: 10.1007/s11204-011-9138-4

18. Samokhvalov, M.A. Vzaimodeystviye buroinyektsionnykh svay, imeyushchikh kontroliruyemoye ushireniye, s pylevato-glinistym gruntovym osnovaniyem: dis. … kand. tekhn. nauk [Interaction of drill-injection piles with controlled broadening with a dusty-clay soil base: dissertation … candidate of technical sciences]: 05.23.02. Tyumen, 2016. (rus)

19. Pachla, H. Conditions of proper interaction of Low-pressure Injection Piles (LIP) with structure and soil, carrying capacity of pile anchorage in foundation. Studia Geotechnica et Mechanica. 2016. 38(4). Pp. 33–49. DOI: 10.1515/sgem-2016-0029

20. Zazulya, J., Melnikov, R., Samokhvalov, M., Mironov, V. Design calculation of drill-injection piles with controlled broadening and silty-clayed soil foundation basic interaction parameters. Proceedings of the MATEC Web of Conferences. Tyumen, 2016. 73 p. DOI: 10.1051/matecconf/20167301009

21. Samokhvalov, M.A., Geidt, A.V., Paronko, A.A. Results of the calculated prediction for interaction of drilling-injection piles, having controlled broadening, with dust-clay ground basis. International Journal of Civil Engineering and Technology. 2018. 9(7). Pp. 484–496.

22. Pronozin, Y.A., Samokhvalov, M.A. Analysis of the Interaction of Drill-Injection Piles with Soil Foundation. Soil Mechanics and Foundation Engineering. 2018. 55(2). Pp. 82–86. DOI: 10.1007/s11204-018-9507-3

23. Bayesteh, H., Sabermahani, M. Full-scale field study on effect of grouting methods on bond strength of hollow-bar micropiles. Journal of Geotechnical and Geoenvironmental Engineering. 2018. 144(12). DOI: 10.1061/(ASCE)GT.1943-5606.0001983

24. Zhu, Y. Study on the mechanism of property change of soft soil pile. Journal of Advanced Oxidation Technologies. 2018. 21(2). DOI: 10.26802/jaots.2018.03030

25. Konyushkov, V.V., Ulitskiy, V.M. Issledovaniye nesushchey sposobnosti buroinyektsionnykh svay s uchetom tekhnologii ikh izgotovleniya [Study of the bearing capacity of drill-injection piles in accordion to the technology of their manufacture]. Izvestiya Orlovskogo gosudarstvennogo tekhnicheskogo universiteta. 2007. Pp. 68–74. (rus)

26. Konyushkov, V.V. Nesushchaya sposobnost buroinyektsionnykh svay na vertikalnuyu i gorizontalnuyu nagruzki s uchetom tekhnologii ikh izgotovleniya: dis. … kand. tekhn. nauk [Bearing capacity of drill-injection piles for vertical and horizontal loads in accordion to their manufacturing technology: dissertation … candidate of technical sciences]: 05.23.02. Sankt-Peterburg, 2007. (rus)

27. Malinin, A.G. Miksernaya stantsiya dlya struynoy tsementatsii gruntov [Mixing station for soils jet cementation]. Transportnoye stroitelstvo. 2008. No. 9. Pp. 27–30. (rus)

28. International standard of Commonwealth of Independent States GOST 5180-2015. Grunty. Metody laboratornogo opredeleniya fizicheskikh kharakteristik [Soils. Laboratory methods for determination of physical characteristics]. (rus)

29. International standard of Commonwealth of Independent States GOST 12248-2010. Grunty. Metody laboratornogo opredeleniya kharakteristik prochnosti i deformiruyemosti [Soils. Laboratory methods for determining the strength and strain characteristics]. (rus)

Contacts:

Ivan Salnyi, salnyy2493@mail.ru

Yakov Pronozin, geofond.tgasu@gmail.com

Alexandr Karaulov, karaulov@stu.ru

Revamp of supporting surfaces of turbogenerating sets foundation frames by composite materials

A.A. Ishchenko[a], T.N. Karpenko[a], V.G. Artiukh[b], N.V. Chernysheva*[b], V.M. Mazur[c]
[a] Pryazovskyi State Technical University, Mariupol, Ukraine
[b] Peter the Great St. Petersburg Polytechnic University, St. Petersburg, Russia
[c] LLC "Saint-Petersburg Electrotechnical Company", Saint-Petersburg, Pushkin
*E-mail: chernat0000@mail.ru

Abstract. Paper shows results of experimental studies of loading capacity of composite material 'Multimetal Stahl 1018' under static and vibrational loads at high temperatures in order to possibly use this material as a leveling layer on supporting surfaces of large-sized units of turbogenerating sets when they are mounted on foundation frames. Tensile strengths of composite samples were obtained at static loading for temperature range +20°C...+80°C on experimental machine 'PM-20'; obtained values do not exceed the maximum compressive stress of the material σ = 160 MPa. Experimental studies have been conducted on a specially created vibration unit because construction of foundation of turbogenerating sets is subjected to vibrations with wide spectrum of frequencies. Parameters of oscillatory process were measured using vibration velocity meter, signals were fixed using ADC 'E 14-140M' and amplifier 'LE-41'; signals processing was performed on 'DSP' processor module. Differential equation of forced oscillations is compiled, amplitudes and dynamics coefficients are determined for constructed dynamic model of vibration unit. Dependence of oscillation amplitude on height of the test samples is presented graphically. Table summarizes values of the dynamic coefficients at different samples heights for the same temperature spectrum as in case of static loads. It was concluded that the dynamic coefficient decreases with increasing temperature for larger height of sample. It was experimentally established that studied composite material withstands dynamic loads significantly exceeding those that can occur when installing turbogenerating sets on foundation frames. This allowed to recommend material 'Multimetal Stahl 1018' for use in installation of turbogenerating sets. Technology has been proposed for revamp of supporting surface of foundation frame in order to perform such works. Industrial tests that were carried out at two thermal power plants when revamping supporting surfaces of foundation frames under turbogenerating set 'TGV 200' and under low pressure cylinder of turbine 'K-20-180 LMP' that confirmed effectiveness of proposed method and its operability.

1. Introduction

Each year many power generating enterprises plan revamping work on equipment of thermal power plants (TPPs) during which large-sized equipment is dismantled and then installed. Necessity to develop new technologies for these works is dictated by facts that installation of heavy equipment of TPPs and multi-stage operation of fitting supporting surfaces are long and laborious processes [1–7] because height of supporting / contact surfaces can differ significantly from design values due to their operation.

What is the reason for changing design level of contact surfaces of foundation frames and, as a consequence, necessity for its restoration in the horizontal plane? Foundation on which foundation frames are installed and fastened depending on design and can experience various loads, e.g. shrinkage cracks may appear in elements of upper reinforced concrete frame foundation which can affect flatness of supporting surface due to uneven shrinkage of concrete during its hardening. In addition, thermal expansion

of turbogenerating sets units can cause their move along plane of foundation frame and can cause wear on contact surfaces. Another reason (and it may be the main one) is vibration loads and subsidence of foundation with significant weight of equipment installed on foundation frame.

As it was shown earlier [8–14] one of ways to solve this problem can be usage of modern composite materials which will qualitatively plan surfaces of foundation frames and protect them from corrosion during operation. The material "multimetall- steel 1018" of the German company Diamant metalplastic GMBH was chosen as the test material, since its modulus of elasticity exceeds the modulus of elasticity of standard similar materials by 2.5 times and is 14 × 103 MPa, while for example, the material "multimetallic-steel standard" has this indicator 6 × 103 MPa. However, the properties of composite materials when operating in conditions close to the operation of turbine units have not previously been studied. Therefore, necessity arises for in-depth study of strength characteristics of composite materials. This task is quite difficult to solve in real operating conditions of equipment of turbogenerating sets. That is why Department of Mechanical Equipment of Ferrous Metallurgical Plants (DMEFMP) of Pryazovskyi State Technical University (PSTU) conducted experimental research in laboratory conditions simulating specific operating conditions.

It is known that design of foundation with reliable mounting of turbogenerating sets must withstand permissible values of deformations and amplitudes of vibrations arising during their operation in addition to significant static loads [15]. Vibration of turbogenerating sets is complex and it is in three mutually perpendicular directions. The most common are vibrations with three frequencies. Vibration prevails with so-called 'reverse' frequency equal to shaft speed. Vibration of doubled revolution frequency occurs during bending anisotropy of rotor when moment of resistance of its cross section changes twice in one revolution. Low-frequency vibration occurs with frequency close to half of reverse frequency. These vibrations are self-sustaining and like oscillations with doubled frequency they cannot be eliminated by ordinary balancing. The most intense vibrations occur when frequency of disturbing forces coincides with frequency of natural vibrations. Vibration of turbogenerating sets is transmitted to their foundation and may cause its subsidence. Therefore, amplitude of loading elements oscillations of foundations (crossbars, beams, racks) is limited to 0.01...0.02 mm. These standards are often violated, e.g. grid of measurements of elevations of foundation frame of low-pressure cylinder at turbogenerating set 'K-300' as a result of operational loads at one of TPPs (refer to Fig. 1).
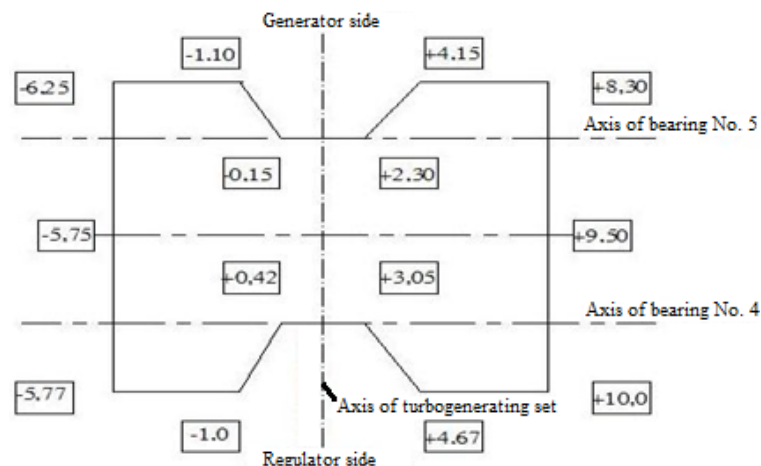
Figure 1. Scheme for measuring vertical coordinates (in mm) of control points on surface of the foundation frame relative to zero level.

First of all, analysis of grid of elevations measurements of the foundation frame indicates that construction of the foundation frame was skewed most likely due to one-sided subsidence of the foundation (from –0.15 mm to –6.25 mm). At the same time, the other side of the turbogenerating set has positive values from +2.3 mm to +10 mm. As a result, further operation of the turbogenerating set with such flatness on the supporting surface leads to additional gaps in connections with the foundation frame and to increase of vibration loads.

Purpose of this work is theoretical and experimental analysis of mechanical strength characteristics of composite material 'Multimetal Stahl 1018' to solve the problem of revamp of the supporting surfaces of turbogenerating sets of TPPs. It is possible to develop a technology for installing turbogenerating sets using the composite material on the basis of obtained results.

Ishchenko, A.A., Karpenko, T.N., Artiukh, V.G., Chernysheva, N.V., Mazur, V.M.

2. Methods

Difficulty in solving problem of reducing amplitude of oscillations is that dynamic stresses that can be determined can only be determined by knowing dynamic coefficient K_d for a specific calculation scheme. Methods for determining mechanical properties of the proposed modern polymeric materials under vibration at different temperatures are also complicated.

Task of estimation of strength characteristics of the material under static conditions was solved by the department staff on experimental machine 'PM-20' with preheating of samples in furnace. Performed experiments allowed to obtain limits of static strength σ of samples which are equal to:

- at t^o = 40°C, σ = 143 MPa;
- at t^o = 60°C, σ = 120 MPa;
- at t^o = 80°C, σ = 111 MPa.

Technical characteristics of this material were obtained at 20°C earlier [16–18] which are equal to:

- maximum compressive stress σ = 160 MPa;
- Young's modulus E = 14·10³ MPa;
- density ρ = 2.4·10⁻⁹ kg/m³.

These results allow the composite material to be used as a leveling element. However, values of stresses under dynamic loading are not known.

That is why special studies were carried out by the second experimental machine for testing under vibration conditions. Scheme of the second experimental machine is shown on Fig. 2. It was manufactured and installed in laboratory of DMEFMP of PSTU. Cylindrical samples with diameter d = 12 mm and height h = 4...8 mm within temperature range +20°C...+80°C and vibration frequency of 100 Hz were tested.
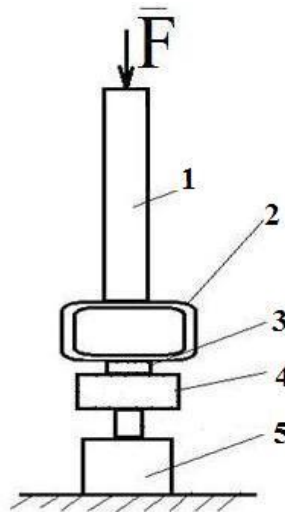
Figure 2. Scheme of the second experimental machine:
1 is pressure screw; 2 is steel ring; 3 is sample; 4 is spacer; 5 is vibration generator.

Parameters of oscillatory process were measured using vibration velocity meter. Signals were fixed using ADC 'E 14-140M' and amplifier 'LE-41'. Signal processing was carried out by programming on a module of digital and signal processor (DSP) produced by company 'Analog Devices'.

3. Results and Discussion

Example of oscillogram of vibration loading the sample with height h = 8 mm at temperature of +40 °C is shown on Fig. 3 where part 2 of the oscillogram is characteristic of stable oscillatory process. Fig. 4 shows graph of dependence of the vibration amplitudes on height of the sample at temperature t^o = 20 °C.

It is advisable to theoretically evaluate effect of dynamic and thermal loads on loading capacity of composite material 'Multimetal Stahl 1018' compared to static load in order to make decisions about possibilities of using the composite material as compensating and leveling layer for foundation frames.

Dynamic coefficient K_d of considered loading cases is determined as a result of theoretical analysis of vibration processes taking into consideration obtained experimental data. According to [19] K_d is equal to:

$$K_d = 1 + \frac{A_{\max}}{\delta_{st}};$$ (1)

where $A_{\max}$ is maximum amplitude, mm;

δ_{st} is static deformation of the sample, mm.

Design scheme of the second experimental machine was used (refer to Fig. 2) to determine A_{max} and δ_{st} for various geometrical parameters of the samples and temperatures under vibration loads.

Differential equation of motion of object has below given view if for generalized coordinate vertical displacement x is taken which is measured from position of static equilibrium:

$$m\ddot{x} + cx = F_{\max} \cdot \sin \omega t$$ (2)

where m is mass of the oscillating object, kg;

m is generalized stiffness coefficient, $\dfrac{N}{m}$;

$F_{\max}$ is amplitude of disturbing force, N;

ω is circular frequency which is associated with oscillation frequency of the vibrator by formula $\omega = 2\pi n$ ($n = 100$ Hz). Amplitude of forced oscillations is equal to (at absence of resonance and according to [19]):

$$A = \frac{F_{\max}}{\left| c - 4m \cdot \pi^2 \cdot n^2 \right|}$$ (3)
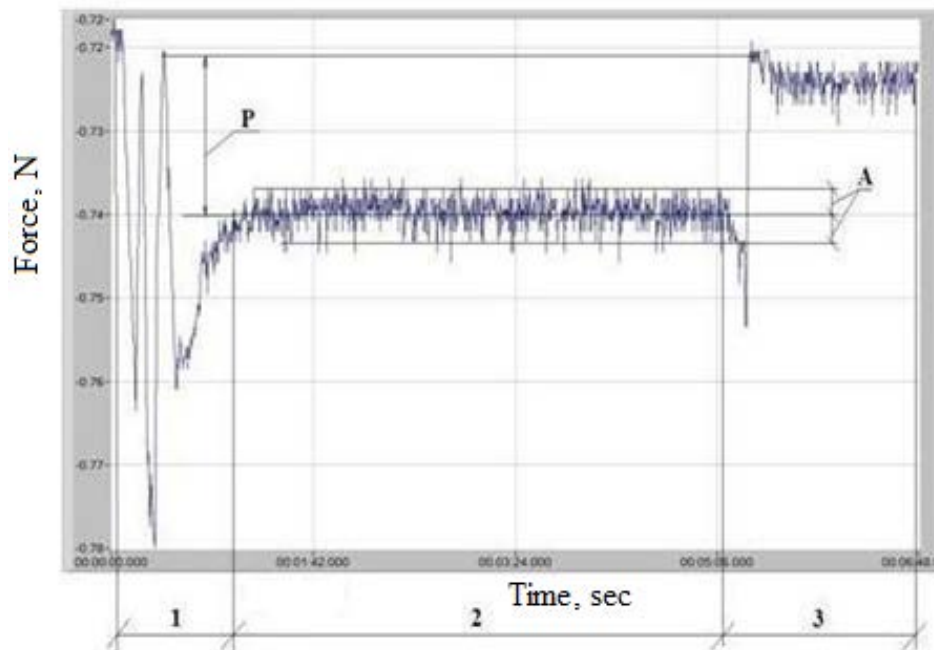
Figure 3. Oscillogram of vibration loading the sample with height
$h = 8$ mm at temperature of +40°C: P is force of preliminary pressing;
2A is amplitude of the load; 1 is area of pre-loading the sample;
2 is area of stable vibration loading; 3 is area of unloading.
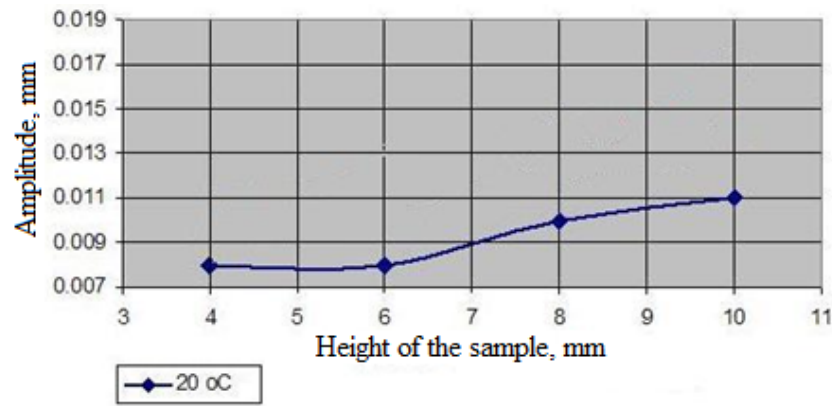
**Figure 4. Graph of dependence of the vibration amplitudes
on height of the sample at temperature t^o = 20°C.**

Values $F_{max} \approx$ 220 N and δ_{st} were determined at different temperatures using oscillograms. Generalized coefficient of rigidity of the second experimental machine c was calculated by formula [19]:

$$\frac{1}{c} = \sum_{i=1}^{4} \frac{1}{c_i}, \tag{4}$$

where c_1, c_2, c_3, c_4 are linear stiffness coefficients of the pressure screw, the steel ring with strain gauges, the sample (made from composite material) and the rubber spacer (refer to Fig. 2).

Stiffness coefficients of the screw and the sample were determined using well-known formulas [19] of linear stiffness coefficients of cylindrical bodies. Stiffness factors of the ring and the spacer were determined experimentally.

Dynamic coefficient K_d at various temperatures were obtained for the sample heights h = 4, 6, 8 mm by the formula (1). Results are presented in Table 1.

Table 1. Values of dynamic coefficients K_d

t,°C — h, mm	40	60	80
4	1.2	1.12	1.09
6	1.15	1.08	1.075
8	1.15	1.056	1.052

As can be seen from Table 1, vibrational loads acting on the composite material within limits of the experiment only slightly reduce allowable ultimate compressive stresses obtained under static loading. It is also clear that the dynamic coefficient decreases with increasing sample temperature and its height. Explanation of this fact (according to (1)), can be as follows: the stiffness coefficient of the sample decreases at higher temperatures that leads to increase in the amplitude of forced vibrations (3) but value of static deformation increases more intensively with increasing sample height than the amplitude.

Obtained results made it possible to develop and introduce at two TPPs technology for revamping supporting surfaces of foundation frames when installing turbogenerating set 'TGV – 200' and a low-pressure cylinder of turbine 'K-20-180 LMP' using composite material 'Multimetal Stahl 1018' instead of known and single way to fit frames by scraping or cladding of surfaces with following machining [12]. The technology for performing such work in general is given below. It is based on example of the low-pressure cylinder (LPC):

− make a test lift of lower half of the LPC by 10–15 mm, make sure that gap between the LPC inlet ports and foundation plates is uniform. Raise the LPC to a height of 500–600 mm, install supports on the foundation plates and lower the lower half of the LPC onto the supports. Make sure that all supports are loaded and that the LPC firmly and stably lays on the supports;

− clean surfaces of the LPC inlet ports from rust and dirt, check by plate and scrap (maximum by 0.5 mm) to eliminate non-flatness of the supporting surfaces. Treat these surfaces with release agent;

− sling the lower half of the LPC, raise it until the supports are released. Remove the supports and lower the lower half of the LPC onto the foundation plates;

- prepare and install adjustment screws;
- raise the lower half of the LPC and install it on the supports. Calculate thickness of applied layer of composite material 'Multimetal Stahl 1018' on the basis of the gaps measurements results;
- mix components of 'Multimetal Stahl 1018' and put its calculated amount in advance in center of place under the inlet ports;
- put and rubbing into the surface (on the foundation plate) adhesive layer of 'Multimetal Stahl 1018' by spatula with some effort;
- apply the next layer to the plates using all 'Multimetal Stahl 1018' prepared for application;
- lowering the LPC into its working place. Lowering should occur smoothly, without jolts. 'Multimetal Stahl 1018' must be laid with excess in gaps so that some of it is extruded from all sides, ensuring uniform filling of the gaps without air bubbles;
- extruded surplus of 'Multimetal Stahl 1018' should be removed by spatula until it is hardened;
- lower the LPC onto the adjustment screws and leave it in this position for 24 hours at +20 ^{0}C.

Surface of the supports is easily formed and composite 'Multimetal Stahl 1018' is evenly distributed in different directions during assembly due to perfectly balanced viscosity of the composite. Thus, ideal fit of the surfaces is achieved without any processing directly on site that is based on excellent shaping of used composite material.

Effectiveness of this method of gaps compensating during installation (which has been repeatedly tested on practice) was also confirmed by The German Institute Of Structural Engineering [20] which in 2013 issued an admission to use composite 'Multimetal Stahl 1018' for complete alignment or filling of irregularities between metal elements of various metal structures in particular for: supporting parts of spans of bridge structures, crane and rail guides, prefabricated steel structures.

4. Conclusions

1. Done experiments show that compressive stresses on the supporting surfaces that occur during operation of turbogenerating sets are much less than those that can withstand composite material 'Multimetal Stahl 1018' without fracture.

2. Obtained results allowed to recommend this material for use as a leveling and aligning spacer between supporting surfaces of turbogenerating sets and foundation frames on which they are installed. Unfortunately, it was not possible to conduct tests of the material in an extreme situation when the frequencies of perturbing forces coincide with the frequency of natural oscillations, since the natural frequencies of the experimental setting $k = 9.53 \times 10^{-3}$ c^{-1}, and the frequency of the perturbing force $\omega = 629$ s^{-1}. At the same time, the study of the material behavior in relation to turbine units does not seem quite relevant, since the resonance mode during their operation is considered unacceptable. Successful implementation of these works at existing TPPs, their subsequent operation are confirmed effectiveness of the proposed method which can be recommended for widespread use.

5. Acknowledgments

References

1. Pestryakov, I.I., Gumerova, E.I., Kupchin, A.N. Assessment of efficiency of the vibration damping material «Teroson WT 129». Construction of Unique Buildings and Structures. 2016. 5 (44). Pp. 46–57.

2. Loginova, I.I., Artamonova, D.A., Stolyarov, O.N., Melnikov, B.E. Effects of structure type on viscoelastic properties of geosynthetics. Magazine of Civil Engineering. 2015. No. 4. Pp. 11–18.

3. Maksarov, V.V., Keksin, A.I. Forming conditions of complex-geometry profiles in corrosion-resistant materials. IOP Conference Series: Earth and Environmental Science. 2018. 194(6):062016. DOI: 10.1088/1755-1315/194/6/062016

4. Kitaeva, D.A., Rudaev, Ya.I., Ordobaev, B.S., Abdykeeva, S.S. Modeling concrete behavior under compression. Applied Mechanics and Materials. 2015. Vol. 725–726. Pp. 623–628.

5. Kukhar, V., Yelistratova, N., Burko, V., Nizhelska, Y., Aksionova O. Estimation of Occupation Safety Risks at Energetic Sector of Iron and Steel Works. International Journal of Engineering & Technology (UAE). 2018. 7 (2.23). Pp. 216–220. DOI: 10.14419/ijet.v7i2.23.11922

Ishchenko, A.A., Karpenko, T.N., Artiukh, V.G., Chernysheva, N.V., Mazur, V.M.

6. Solomonov, K.N. Application of CAD/CAM systems for computer simulation of metal forming processes. Materials Science Forum. 2012. Vol. 704–705. Pp. 434–439.

7. Maniak, I., Melnikov, B., Semenov, A., Saikin, S. Experimental Investigation and Finite Element Simulation of Fracture Process of Polymer Composite Material with Short Carbon Fibers. Applied Mechanics and Materials. 2015. Vol. 725–726. Pp. 943–948.

8. Ishchenko, A., Rassokhin, D., Nosovskaya, E. Experimental study of cavitation destruction of a protective composite polyurethane-based material. Eastern-European Journal of Enterprise Technologies. 2019. 5/12 (101). Pp. 23–28.

9. Artiukh, V.G., Galikhanova, E.A., Mazur, V.O., Kargin, S.B. Energy intensity of parts made from polyurethane elastomers. Magazine of Civil Engineering. 2018. 81(5). Pp. 102–115. DOI: 10.18720/MCE.81.11

10. Ishchenko, A., Artiukh, V., Mazur, V., Poberezhskii, S., Aleksandrovskiy M. Experimental study of repair mixtures as glues for connecting elastomers with metals. MATEC Web of Conferences. 2019. Vol. 265. Pp. 01016. DOI: 10.1051/matecconf/201926501016

11. Artiukh, V., Mazur, V., Kukhar, V., Vershinin,V., Shulzhenko, N. Study of polymer adhesion to steel. E3S Web of Conferences. 2019. Vol. 110. Pp. 01048. DOI: https://doi.org/10.1051/ e3sconf/201911001048

12. Anishchenko, O.S., Kukhar, V.V., Prysyazhnyi, A.H., Agarkov, V.V., Klimov, E.S., Chernenko, S.M. The Material for Physical Simulation of Metal-Forming Processes in Super-Plastic State. IOP Conf. Series: Materials Science and Engineering. IOP Publishing, 2019. Vol. 473(1). Pp. 012040. DOI: 10.1088/1757-899X/473/1/012040

13. Efremov, D.B., Gerasimova, A.A., Gorbatyuk, S.M., Chichenev, N.A. Study of kinematics of elastic-plastic deformation for hollow steel shapes used in energy absorption devices. CIS Iron and Steel Review. 2019. Vol. 18. Pp. 30–34.

14. Glukhov, L.M., Gorbatyuk, S.M., Morozova, I.G., Naumova, M.G. Effective laser technology for making metal products and tools. Metallurgist. 2016. 60 (3-4). Pp. 306–312. DOI: 10.1007/s11015-016-0291-x

15. Ischenko, A.O., Kravchenko, V.M., Dashko, O.V., Kakareka, D.V. New technologies for restoration and protection of power equipment with the aid of composite materials. Energetika. Proceedings of CIS Higher Education Institutions and Power Engineering Associations. 2017. Vol. 60. No. 2. Pp. 160–166.

16. Ishchenko, A., Solek, K., Kalisz, D., Arustamian, A. Analysis of strength characteristics of composite materials under vibration loads at higher temperatures. Journal of Machine Construction and Maintenance – Problemy Ecpluatacij. 2017. No. 1. Pp. 93–97.

17. Kukhar, V., Prysiazhnyi, A., Balalayeva, E., Anishchenko O. Designing of induction heaters for the edges of pre-rolled wide ultrafine sheets and strips correlated with the chilling end-effect. Modern Electrical and Energy System (MEES'2017). Kremenchuk, Ukraine, Kremenchuk Mykhailo Ostrohradskyi National University, 2017. Pp. 404–407. DOI: 10.1109/ME-ES.2017.8248945

18. Ogorodov, L.I., Lustina, O.V. Mechanical characteristics of polyethylene. Magazine of Civil Engineering. 2017. No. 6. Pp. 17–32. DOI: 10.18720/MCE.74.2

19. Artiukh, V.G., Karlushin, S.Yu., Sorochan E.N. Peculiarities of Mechanical Characteristics of Contemporary Polyurethane Elastomers. Procedia Engineering. 2015. No. 117. Pp. 938–944. DOI: 10.1016/j.proeng.2015.08.180

20. Sotnikov, A.L., Sholomitskii, A.A. Monitoring alignment of mold oscillatory motion with CCM process stream axis. Metallurgist. 2017. Vol. 60. No. 9-10. Pp. 1046–1053.

Contacts:

Anatoliy Ishchenko, kafedramz@gmail.com

Taisiya Karpenko, taisktn2013@gmail.com

Viktor Artiukh, artiukh@mail.ru

Natalia Chernysheva, chernat0000@mail.ru

Vladlen Mazur, vladlenmazur@gmail.com

Ishchenko, A.A., Karpenko, T.N., Artiukh, V.G., Chernysheva, N.V., Mazur, V.M.

Experimental characterization
of brick masonry for lateral strength evaluation

I. Khan, M. Ashraf, M. Fahim*
University of Engineering and Technology, Peshawar, Pakistan
*E-mail: drmfahim@uetpeshawar.edu.pk

Keywords: brick masonry, compressive strength, shear strength, mechanical properties, regression analysis

Abstract. Brick masonry in solid clay units and cement-sand mortar is practised in many seismically active regions of Pakistan and also in other South Asian countries like India, Bangladesh, and others. The strength and behavior of brick masonry buildings are predominantly governed by the in-plane response of walls. The mechanical properties of masonry are essential input for the numerical models employed to estimate the in-plane response of brick masonry walls. This paper presents the mechanical properties of masonry constituent materials (brick and mortar) and brick masonry wallets for mechanical characterization. Masonry prisms (9 specimens) in three different mortar mix are tested for compression strength. A new test setup is developed and employed as part of this research study to conduct diagonal tension tests on masonry wallets (12 specimens) in a more stable and convenient position. Empirical relationships are also developed using regression analysis whereby the compressive strength of mortar is related to the compressive strength and diagonal tension strength of brick masonry. The mechanical characterization and the empirical relations will help in future applications in the context of design and assessment studies of brick masonry buildings.

1. Introduction

Brick masonry is one of the most widely used construction technique throughout the world, especially in the underdeveloped and developing countries. Brick masonry in solid clay units and cement-sand mortar is practiced throughout Pakistan and also in other South Asian countries like India, Bangladesh, and others. Unreinforced masonry (URM) has experienced major damages and collapses in the past earthquakes causing significant casualties and property loss [1–4]. After Kashmir earthquake of 2005, brick masonry has been extensively investigated experimentally at the Civil Engineering Department, University of Engineering and Technology, Peshawar, Pakistan [5–8]. However, there is a dire need for the development of analytical and numerical tools for the analysis and design of brick masonry structures. Mechanical characterization is an essential first step towards the development of more reliable numerical tools.

The behavior of unreinforced masonry material under lateral loads is dramatically different than steel and concrete due to its composite nature. The factors affecting the performance and behavior of unreinforced masonry structure are geometry, vertical stress and properties of constituent's material [5, 9, 10]. The mechanical properties of unreinforced masonry as a composite material are functions primarily of the mechanical properties of the individual masonry units, mortars, and the bond characteristics between units and mortar. Since the simplified hypotheses employed for concrete and steel cannot be utilized for brick masonry, the mechanical characterization of masonry can be performed through experimental investigations.

In brick masonry, when the connections at orthogonal walls and at floor-to-wall is properly achieved, the lateral loads are primarily resisted by in-plane response of walls [11, 12]. Many analytical models are available to estimate the in-plane response of brick masonry walls [12–16]. The mechanical properties of masonry are essential input for all these models. This paper presents mechanical properties of masonry constituent materials (brick and mortar) and brick masonry wallets for mechanical characterization. The

paper also discusses the development of empirical relationships using regression analysis whereby the compressive strength of mortar is related with the compressive strength and diagonal tension strength of brick masonry. The mechanical characterization and the empirical relations will help in future applications in the context of design and assessment studies of brick masonry buildings.

2. Methods

The mechanical properties of masonry constituent materials were determined first, followed by compression and diagonal compression tests of masonry prims. Four types of tests were conducted on masonry units i.e. compressive strength of full unit, compressive strength of half unit, water absorption, and flexural tensile strength. The tests were performed following procedures specified in American Society of Testing and Materials (ASTM C-67). The most common ratio of cement sand mortar ranges from 1:4 to 1:8 in the prevailing masonry construction in Pakistan. Therefore, three different mortars with ratios 1:4, 1:6, and 1:8 were tested in compression according to ASTM C109.

Compression tests were conducted on masonry prisms of size 16 in. × 19 in. × 9 in. according to ASTM C 1314-03b as shown in Fig. 1. A total number of 9 prims were fabricated in running bond. However, one prism prepared in 1:8 mortar was damaged during handling.

Figure 1. Test setup for compressive strength of masonry prisms.

Tests were performed on masonry panels of size 48 in. × 48 in × 9 in. for the estimation of diagonal tension strength according to ASTM E519-02. The general practice is to fix the panel diagonally in two vertical jaws and the load is applied in vertical direction. However, as part of this research study, a new test setup was developed where the specimen are placed in a more stable horizontal position and the load is applied along the diagonal in an inclined direction as shown in Fig. 2.
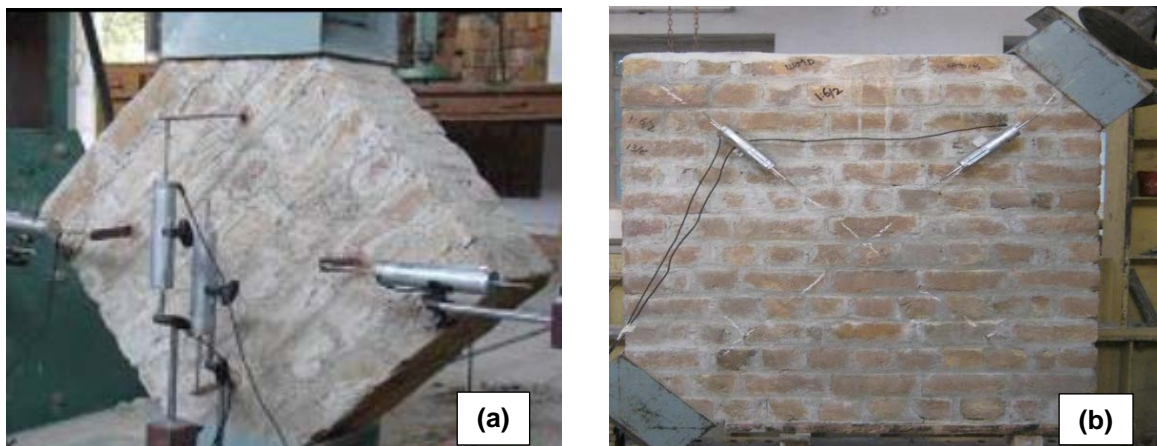
Figure 2. Test setup (a) previously used (b) newly developed.

3. Results and Discussion

3.1. Compressive Strength of Full Units

The results of compressive strength of full brick units are given in Table 1. The average value obtained for compressive strength is found to be 3194 psi and the coefficient of variation is found to be 16 %.

Table 1. Compressive strength of masonry units.

Sample No.	Length (in)	Width (in)	Area (in2)	Maximum Load (Tons)	Strength (psi)	Mean (psi)	COV (%)
1	9.00	4.25	38.25	25.8	1487		
2	8.75	4.12	36.09	41.7	2546		
3	8.75	4.12	36.09	63.3	3865		
4	8.62	4.06	35.04	63.5	3994	3194	15.88
5	8.50	4.06	34.53	62.9	4015		
6	8.75	4.00	35.00	35.4	2229		
7	8.75	4.12	36.09	53.4	3261		
8	8.62	4.06	35.04	66.1	4158		

The average compressive strength of masonry units found in various research studies conducted at University of Engineering and Technology, Peshawar is given in Table 2.

Table 2. Compressive strength of masonry units obtained during local research work.

S.No.	Title of Research Topic	Mean Compressive Strength of Unit (psi)	COV (%)
1	To Study the Modulus of Rigidity of Local Brick Masonry System [17]	2452	22.89
2	Seismic Risk Assessment of Unreinforced Brick Masonry Building System of Northern Pakistan [7]	3200	23.4
3	Performance Behavior of Confined Brick Masonry Building Under Seismic Demand [18]	2338	25
4	Seismic Risk Assessment of Buildings in Pakistan (Case Study Abbottabad City) [19]	1803	26.7
5	Development of low cost and efficient Retrofitting Technique for Unreinforced Masonry Buildings [6]	3170	13.8
6	This study	3194	15.88
	Overall Mean compressive strength	2692	21.28

The results obtained by various researchers reveal a significant variation in the compressive strength of masonry units available in the local market. The main reasons are the difference in properties of the raw material used and burning temperature during manufacturing. According to guidelines of Earthquake Rehabilitation and Reconstruction Authority (ERRA) Pakistan, the mean compressive strength of masonry unit should comply with the minimum value of 1000 psi or 6.89 MPa, whereas according to Eurocode-8, the minimum acceptable normalized compressive strength of a masonry unit, normal to the bed face, should be equal or greater than 725 Psi or 5.0 MPa. The results of the previous research work and this research show that the strength of local manufactured brick is quite satisfactory and in compliance with code requirements irrespective of variability in the mean strength.

3.2. Compressive Strength of Half Units

The ASTM standard recommends compressive strength tests to be performed on half unit, although many researchers use full units to find compressive strength of masonry units. Therefore, in this study both full and half bricks were used for finding compressive strength of bricks. The result of compressive strength of half scale brick units are given in Table 3. The mean strength was found to be 2216 psi and coefficient of variation is 28 %.

Table 3. Compressive strength of half masonry units.

Sample No.	Length (in)	Width (in)	Area (in²)	Maximum Load (Tons)	Strength (psi)	Mean (psi)	COV (%)
1	4.3125	4.125	17.79	23.5	2912		
2	4.25	4.125	17.53	23.7	2980		
3	4.3125	4.1875	18.06	13.3	1623		
4	4.4375	4.25	18.86	10.8	1262	2216	27.96
5	4.1875	4.0625	17.01	15.6	2021		
6	4.25	4.125	17.53	21.9	2753		
7	4.375	4.25	18.59	17.7	2098		
8	4.1875	4.25	17.80	16.8	2081		

A comparison of the results obtained for full and half units reveal that the mean strength in the former case is 44 % more than the latter. However, in both cases the mean strength is well above the Building Code of Pakistan recommended minimum limit of 8.25 MPa (1200 psi) [20].

3.3. Water Absorption of Masonry Units

The results of water absorption of the brick specimens carried out according to ASTM C-67 are shown in Table 4. Water absorption is very important parameter which influence masonry and mortar bond significantly. A total of five specimens were tested for water absorption. The mean value for water absorption was found to be 21.36 % and coefficient of variation was found to be 10 %. Farhat [17], Naseer [18] and Shahzada [19] found water absorption for brick units as 19.3 %, 19.33 % and 23.00 % respectively.

Table 4. Water absorption of masonry units.

Sample No.	Dry Weight of Samples (lbs)	Wet Weight of Samples (lbs)	% Absorption	Mean	% CV
1	5.757	6.797	18.1		
2	5.761	6.956	20.7		
3	5.885	7.198	22.3	21.36	10 %
4	6.114	7.555	23.6		
5	6.422	7.842	22.1		

The absorption of brick greatly influence the tensile and shear bond strength of the masonry. The highly absorptive unit has lesser strength due to that fact that brick unit absorb water from mortar layer after laying and leaves small amount of water for cement hydration which results in weak mortar formation and consequently in the weakening of masonry. The recommended value of water absorption for first class brick is not more than 20 %. Hence mean value of water absorption of local manufactured brick is almost equal to the recommended value.

3.4. Flexural Tensile Strength of Masonry Units

The tests for flexural tensile strength of brick specimens was carried out according to section 6 of ASTM C-67. The results are shown in Table 5. The mean value for tensile strength was found to be 913 psi whereas the coefficient of variation was 34 %. Ashraf [6] and Shazada [19] obtained the values of flexural tensile strength of masonry units as 919 psi and 479 psi respectively.

Table 5. Flexural tensile strength of masonry units.

Sample No.	Size (in)	Ultimate Vertical Load (Ton)	Section Modulus (in³)	M_{cent} (lb.in)	Flexure tensile strength (psi)	Mean (psi)	COV (%)
1	9×4.25×3	0.98	6.4	4320	678		
2	8.69×4.12×3.0	1.65	6.2	6989	1130		
3	8.88×4×2.75	1.56	5.0	6769	1343	913	34 %
4	9×4.25×3.0	1.16	6.4	5113	802		
5	9×4.25×3.0	0.89	6.4	3923	615		

3.5. Compressive Strength of Mortar

In order to obtain a workable mortar, water cement ratio was determined taking into account the moisture content of sand. Gradation curves for two sand samples are shown in Fig. 3 and 4. The fineness modulus of sand in all tests was found in the ASTM recommended range of 2.3 to 3.1. Hence the sand is well graded for mortar preparation.
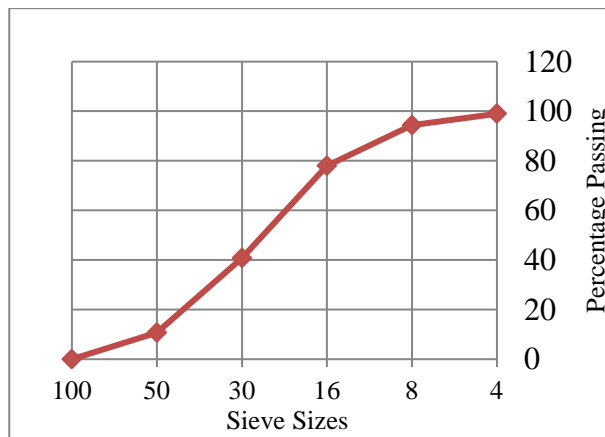
Figure 3. Gradation curve for sand sample 1.
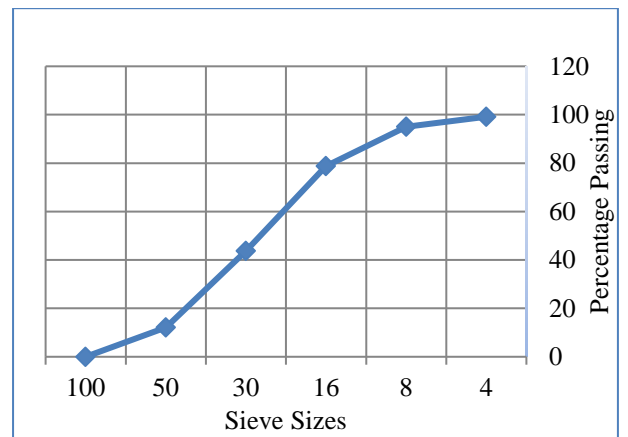
Figure 4. Gradation curve for sand sample 2.

Mortar cubes of size 2" x2"x2" were prepared with specified ratio of mortar using the determined water cement ratio. The average compressive strengths were found to be 1961 psi, 840 psi, and 311 psi as shown in Fig. 5. These results show a significant increase in mortar strength with the increase in cement content.
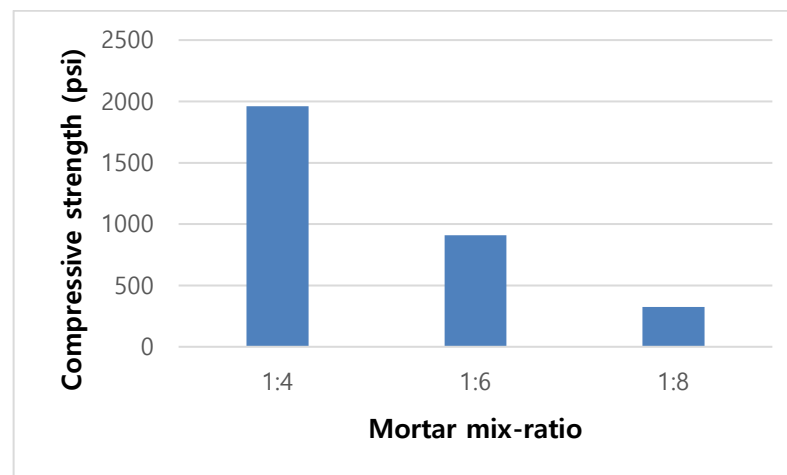
Figure 5. Mean compressive strength (28 days) of mortar cubes.

3.6. Compressive Strength of Masonry Prism

The average compressive strengths were found to be 518, 586 and 408 psi for 1:4, 1:6, and 1:8 mortars respectively as given in Table 6. Surprisingly, the compressive strength of prims in 1:6 mortar was more than the ones in 1:4 mortar.

Table 6. Compressive strength of masonry prisms.

Mortar mix Ratio	W/C Ratio	No	Area (in²)	Maximum Load (Tons)	Strength (psi)	Mean (psi)	COV (%)
1:4	1	1	135.78	27.6	448	518	22 %
		2	137.38	28.5	457		
		3	135.11	39.8	649		
1:6	1.5	1	139.18	32.6	516	586	13 %
		2	136.82	35.5	572		
		3	137.53	41.8	670		
1:8	1.8	1	140.86	23.6	369	408	13 %
		2	138.74	28.1	446		

The compressive strength of masonry has also been investigated by various other researchers at UET Peshawar, Pakistan. The results are summarized in Table 7.

Table 7. Mean compressive strength of masonry obtained during local research work.

S. No.	Title of Research Topic	Mortar Type	Mortar Mix Ratio	Mean Compressive Strength (psi)
1	To Study the Modulus of Rigidity of Local Brick Masonry System [17]	Cement Sand (CS)	1:4	655
			1:6	575
			1:8	525
			1:10	395
		Cement Khaka (CK)	1:4	781
			1:6	719
			1:8	685
			1:10	532
		Cement Sand Khaka (CSK)	1:2:2	685
			1:3:3	648
			1:4:4	628
			1:5:5	516
2	Seismic Risk Assessment of Unreinforced Brick Masonry Building System of Northern Pakistan [7]	CSK	1:4:4	658
3	Performance Behavior of Confined Brick Masonry Building Under Seismic Demand [18]	CSK	1:4:4	839
4	Seismic Risk Assessment of Buildings in Pakistan (Case Study Abbottabad City) [19]	CS	1:6	438
5	Development of low cost and efficient Retrofitting Technique for Unreinforced Masonry Buildings [6]	CS	1:8	656

3.7. Diagonal Tension Tests of Masonry Prism

Diagonal tension test setup is used based on the assumption that pure shear is introduced in the specimen and the specimen cracks when the principal stress at the center of specimen reaches tensile strength of masonry. However, due to non-uniformity of stresses, the specimen is not under pure shear [21, 22]. Therefore, the analytical relation developed by Magenes et al. [22] is used to estimate the diagonal tensile strength of the specimens.

$$f_t = \frac{0.5P}{t(l_1 + l_2)} \tag{1}$$

where f_t denotes diagonal tensile strength, P is the maximum applied load, l_1 and l_2 are lengths of the two sides of the specimen, and t is the thickness of specimen. A total number of 12 specimens were tested for tensile strength estimation and the results are given in Table 8.

Table 8. Shear strength of masonry prisms.

Sample Size	Mortar mix Ratio	No	Shear Strength (psi)	Mean strength (psi)	COV (%)
48" × 48"	1:4	1	41.35	33.66	20
		2	31.28		
		3	28.35		
48" × 48"	1:6	1	20.71	26.16	38
		2	20.00		
		3	37.78		
48" × 48"	1:8	1	28.38	19.36	40
		2	14.84		
		3	14.85		
29" × 27"	1:6	1	30.40	32.46	11
		2	30.28		
		3	36.71		

The typical damage patterns during diagonal tension tests are shown in Fig. 6. The crack at failure follows bed and head joints of masonry. This implies that mortar and the bond strength between mortar and bricks contribute significantly to the masonry strength. Specimens in mortar mix 1:6 were tested in two different sizes, namely 48" × 48" and 29" × 27". The mean shear strength was found to be 24 % higher in case of smaller specimens.

Figure 6. Typical damage pattern during diagonal tension tests.

4. Empirical Relationships for Mechanical Properties of Masonry

The mechanical properties of masonry (compressive and tensile strength) obtained experimentally are related to the compressive strength of mortar in order to develop simple empirical relationships for future applications.

4.1. Mortar Strength to Compressive Strength of Masonry

The mortar compressive strength is correlated with the masonry compressive strength using past data and results obtained in this study. The mean mortar compressive strength for a particular mix ratio is plotted against mean compressive strength of masonry as shown in Fig. 7. The past data of Shah [17], Shazada [19], and Ashraf [6] have been plotted. Linear regression analysis is used to develop an empirical relationship between mortar compressive strength and masonry compressive strength as:

$$f_{mc} = 0.0881 f_m + 451.91 \qquad (2)$$

where f_{mc} is masonry compressive strength (psi) and f_m is mortar compressive strength (psi).
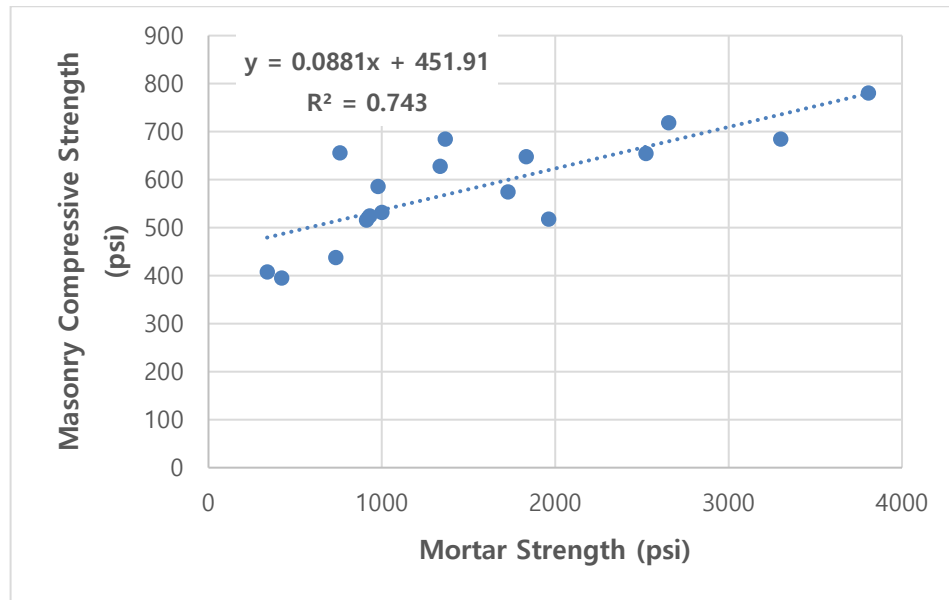
Figure 7. Relation between mortar strength and masonry compressive strength.

4.2. Mortar Strength to Masonry Tensile Strength

The mortar compressive strength is correlated with the masonry diagonal tension strength using past data [19] and results obtained in this study. The mean mortar compressive strength for a particular mix ratio is plotted against mean diagonal tension strength of masonry as shown in Fig. 8. Linear regression analysis is used to develop an empirical relationship between mortar compressive strength and masonry diagonal tension strength as:

$$f_t = 0.0085 f_m + 18.79 \qquad (3)$$

where f_t is masonry diagonal tension strength (psi) and f_m is mortar compressive strength (psi).
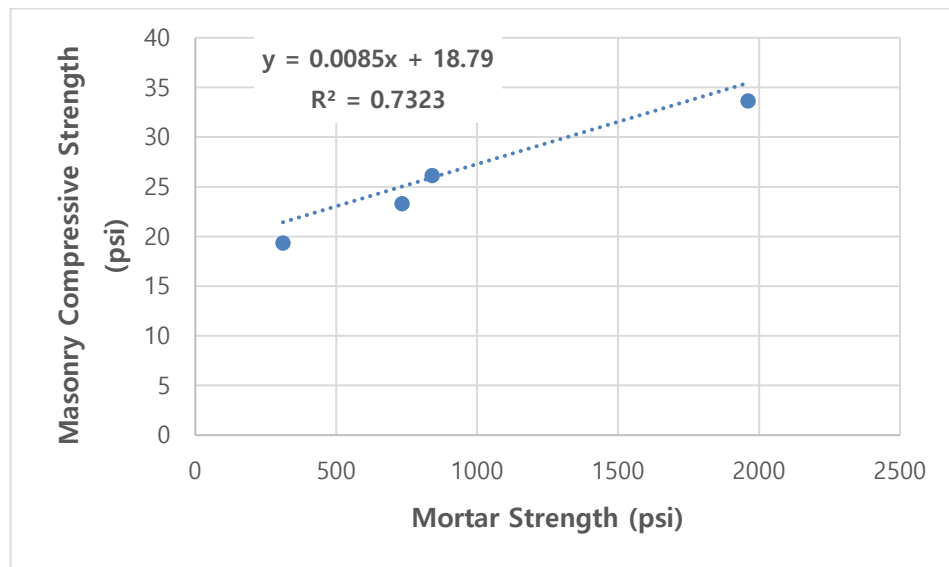
Figure 8. Relation between mortar strength and masonry tensile strength.

5. Conclusions

The following conclusions can be derived based on the results obtained in the experimental part of this study.

1. The mean compressive strength of masonry units (3706 psi for full units and 1928 psi for half units) is well above the minimum recommended values of national and international building codes. However, there is a large variation in the compressive strength of commonly used mortar (1961 psi for 1:4

mortar and 311 for 1:8 mortar). Therefore, the masonry strength is generally governed by the strength of mortar and the bond between mortar and masonry units.

2. The past practice for diagonal tension tests was to fix the masonry wallets diagonally in two vertical jaws and the load was applied in the vertical direction. However, as part of this research study, a new test setup was developed where the specimen are placed in a more stable horizontal position and the load is applied along the diagonal in an inclined direction. The new test setup was successfully used for diagonal tension tests of 12 specimens.

3. Masonry compressive strength and diagonal tension strength decreases with increase of sand proportion in mortar mix. The mean compressive strength is decreased by 21.24 % for specimens in 1:8 mortar as compared to specimens in 1:4 mortar. Similarly, the mean diagonal tension strength is decreased by 42.48 % for specimens in 1:8 mortar as compared to specimens in 1:4 mortar.

4. Two empirical relationships are developed correlated mortar compressive strength with masonry compressive strength and diagonal tension tests.

References

1. Durrani, A.J., et al. The Kashmir Earthquake of October 8, 2005: A Quick Look Report. 2005: Mid-America Earthquake Center, University of Illinois at Urbana-Champaign.

2. EERI, The Kashmir earthquake of October 8, 2005: Impacts in Pakistan. 2006: Earthquake Engineering Research Institute, Oakland, California, United States.

3. Javed, M., Khan, A.N., Magenes, G. Performance of masonry structures during earthquake-2005 in Kashmir. Mehran University Research Journal of Engineering and Technology. 2008. 27(3). Pp. 271–282.

4. Naseer, A., Khan, A., Hussain, Z., Ali, Q. Observed seismic behavior of buildings in Northern Pakistan during the 2005 Kashmir earthquake. Earthquake Spectra. 2010. 26. DOI: 10.1193/1.3383119

5. Ali, Q. Seismic Performance Study of Brick Masonry Building Systems in Peshawar Region. Civil Engineering Department. 2004. University of Engineering and Technology: Peshawar, Pakistan.

6. Ashraf, M. Development of Low-cost and Efficient Retrofitting Technique for Unreinforced Masonry Buildings. Civil Engineering Department. 2010. University of Engineering and Technology: Peshawar, Pakistan.

7. Javed, M. Seismic Risk Assessment of Unreinforced Brick Masonry Buildings System of Northern Pakistan. Civil Engineering Department. 2009. University of Engineering and Technology: Peshawar, Pakistan.

8. Shahzada, K., Kahn, A.N., Elnashai, A., Ashraf, M., Javed, M., Naseer, A. Experimental seismic performance evaluation of unreinforced brick masonry buildings. Earthquake Spectra. 2012. 28(3). Pp. 1269–1290. DOI: 10.1193/1.4000073

9. Ashraf, M., Akhtar, N., Khan, A., Ali, Q., Shahzada, K., Naseer, A. Experimental Behavior of Full Scale URM Building Retrofitted with Ferrocement Overlay. Advanced Materials Research. 2011. Pp. 255–260.

10. Dizhur, D., Jiang, X., Qian, C., Almesfer, N., Ingham, J. Historical development and observed earthquake performance of unreinforced clay brick masonry cavity walls. SESOC Journal. 2015. 28. Pp. 55–67.

11. Magenes, G. Masonry building design in seismic areas: Recent experiences and prospects from a European standpoint. 2006.

12. Tomazevic, M. Earthquake-Resistant Design of Masonry Buildings. Earthquake-Resistant Design of Masonry Buildings. 1999.

13. Abrams, D.P. Performance-based engineering concepts for unreinforced masonry building structures. Progress in Structural Engineering and Materials. 2001. 3(1). Pp. 48–56.

14. CEN, Eurocode 6: Design of masonry structures. (n.d.). DOI: 10.3403/bsen1996-1. 1994, Comité Européen de Normalisation: Brussels, Belgium.

15. FEMA, Prestandard and Commentary for the Seismic Rehabilitation of Buildings. 2000, Federal Emergency Managment Agency (FEMA): Washington, DC, USA.

16. Magenes, G., Calvi, G.M. In-plane seismic response of brick masonry walls. Earthquake Engineering & Structural Dynamics. 1997. 26(11). Pp. 1091–1112.

17. Banori, F.A.S. To Study the Modulus of Rigidity of Local Brick Masonry System. Department of Civil Engineering. 2006. University of Engineering and Technology, Peshawar, Pakistan.

18. Naseer, A. Performance Behavior of Confined Brick Masonry Buildings under Seismic Demand. Civil Engineering Department. 2009. University of Engineering and Technology: Peshawar, Pakistan.

19. Shahzada, K. Seismic Risk Assessment of Buildings in Pakistan (Case Study Abbottabad City). Department of Civil Engineering. 2011. University of Engineering and Technology, Peshawar, Pakistan.

20. BCP/SP-07, Building Code of Pakistan (Seismic Provisions - 2007). 2007, Government of Islamic Republic of Pakistan, Ministry of Housing & Works, Islamabad, Pakistan.

21. Brignola, A., Frumento, S., Lagomarsino, S., Podestà, S. Identification of shear parameters of masonry panels through the in-situ diagonal compression test. International Journal of Architectural Heritage. 2008. 3. Pp. 52–73. DOI: 10.1080/15583050802138634

22. Magenes, G., Penna, A., Galasco, A., Rota, M. Experimental Characterisation of Stone Masonry Mechanical Properties. 8th International Masonry Conference Dresden. 2010. Pp. 247–256.

Contacts:

Imtiaz Khan, engrimtiaz84@gmail.com

Mohammad Ashraf, mashraf@uetpeshawar.edu.pk

Muhammad Fahim, drmfahim@uetpeshawar.edu.pk

Dynamic tests and monitoring of the dynamic state of buildings and structures based on microseismic vibrations

E.A. Khoroshavin
Krasnoyarsk Institute of Railway Transport - branch Irkutsk State Transport University, Krasnoyarsk, Russia
* E-mail: zkpd2007@ya.ru

Abstract. The article considers organizing and conducting dynamic testing of a multi-story residential panel building in Krasnoyarsk. For dynamic testing, a hardware-software complex was developed that implements the standing wave method, allowing to determine the dynamic characteristics of a building by registering microseismic vibrations of building structures. The dynamic test results determined actual natural (resonant) frequencies and their oscillations modes for the building structures. From the analysis of the distribution of the peak values of the amplitudes of natural vibrations, we determined the dangerous zones of the occurrence of destructive processes in the soil of the base of the building, affecting its safe functioning.

1. Introduction

The study of the technical condition of building structures is an independent area of construction activity, covering a number of issues related to the creation of normal working and living conditions of people in buildings and structures and ensuring the operational reliability of buildings and structures. Assessment of the technical condition of buildings and structures on the basis of the standard² is determined by instrumental examination methods that allow obtaining objective and sufficient information about the properties of materials, the behavior of structures and the actual operation of the structure [1–4]. Known methods of non-destructive testing and diagnostics of the state of building structures of buildings and structures (mechanical, ultrasonic, etc.) make it possible to determine the physic mechanical properties of concrete, reinforced concrete or metal structures, as well as the state of foundation of foundations of structures in a limited measurement area and to carry out defectoscopy of building structures. To determine the integral strength characteristics of building structures of buildings and structures, these methods are generally unsuitable.

Existing systems for assessing and monitoring buildings and structures in the Russian Federation and abroad, created by individual ministries and departments on a sectoral basis, also do not satisfy the modern security requirement. They do not provide the necessary accuracy in determining the parameters of the technical condition, do not allow combining the monitoring of technical condition with the registration of earthquakes at objects located in seismically dangerous areas. Currently there is no single system for assessing and monitoring the technical condition of buildings and structures to ensure their safe operation [5–16].

Experimental methods for studying the vibrations of buildings and structures (dynamic tests) have been and continue to be an effective research tool for modern building science [17–26], since the parameters determined during these studies are it is an individual set of parameters of the dynamic characteristics of natural vibrations inherent in each building and structure. They depend on the properties of the soil at the base of the building, on the structural design of the building, workmanship, characteristics

of the material and structures, on existing defects, i.e. from the set of components that determine the bearing capacity of structures and allow to evaluate its technical condition.

Research methods for the natural vibrations of buildings can be divided:

1. Impact testing;

2. Testing by pulling (quick release of load);

3. Tests of buildings and structures with powerful vibrators mounted on the roof;

4. Vibration testing of buildings and structures with a source located outside of buildings and structures;

5. Studies of fluctuations of buildings and structures under the influence of industrial explosions and special explosions in lakes;

6. Studies of the reactions of buildings and structures to earthquakes;

7. The study of buildings and structures based on the study of microseismic vibrations.

Each of the mentioned methods has its advantages and disadvantages and with one degree or another solves the tasks assigned to it [27–39].

The study of buildings using microseismic noise has always been attractive because there is no cost to excite vibrations. The cheapest method, however, it was commonly believed that the results obtained with microseismic noise are inferior in accuracy to all other methods. With the advent of high sensitivity sensors (from 100 mV/(m/s²)) and digital signal processing, it became possible to register and isolate building vibrations arising from the action of a load applied to its structures, the intensity of which is comparable to the background from natural microseisms. This stimulated the development and creation of modern mobile diagnostic systems [40–44]. Such diagnostic complexes of the All-Russian Research Institute of Civil Defense and Emergencies as "Struna" and "Strela", which are actively used to assess seismic resistance and diagnostics of buildings and structures. A distinctive feature of dynamic tests using these complexes is the registration of microoscillations of the objects under investigation (from fractions of millimeters to several millimeters), which has been known for a long time, but until recently its use was limited both by the capabilities of the recording equipment and sensors and by the level of processing the received signal. This method was called the method of free oscillations.

The methodology for determining the dynamic characteristics of building structures by their free vibrations excited by the action directly on the structure external pulse load, includes the following operations:

- arrangement of measuring sensors on structures;

- excitation and registration of oscillations;

- calculation of their Fourier spectra;

- analysis of Fourier spectra in order to isolate resonant peaks corresponding to various forms of free vibrations;

- obtaining, using the inverse Fourier transform, pulsed implementations of the selected resonant peaks for each form of free oscillations;

- identification and graphic representation of various forms of vibrations.

Roughly speaking, this technique is a measurement of the characteristics of a linear system as a result of a reaction to a broadband effect in the form of a δ-function or step. The idea is reasonable, widely used in practice in the study of linear systems [2, 3, 11, 13, 26]. The disadvantage is the low detail of the data and the low accuracy of the results.

Another method, called the standing wave method, was developed by the Geophysical Service of the Siberian Branch of the Russian Academy of Sciences (GS SB RAS, Doctor of Engineering A.F. Emanov) [17–19, 45] for a detailed study of the physical condition of buildings and structures at the level of structural elements. Unlike other methods, this method uses the natural vibrations of many frequencies. The only method that determines the phase parameters of the field of standing (natural) waves. Studying the field of standing waves with any detail makes it possible to obtain information about local hidden defects in the structure.

The idea of the method is that a small number of sensors moving in space that record microseismic vibrations determine their own (standing) waves with the required detail in buildings or engineering structures of any complexity. In other words, using small-channel equipment (using ten sensors), large

engineering structures (hydroelectric power stations, bridges, high-rise buildings, etc.) can be examined [43, 47–51].

The essence of the method is to determine the field of its own (standing) waves of the structures of the structure. It is these vibrations that characterize the internal structure of the building and the state of its structures. The natural vibrations of a building are a set of standing waves, the dynamic characteristics of which are individual for each building and do not depend on time or on external influences. They are the reaction of the object to any external influences that come to it through the foundation (microseisms) or walls (wind load). The dynamic properties of buildings and structures are determined by the properties of the underlying soil and foundation, the mass and elastic characteristics of structures, the type and quality of the connection of individual blocks, parts and elements of buildings and structures. A change in these properties over time during operation leads to corresponding changes in the parameters of the dynamic characteristics of vibrations of buildings and structures. An analysis of the obtained frequency, amplitude and phase characteristics of the wave field of the object allows us to establish the presence of changes in the properties of the soil of the base and defects in the structure of the object that arise during its operation, and also allows you to get estimates of the technical condition of the object. This technology is unique and has no analogues abroad.

The purpose of this study, as a result of dynamic testing of a building based on the standing wave method, is:

- Determination of the main dynamic characteristics of the building (frequencies and forms of natural vibrations, amplitudes and phases, characteristics of the damping of oscillations) on a dense measurement system;

- Obtaining a distribution of the dynamic characteristics of natural vibrations among structural elements of a building;

- Identification of hazardous areas and weaknesses (defects and cracks) in the building;

- Obtaining a detailed (with the required degree of detail) reliable picture of the technical condition of the building.

The technology for conducting dynamic tests of a building based on the standing wave method requires solving the following problems:

- Definition of the arrangement of recording sensors;

- Conducting sequential registration of seismic micro-noise with low-channel equipment on all load-bearing structural elements of the building. Registration is carried out continuously in one or more reference points;

- Processing of registration data of microseismic vibrations of building structures, which is performed on the basis of the standing wave recalculation methodology (GS SB RAS, A. F. Emanov) [19, 22]. As a result of processing the micro-noise records, for the object being examined, simultaneous records of standing waves are obtained from simultaneous consecutive observations with reference points;

- Building a 3D geographic information system (GIS) - a model for representing the amplitudes and phases of the natural oscillation fields of a building and its structural elements;

- Construction of coherence spectra and error spectra to highlight the natural frequencies of the parameters of the field of standing (natural) waves and their modes of vibration, allowing to identify defects and weaknesses in the building structures;

- Analysis of the distribution of the dynamic parameters of the wave field over the structural elements of the building to assess the technical condition of the building.

2. Methods

The studies were conducted in the hostel No. 22 of the Siberian Federal University. The dormitory building consists of four reinforced concrete panel sections and a monolithic public block connecting interconnected panel double sections. In the first section of the hostel, during its operation, cracks appeared in the interface nodes of structural elements along the entire height of the building. Dynamic tests were carried out as part of the inspection and monitoring of the technical condition of the building to assess the possibility of its further trouble-free operation or the need for its restoration and strengthening of structures. For dynamic testing, a hardware-software complex was developed that implements the standing wave method [25, 42, 43, 51].

Microseismic vibrations of the dormitory building structures were recorded using the Standing Waves Method (MSW-1) mobile diagnostic complex, which is a multi-module system of 10 three-component recorders of the Baikal-ASN8 extended frequency range (Figure 1). Table 1 presents its technical characteristics.

Table 1. Technical characteristics of the Baikal-ASN8 microseismic oscillation registration system.

No	Characteristic	Units rev.	Value
1	The number of channels of one module		3
2	Data capacity	Bit	24
3	Input Type		differential
4	Input impedance	Ком	20
5	Max. sampling frequency	Hz	16000
6	Working frequency band (- 3 dB)	Hz	4000
7	Reference Generator Stability		2*10-8
8	Power consumption	Wat	<0.5
9	Диапазон рабочих температур	°C	-30 + +60
10	Weight	kg	4.5

Figure 1. Baikal-ASN8 recorders with A1637 sensors.

The recorders have time synchronization via GPS and a USB 2.0 channel for communication with a computer for programming and data transfer. The recorder is powered by built-in batteries. Data microseismic oscillations are recorded on the built-in drive (SD card), followed by transfer to a computer via USB.

The software runs on WindowsXP. The controls allow manual control of the registrar. Three-component accelerometers A-1637 are used as geophones.

The three-component accelerometer (seismic receiver) A1637 (Figure 2) is designed to convert vibrational acceleration into a proportional electrical signal. The seismic receiver is used as a primary transducer in the composition of seismic and vibration measuring systems and complexes, and can also be used in various fields of science and technology when measuring (recording) low-frequency low-level vibration parameters.

Figure 2. General view of the A1637 seismic receiver.

Khoroshavin, E.A.

The scope of the A1637 seismic receiver: seismic exploration, control of vibrations of buildings and structures, as well as vibration of turbines and shafts of power plants.

Normal conditions for the use of a seismic receiver:

- ambient temperature from 18 to 25 °C;

- relative air humidity from 45 to 80 %;

- atmospheric pressure from 84 to 106.7 kPa;

- sound pressure level of acoustic fields no more than 60 dB;

- power supply voltage of the seismic receiver ± (12 +0.5) V;

- instability of supply voltage no more than 0.5%;

- voltage ripple no more than 1 mV.

Operating conditions for use:

- ambient temperature from minus 40 to plus 50 °C;

- relative air humidity up to 90% at 30 °C;

- atmospheric pressure from 84 to 106.7 kPa;

- power supply voltage of the geophone + (12 ± 2) V;

- instability of supply voltage no more than 0.5%;

- voltage ripple no more than 1 mV.

Microseismic oscillations were recorded in two stages. The first stage in 2014. Microseismic vibrations of the dormitory building structures were recorded in two sections, in axes I-III (Figure 3) at the attic floor mark and on the floors of the building with a pitch of geophones 3 meters apart.
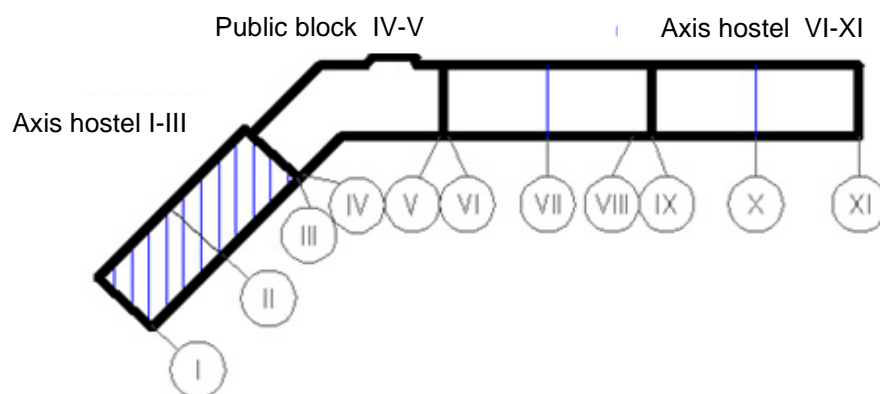
Figure 3. Scheme of the investigated object.

At the attic floor mark, the registration of microseismic vibrations with small-channel equipment was carried out at 120 observation points (Figure 4).
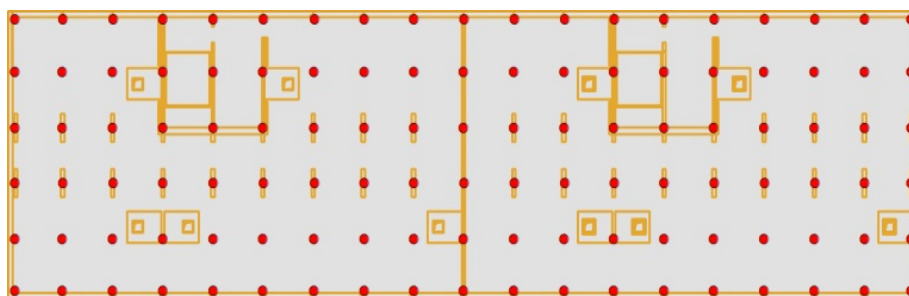
Figure 4. Observation points of microseismic noise at the attic of the hostel in 2014.

Microseismic vibrations with small-channel equipment on the floors of two sections of the hostel were recorded at 180 observation points (Figure 5).
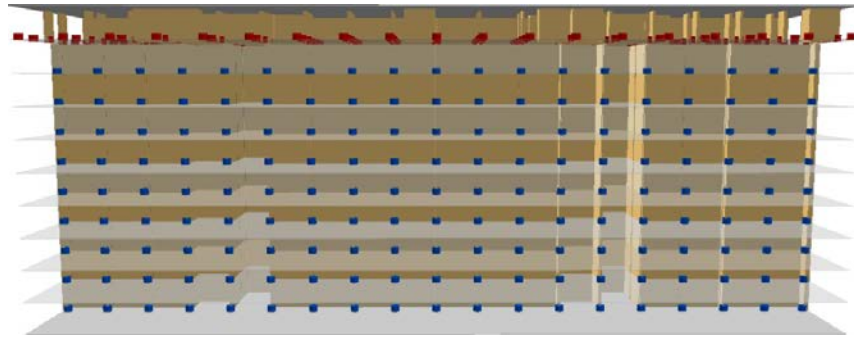
Figure 5. Observation points of microseismic noise on the floors of the hostel in 2014.

The second stage was held in 2015. Re-registration of microseismic vibrations of the dormitory building structures was carried out in axes I-II (Figure 6) at the attic floor mark.
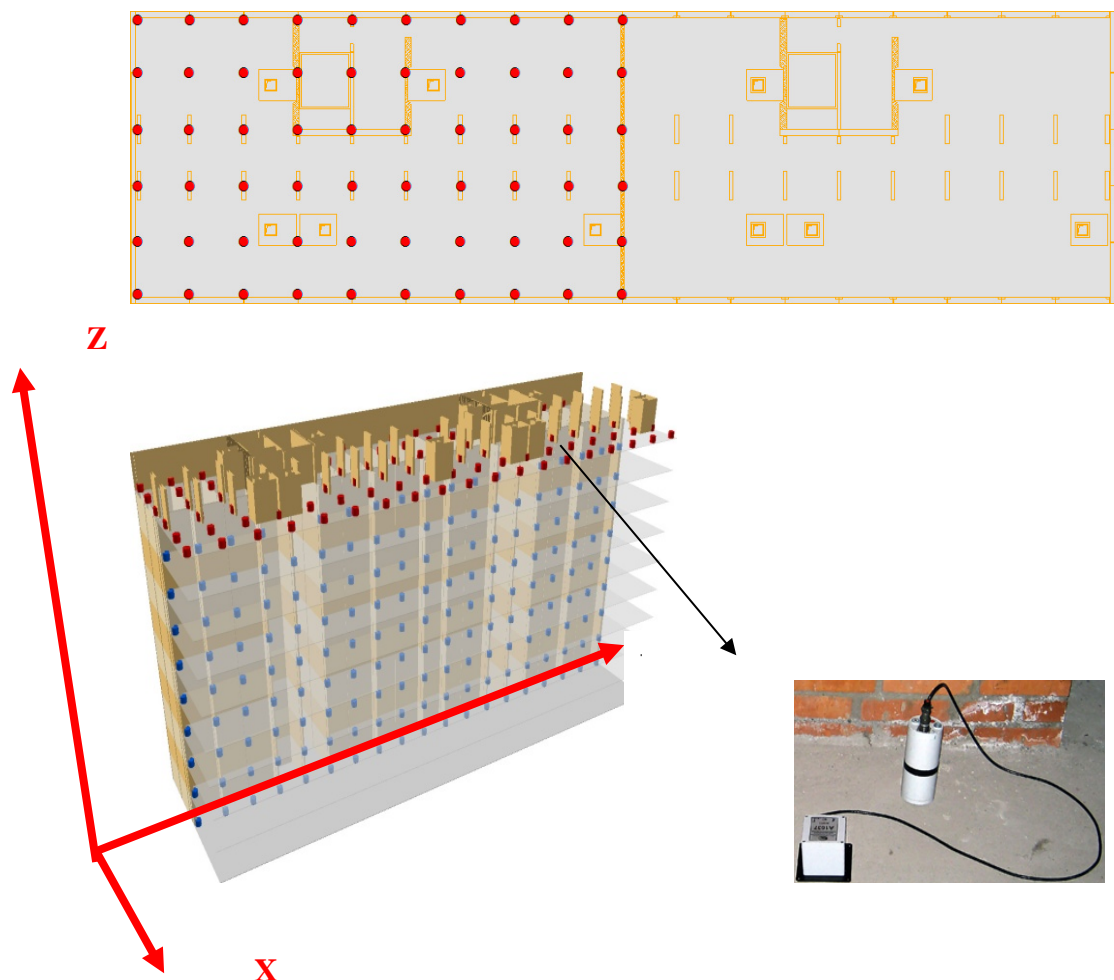
Figure 6. Observation points of microseismic noise at the attic of the hostel in 2015.

To record microseismic noise with small-channel equipment, 10 seismic detectors were used. The registration time was 15 minutes, after which the equipment moved to the following observation points. The sensor at the reference point remains in place during the entire measurement cycle.

As a result of the processing of micro-noise records, obtained simultaneous records of standing waves from different-time, sequential observers with reference points. The processing procedure is reduced to the following operations:

- Primary processing of micro-noise records, open input data for calculating functions between observer points;
- Calculation of vibration functions at reference points with oscillations at each observation point;
- Recalculation of standing waves from reference points to all points of the object being examined.

The oscillations are recorded simultaneously at two reference points and at each i-th (or group of i-x) points in turn. Obtaining simultaneous recordings of standing waves from different time observations

with two reference points is reduced to the following operations. Simultaneous recordings are divided into separate intervals (implementations) with a recording length of ~ 16 seconds. The frequency characteristics of the Wiener two-channel filter are estimated using the formulas:

$$L_{1i}(\omega) = \frac{\sum\limits_{j-1}^{n} \overline{F}_{1,j}(\omega)\overline{F}_{i,j}^{*}(\omega)\left[1 - \dfrac{\sum\limits_{j-1}^{n}\overline{F}_{1,j}(\omega)\overline{F}_{2,j}^{*}(\omega)\sum\limits_{j-1}^{n}\overline{F}_{2,j}(\omega)\overline{F}_{i,j}^{*}(\omega)}{\sum\limits_{j-1}^{n}\overline{F}_{1,j}(\omega)\overline{F}_{i,j}^{*}(\omega)\sum\limits_{j-1}^{n}\left|\overline{F}_{2,j}(\omega)\right|^2}\right]}{\sum\limits_{j-1}^{n}\left|\overline{F}_{1,j}(\omega)\right|^2\left[1 - \dfrac{\left|\sum\limits_{j-1}^{n}\overline{F}_{1,j}(\omega)\overline{F}_{2,j}^{*}(\omega)\right|^2}{\sum\limits_{j-1}^{n}\left|\overline{F}_{1,j}(\omega)\right|^2\sum\limits_{j-1}^{n}\left|\overline{F}_{2,j}(\omega)\right|^2}\right]} \tag{1}$$

$$L_{2i}(\omega) = \frac{\sum\limits_{j-1}^{n} \overline{F}_{2,j}(\omega)\overline{F}_{i,j}^{*}(\omega)\left[1 - \dfrac{\sum\limits_{j-1}^{n}\overline{F}_{2,j}(\omega)\overline{F}_{1,j}^{*}(\omega)\sum\limits_{j-1}^{n}\overline{F}_{1,j}(\omega)\overline{F}_{i,j}^{*}(\omega)}{\sum\limits_{j-1}^{n}\overline{F}_{2,j}(\omega)\overline{F}_{i,j}^{*}(\omega)\sum\limits_{j-1}^{n}\left|\overline{F}_{1,j}(\omega)\right|^2}\right]}{\sum\limits_{j-1}^{n}\left|\overline{F}_{2,j}(\omega)\right|^2\left[1 - \dfrac{\left|\sum\limits_{j-1}^{n}\overline{F}_{1,j}(\omega)\overline{F}_{2,j}^{*}(\omega)\right|^2}{\sum\limits_{j-1}^{n}\left|\overline{F}_{1,j}(\omega)\right|^2\sum\limits_{j-1}^{n}\left|\overline{F}_{2,j}(\omega)\right|^2}\right]} \tag{2}$$

These formulas allow you to connect two reference points with two-channel Wiener filters, recalculating standing waves, with all points of the observation system. Thus, for each observation point, we obtain the coupling functions L_1 and L_2 that allow us to obtain the wave field parameters in it from simultaneous recordings at reference points.

Choosing any implementation F at the reference points, we recalculate it into a simultaneous wave field at all observation points using the following formula:

$$F'_i(\omega) = L_{1,i}(\omega)\overline{F}(\omega) + L_{2,i}(\omega)\overline{F}(\omega) \tag{3}$$

To build the relationships between the points of the building and build a model of propagation and transmission of wave effects, coherence spectra and error spectra are calculated. The coherence spectrum $\gamma(\omega)$ is a measure of the linearity of the coupling of vibrations between two points of an engineering structure. The values of the coherence spectra increase at the frequencies of normal modes and decrease between them. In the error spectrum, on the contrary, $\sigma^{(\omega)}$ - the values decrease at the frequencies of the normal modes and increase between them. The ratio of these spectra allows us to select the eigenfrequencies.

The recording coherence spectrum at the i point relative to one of the reference points is calculated by the formula:

$$\gamma^2(\omega) = \frac{\left|\sum\limits_{j-1}^{n}\overline{F}_i(\omega)\overline{F}_0^{*}(\omega)\right|^2}{\sum\limits_{j-1}^{n}\left|\overline{F}_0(\omega)\right|^2\sum\limits_{j-1}^{n}\left|\overline{F}_i(\omega)\right|^2}, \tag{4}$$

where $F_i(\omega)$, $F_0(\omega)$ are the spectra of simultaneous recordings of standing waves at the i-th point of the object being examined, and the base point

Taking into account that in the filter for recalculation of standing waves the phase spectra are averaged over n independent realizations, it can be argued that the variance of the random error will

decrease n times. With this in mind, the standard error of the phase characteristic (error spectrum) of the eigenfrequency separation is calculated by the formula:

$$\sigma_\theta(\omega) \approx \frac{\sqrt{1-\gamma_{oi}^2(\omega)}}{|\gamma_{oi}(\omega)|\sqrt{2n}}. \tag{5}$$

3. Results and Discussion

To process the data of dynamic tests, a software package "Standing Waves Method" was developed [25, 42, 43, 51], which makes it possible to determine the dynamic characteristics of an object, select natural frequencies and visualize test results in a three-dimensional geoinformation system (GIS) – a model of the object under study (Figure 7–11).

The program provides:

1. Binding of sensors to the building plan and registration time (Figure 7);

2. Import of microseismic vibration logs (Figure 8);

3. Storage of initial, intermediate and output information;

4. Construction of coherence spectra, normalized to spectra of errors of microseismic vibrations to identify natural frequencies of the building (Figure 9);

5. Determination of natural frequencies and modes of vibration of the building. Determination of phase and amplitude characteristics of the wave field of natural oscillations of the building (Figure 10–11);

6. Ability to work within the program with a three-dimensional model of the building;

7. Possibility of constructing various types of diagrams using the standing wave technique.
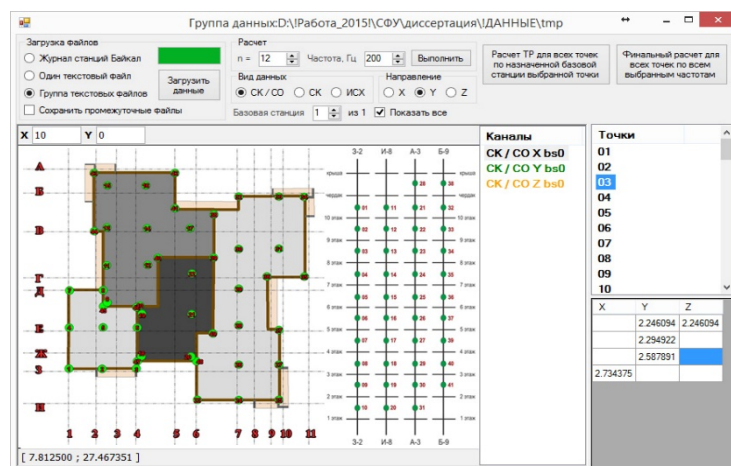
Figure 7. Interface of the "Standing Wave Method" program. Arrangement diagram of the recording sensors.
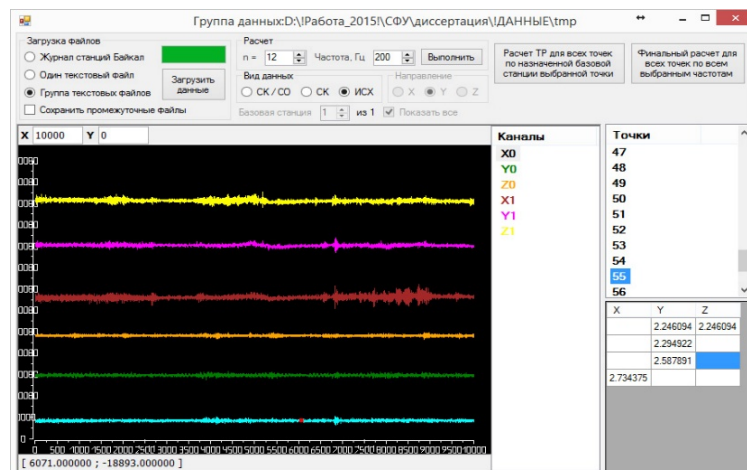
Figure 8. Interface of the "Standing Wave Method" program. Primary data of monitoring of microseismic vibrations recorded by Baikal-ASN8 stations.

Figure 9 shows the calculation of the coherence spectra.
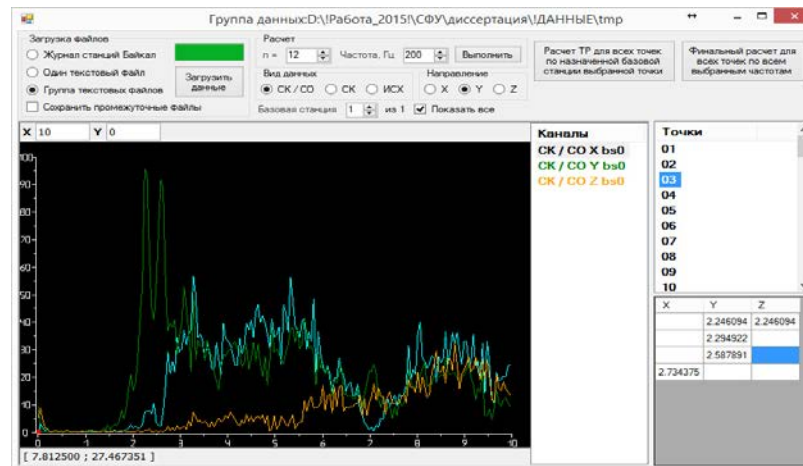
Figure 9. Interface of the "Standing Wave Method" program. Construction of coherence spectra normalized to error spectra.
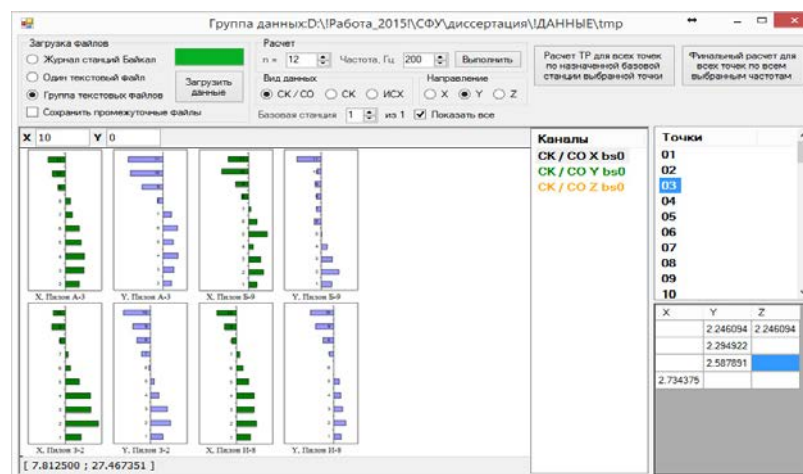
Figure 10. Interface of the "Standing Wave Method" program. Construction of phase diagrams of natural vibrations. Forms of natural vibrations.
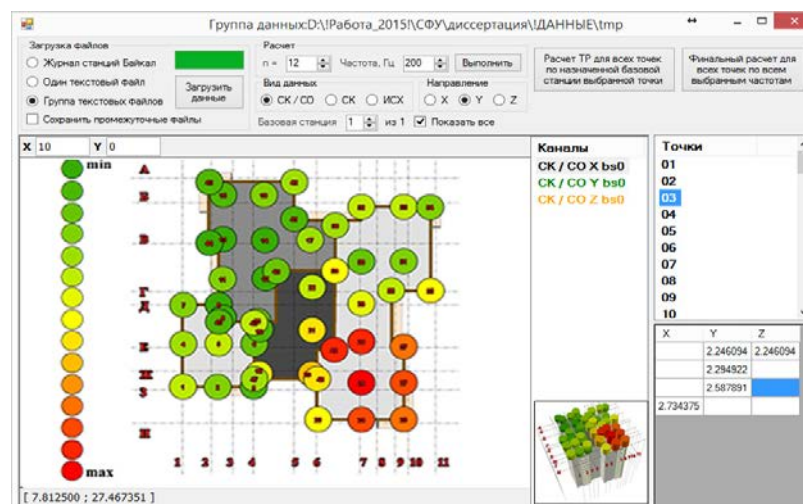
Figure 11. Interface of the "Standing Wave Method" program. Construction of diagrams of natural vibration amplitudes.

As a result of dynamic tests of the dormitory building at the first stage in 2014. the actual frequencies of the first and second modes of natural vibrations were obtained (Figure 12).

a)   b)
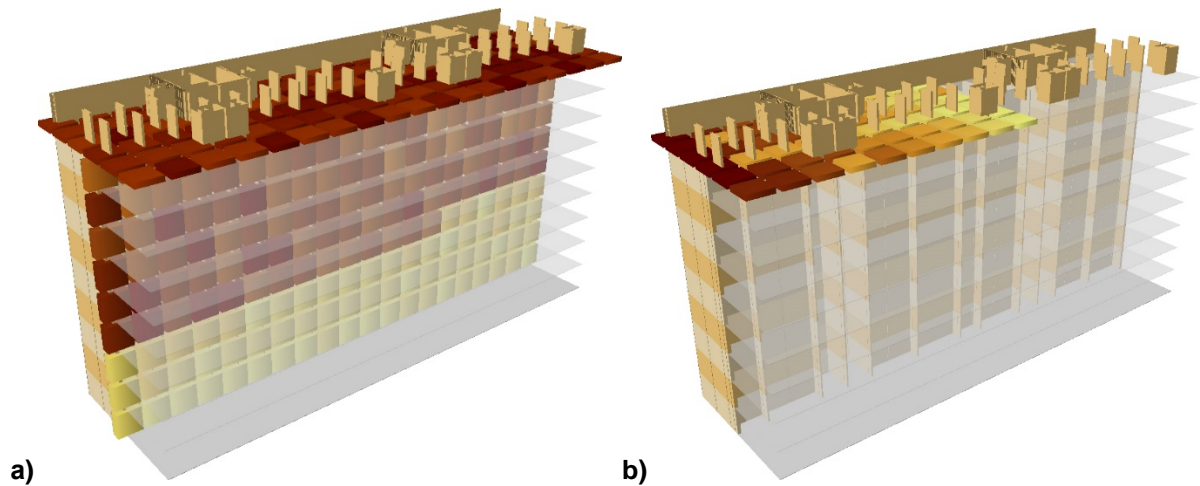
Figure 12. 3D GIS-model of the studied object. a) Maximum amplitudes of the 1st form of natural vibrations at a frequency of 2.34 Hz along the Y-component in 2014. b) Maximum amplitudes of the 2nd form natural vibrations at a frequency of 2.67 Hz along the Y-component in 2014.

Figure 13 shows the isolines of the maximum amplitudes on the plan of the attic space obtained in 2014.

a)   b)
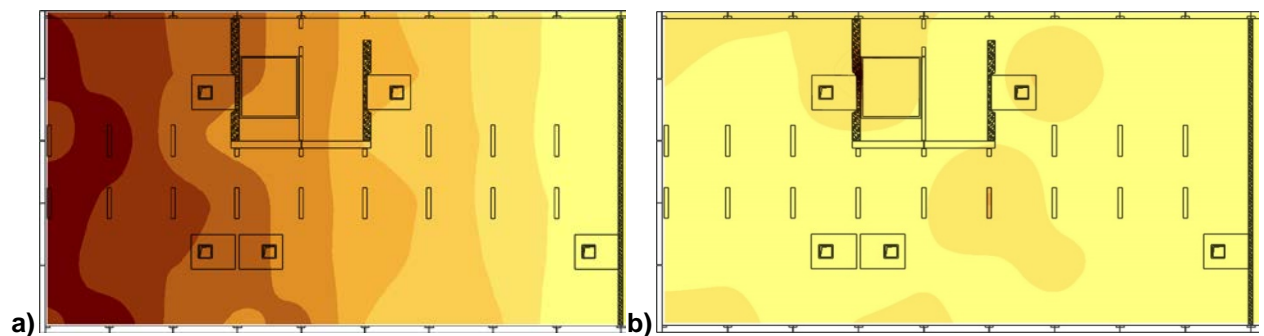
Figure 13. Isolines of maximum amplitudes on the plan of the attic space obtained in 2014. a) Maximum amplitudes of the 2nd form natural vibrations at a frequency of 2.67 Hz along the Y-component. b) Maximum amplitudes of the 2nd form natural vibrations at a frequency of 2.67 Hz along the Z-component.

At the second stage in 2015. as a result of dynamic tests of the dormitory building, the actual frequencies of the first and second forms of natural vibrations were re-obtained (Figure 14).

a)   b)
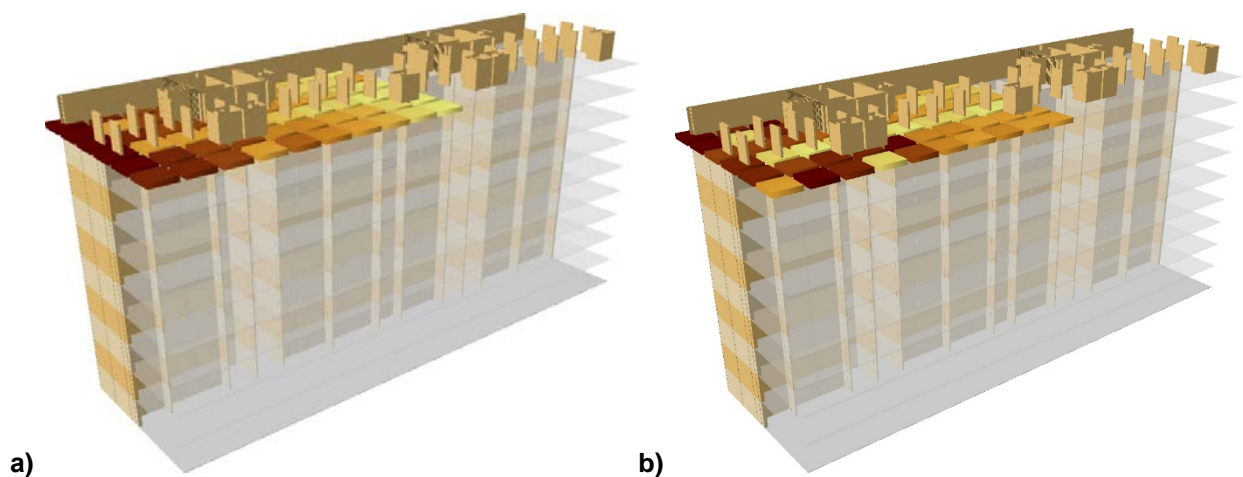
Figure 14. 3D GIS-model of the investigated object. a) Maximum amplitudes of the 1st form of natural vibrations at a frequency of 2.29 Hz along the Y-component in 2015. b) Maximum amplitudes of the 2nd form natural oscillations at a frequency of 2.59 Hz along the Y-component in 2015.

Figure 15 shows the isolines of the maximum amplitudes on the plan of the attic space obtained in 2015.
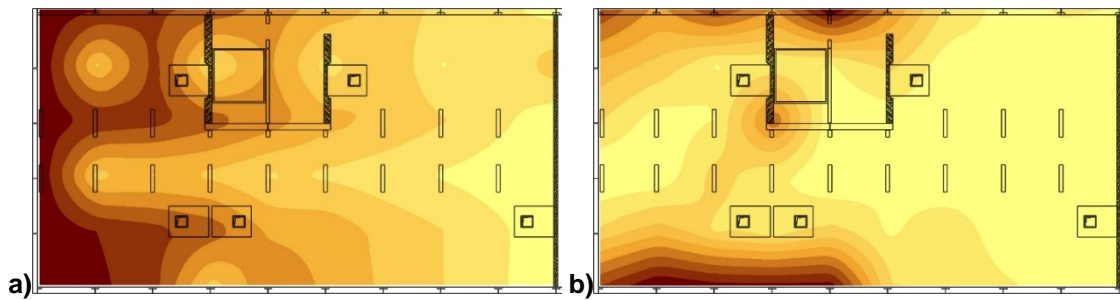
Figure 15. Isolines of maximum amplitudes on the plan of the attic space obtained in 2015. a) Maximum amplitudes of the 2nd form natural vibrations at a frequency of 2.59 Hz along the Y-component. b) Maximum amplitudes of the 2nd form natural vibrations at a frequency of 2.59 Hz along the Z-component.

As can be seen from Figure 14, there have been changes in the natural frequencies of the building during the observation period from 2014 to 2015, and in particular a decrease in the natural frequencies of the first form from 2.34 Hz to 2.29 Hz and the second form from 2.69 Hz to 2.59 Hz. This fact indicates a decrease in the overall stiffness of the building. The reason for the weakening of the stiffness of the building, as can be seen from Figure 15 b), was the peak amplitudes in the Z-component, which appeared at the second stage of testing in 2015. The occurrence of vertical components of relative displacements in the field of standing waves indicates a decrease in the bearing capacity of the building foundation in these zones.

Figure 16 shows the changes in the field of standing waves of the building obtained during the observation period from 2014 to 2015.
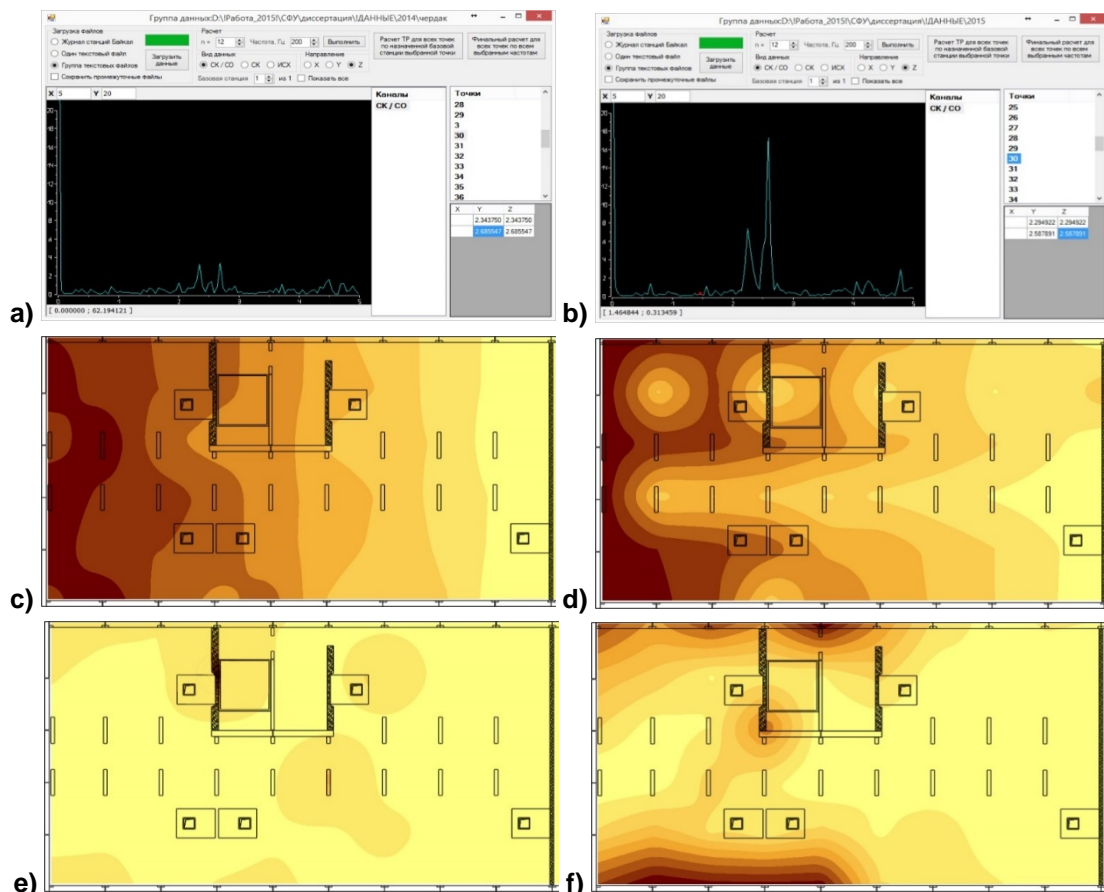
Figure 16. Changes in the field of standing waves of the building obtained during the observation period from 2014 to 2015. a) Construction of the coherence spectra normalized to the spectra of the error in the Z-component in 2014. b) Construction of the coherence spectra normalized to the spectra of the error in the Z-component in 2015. c) Maximum amplitudes of the 2nd form of natural oscillations at a frequency of 2.67 Hz along the Y-component in 2014. d) Maximum amplitudes of the 2nd form of natural oscillations at a frequency of 2.59 Hz along the Y-component in 2015. e) Maximum amplitudes of the 2nd form of natural vibrations at a frequency of 2.67 Hz along the Z-component in 2014. f) Maximum amplitudes of the 2nd form of natural vibrations at a frequency of 2.59 Hz along the Z-component in 2015.

Khoroshavin, E.A.

As can be seen from Figure 16, during the repeated dynamic testing of the building, zones of the occurrence of peak amplitudes along the Z-component appeared, indicating a weakening of the bearing capacity of the soil of the pile foundation in these zones.

The obtained research results are unique and cannot be compared with the results of other authors. This is due to the features of the standing wave field, which is individual for each building. It should be noted that the results of studying the features of the standing wave field in buildings and structures obtained on the basis of the standing wave method were published in [6, 48, 50, 51].

4. Conclusions

The microseismic vibrations of building structures were recorded with the mobile diagnostic complex Method of Standing Waves (MSW-1). According to the results of dynamic tests of a residential multi-storey panel building, its dynamic characteristics are obtained. The natural frequencies, peak amplitudes and phase characteristics of the wave field of the building are determined. To distinguish the building's natural frequencies, a software package has been developed that implements the standing wave method. A GIS is built - a model for representing the amplitudes and phases of the natural oscillation fields of a building and its structural elements. An analysis of the frequency, amplitude, and phase characteristics of the wave field obtained as a result of monitoring a residential multi-storey panel building made it possible to establish the causes of cracks in the interface nodes of structural elements. The causes of cracks were the destructive processes of the soil in the pile foundation of the building, associated with a seasonal increase in groundwater. Defects of the building foundation identified as a result of diagnostics require measures to lower the groundwater level on the construction site.

Currently, the Standing Wave Method (MSW-1) mobile diagnostic complex has been used to diagnose large-span bridge structures, assess the earthquake resistance of a building with a stationary seismic isolation system, and monitor the technical condition of the Musical Theater and residential buildings. The complex can be used to solve the widest range of tasks:

- inspection of emergency buildings;
- assessment of earthquake resistance of buildings;
- audit of the quality of construction work;
- reconstruction and resumption of construction;
- scheduled inspections of industrial buildings and especially hazardous facilities;
- study of the impact of external influences on objects (explosions, construction work, etc.);
- inspection and monitoring of the technical condition of buildings and structures;
- determination of the parameters of the fundamental tone of natural vibrations for the building passport.

References

1. Gordeyeva, O.G., Sushchev, S.P. Sovremennyye sredstva diagnostiki tekhnicheskogo sostoyaniya zdaniy i sooruzheniy. [Modern diagnostic tools for the technical condition of buildings and structures]. Mezhdunarodnyy simpozium "Kompleksnaya bezopasnost Rossii - issledovaniya, upravleniye, opyt". [International Symposium "Integrated Security of Russia - Research, Management, Experience"]. Sbornik materialov. © VNII GOChS. 2002. Pp. 98–99. (rus)

2. Savin, S.N. The use of elastic vibrations with different wavelengths to evaluate the dynamic parameters of buildings and structures and assess the strength of materials of the building construction. Earthquake engineering. Constructions safety. 2017. No. 4. Pp. 43–54.

3. Nigmetov, G.M., Savinov, A.M. O dinamiko-geofizicheskom metode otsenki nesushchey sposobnosti sooruzheniy. Sbornik trudov XXVIII Mezhdunarodnoy nauchno-prakticheskoy konferentsii. Akademiya grazhdanskoy zashchity MChS Rossii. [Proceedings of the XXVIII International Scientific and Practical Conference. Academy of Civil Protection EMERCOM of Russia].2018. Pp. 66–68.

4. Nigmetov, G.M. Application of natural oscillation frequency for evaluation of technical condition category of structures. Natural and Technological Risks. Building Safety. 2019. No. 5(42). Pp. 24–27. (rus)

5. Zolotukhin, E.P., Kuzmenko, A.P., Saburov, V.S., Korolenko, D.B., Neskorodev, V.D. Seysmometricheskiy monitoring tehnicheskogo sostoyaniya nesuschih stroitelnyih konstruktsiy zdaniy i sooruzheniy po dinamicheskim harakteristikam [Seismometric monitoring of the technical condition of load bearing constructions of buildings and structures by their dynamic characteristics]. Computational Technologies. 2013. Vol. 18. Special issue. Pp. 29−36. (rus)

6. Kuzmenko, A.P., Saburov, V.S., Korolenko, D.B. Application features of the engineering seismometric method of survey and monitoring the technical condition of buildings and structures. Journal of Siberian Federal University. Engineering & Technologies. 2019. Vol. 12. No. 2. Pp. 231–239. DOI: 10.17516/1999-494X-0132.

7. Belostotskiy, A.M., Novikov, P.I. Identifying real stiffness properties of structural elements of adapted finite-element models of buildiygs and structures: part 2: computational-experimental methodology. Applied mechanics and materials. 2014. Vol. 670–671. Pp. 736–741. DOI: 10.4028/www.scientific.net/AMM.670-671.736.

8. Lunatsii, M., Shpolyansky, I.V., Sobolev, V.I. Belendir, E.N., Belostotskiy, A.M., Lisichkin, S.E., Bershov, A.V. Concept for developing the architecture of a hardwaresoftware package to monitor hydraulic installation status. Power Technology and Engineering. 2016. Vol. 50. No.4. Pp. 347–351. DOI: 10.1007/s10749-016-0710-y

9. Novikov, P.I., Belostotskiy, A.M. Identifying real stiffness properties of structural elements of adapted finite-element models of buildings and structures: part 3: approbation of experimental methodology. Applied Mechanics and Materials. 2014. Vol. 670–671. Pp. 742–746. DOI: 10.4028/www.scientific.net/AMM.670-671.742

10. Belostotsky, A.M., Akimov, P.A., Negrozov, O.A., Petryashev, N.O., Petryashev, S.O., Sherbina, S.V., Kalichava, D.K., Kaytukov, T.B. Adaptive finite-element models in structural health monitoring systems. Magazine of Civil Engineering. 2018. No. 78(2). Pp. 169–178. doi: 10.18720/MCE.78.14.

11. Nigmetov, G.M., Yegorova, A.A. Diagnostics and monitoring of buildings, structures using the methods of dynamic and geophysical testing. Materialy XII mezhdunarodnoy nauchno-prakticheskoy konferentsii. Pozharnaya i avariynaya bezopasnost. [Materials of the XII International Scientific and Practical Conference. Fire and emergency safety]. 2017. Pp. 847–850. (rus)

12. Savin, S.N., Aleksandrova, A.A., Grabarovskaya, K. Monitoring dinamicheskikh parametrov zdaniy i sooruzheniy kak sredstvo ikh bezopasnoy ekspluatatsii. [Monitoring the dynamic parameters of buildings and structures as a means of their safe operation]. Materialy IV Vserossiyskoy nauchno-prakticheskoy konferentsii s uchastiyem "Bezopasnost v stroitelstve". [Materials of the IV All-Russian scientific-practical conference with the participation of "Safety in construction"].Sankt-Peterburg. 2019. Pp. 145–149.

13. Savin, S.N. Dynamic monitoring of building structures on the example of the concert hall "Pushkinskiy" ramp in Moscow. Magazine of Civil Engineering. 2012. 33(7). Pp. 58–62. (rus). DOI: 10.5862/MCE.33.7

14. Savin, S.N., Demishin, S.V., Sitnikov, I.V. Monitoring of unique buildings with using of dynamic parameters according to GOST R 53778-2010. Magazine of Civil Engineering. 2011. 25(7). Pp. 33–39. (rus). DOI: 10.5862/MCE.25.5

15. Bol'shakov, V.I., Chaika, A.L., Sushchev, S.P., Suslonov, A.A., Yur'yev, A.B., Bugaev, S.F., Panchokha, G.V., Borodulin, A.V. New methods for monitoring the technical state of blast furnace enclosure without stopping the technological process. Refractories and industrial ceramics. 2007. Vol. 48. No. 3. Pp. 178–182. DOI: 10.1007/s11148-007-0055-z

16. Soloviev, V.M., Seleznev, V.S., Emanov, A.F., Kashun, V.N., Elagin, S.A., Romanenko, I.E., Schoenmeier, A.E., Serezhnikov, N.A. Active Seismic monitoring using high-power moveable 40-tons vibration sources-results, outlooks. International congress "Natural cataclysms and global problems of the modern civilization - Geocataclysm 2011" Istanbul, Turkey. "SWB" International Publishing House. 2011. P. 71.

17. Emanov, A.F. On application of vibrators for determination of seismic stability of buildings and in microseismic regionalization. Russian Geology and Geophysics. 1995. Vol. 36. No. 7. Pp. 84–90.

18. Seleznev, V.S., Emanov, A.F. Conversion of head-wave fields by the wiener filters. Russian geology and geophysics. 1998. Vol. 39. No. 4. Pp. 548–559.

19. Yemanov, A.F. Vosstanovleniye kogerentnykh sostavlyayushchikh volnovykh poley v seysmike: dis. doktora tekhn. nauk: 25.00.10: zashchishchena 20.12.04. [Reconstruction of coherent components of wave fields in seismic: dis. doctor tech. Sciences: 25.00.10: is protected 12.20.04]. Yemanov Aleksandr Fedorovich. Novosibirsk, 2004. P. 280.

20. Yemanov, A.F., Seleznev, V.S., Bakh, A.A., Gritsenko, S.A., Danilov, I.A., Kuzmenko, A.P., Saburov, V.S., Tatkov, G.I. Pereschet stoyachikh voln pri detalnykh inzhenerno-seysmologicheskikh issledovaniyakh. [Recalculation of standing waves for detailed engineering and seismological studies]. Geologiya i geofizika. [Geology and Geophysics]. 2002. Vol. 43. No. 2. Pp. 192–207. (rus)

21. Dergachev, A.A., Emanov, A.F., Toloshinov, A.V. Seismic observations in the geodynamic proving at the sayano-shushenskaya HPP. Power Technology and Engineering. 2007. Vol. 41. No. 5. Pp. 268–277. DOI: 10.1007/s10749-007-0050-z

22. Yemanov, A.F., Seleznev, V.S., Bakh, A.A. Kogerentnoye vosstanovleniye poley stoyachikh voln kak osnova detalnogo seysmologicheskogo obsledovaniya inzhenernykh sooruzheniy. [Coherent reconstruction of standing wave fields as the basis for a detailed seismological survey of engineering structures]. Earthquake engineering. Constructions safety. 2007. No. 3. Pp. 20–23.

23. Emanov, A.F., Krasnikov, A.A., Bach, A., Seleznev, V.S. Standing waves in buildings and engineering constructions. European conference on earthquake engineering. Ohrid. Macedonia Association for Earthquake Engineering. 2010. P. 900.

24. Abovsky, N.P., Inzhutov, I.S., Khoroshavin, E.A., Deordiyev, S.V., Palagushkin, V.I. Importance of foundations in earthquake-resistant construction. seismically protective foundation (In order of discussion). Soil Mech Found Eng. 2012. 49. Pp. 200–201. DOI: 10.1007/s11204-012-9190-8

25. Khoroshavin, E.A. Dynamic tests of the administrative building with a stationary seismic isolation system in Irkutsk. Earthquake Engineering. Constructions Safety. 2019. No. 6. Pp. 62–69.

26. Sushchev, S.P., Larionov, V.I., Galiullin, R.R., Nigmetov, G.M., Savin, S.N., Samarin, V.V. O prakticheskom primenenii metoda dinamicheskikh ispytaniy dlya otsenki kategorii tekhnicheskogo sostoyaniya i seysmostoykosti zdaniy i sooruzheniy pri slabykh i silnykh impulsnykh vozdeystviyakh. [On the practical application of the dynamic test method to assess the category of technical condition and seismic resistance of buildings and structures under weak and strong impulse influences]. Earthquake Engineering. Constructions Safety. 2014. No. 3. Pp. 52–59.

27. Frolova, N.I., Larionov, V.I., Suschev, S.P., Bonin, J. Estimation of loss caused by earthquakes and secondary technological hazards. Natural Hazards and Earth System Science. 2011. Vol. 11. No. 11. Pp. 3025–3033. DOI: 10.5194/nhess-11-3025-2011.

28. Frolova, N.I., Larionov, V.I., Ugarov, A.N., Bonnin, Zh., Sushchev, S.P., Kozlov, M.A. Loss caused by earthquakes: rapid estimates. Natural hazards. 2017. Vol. 88. No. S1. Pp. 63–80. DOI: 10.1007/s11069-016-2653-x.

29. Osipov, V.I., Larionov, V.I., Burova, V.N., Frolova, N.I., Sushchev, S.P. Metodology of natural assessment in Russia. Natural hazards. 2017. Vol. 88. No. S1. Pp. 17–41. DOI: 10.1007/s11069-017-2780-z.

30. Frolova, N.I., Larionov, V.I., Ugarov, A.N., Bonnin, Zh., Sushchev, S.P., Kozlov, M.A. Seismic risk assessment and mapping at different levels. Natural hazards. 2017. Vol. 88. No. S1. Pp. 43–62. DOI: 10.1007/s11069-016-2654-9.

31. Kolesnikov, Y.I., Hogoev, E.A., Emanov, A.F., Krasnikov, A.A. Study of potential landslide slope using active and passive seismic techniques. 18thTH European meeting of environmental and engineering geophysics. Paris. 2012. Pp. 479-483.

32. 32. Emanov A. F., Bach A., Krasnikov A.A., Seleznev V. S. Standing Waves Method in engineering seismology. 18th European meeting of environmental and engineering geophysics. European Association of Geoscientists and Engineers. Paris. 2012. Pp. 94–98.

33. Kolesnikov, Y.I., Fedin, K.V., Kargapolov, A.A., Emanov, A.F. Diagnostics of construction units by noise field (physical simulation data). Journal of mining science. 2012. Vol. 48. No. 1. Pp. 1–8. DOI: 10.1134/S1062739148010017.

34. Kolesnikov, Y.I., Fedin, K.V., Kargapolov, A.A., Emanov, A.F. Instability detection in piping supports by acoustic noise. Journal of Mining Science. 2012. Vol. 48. No. 4. Pp. 642–648. DOI: 10.1134/S1062739148040077.

Khoroshavin, E.A.

35. Yemanov, A.F., Seleznev, V.S., Bakh, A.A., Krasnikov, A.A. Metod stoyachikh voln v inzhenernoy seysmologii. [Standing wave method in engineering seismology]. VIII nauchno-prakticheskaya konferentsiya i vystavka «Inzhenernaya geofizika 2012. Geofizicheskiye issledovaniya i inzhenernyye izyskaniya». [VIII scientific-practical conference and exhibition "Engineering Geophysics]. Gelendzhik. SAGE Publications BV. 2012. DOI: 10.3997/2214-4609.20146016 (rus)

36. Kolesnikov, Y.I., Fedin, K.V., Emanov, A.F. Detailed study of near surface resonance properties using low channel microtremor measurements - physical modelling data. 19thTH European meeting of environmental and enginttring geophysics of the near surface geoscience division of EAGE, near surface geoscience 2013. European Association of Geoscientists and Engineers. Bochum. 2013. Pp. 470–474.

37. Emanov, A.F., Krasnikov, A., Bach, A., Seleznev, V.S., Shevtsov, A. The Standing waves method in microseismic zoning and studying of buildings and engineering constructions. The 10th Asian seismological commission (FSC) general assembly. Makati city, Philippines. 2014. 105 p.

38. Savin, S.N., Smirnova, Ye.E. The problem of determining theb dynamic parameters for forecasting the service life of buildings and facilities under conditions of natural and man-made emergencies. Bulletin of Civil Engineers. 2019. No. 3(74). Pp. 14–19. DOI: 10.23968/1999-5571-2019-16-3-14-19

39. Osipov, V.I., Larionov, V.I., Burova, V.N., Frolova, N.I., Sushchev, S.P. Methodology of natural risk assessment in Russia. Natural Hazards. 2017. Vol. 88. No. S1. Pp. 17–41. DOI: 10.1007/s11069-017-2780-z.

40. Larionov, V.I., Nigmetov, G.M., Sotin, V.N., Sushchev, S.P., Shakhramanyan, M.A. Mobilnyye diagnosticheskiye kompleksy dlya otsenki seysmostoykosti zdaniy i sooruzheniy. [Mobile diagnostic systems for assessing the seismic resistance of buildings and structures]. Earthquake engineering. Constructions safety. 1999. No. 2. Pp. 41–43.

41. Savin, S.N. Osobennosti ispolzovaniya izmeritelnykh kompleksov razlichnykh tipov dlya polucheniya dinamicheskikh parametrov zdaniy i sooruzheniy [Features of the use of measuring complexes of various types to obtain the dynamic parameters of buildings and structures]. Materialy IX nauchno-prakticheskoy konferentsii "Obsledovaniye zdaniy i sooruzheniy: problemy i puti resheniya". [Materials of the IX scientific-practical conference "Inspection of buildings and structures: problems and solutions"]. Sankt-Peterburg. 2018. Pp. 244–252.

42. Khoroshavin, E.A. Otsenka seysmostoykosti zdaniy i sooruzheniy na osnove metoda stoyachikh voln. [Assessment of the seismic resistance of buildings and structures based on the method of standing waves]. Sbornik: Modernizatsiya ekonomiki i eksport tekhnologiy v torgovo-ekonomicheskikh otnosheniyakh i nauchnykh issledovaniyakh Rossii i Germanii. Materialy V mezhdunarodnoy konferentsii. [Proceedings: Modernization of the economy and export of technologies in trade and economic relations and scientific research of Russia and Germany. Materials of the V international conference]. Moscow: Moskovskiy finansovo-yuridicheskiy universitet MFYuA. 2016. Pp. 85–98.

43. Khoroshavin, E.A. Otsenka seysmostoykosti zdaniy i sooruzheniy na osnove metoda stoyachikh voln [Assessment of the seismic resistance of buildings and structures based on the method of standing waves]. Sbornik trudov XIII Rossiyskoy natsionalnoy konferentsii po seysmostoykomu stroitelstvu i seysmicheskomu rayonirovaniyu. [Proceedings of the XIII Russian National Conference on Earthquake Engineering and Seismic Zoning]. 2019. Sankt-Peterburg. Pp. 103–106.

44. Kotlyarovskiy, V.A., Sushchev, S.P., Larionov, V.I., Perepelitsin, A.I. Primeneniye mobilnykh diagnosticheskikh kompleksov dlya otsenki prochnosti, ustoychivosti i ostatochnogo resursa zdaniy i sooruzheniy. [Application of mobile diagnostic systems for assessing the strength, stability and residual life of buildings and structures]. Occupational Safety in Industry. 2004. No. 3. Pp. 42–45.

45. Emanov, A.F., Seleznev, V.S., Bach, A.A., Gritsenko, S.A., Danilov, I.A., Kuzmenko, A.P., Saburov, V.S., Tatkov, G.I. Standing waves in engineering seismology. Russian Geology and Geophysics. 2002. Vol. 43. No. 2. Pp. 181–196.

46. Yemanov, A.F., Krasnikov, A.A. Primeneniye metoda stoyachikh voln dlya issledovaniya seysmoizolirovannykh zdaniy. [Application of the method of standing waves for the study of seismically isolated buildings]. Voprosy inzhenernoy seysmologii. 2015. Vol. 42. No. 4. Pp. 37–64.

47. Yemanov, A.F., Bakh, A.A., Yemanov, A.A. Application of the method of standing waves in the study of engineering structures and complex structures in seismic micro zoning. Natural and Technological Risks. Building Safety. 2017. No. 4(31). Pp. 36–37.

48. Yemanov, A.A., Yemanov, A.F., Kletsin, V.I. Research of dam at Boguchany HPP by the standing waves method. Interekspo GEO-Sibir. 2018. Vol. 3. Pp. 138-144.

49. Yemanov, A.F., Bakh, A.A. Development of Algorithms for Interpreting the Method of Standing Waves for the Study of Buildings and Structures of Complex Constructions. Earthquake Engineering. Constructions Safety. 2019. No. 5. Pp. 28–35.

50. Yemanov, A.F., Bakh, A.A. Standing waves in engineering objects of complex constructions. Interekspo GEO-Sibir. Novosibirsk. 2019. Vol. 2. No. 2. Pp. 67–73. DOI: 10.33764/2618-981X-2019-2-2-67-73.

51. Khorochavin, E.A., Sarcyenko, V.I. Seismic Resistant Design of Tall RC Structures - Some Special Considerations. SEWC 2015. 5th Structural Engineers World Congress. Singapore. 2015. P. 17.

Contacts:

Evgeny Khoroshavin, zkpd2007@ya.ru

Determination of the multicomponent lightweight mixture optimal composition

L.I. Dvorkin*, O.M. Bordiuzhenko, I.V. Kovalyk
National University of Water Environmental Engineering, Rivne, Ukraine
*E-mail: dvorkin.leonid@gmail.com

Abstract. Designing of multi-component building compositions is usually done by an empirical method, which is a laborious and time-consuming process. The article deals with the method of designing the optimal building mixture composition based on the criterion of minimal costs. In this study, the effect of composition factors (water demand, binder content, fillers and additives) on compressive and flexural strengths of the gypsum-based mortar and the expanded lightweight filler was determined. According to the results of experiments, the corresponding mathematical models of mortar properties were obtained. Such models have made it possible to develop a design methodology for the mixture composition, which uses methods of mathematical programming. It allows obtaining the optimal composition of the construction mixture, which provides the required properties of the mortar at its minimal cost.

1. Introduction

The object of research is the methodology for designing the optimal compositions of multicomponent building materials, which include modern concretes and mortars. The designing determination of their compositions is complicated by the lack of common dependencies and requires significant experimental work. For example, about 180 trial mixes were tried before arriving at the final mix composition for roller compacted concrete [1]. Therefore for the design of compositions of multicomponent mixtures, experimentally-statistical models are especially promising. Such models incorporate the effects of specific factors that determine the mixture properties and effects of their interaction on material properties. For obtaining models effectively using the methods of mathematical experiment planning.

The experiment planning methodology is shown in the works [2–4]. Experimentally-statistical (mathematical) models allow to solve some practical problems. V. Voznesenskiy [4] has formulated and developed a methodology for ten typical problems that can be solved individually or jointly based on a polynomial models. These are interpolation, extrapolation problems, problems of achieving the minimum or maximum value of the output parameters, etc.

One of the important problems solved by the mathematical models is optimization of compositions with different optimality criterions [5]. One of the most important criteria is the minimum cost criterion while ensuring the necessary quality indicators of the composite materials. In this case, the problem of designing the building mixture composition while providing a complex of specified properties and minimizing its total cost becomes much more complicated. Along with differential analysis using canonical and isoparametrical analysis as well as linear programming and alternative methods for getting optimal solutions is also possible [2, 6, 7].

In most works performed by the traditional experimental approach, it is proposed to reduce the cost of the mixture by reducing the content of the most expensive component. At the same time, the cost of other components that significantly affect the properties of the mixture is not taken into account. Examples of solved problems for designing of the optimal composition of building mixtures are given in works [8–14]. Parveen and Singhal [15] proposed a method for designing a mixture fof geopolymer concrete. In this work, the authors suggest to minimize the cost of the mixture by reducing the number of the most expensive

component, but in doing so not to take into account the costs of other components that determine the cost of the mixture.

To take into account the characteristics of aggregates and additives in the designation of concrete compositions, a number of calculated and experimental dependencies have been proposed [16–20]. But these dependencies did not take into account the criterion of optimality.

Some authors proposed methods, based on mathematical experiment planning methodology, but these works excluded cost aspect [21–26]. The compositions' design usually is limited to minimize the cost of binder and additives. At that, only one of the required indicators of the material quality is ensured, for example, compressive strength. The dependence between concrete cost and its strength was determined [27]. It allowed to propose a method for composition design. However, this method did not allow to find the optimal composition, providing both the specified strength value and the minimum cost. Furthermore, the method requires to use a nomogram of concrete properties which significantly complicates the procedure of designing the composition. In the work [11], the optimum self-compacting mortar mix is defined as that mixture which maximizes durability while minimizing cost. But in this case, the total cost of all components of the mixture is not calculated.

The method of dynamic optimization in the process of designing concrete composition was used [28]. The optimization of the mixture components was performed using a nonlinear dynamic model to study the behavior of the variables. However, the cost criterion was not considered in this study.

The problem of finding the optimal building mixture composition with designed quality parameters can be formulated as follows: find the values of mixture factors $x_1 \dots x_n$, allowing to minimize its cost:

$$E_c = E_1 C_1 + E_2 C_2 + \dots + E_n C_n \to \min \tag{1}$$

While the necessary quality parameters are provided

$$P_1 \geq f\left(x_1, x_2, \dots, x_n\right) \tag{2}$$
$$P_2 \geq f\left(x_1, x_2, \dots, x_n\right)$$
$$P_m \geq f\left(x_1, x_2, \dots, x_n\right)$$

While

$$x_1 \dots, x_n \in \left[a \dots b\right] \tag{3}$$

where,

$E_1, E_2, \dots, E_n$ are the cost (expenses) of mixture's components, \$/kg;

$C_1, C_2, \dots, C_n$ are the consumptions of dry mixture's components, respectively, kg/t (kg/m^3) of mixture;

$P_1 \dots P_m$ are the given quality mixture parameters;

$x_1 \dots x_n$ are the composition factors;

a, b are the limitations of factors' possible values.

The solution of this problem can be found using mathematical programming methods [4]. These methods may be implemented using originally developed algorithms in the MS Excel Solver software. This problem is especially relevant for dry building mixtures containing many components that simultaneously affect both the cost and properties of the mixture.

The aim of the research was to develop a calculation method for designing the gypsum-perlite dry mixture composition (GPM) with specified values of compressive strength, flexural strength, and density.

Achieving this aim required the solution of the following tasks:

1. To obtain a complex of polynomial models of the normalized mixture properties depending on the composition parameters.

2. To analyze the influence of the main composition factors on the mixture properties.

3. To solve the task of GPM designing using MS Excel Solver software.

2. Methods and Materials

A series of experiments, based on algorithm according to the five-factor experiment plan (type Ha_5) [1], were implemented in order to determine the GPM design parameters under the planning conditions given in Table 1.

Table 1. Experiment Planning Conditions.

No.	Factors		Varying levels			Interval
	Coded	Parameter	-1	0	+1	
1	x_1	Perlite-gypsum ratio (P/G)	0.02	0.04	0.06	0.02
2	x_2	Limestone powder – gypsum ratio (L/G)	0.4	0.6	0.8	0.2
3	x_3	Hydrated lime – gypsum ratio (HL/G)	0.17	0.37	0.57	0.2
4	x_4	Cellulose ether content (CE), % by weight of mixture	0.23	0.25	0.27	0.02
5	x_5	Starch ether content (SE), % by weight of mixture	0.03	0.05	0.07	0.02

As components of the GPM were used construction gypsum marked with A1 in accordance with EN 13279-1:2009, limestone powder (0–3 mm), hydrated calcium lime (marked with CL 90 in accordance with EN 459-1:2010), cellulose ether, starch ether and expanded perlite sand (0.16–1.25 mm). Granulometry of perlite sand within the specified fraction was selected with the maximum packing density of grains. The density of perlite sand was 100.4 kg/m^3.

Table 2. Technical and chemical characteristic of limestone powder.

Technical characteristic:	- Humidity to 1 %, - Grinding fineness (the rest on a sieve of 0.2 mm) no more than 30 %, - Fraction of 0-3 mm.
Chemical composition, %:	- CaO – 53.0-54.0 - Al_2O_3 – 0.1 - Fe_2O_3 – 0.14 - MgO – 0.62 - SiO_2 – 0.5 - The insoluble rest – 1.97 - Loss of ignition – 44.0-45.0

Table 3. Characteristics of cellulose ether.

Indicators	Value
Methoxy group content, %	19.0 – 24.0
Hydroxypropyloxy group content, %	4.0 – 12.0
Gel formation temperature, °C	70 – 90
Moisture content, %, max.	5.0
Ash content, %, max.	1.0
pH (1 % solution at 25 ºC)	5.0 – 8.0

Table 4. Characteristics of starch ether.

Indicators	Value
Moisture content, %, max.	10
Ash content, %, max.	10
pH (1 % solution)	7.0 – 10.0
Hydroxypropyloxy-group content, %	19.0 – 24.0
Viscosity (5 % solution) by Brookfield rotational viscometer, mPa·s	300 – 500

Water consumption was determined experimentally to ensure the mixture workability of 8 cm. After measuring the mixture workability, it was used for casting the test specimens. Three identical specimens were prepared for each mixture composition. The specimens had a prismatic form with dimensions of 40×40×160 mm. The specimens were kept in the forms during 24 h and after that they had hardened in special chambers with humidity no more than 60 % and the temperature was 18±2 °C. The specimens were tested in 7 days age to obtain their compressive and flexural strengths.

The strength characteristics were measured using a test machine FP 100/1 with a 100 kN load capacity and accuracy S = ±1.0 %. To obtain the flexural strength the specimens were located on two cylindrical supports. The distance between the supports was 100 mm. The load was applied in the middle of the span (ISO 679:2009 [29]). The parts of the tested specimens were further used to measure their compressive strength using a standard method (ISO 679:2009 [29]).

3. Results and Discussion

Experimental results are presented in Tables 5-6. For this data corresponding statistical characteristics was obtained and coefficients of regression equation was calculated [2]. After the significance of the coefficients were estimated, the adequacy of equations were checked by calculating the adequacy dispersion, design value of Fishcer's criterion (F-criterion) and comparing the last with a normalized one [30].

Table 5. Planning matrix and compositions of gypsum-perlite mixture.

No.	Natural values of factors					Component consumption					
	P/G	L/G	HL/G	CE	SE	Gypsum (G), kg/t	Expanded perlite sand (P), kg/t	Limestone powder (L), kg/t	Hydrated calcium lime (HL), kg/t	Cellulose ether (CE), %	Starch ether (SE), %
1	0.06	0.8	0.057	0.27	0.07	520	31.2	416	29.6	2.7	0.7
2	0.02	0.4	0.057	0.27	0.07	675	13.5	269	38.5	2.7	0.7
3	0.02	0.8	0.017	0.23	0.03	543	10.9	434	9.2	2.3	0.3
4	0.06	0.4	0.017	0.23	0.03	675	40.5	270	11.5	2.3	0.3
5	0.02	0.8	0.017	0.27	0.07	543	10.9	434	9.2	2.7	0.7
6	0.06	0.4	0.017	0.27	0.07	675	40.5	269	11.5	2.7	0.7
7	0.06	0.8	0.057	0.23	0.03	520	31.2	416	29.7	2.3	0.3
8	0.02	0.4	0.057	0.23	0.03	675	13.5	270	38.5	2.3	0.3
9	0.02	0.8	0.057	0.27	0.03	531	10.6	424	30.3	2.7	0.3
10	0.06	0.4	0.057	0.27	0.03	657,	39.4	262	37.5	2.7	0.3
11	0.06	0.8	0.017	0.23	0.07	531	31.9	424	9.0	2.3	0.7
12	0.02	0.4	0.017	0.23	0.07	693	13.9	277	11.8	2.3	0.7
13	0.02	0.8	0.057	0.23	0.07	531	10.6	424	30.3	2.3	0.7
14	0.06	0.4	0.057	0.23	0.07	657	39.4	262	37.5	2.3	0.7
15	0.06	0.8	0.017	0.27	0.03	531	31.9	424	9.0	2.7	0.3
16	0.02	0.4	0.017	0.27	0.03	693	13.9	277	11.8	2.7	0.3
17	0.06	0.6	0.037	0.25	0.05	587	35.3	352	21.7	2.5	0.5
18	0.02	0.6	0.037	0,25	0.05	601	12.0	361	22,3	2.5	0.5
19	0.04	0.8	0.037	0.25	0.05	531	21.2	424	19,7	2.5	0.5
20	0.04	0.4	0.037	0.25	0.05	675	27.0	270	25.0	2.5	0.5
21	0.04	0.6	0.057	0.25	0.05	587	23.5	352	33.5	2.5	0.5
22	0.04	0.6	0.017	0.25	0.05	601	24.1	361	10.2	2.5	0.5
23	0.04	0.6	0.037	0.27	0.05	594	23.8	356	22.0	2.7	0.5
24	0.04	0.6	0.037	0.23	0.05	594	23.8	356	22.0	2.3	0.5
25	0.04	0.6	0.037	0.25	0.07	594	23.8	356	22.0	2.5	0.7
26	0.04	0.6	0.037	0.25	0.03	594	23.8	356	22.0	2.5	0.3
27	0.04	0.6	0.037	0.25	0.05	594	23.8	356	22.0	2.5	0.5

Table 6. Experimental values of the properties of the gypsum-perlite mixture mortar.

No.	Strengths of the mortar at 7 days, MPa		Density ρ_o, kg/m^3	Water consumption W, %
	compressive f_m	flexural f_{tf}		
1	2	1.5	1031	54
2	3.1	2	1064	49
3	3	2.2	929	57
4	1.95	1.6	1080	50
5	2.9	2.05	910	58
6	1.75	1.46	976	54
7	1.9	1.7	1087	54
8	2.6	2.1	1093	55
9	2.3	2.2	931	57
10	1.95	1.6	936	54
11	1.8	1.53	1084	53
12	2.9	2	1093	50
13	3.3	1.95	942	58
14	1.8	1.55	960	54
15	2.3	1.46	1085	52
16	3	2.1	938	56
17	1.9	1.8	1088	49
18	2.9	1.8	980	53
19	2.4	1.92	973	52
20	2.3	1.82	975	53
21	2.3	1.82	976	52
22	2.1	1.92	974	53
23	2.3	1.87	975	52
24	2.4	1.86	976	52
25	2.3	1.85	977	52
26	2	1.87	975	52
27	2.5	1.86	978	52

Adequate experimental-statistical models of GPM compressive and flexural strengths (f_m and f_{tf}, MPa, respectively) and also density (ρ_o, kg/m^3) at 7 days, in the terms of the coded variables are as follows:

– compressive strength

$$f_m = 2.46 - 0.05x_1 + 0.04x_2 + 0.01x_3 -$$
$$- 0.11x_4 + 0.18x_5 + 0.16x_1^2 + 0.21x_2^2 + 0.56x_3^2 -$$
$$- 0.34x_4^2 - 0.44x_5^2 - 0.14x_1x_2 - 0.07x_1x_3 - 0.16x_1x_5 -$$
$$- 0.07x_2x_3 - 0.16x_2x_5 + 0.27x_3x_5$$

(4)

– flexural strength

$$f_{tf} = 1.86 - 0.02x_1 + 0.02x_2 - 0.04x_3 -$$
$$- 0.01x_4 + 0.02x_5 + 0.13x_1^2 + 0.13x_2^2 - 0.02x_3^2 -$$
$$- 0.07x_4^2 + 0.08x_5^2 + 0.01x_1x_2 + 0.03x_1x_4 -$$
$$- 0.09x_1x_5 - 0.04x_2x_4 + 0.08x_3x_4 + 0.014x_3x_5$$

(5)

– density

$$\begin{aligned}
\rho_o =\ & 999 - 67.9x_1 + 9.45x_2 + 3.55x_3 - \\
& - 3.39x_4 - 4.49x_5 + 37.19x_1^2 + 0.69x_2^2 - \\
& -0.31x_3^2 + 0.19x_4^2 + 0.19x_5^2 + 4.81x_1x_2 + \\
& + 5.18x_1x_3 + 6.18x_2x_3 + 6.81x_2x_4 + 2.56x_2x_5 - \\
& - 6.56x_3x_4 - 2.06x_3x_5 - 5.43x_4x_5.
\end{aligned} \tag{6}$$

To determine the optimal water consumption the following mathematical model was developed, % of the mixture mass:

$$\begin{aligned}
W =\ & 53.31 + 2.06x_1 - 1.22x_2 + 0.49x_3 + \\
& + 0.33x_4 - 0.19x_5 + 0.79x_1^2 + 0.79x_2^2 + 0.29x_3^2 + \\
& + 0.29x_4^2 - 0.22x_1x_2 - 0.53x_1x_3 - 0.28x_1x_4 + \\
& + 0.41x_2x_4 - 0.28x_2x_5 + 0.22x_3x_4 - 0.34x_3x_5.
\end{aligned} \tag{7}$$

Using the models (Eqs. 4–7), graphic dependences of the output parameters on two influence factors were obtained (see Fig. 1–3). The other factors, which are not shown in each of the graphs, was fixed at main (zero) level.
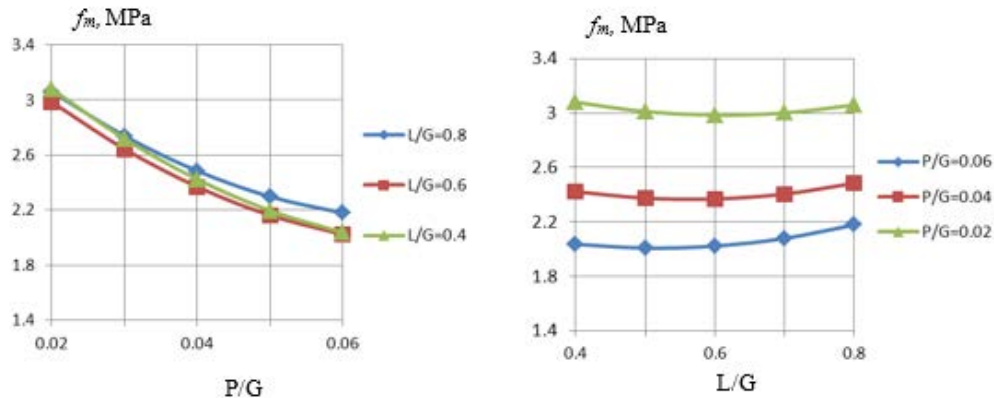
**Figure 1. Dependence of the GPM mortar compressive strength
on perlite content (P/G) and limestone powder (L/G).**

Analyzing the obtained experimental and statistical compressive strength model (Eq. 4), it can be noted that, the most significant influencing factor is the perlite-gypsum ratio (x_1). Varying it from -1 to +1 (from P/G = 0.02 to P/G= 0.06) leads to a decrease in strength of 35 % (see Fig. 1).

The character of the flexural strengths dependences based on the model (Eq. 5) is not significantly different (see Fig. 2). The factor that has the most influence on flexural strength is also the content of perlite in GPM (x_1). Increasing the limestone powder content (x_2) and other variable factors in varied limits did not significantly influence to the mortar strength.
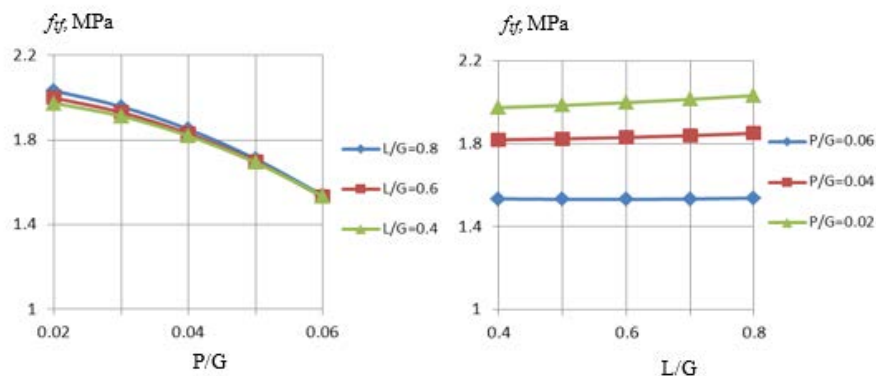
**Figure 2. Dependence of the GPM mortar flexural strength
on perlite content (P/G) and limestone powder (L/G).**

Analyzing the obtained density model (Eq. 6) and related graphical dependencies (Fig. 3), it can be noted that the most influential factor that reduces the density of the GPM is also the content of perlite P/G (x_1). The value of its linear coefficient in the regression (Eq. 6) significantly exceeds than those of four other factors.
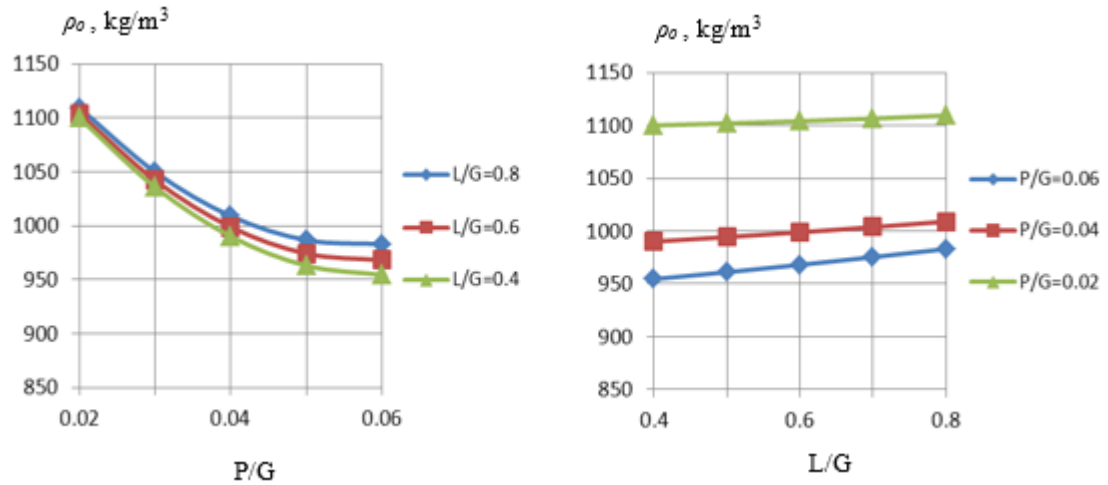
**Figure 3. Dependence of the GPM mortar density
on perlite content (P/G) and limestone powder (L/G).**

The experimental and statistical water consumption model (Eq. 7) and graphical dependencies (Fig. 4) show that, with an increase in the perlite content (P/G) from 0.02 to 0.06, the water consumption increases on average by 10 %. The influence of other investigated factors can be considered insignificant.
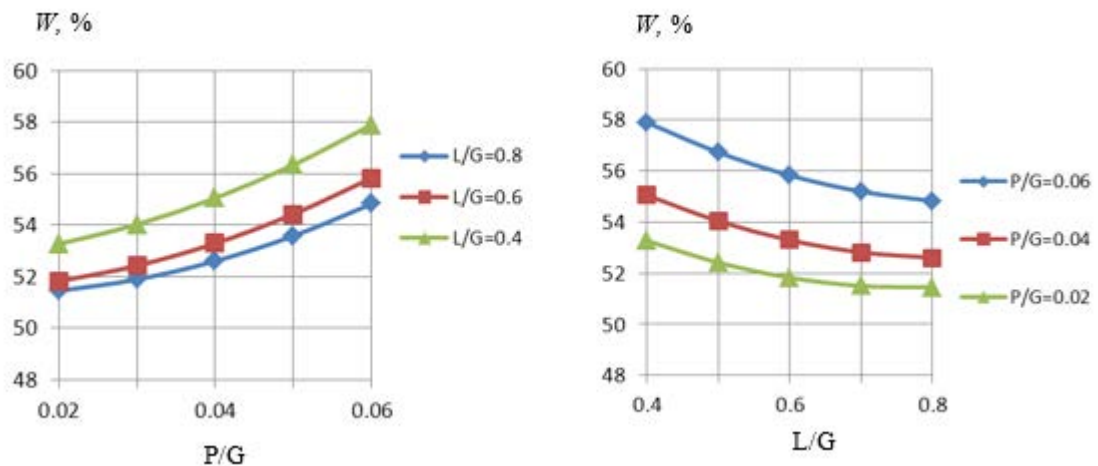
**Figure 4. Dependence of the GPM mortar water consumption
on perlite content (P/G) and limestone powder (L/G).**

In order to obtain the optimal composition of the gypsum-perlite mixture, it is necessary to solve the problem of mathematical programming with the following formulation: to find such a composition of mixture which would allow to provide the necessary quality parameters of the GPM mortar and allowing to minimize the mortar cost in limits of admissible factors' values.

For example, the defining parameters of the mortar quality are its compressive strength and its density. Moreover, the strength must be at least of a certain value, and the density of the mortar is not more than of a certain value. Then the mathematical setting of this problem can be formulated as follows

$$
\begin{aligned}
E_M = E_G \cdot G + E_P \cdot P + E_L \cdot L + \\
+ E_{HL} \cdot HL + E_{CE} \cdot CE + E_{SE} \cdot SE \to min
\end{aligned}
\tag{8}
$$

While the necessary quality parameters is provided

$$
\begin{aligned}
f_m \geq \left(x_1, \ x_2, \ldots, \ x_5 \right) \\
\rho_o \leq \left(x_1, \ x_2, \ldots, \ x_5 \right)
\end{aligned}
\tag{9}
$$

Dvorkin, L.I., Bordiuzhenko, O.M., Kovalyk, I.V.

While

$$x_1 \ldots x_5 \in \left[-1 \ldots +1\right] \tag{10}$$

Where,

E_G, E_P, E_L, E_{HL}, E_{CE}, E_{SE} are the cost of gypsum binder, perlite sand, limestone powder, hydrated lime, cellulose ether and starch ether, respectively, \$/kg;

G, P, L, HL, CE, SE are the consumption of gypsum binder, perlite sand, limestone powder, hydrated lime, cellulose ether and starch ether, respectively, kg/m³ of dry mixture.

The conversion of the GPM composition parameters into the codified form is carried out as follows:

$$x_1 = \frac{P/G - 0.04}{0.02}; \quad x_2 = \frac{L/G - 0.6}{0.2}; \quad x_3 = \frac{HL/G - 0.37}{0.2};$$

$$x_4 = \frac{CE - 0.25}{0.02}; \quad x_5 = \frac{SE - 0.05}{0.02}. \tag{11}$$

The calculation sequence is as follows.

- Substitute in the models (Eq. 4 and 6) the values of strength and density to be ensured, and in Eq. (8) – the GPM components value.
- Set in Eq. (10) the limit values of factors (in coded values from –1 to 1).
- The MS Excel Solver software picking up various combinations of factors, providing at least the specified strength value and not more than the specified density value by Eqs. (4) and (6) while minimizing function (Eq. 8).

A result of such iterations is determining the optimal values of composition factors: P/G ratio, L/G ratio, HL/G ratio, cellulose ether content and starch ether content. Water demand can be calculated by Eq. (7).

The gypsum binder consumption can be founded by Eq. (12):

$$G = \frac{1000 - (CE + SE)}{P/G + L/G + HL/G + 1}. \tag{12}$$

3.1. Numerical example

Determine the gypsum-perlite mixture composition with the following properties at 7 days: compressive strength of 2.3 MPa; density of 950 kg/m³ as well as with a mixture workability of 8 cm. Were used experimental-statistical models (Eqs. 4-6) Assume the cost of the main mixture components as follows, \$/kg: $G = 2$; $P = 10$; $L = 1$; $HL = 4$; $CE = 190$; $SE = 104$.

1. Substituting the compressive strength value ($f_m \geq 2{,}3$) in Eq. (4) and density ($\rho_o \leq 950$) in Eq. (5), obtain the restriction function (Eq. 9) of the problem:

$$f_m = 2.46 - 0.05x_1 + 0.04x_2 + 0.01x_3 -$$
$$- 0.11x_4 + 0.18x_5 + 0.16x_1^2 + 0.21x_2^2 + 0.56x_3^2 -$$
$$- 0.34x_4^2 - 0.44x_5^2 - 0.14x_1x_2 - 0.07x_1x_3 -$$
$$- 0.16x_1x_5 - 0.07x_2x_3 - 0.16x_2x_5 + 0.27x_3x_5 \geq 2.3;$$

$$\rho_o = 999 - 67.9x_1 + 9.45x_2 + 3.55x_3 -$$
$$- 3.39x_4 - 4.49x_5 + 37.19x_1^2 + 0.69x_2^2 -$$
$$- 0.31x_3^2 + 0.19x_4^2 + 0.19x_5^2 + 4.81x_1x_2 +$$
$$+ 5.18x_1x_3 + 6.18x_2x_3 + 6.81x_2x_4 +$$
$$+ 2.56x_2x_5 - 6.56x_3x_4 - 2.06x_3x_5 - 5.43x_4x_5 \leq 950.$$

2. Substitute the values of GPM components cost into Eq. (8), and specify the limitation of the factors values: from -1 to 1 (in coded form).

3. By varying different combination factors the values that satisfy the problem and minimize the total GPM cost. The following parameters were obtained by using originally developed routines implemented using the MS Excel Solver software:

$$x_1 = 0.89; \ x_2 = -0.44; \ x_3 = -1; \ x_4 = 0.6; \ x_5 = 1.$$

For the obtained factors' values, from Eqs. (4 and 6) follows that f_c = 2.4 MPa, which corresponds to the required compressive strength value, and ρ_o = 950 kg/m^3, which provides the required density value.

4. Determine the natural factors using Eq. (11):

$$P/G = 0.02 \cdot x_1 + 0.04 = 0.02 \cdot 0.89 + 0.04 = 0.057$$
$$L/G = 0.2 \cdot x_2 + 0.6 = 0.2 \cdot (-0.44) + 0,6 = 0.512$$
$$HL/G = 0.2 \cdot x_3 + 0.37 = 0.2 \cdot (-1) + 0.37 = 0.17$$
$$CE = 0.02 \cdot x_4 + 0.25 = 0.02 \cdot 0.6 + 0.25 = 0.26 \ \text{kg/m}^3$$
$$SE = 0.02 \cdot x_4 + 0.05 = 0.02 \cdot 1 + 0.05 = 0.07 \ \text{kg/m}^3.$$

5. The water consumption which provide a mixture workability of 8 cm according to Eq. (7) is, – by %:

$$W = 53.31 + 2.06x_1 - 1.22x_2 + 0.49x_3 +$$
$$+ 0.33x_4 - 0.19x_5 + 0.79x_1^2 + 0.79x_2^2 + 0.29x_3^2 +$$
$$+ 0.29x_4^2 - 0.22x_1x_2 - 0.53x_1x_3 - 0.28x_1x_4 + 0.41x_2x_4 -$$
$$- 0.28x_2x_5 + 0.22x_3x_4 - 0.34x_3x_5 = 57\%$$

– by mass:

$$W = W' \cdot 1000 \ / \ 100 = 57 \cdot 1000 \ / \ 100 = 570 \ l.$$

6. The gypsum binder consumption determined by Eq. (12):

$$G = \frac{1000 - (CE + SE)}{P/G + L/G + HL/G + 1} = \frac{1000 - (0.26 + 0.07)}{0.057 + 0.512 + 0.17 + 1} = 572.7 kg.$$

7. The minimum possible cost value per 1000 kg of GPM is found during the iterations in the "Solver" application according to Eq. (8):

$$E_{GPM} = 10 \cdot 33.1 + 1 \cdot 293 + 4 \cdot 97.4 + 190 \cdot 2.63 + 104 \cdot 0.7 + 2 \cdot 573 = \$2731.5.$$

8. The final GPM composition, kg is:

$$G = 573; \ P = 33; \ L = 293; \ HL = 97; \ CE = 2.6; \ SE = 0.7.$$

Proposed methodology allows to design of the mixture composition with a minimum cost and at the same time takes into account a greater number of factors than in the well-known manual [31]. At problem formulation stage for finding the GPM composition the desired values of strength and density should be correctly set. Obviously, these values are supposed to within the minimum and maximum possible value of the output parameter, since it is within these limits that the polynomial model adequately describes studied parameter. Such values can be easily found using the above - mentioned routines implemented in MS Excel Solver. For the above example, the limit values of strength and density within the factors variation range will be as follows:

$$f_m(min) = 1.5 \ \text{MPa}; \ f_m(max) = 3.4 \ \text{MPa}; \ \rho_o \ (min) = 926 \ \text{kg/m}^3; \ \rho_o \ (max) = 1120 \ \text{kg/m}^3.$$

Some deviation way beyond the output parameters limits is also possible. In this case, along with the optimization problem, an extrapolation problem is also solved, allowing to take the factor`s values outside the variation range (for example, x_1 ... x_3 = 1.1; 1.2; 1.3). However, it should be borne in mind that extrapolation may be due to certain errors, and these errors become more significant, the farther beyond the variation range limits. Extrapolation is possible, if according to the research results there is no doubt that outside the factors variation region the function nature remains unchanged.

4. Conclusions

Adequate mathematical models gypsum-perlite mixture mortar properties (compressive and flexural strengths, water consumption required for achieving the desired mixture workability) were obtained using mathematical experiments planning methodology. The models consider the influence of such main factors as perlite-gypsum ratio, limestone powder-gypsum ratio, hydrated lime-gypsum ratio, cellulose ether content and starch ether content.

Analysis of the obtained models shows that gypsum-perlite mixture mortar compressive strength depends mainly on the content of cellulose ether and starch ether, but the influence of the perlite-gypsum ratio also affects. As well, the perlite content is a main factor affecting the density and water demand.

Based on the obtained mathematical models, a method of design for building mixture composition was proposed. This method allows taking into account the special properties of the investigated materials and provides the most simple possibility for mixture composition optimization by a given minimum cost criterion. An additional advantage of the proposed method is a possibility to add a certain number of limitations. It allows simultaneous satisfaction of many quality indexes according to the given value.

In the authors' opinion, application of the proposed method in the production of building mixtures will allow more efficient use of raw materials and ensure high-quality mortars.

References

1. Ashtankar, V., Chore, H. Development of design mix roller compacted concrete dam at Middle Vaitarana. Advances in Concrete Construction. 2014. 2(2). Pp. 125–144.
2. Dvorkin, L., Dvorkin, O., Ribakov Y. Mathematical experiments planning in Concrete Technology. Nova Science Publishers. New York, 2012. 173 p.
3. Montgomery, D. Design and analysis of experiments. John Wiley & Sons. New York. 2001. 752 p.
4. Voznesenskiy, V.A., Lyashenko, T.V., Ogarkov, B.L. Chislennyie metodyi resheniya stroitelno-tehnologicheskih zadach na EVM [Numerical methods for solving problems of construction technology using computers]. Kiev: Vyshcha shkola, 1989. 324 p.
5. Dvorkin, L., Dvorkin, O. Basics of concrete science: optimum design of concrete mixtures. Saint-Peterburg: Amason (Kindle edition) Stroi-Beton, 2006. 692 p.
6. Barker, T. Quality by Experimental Design, Marcel Dekker Inc. New York, 1985. 384 p.
7. Box, G., Hunter, W., Hunter, J. Statistics for Experimenters: An Introduction to Design, Data Analysis, and Model Building. John Wiley and Sons, New York, 1978. 653 p.
8. Correia, S., Partala, T., Felipe, C., Loch, A. Segadães Factorial design used to model the compressive strength of mortars containing recycled rubber. Composite Structures. 2010. 92 (9). Pp. 2047–2051.
9. Dvorkin, L., Dvorkin, O., Gots, V. Ispytaniya betonov i rastvorov. Proyektirovaniye ikh sostavov. Moskva: Infra-Inzheneriya, 2014. 422 s.
10. Kosmatka, S., Kerkhoff, B. Panarese, W. Design and Control of Concrete Mixture. 14th Edition. PSA, Skokie, Illinois, 2014. 358 p.
11. Nunes, S., Matos, M., Duarte, T., Figueiras, H., Sousa-Coutinho, J. Mixture design of self-compacting glass mortar. Cement and Concrete Composites. 2013. No.43. Pp. 1–11.
12. Sebaalya, H., Varmab, S., James W. Optimizing asphalt mix design process using artificial neural network and genetic algorithm. Construction and Building Materials. 2018. 168 (20). Pp. 660–670.
13. Vimmrová, A., Keppert, M., Michalko, O., Černý, R. Calcined gypsum-lime-metakaolin binders: Design of optimal composition. Cement and Concrete Composites. 2014. No. 52. Pp. 91–96.
14. Dvorkin, L. Modified water-cement ratio rule for the design of air-entrained concrete. Magazine of Civil Engineering. 2019. 85(1). Pp. 123–135. DOI: 10.18720/MCE.85.10
15. Parveen, P., Singhal, D. Development of mix design method for geopolymer concrete. Advances in Concrete Construction. 2017. 5(4). Pp. 377–390. DOI: 10.12989/acc.2017.5.4.377
16. Barabanshchikov, Yu., Belyaeva, S., Arkhipov, I., Antonova, M., Shkol'nikova, A., Lebedeva, K. Influence of superplasticizers on the concrete mix properties. Magazine of Civil Engineering. 2017. 74(6). Pp. 140–146. DOI: 10.18720/MCE.74.11
17. Hendi, A., Mostofinejad, D., Sedaghatdoost, A., Zohrabi, M., Naeimi, N., Tavakolinia, A. Mix design of the green self-consolidating concrete: Incorporating the waste glass powder. Construction and Building Materials. 2019. No. 199. Pp. 369–384. DOI: 10.1016/j.conbuildmat.2018.12.020
18. Ashish, D.K., Verma, S.K. Determination of optimum mixture design method for self-compacting concrete: Validation of method with experimental results. Construction and Building Materials. 2019. Vol. 217. Pp. 664–678. DOI: 10.1016/j.conbuildmat.2019.05.034
19. Andrade, G., Polisseni, G., Pepe, M., Toledo Filho, R. Design of structural concrete mixtures containing fine recycled concrete aggregate using packing model. Construction and Building Materials. 2020. Vol. 252. 119091. DOI: 10.1016/j.conbuildmat.2020.119091
20. Soto-Pérez, L., López, V., Hwang, S. Response Surface Methodology to optimize the cement paste mix design: time-dependent contribution of fly ash and nano-iron oxide as admixtures. Materials and Design. 2015. Vol. 86. Pp. 22–29. DOI: 10.1016/j.matdes.2015.07.049
21. Sonebi, M. Medium strength self-compacting concrete containing fly ash: Modeling using factorial experimental plans. Cement and Concrete Research. 2004. Vol. 34 (7). Pp. 1199–1208. DOI: 10.1016/j.cemconres.2003.12.022

Dvorkin, L.I., Bordiuzhenko, O.M., Kovalyk, I.V.

22. Ferrándiz-Mas, V., Sarabia, L., Ortiz, M., Cheeseman, C., García-Alcocel, E. Design of bespoke lightweight cement mortars containing waste expanded polystyrene by experimental statistical methods. Materials and Design. 2016. No. 89. Pp. 901–912.

23. Nepomuceno, M., Oliveira, L., Lopes, S. Methodology for mix design of the mortar phase of self-compacting concrete using different mineral additions in binary blends of powders. Construction and Building Materials. 2012. 26(1). Pp. 317–326.

24. Nizina, T., Balykov A., Volodin V., Korovkin D. Fiber fine-grained concretes with polyfunctional modifying additives. Magazine of Civil Engineering. 2017. No. 4. Pp. 73–83. DOI: 10.18720/MCE.72.9

25. Jiao, D., Shi, C., Yuan, Q., An, X., Liu, Yu. Mixture design of concrete using simplex centroid design method. Cement and Concrete Composites. 2018. Vol. 89. Pp. 76–88. DOI: 10.17632/xhss7xv6wz.1

26. DeRousseau, M., Kaspzyk, J., Srubar, W. Computational design optimization of concrete mixtures: A revier. Cement and Concrete Reseach. 2018. Vol. 109. Pp. 42–53.

27. Guemmadi, Z., Resheidat, M., Chabil, H., Toumi, B. Modeling the Influence of Limestone Filler on Concrete: A Novel Approach for Strength and Cost. Jordan Journal of Civil Engineering. 2009. 3(2). Pp. 158–171.

28. Ziaei-Niaa, A., Tadayonfara, G., Eskandari-Naddaf, H. Dynamic Cost Optimization Method of Concrete Mix Design. Materials Today: Proceedings. 5 (2), Part 1. 2018. Pp. 4669–4677. DOI: 10.1016/j.matpr.2017.12.038

29. ISO 679:2009. Cement – Test methods – Determination of strength. International organization for standardization. 59 p.

30. Živorad, R. Design of experiments in chemical engineering: A practical guide. Wiley-VCH Verlag GmbH & Co. KGaA, Weinheim, 2004. 620 p. DOI: 10.1002/3527604162

31. Rukovodstvo po sostavam i primeneniyu teploizolyatsionnykh i ognestoykikh perlitovykh shtukaturok [Guidelines for the composition and application of heat-insulating and fire-resistant perlite plasters]. M., Stroyizdat, 1975. 15 p. (rus)

Contacts:

Leonid Dvorkin, dvorkin.leonid@gmail.com
Oleh Bordiuzhenko, o.m.bordiuzhenko@nuwm.edu.ua
Iryna Kovalyk, i.v.kovalyk@nuwm.edu.ua

Ultimate load capacity
of high-performance fibre-concrete hollow square columns

K. Buka-Vaivade[a], D. Serdjuks*[a], J. Sliseris[a], L. Pakrastins[a], N. Vatin[b]
[a] *Riga Technical University, Riga, Latvia*
[b] *Peter the Great St. Petersburg Polytechnic University, St. Petersburg, Russia*
*E-mail: Dmitrijs.Serdjuks @rtu.lv

Abstract. High-performance fibre-reinforced concrete is gaining popularity due to fibres ability to improve the poor properties of high-performance concrete. High-performance materials make using of thin-wall structures possible. Square section with square hollow provides decreasing of non-renewable material consumption, column's high stiffness in the both planes and possibility to integrate the engineering communication inside of columns. The current study focuses on the development of analytical simplified calculation method that approximate output results of finite elements calculations for columns under eccentric loading with complicate hollow square-section. Analytical simplified calculation method to determine column's load-carrying capacity is developed as the second-degree polynomial equation which is based on response surface method. The variables of equation are column height and material consumptions of the high-performance fibre reinforced concrete and steel of the additional longitudinal reinforcement. Data set of 27 experiments calculations was used to get the coefficients of adequate equation. Based on the results, the obtained equation makes it possible to predict the load-carrying capacity of the column in selected the factors interval on which a function was defined with sufficient precision. The difference between load-carrying capacities determine by numerical model based on the finite element method and by obtained second-degree equation does not exceeds 3.3 %.

1. Introduction

The object of this investigation is determination of ultimate load capacity of hollow high-performance steel fibre reinforced concrete column with height 3.5–4.5 m and variable consumptions of concrete and steel of additional longitudinal reinforcement.

As total world population continues to grow rapidly, the principle of sustainable development is becoming ever more important. Therefore, the problem of how to make the best use of limited non-renewable resources to satisfy unlimited human wants is actual now. Concrete is the most used man-made construction material. High-performance concrete is characterized by higher specific strengths than ordinary concrete, so its use in load-bearing structures is more rational. Fibres can be used to decrease fragility of the high-performance concrete and to improve the deformative properties of the concrete [1–14]. High-performance steel fibre reinforced concrete allows constructive solutions like thin-wall structures, which reduce material consumption and dead load of structures.

The interest of the use of hollow concrete columns is growing due to several reasons, including their effective section properties in terms of higher strength/mass and stiffness/mass ratios compared to solid sections with the same cross-section area; reduced weight of the structure and, accordingly, the overall foundation sizes, therefore also reduced cost and environmental impact; provided space to integrate the engineering communications inside of columns and to allow access for services of plumbing and electric wiring [15–21]. In addition to these benefits, as investigations of hollow concrete columns behaviour show,

the capacity of hollow concrete columns is comparable to solid columns or even higher, because of difference in the stress distributions in the column sections. The absence of the concrete core changes triaxial stress state as it is in solid concrete columns to biaxial stress distribution in hollow concrete columns sections [19]. One of the most important problem of the hollow concrete columns is low deformation capacity resulting in brittle failure behaviour [18–19]. The use of discrete fibres is recognized as a successful solution to this problem [17, 21].

There are many studies [22–26] that confirm high computational cost of high-performance fibre reinforced concrete structural analyses based on finite element models. Calculations with the 3D numerical model with huge number of finite elements are complex and time-consuming, therefore the options of using finite element models with larger element sizes [22], symmetrical conditions [23–25] and two or one-dimensional numerical models [26–27] are generally selected to achieve reliable results with less computational time. So, the aim of this investigation is to develop simplified analytical calculation method that approximate ultimate load capacity output results of finite elements calculations for hollow high-performance steel fibre reinforced concrete column under eccentric loading. Proposed method is based on response surface methodology. Several tasks of the study have been set for this purpose. The first task is validation of the 3D numerical model by experimental data to determine accuracy of finite element model of high-performance fibre reinforced concrete structure. The second task is comparison of calculation results obtained by 3D numerical model and 1D numerical model, to evaluate possibility of reducing of computational time by using simplified 1D numerical model. And the last task is experimental design to get experimental data set for development of the second order polynomial equation on which the method to be developed is based. The field of application of the simplified analytical calculation method, which makes it possible to predict the results of the ultimate load capacity of the hollow high-performance fibre reinforced concrete column in selected region of interest is the initial design stage, during which it is necessary to determine the used structures approximate dimensions and materials.

2.   Methods

2.1. Object of investigation

A hollow square-section column (Fig. 1) subjected to the compression and bending was considered as an object of this investigation. Constant 500×500 mm external dimensions and variable hollow square-section wall thickness t was taken. As a basis of the high-performance steel fibre reinforced concrete material high-performance concrete of class C60 /75 [28] with 1 % of steel RC 65/35 BN-type fibres are used. Composition of used material is taken from the publication [29]. Steel of class B550 is used for additional longitudinal reinforcement of the column.
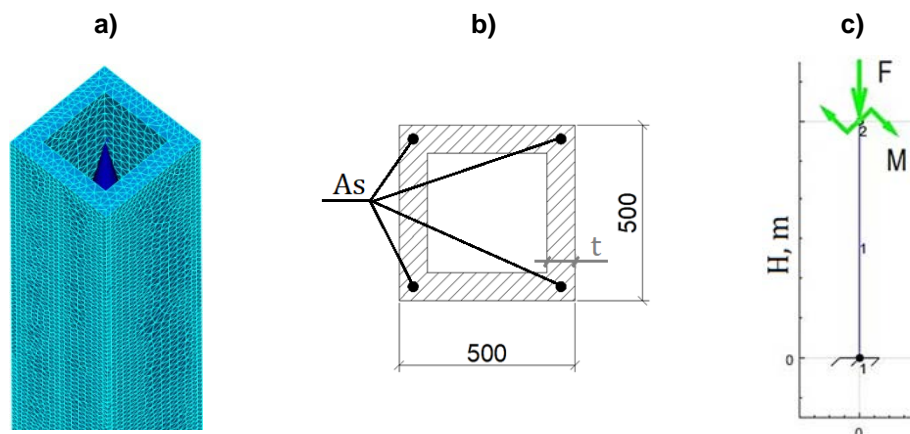
Figure 1. Details of column structure: a) column 3D numerical model with meshing; b) hollow square-section of column with longitudinal reinforcement; c) design scheme of the column.

As the factors interval on which a function was defined for the column subjected to the compression and flexure variable parameters for analytical simplified calculation method to determine column ultimate load capacity are chosen column height H from 3.5 to 4.5 m and material consumption of the high-performance fibre reinforced concrete and steel of the additional longitudinal reinforcement by regulation of variable from 5 to 12 cm wall thickness t of the column hollow square-section and area of the additional longitudinal steel reinforcement in column cross-section A_s with limits from 0 to 1.5 % of concrete area of the column cross-section.

The compression stress-stain curve of the used high-performance fibre reinforced concrete is summarised in Fig. 2.
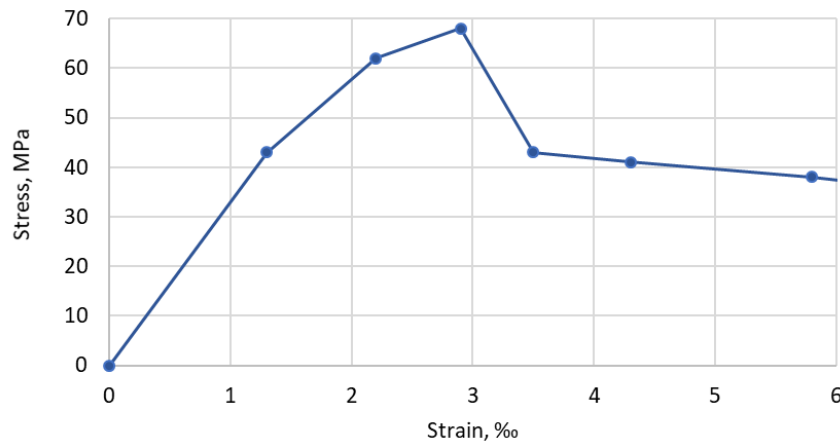
Figure 2. Compression stress-stain curve for high-performance steel fibre concrete.

2.2. Development of analytical simplified ultimate
load capacity calculation method

To develop analytical simplified calculation method of column ultimate load capacity for variable column height and material consumption of the steel of the additional longitudinal reinforcement and high-performance concrete, response surface methodology is used. Response surface method is based on the search of adequate polynomial equation, which describes the behaviour of the experimental data set with the objective and makes it possible to predict the results of the objective in some factors interval on which a function was defined.

The dependences of ultimate load capacity of the columns on the height, wall thickness of the hollow square-section and area of the additional longitudinal steel reinforcement in column cross-section as a percentage of the concrete area were obtained as the second-degree polynomial equations. The second-degree polynomial equation is chosen in accordance with the reference's recommendations due to its simplicity and precision [30]. Equation (1) was written for the case, when ultimate load capacity was considered as a parameter of optimization.

$$F,M = b_0 + b_1 H + b_2 t + b_3 A_s + b_{12} Ht +$$
$$+ b_{13} HA_s + b_{23} tA_s + b_{11} H^2 + b_{22} t^2 + b_{33} A_s^2$$

(1)

where: F, M are axial load and bending moment, which characterize ultimate load capacity of the column;

b_i, b_{ij} are coefficients;

H is height of the column, m;

t is wall thickness, cm;

A_s is area of the longitudinal steel reinforcement in column cross-section as a proportion of the concrete area, %.

To receive experimental data set for the prediction of the ultimate load capacity of the column, experimental design with 3 input variables – H, t and A_s with 3 levels of each factor was made. Accepted values for the experiments are shown in Table 1.

Table 1. Experimental design.

Nr.	1	2	3	4	5	6	7	8	9	10	11	12	13	14	15	16	17	18	19	20	21	22	23	24	25	26	27
H, m	3.5	4	4.5	3.5	4	4.5	3.5	4	4.5	3.5	4	4.5	3.5	4	4.5	3.5	4	4.5	3.5	4	4.5	3.5	4	4.5	3.5	4	4.5
t, cm		5			8.5			12			5			8.5			12			5			8.5			12	
A_s, %					0									0.2									1.5				

For all of the 27 experiments calculations are made and ultimate load capacity as a function $F,M = f(H, t, A_s)$ are determined. Relationship between axial force and bending moment value is characterized by equation (2).

$$M = F \cdot e$$

(2)

where: M is bending moment acting on the column, kNm;

F is axial load acting on the column, kN;

e is eccentricity, m.

Simplified design scheme of the multi-storey building, where one of the ends of the column is fixed, and loads are transferred from each storey to the column with eccentricity by beams has been adopted, so that the eccentricity of the axial load, which forms a bending moment, is equal to the distance from the centre of the column cross-section to the centre of the hollow square-section wall of the column, according to the Fig. 3.
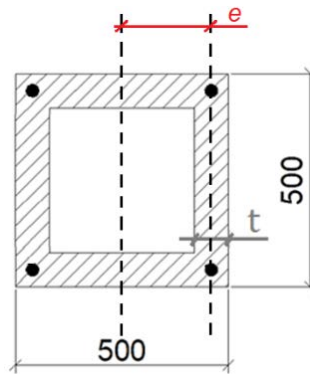
Figure 3. Eccentricity *e* of the column hollow square-section.

The developed 3D and 1D column numerical models, which considered non-linear behaviour of high-performance steel fibre reinforced concrete material by degradation of Young's modulus cause of cracking, are used for the experiment calculations. For the prediction of behaviour of high-performance steel fibre reinforced concrete damage variable is used [3].

Used 3D numerical model is validated by the experimental data from the publication [29] for high-performance steel fibre concrete column with pinned supports at both ends with additional longitudinal reinforcement subjected to compression and flexure, and then, verification of the 1D numerical model of column with fixed support at one end, according to an embodiment, has been done.

2.3. 3D model validation at compressive stress

The developed modelling procedure is validated for high-performance steel fibre reinforced concrete (HPSFRC) column subjected to combined action of compression and bending with additional longitudinal reinforcement. Experimental data from the publication [29] have been used to validate the model.
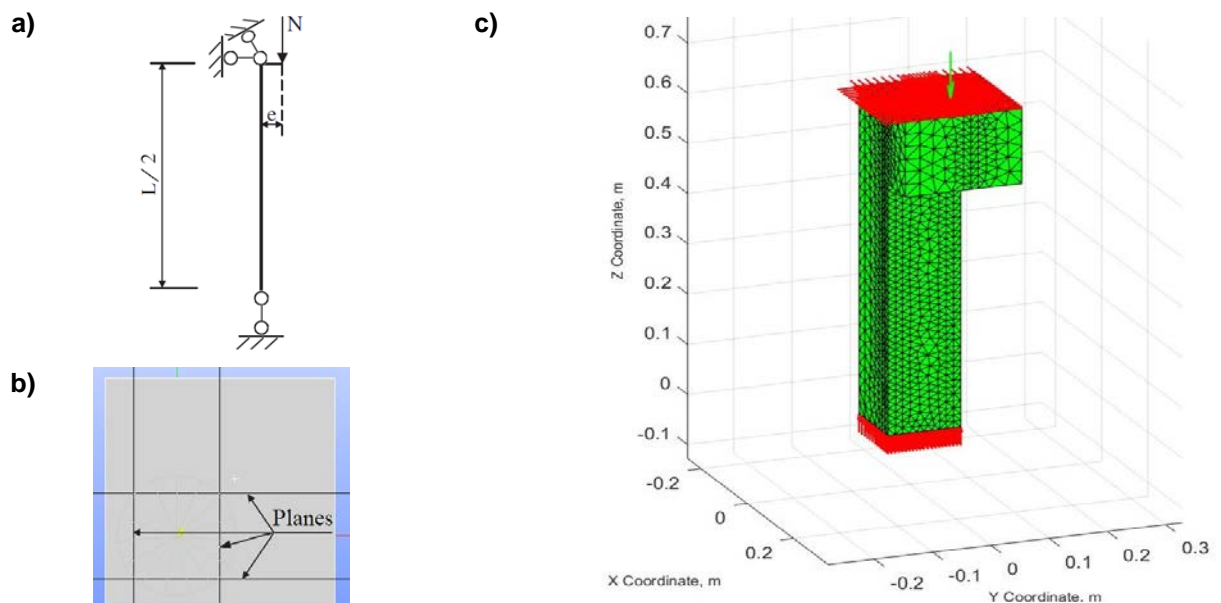
Figure 4. Process of modelling: a) design scheme for calculation of ½ column with
***e* = 50 mm and *L*/2 = 650 mm; b) view from top to column with additional planes for meshing;**
c) column mesh.

The column 3D model is designed for one-half the length of the column (Fig. 4 a)) to reduce the time of calculation by using symmetry conditions. The model is divided into finite elements in such a way that the volume-type finite elements nodes coincide with the beam-type finite elements nodes, thus ensuring collaboration between concrete and longitudinal reinforcement. For this purpose, additional planes passing through longitudinal bars (Fig. 4 b)) are defined in the modelling process. The meshing of the model in the finite elements is related to these planes (Fig. 4 c)).

2.4. Verification of the 1D numerical model

Calculations with the 3D numerical model are complex and time-consuming, therefore verification of the 1D numerical model of the column with fixed support at one end, which is subjected to the compression and flexure has been done by comparison of the results of calculations with both models.

Calculations of 3 experiments with 3D and 1D model have been made. The values of input variables of these 3 experiments are shown in Table 2.

Table 2. Input variables for 1D model verification.

Nr.	1	2	3
H, m	3.5	4	4.5
t, mm	5	12	8.5
A_s, %	0.2	0	1.5

Verification of the 1D model is made by comparison of either crushing axial load values or load value at displacement value H/250, depending on which value is reached first with calculation results obtained by 3D numerical model. This value of axial load will be called the ultimate load capacity.

3. Results and Discussions

3.1. Accuracy of the 3D model

Based on results of validation, character of the failure scheme for both of 3D numerical model and experimental specimen are similar [31]. Load-displacement curves of column specimen subjected to the compression with flexure, according to laboratory tests and 3D numerical model calculations, are summarized in Fig. 5.
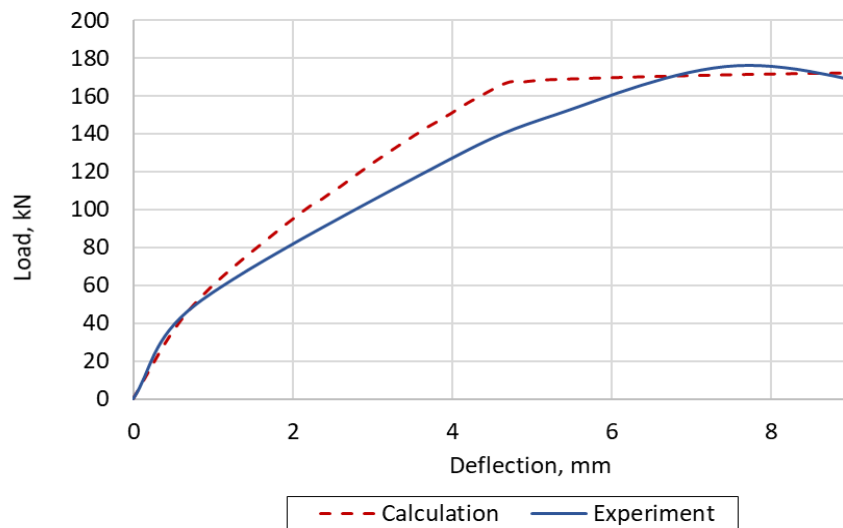
Figure 5. Load-displacement curves for column specimen.

According to the results obtained, the crushing axial load obtained from the laboratory test was 176 kN and bending moment 898.48 kNm, while the calculated by 3D non-linear numerical model crushing axial load was 172.462 kN and corresponding bending moment 862.31 kNm. The difference between design and experimentally determined axial load and bending moment is 2.0 % and 4.0 %, respectively. The behaviour of the calculation model at the linear stage is identical to the actual operation of the column specimen. The plastic behaviour of material is also similar in both cases. The behaviour of the calculation model is like the actual operation of the column specimen and it can be concluded, that developed model is safe for prediction of the behaviour of high-performance steel fibre reinforced concrete material.

3.2. Accuracy of the 1D model

The resulting load-displacement curves of 1D numerical model verification are enclosed in the Fig. 6. According to the results obtained, the load value at displacement value $H/250$ calculated by 3D and 1D non-linear numerical models for experiment Nr.1 is 353.9 kN and 342 kN, respectively; for experiment Nr.2 is 703.0 kN and 682 kN and for experiment Nr.3 is 823.8 kN and 805 kN. The difference between axial load values determined by 3D and 1D models is between 2.3 % and 3.4 %. As it can be seen from Fig. 6, linear-elastic stage of load-deflection curve obtained by 3D numerical model is until about 96 % of ultimate load capacity of columns, after what plastic stage is started. The 1D model produces more conservative results of the behaviour of the column subjected to the compression and flexure than 3D model. The load-deflection curve obtained by the 1D model is characterized by a more pronounced elastic-plastic stage, especially for specimens with large percentage of additional longitudinal reinforcement.
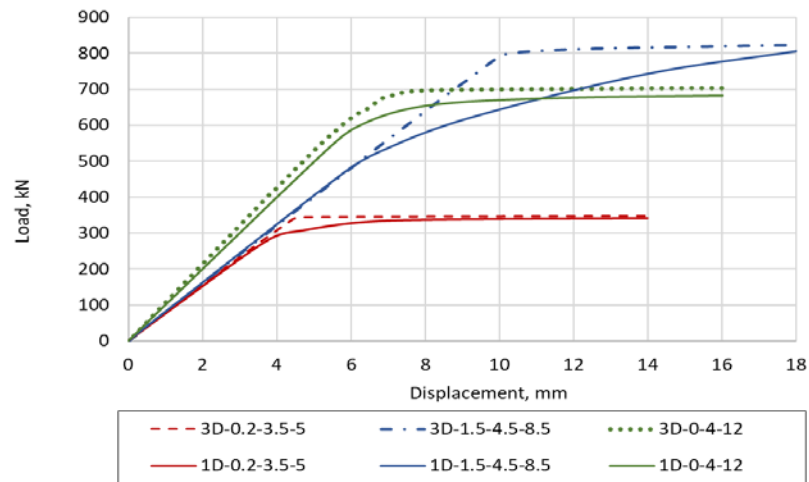
Figure 6. Load-displacement curves for columns, where 3D/1D – results obtained from 3D or 1D model, respectively; -A_s-H-t – values of input variables according Table 2.

The stress and strain profile for typical specimen with input variables 0.2-4-8.5 obtained by 1D model are summarized in Fig. 7. As it can be seen from the Fig. 7, the concrete in the compressed zone still continues to work in the elastic deformation region, while significant plastic deformations develop in the concrete in the tensile zone. The strains in the section are approaching the limiting values that precede the formation of normal cracks in the tensioned zone of the section.

a)

b)

c)

Neutral axis =0.088984
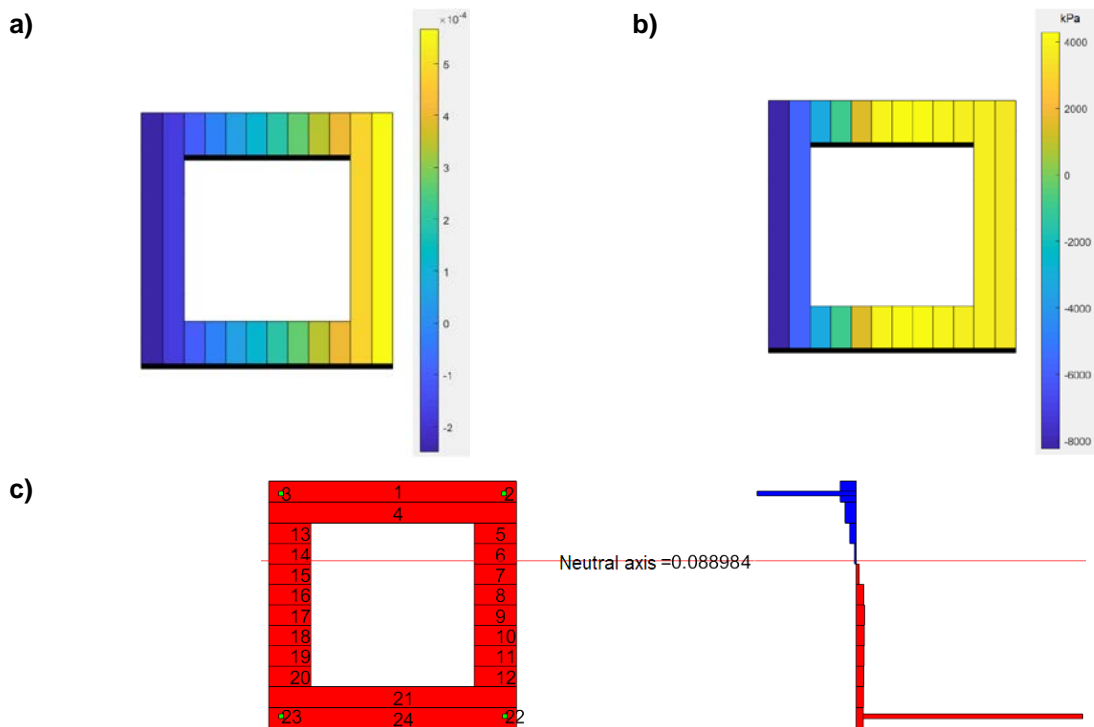
Figure 7. Profiles for specimen with A_s = 0.2 %, H = 4 m, t = 8.5 cm: a) of the strain in concrete material; b) of the stress in concrete material; c) of the stress in all materials of the section.

Taking into account, that the load value at displacement value $H/250$ refers to the plastic stage of the load-deflection curve obtained by both of models, 1D model will be used for the further calculations of the experiments.

3.3. Effect of the input variables on the column characteristics

The column height, wall thickness of the hollow square-section and area of the additional longitudinal steel reinforcement in column cross-section as a percentage of the concrete area have different effect on the column characteristics such as ultimate load capacity, column stiffness and energy absorption. The effect of changing the input variables on ultimate load capacity is summarized in the Table 3.

As it can be seen, column height has not large effect on the ultimate load capacity for columns with low percentage of longitudinal reinforcement, only for columns with $A_s = 1.5$ % ultimate load capacity decreases by 10-11 %.

The biggest effect on the ultimate load capacity leaves a change in the wall thickness of the hollow square-section. For the columns with wall thickness 8.5 and 12 cm the value of ultimate load capacity increases by 59.8-61.9 % and 113-119 %, correspondingly, in comparison with $t = 5$ cm.

Changes in the amount of reinforcement also have a significant effect. For the column with $H = 3.5$ m, the ultimate load capacity increases by 6.5-8.4 % and 73.5-78.6 % for the columns with the area of the additional longitudinal steel reinforcement in column cross-section as a percentage of the concrete area 0.2 and 1.5 %, correspondingly, in comparison with column without additional longitudinal reinforcement. But with increasing column height, this effect on ultimate load capacity decreases. At $A_s = 1.5$ % for columns with height 4 and 4.5 m the effect decreases by 14 and 24 %, correspondingly.

The effect of changing the input variables on column stiffness is summarized in the Fig. 8.
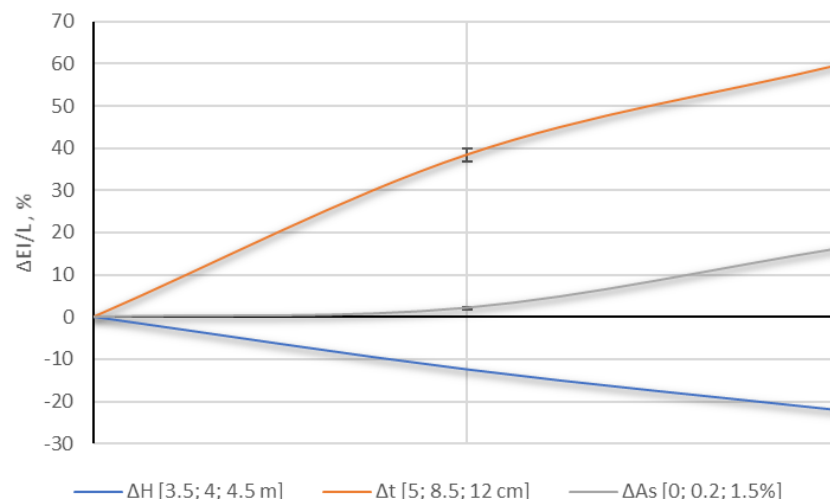
Figure 8. Effect of the changing of input variables H, t and A_s on the column bending stiffness.

As it can be seen from the Fig. 8, the biggest effect on the column bending stiffness, similar as on the ultimate load capacity, leaves a change in the wall thickness of the hollow square-section. For the columns with wall thickness 8.5 and 12 cm the value of bending stiffness increases by 37.2–39.7 % and 57.0–62.7 %, correspondingly, in comparison with $t = 5$ cm.

Changes in the amount of reinforcement do not have a significant effect on stiffness. For the column with $A_s = 0.2$ % and $A_s = 1.5$ %, the bending stiffness increases by 1.9–2.4 % and 14.2–18.3 %, correspondingly, in comparison with columns without additional longitudinal steel reinforcement.

As the height of the column increases, the column bending stiffness decreases. For the columns with height 4 and 4.5 m the value of bending stiffness decreases by 12.5 % and 22.2 %, correspondingly, in comparison with $H = 3.5$ m.

Table 3. Effect of the input variables on ultimate load capacity.

H, m	3.5	4	4.5	3.5	4	4.5	3.5	4	4.5	3.5	4	4.5	3.5	4	4.5	3.5	4	4.5	3.5	4	4.5	3.5	4	4.5	3.5	4	4.5
t, cm	5			8.5			12			5			8.5			12			5			8.5			12		
A_s, %	0									0.2									1.5								
N_{1D}, kN	321	320	320	513	512	511	683	682	680	342	340	339	550	547	545	740	735	731	557	525	500	902	847	805	1220	1145	1090
ΔH, %	0	-0.3	-0.3	0	-0.2	-0.4	0	-0.1	-0.4	0	-0.6	-0.9	0	-0.5	-0.9	0	-0.7	-1.2	0	-5.7	-10	0	-6.1	-11	0	-6.1	-11

H, m	3.5			4			4.5			3.5			4			4.5			3.5			4			4.5		
t, cm	5	8.5	12	5	8.5	12	5	8.5	12	5	8.5	12	5	8.5	12	5	8.5	12	5	8.5	12	5	8.5	12	5	8.5	12
A_s, %	0									0.2									1.5								
N, kN	321	513	683	320	512	682	320	511	680	342	550	740	340	547	735	339	545	731	557	902	1220	525	847	1145	500	805	1090
Δt, %	0	59.8	113	0	60	113	0	59.7	113	0	60.8	116	0	60.9	116	0	60.8	116	0	61.9	119	0	61.3	118	0	61	118

H, m	3.5									4									4.5								
t, cm	5			8.5			12			5			8.5			12			5			8.5			12		
A_s, %	0	0.2	1.5	0	0.2	1.5	0	0.2	1.5	0	0.2	1.5	0	0.2	1.5	0	0.2	1.5	0	0.2	1.5	0	0.2	1.5	0	0.2	1.5
N, kN	321	342	557	513	550	902	683	740	1220	320	340	525	512	547	847	682	735	1145	320	339	500	511	545	805	680	731	1090
ΔA_s,%	0	6.5	73.5	0	7.2	75.8	0	8.4	78.6	0	6.3	64.1	0	6.8	65.4	0	7.8	67.9	0	5.9	56.3	0	6.7	57.5	0	7.5	60.3

Table 4. Ultimate load capacity of the columns of 27 experiments.

Nr.	1	2	3	4	5	6	7	8	9	10	11	12	13	14	15	16	17	18	19	20	21	22	23	24	25	26	27
H, m	3.5	4	4.5	3.5	4	4.5	3.5	4	4.5	3.5	4	4.5	3.5	4	4.5	3.5	4	4.5	3.5	4	4.5	3.5	4	4.5	3.5	4	4.5
t, cm	5			8.5			12			5			8.5			12			5			8.5			12		
A_s, %	0									0.2									1.5								
N_{1D}, kN	321	320	320	513	512	511	683	682	680	342	340	339	550	547	545	740	735	731	557	525	500	902	847	805	1220	1145	1090
N_{eq}, kN	314	319	329	512	510	514	688	680	677	339	338	342	554	547	544	748	734	724	569	526	488	898	849	804	1207	1150	1099
Δ, %	2.3	0.3	2.9	0.3	0.3	0.5	0.7	0.3	0.5	0.9	0.6	0.8	0.8	0.1	0.2	1.1	0.2	0.9	2.1	0.2	2.3	0.4	0.2	0.1	1.1	0.5	0.8

The effect of changing the input variables on column energy absorption, what is defined as the surface below the load-displacement curve [32], is summarized in the Fig. 9.
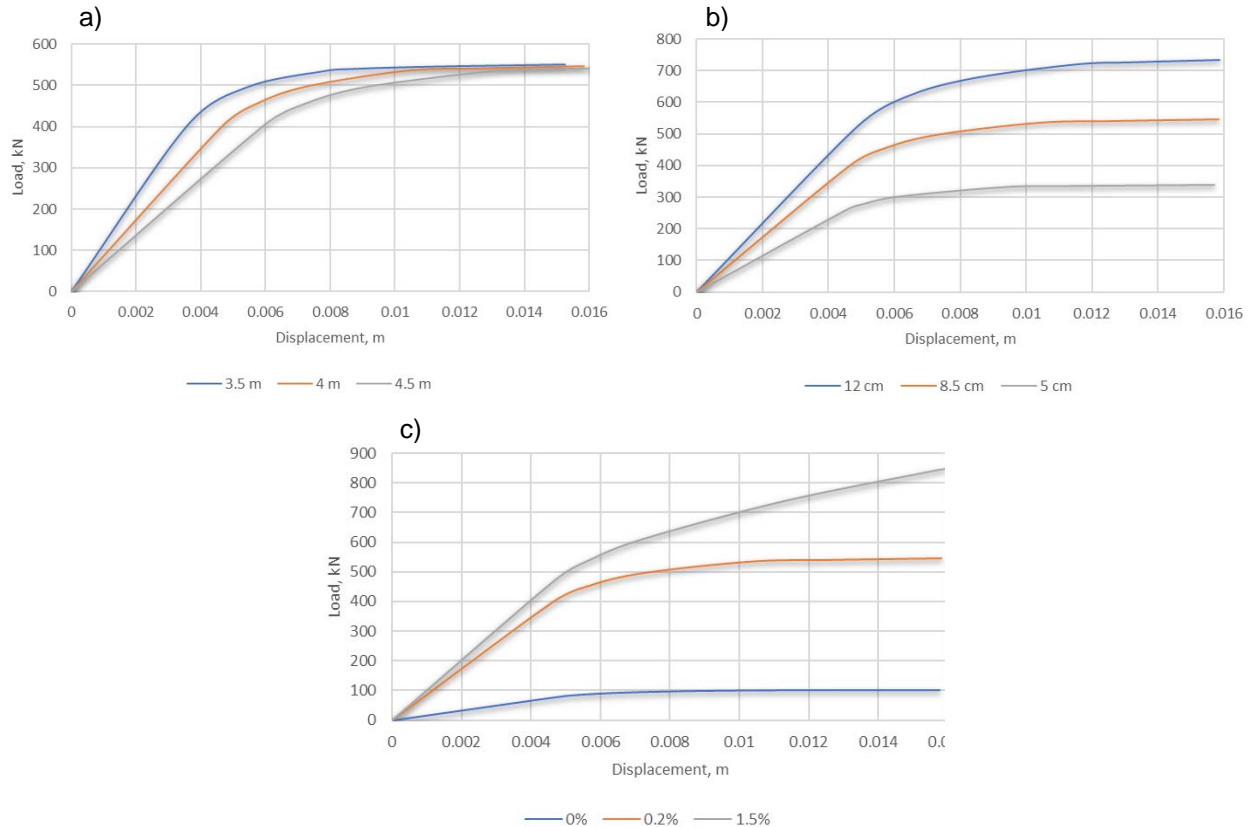
Figure 9. Dependence of the energy absorption for column with H = 4 m, t = 8.5 m and A_s = 0.2 % on changing of a) height, b) wall thickness of the hollow square-section, c) the area of the additional longitudinal steel reinforcement in column cross-section as a percentage of the concrete area.

As it can be seen from the Fig. 9 a) the effect of the column height on the energy absorption is insignificant. The largest increase of energy absorption is observed from the changes in the amount of additional longitudinal reinforcements (Fig. 9 c)). The thickness of the hollow square-section wall has also significant effect. The results obtained coincide with other published researches [33].

3.4. Analytical simplified ultimate load capacity calculation method

Statistic data set of column ultimate load capacity, obtained from calculations of the 27 experiments, makes regression analyses possible. Based on the results of calculations, the coefficients for dependences (3) of ultimate load capacity of the columns on the height, wall thickness of the hollow square-section column and area of the longitudinal steel reinforcement in column cross-section as a percentage of the concrete area were obtained.

$$
\begin{aligned}
F,M = {} & 21.48 - 41.4 \cdot H + 81.91 \cdot t + \\
& + 218.21 \cdot A_s - 3.86 \cdot Ht - 64.18 \cdot HA_s + \\
& + 25.1 \cdot tA_s + 9.56 \cdot H^2 - 0.88 \cdot t^2 + 33.99 \cdot A_s^2
\end{aligned}
\tag{3}
$$

where designations are as for equation (1).

The dependence of column ultimate load capacity on material consumption of the steel of the longitudinal reinforcement and high-performance concrete for column with height of 4 m is shown in the Fig. 9.

**Figure 9. The dependence of column ultimate load capacity (F)
on the wall thickness (t) and amount of longitudinal reinforcement (A_s).**

The values of ultimate load capacity of the columns of 27 experiments calculated by 1D numerical models (N_{1D}) and by the equation obtained (N_{eq}) and their percentage comparison are summarized in Table 4.

As it can be seen from the Table 4 relative error of ultimate load capacity of the columns predicted by obtained second order polynomial equation (3) for the 27 designed experiments is with limits from 0.1 to 2.9 %.
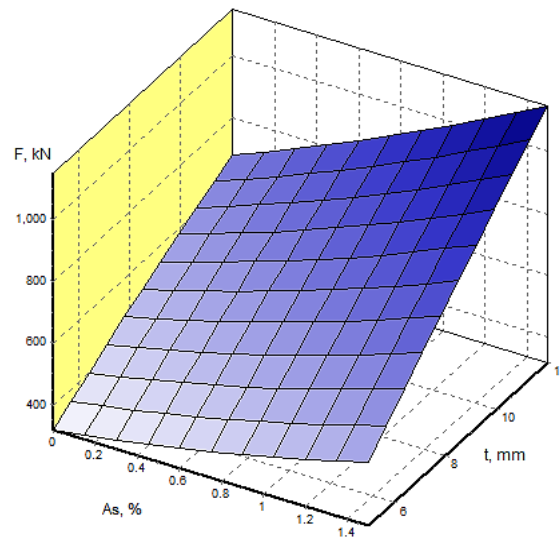
To check adequacy of the obtained dependence (3) of ultimate load capacity of the columns on the height, wall thickness of the hollow square-section column and area of the additional longitudinal steel reinforcement in column cross-section as a percentage of the concrete area, 3 control calculations for column with random chosen input variables from the region of the interest have been made. The values of input column variables and comparison of obtained results for control calculations are summarized in Table 5.

Table 5. Input variables for control calculations.

Nr.	1	2	3
H, m	3.7	4.1	4.3
t, cm	7	11	6
A_s, %	1.2	0.2	0.7
N_{1D}, kN	676	682	478
N_{eq}, kN	666	681	462
Δ, %	1.5	0.2	3.3

As it can be seen from the results of 3 control calculations (Table 4) relative error of load-bearing capacity predicted by obtained polynomial equation (3) for the 3 control calculations is from 0.2 to 3.3 %, so the obtained by regression analyses equation fits well the ultimate load capacity of the 1D numerical model of the column subjected to the compression and flexure, therefore the use of the equation (3) as analytical simplified column load-bearing capacity calculation method is justified.

4.   Conclusions

Numerical models of high-performance steel fibre reinforced concrete columns were checked and showed adequate results. Analytical simplified calculation method that approximate output results of finite elements calculations for high-performance steel fibre reinforced concrete columns subjected to the compression and flexure with complicate hollow square-section was developed. The obtained second-degree polynomial equation makes it possible to predict the results of the ultimate load capacity of the column in selected the factors interval on which a function was defined with sufficient precision.

The results showed that:

Buka-Vaivade, K., Serdjuks, D., Sliseris, J., Pakrastins, L., Vatin, N.

- 3D numerical model fits the behaviour of compression elements and makes it possible to determine ultimate load of column with about 98 % precision;

- The using of 1D numerical model provides more conservative result than 3D numerical model, the difference of determined ultimate load capacity is up to 3.4 %, but 1D model can significantly reduce the time required for calculations;

- The wall thickness of the hollow square-section and area of the additional longitudinal steel reinforcement in column cross-section as a percentage of the concrete area have significant effect on the column characteristics such as ultimate load capacity, column bending stiffness and energy absorption, at the time when changes of the column height have negligible impact on the column characteristics;

- Obtained equation for prediction of ultimate load capacity of the column with random chosen parameters of cross-section from the factors interval on which a function was defined allows to determine it with precision more than 96 %.

5. Acknowledgements

References

1. Vougioukas, E., Papadatou, M. A model for the prediction of the tensile strength of fiber-reinforced concrete members, before and after cracking. Fibers. 2017. Vol. 5. No. 3. Article No. 27.

2. Olivito, R.S., Zuccarello, F.A. An experimental study on the tensile strength of steel fiber reinforced concrete. Composites: Part B. 2010. Vol. 41. Pp. 246–255.

3. Buka-Vaivade, K., Sliseris, J., Serdjuks, D., Pakrastins, L., Vatin, N.I. Rational use of HPSFRC in multi-storey building. Magazine of Civil Engineering. 2018. Vol. 84. No. 8. Pp. 3–14.

4. Klyuev S.V., Klyuev A.V., Abakarov A.D., Shorstova E.S., Gafarova N.G. The effect of particulate reinforcement on strength and deformation characteristics of fine-grained concrete. Magazine of Civil Engineering. 2017. Vol. 75. No. 7. Pp. 66–75.

5. Singh, H. Steel fiber reinforced concrete – behavior, modelling and design. Ludhiana: Springer, 2017, 172 p.

6. Kazemi, M.T., Golsorkhtabar, H., Beygi, M.H.A., Gholamitabar, M. Fracture properties of steel fiber reinforced high strength concrete using work of fracture and size effect methods. Construction and Building Materials. 2017. Vol. 142. Pp. 482–489.

7. Ulas, M.A., Alyamac, K.E., Ulucan, Z.C. Effects of aggregate grading on the properties of steel fibre-reinforced concrete. IOP Conference Series: Materials Science and Engineering. 9th International Conference Fibre Concrete 2017, Prague, Czech Republic, September 13-16, 2017. Vol. 246, No. 1. Article No. 012015.

8. Nikolenko, S.D., Sushko, E.A., Sazonova, S.A., Odnolko, A.A., Manokhin, V.Ya. Behaviour of concrete with a disperse reinforcement under dynamic loads. Magazine of Civil Engineering. 2017. No. 7. Pp. 3–14.

9. Simões, T., Octávio, C., Valença, J., Costa, H., Dias-da-Costa, D., Júlio, E. Influence of concrete strength and steel fibre geometry on the fibre/matrix interface. Composites Part B: Engineering. 2017. Vol. 122. Pp. 156–164.

10. Balanji, E. K. Z., Sheikh, M.N., Hadi, M.N.S. Behavior of hybrid steel fiber reinforced high strength concrete. Proceedings of the First European and Mediterranean Structural Engineering and Construction Conference EURO-MED-SEC-1, Istanbul, Turkey, May 24-29, 2016. Pp. 29–34.

11. Travush, V.I., Konin, D.V., Krylov, A.S. Strength of reinforced concrete beams of high-performance concrete and fiber reinforced concrete. Magazine of Civil Engineering. 2018. No. 1. Pp. 90–100.

12. Savita, Shwetha S., Malanbi, Shweta, Saksheshwari, Manjunath K. Experimental study on strength parameters of steel fiber reinforced concrete using GI wire & fly ash. International Research Journal of Engineering and Technology. 2018. Vol. 5. No. 5. Pp. 3271–3277.

13. Kirsanov, A.I., Stolyarov, O.N. Mechanical properties of synthetic fibers applied to concrete reinforcement. Magazine of Civil Engineering. 2018. Vol. 80. No. 4. Pp. 15–23.

14. Taheri Fard, A.R., Soheili, H., Ramzani Movafagh, S., Farnood Ahmadi, P. Combined effect of glass fiber and polypropylene fiber on mechanical properties of self-compacting concrete. Magazine of Civil Engineering. 2016. Vol. 62. No. 2. Pp. 26–31.

15. Lignola, G.P., Prota, A., Manfredi, G., Cosenza E. Modeling of RC hollow square columns wrapped with CFRP under shear-type load. 2008. Proceedings of the 4th International Conference on FRP Composites in Civil Engineering, CICE 2008.

16. Liang, X., Sritharan, S. Effects of confinement in square hollow concrete column sections. Engineering Structures. 2019. Vol. 191. Pp. 526–535.

17. Abbass, A.A., Abid, S.R., Arna'ot, F.H., Al-Ameri, R.A., Ozakca, M. Flexural response of hollow high strength concrete beams considering different size reductions. Structures. 2020. Vol. 23. Pp. 69–86.

18. Al-Gasham, T.S., Mhalhal, J.M., Jabir, H.A. Influence of post-heating on the behavior of reinforced self-compacting concrete hollow columns. Structures. 2019. Vol. 22. Pp. 266–277.

19. AlAjarmeh, O.S., Manalo, A.C., Benmokrane, B., Karunasena, K., Ferdous, W., Mendis, P. Hollow concrete columns: Review of structural behavior and new designs using GFRP reinforcement. Engineering Structures. 2020. Vol. 203. 109829.

20. Cassese, P., Ricci, P., Verderame, G.M. Experimental study on the seismic performance of existing reinforced concrete bridge piers with hollow rectangular section. Engineering Structures. 2017. Vol. 144. Pp. 88–106.

21. Azzawi, R., Abolmaail, A. Experimental investigation of steel fiber RC hollow columns under eccentric loading. Structures. 2020. Vol. 24. Pp. 456–463.

22. Arani, K.S., Zandi, Y., Pham, B.T., Mu'azu, M.A., Katebi, J., Mohammadhassani, M., Khalafi, S., Mohamad, E.T., Wakil, K., Khorami, M. Computational optimized finite element modelling of mechanical interaction of concrete with fiber reinforced polymer. Computers and Concrete. 2019. Vol. 23. No. 1. Pp. 61–68.

Buka-Vaivade, K., Serdjuks, D., Sliseris, J., Pakrastins, L., Vatin, N.

23. Tysmans, T., Wozniak, M., Remy, O., Vantomme, J. Finite element modelling of the biaxial behaviour of high-performance fibre-reinforced cement composites (HPFRCC) using Concrete Damaged Plasticity. Finite Elements in Analysis and Design. 2015. Vol. 100. Pp. 47–53.

24. Hameed, R., Sellier, A., Turatsinze, A., Duprat, F. Metallic fiber-reinforced concrete behaviour: Experiments and constitutive law for finite element modeling. Engineering Fracture Mechanics. 2013. Vol. 103. Pp. 124–131.

25. Ibrahim, A.M., Mahmood, M.S. Finite element modeling of reinforced concrete beams strengthened with FRP laminates. European Journal of Scientific Research. 2009. Vol. 30. No. 4. Pp. 526–541.

26. Buljak, V., Oesch, T., Bruno, G. Simulating fiber-reinforced concrete mechanical performance using CT-based fiber orientation data. Materials (Basel). 2019. Vol. 12. No. 5. 717.

27. Buka-Vaivade, K., Sliseris, J., Serdjuks, D., Sahmenko, G., Pakrastins, L. Numerical Comparison of HPFRC and HPC Ribbed Slabs. IOP Conference Series: Materials Science and Engineering. 2019. Vol. 660. 012054.

28. EN 1992-1-1: Eurocode 2: Design of concrete structures – Part 1-1: General rules and rules for buildings.

29. Tokgoz, S., Dundar, C., Tanrikulu, A. K. Experimental behavior of steel fiber high strength reinforced concrete and composite columns. Journal of Constructional Steel Research. 2012. Vol. 74. Pp. 98–107.

30. Saknite, T., Serdjuks, D., Goremikins, V., Pakrastins, L., Vatin, N.I. Fire design of arch-type timber roof. Magazine of Civil Engineering. 2016. Vol. 64. No. 4. Pp. 26–39.

31. Sliseris, J., Buka-Vaivade, K. Numerical Modelling of High Strength Fibre-Concrete's columns in Multi-Storey Building. IOP Conference Series: Materials Science and Engineering. 2019. Vol. 660. 012062.

32. Nurul Fazita, M.R., Abdul Khalil, H.P.S., Nor Amira Izzati, A., Rizal, S. Effects of strain rate on failure mechanisms and energy absorption in polymer composites. Failure Analysis in Biocomposites, Fibre-Reinforced Composites and Hybrid Composites. 2018. Pp. 51–78.

33. Kim, C.S., Hwang, H.J. Numerical Investigation on Load-carrying Capacity of HSC Encased Steel Angle Columns. Int. J. Concr. Struct. Mater. 2018. Vol. 12. 11.

Contacts:

Karina Buka-Vaivade, karina.buka.vaivade@gmail.com

Dmitrijs Serdjuks, Dmitrijs.Serdjuks@rtu.lv

Janis Sliseris, janis.sliseris@rtu.lv

Leonids Pakrastins, leonids.pakrastins@rtu.lv

Nikolai Vatin, vatin@mail.ru

DOI: 10.34910/MCE.104.13

Elasticity modulus of cement composites predicting using layer structure model

A.S. Korolev*a, N.I. Vatinb
a South Ural State University, Chelyabinsk, Russia
b Peter the Great St. Petersburg Polytechnic University, St. Petersburg, Russia
*E-mail: korolev@sc74.ru

Abstract. The deformability of concrete along with the compressive strength is the determining factor in the calculation of concrete and reinforced concrete structures. In practice, with the same strength, the deformative properties of concrete, especially monolithic, can vary in a significant range, which affects the actual deflection of span structures and their reinforcement coefficient. However, the modulus of elasticity/deformation of concrete in production is not normed, and the introduction of the norm requires obtaining available bases for calculating the deformability of concrete under load from the composition of the concrete mix. The use of a layer calculation model allows you to quickly and accurately predict the elastic modulus and deformation of concrete. On the base of this model elasticity modulus depending on concrete mix components characteristics and proportions calculation method received and tested.

1. *Introduction*

Currently, the issues of estimating and predicting the composite materials elastic modulus, including cement composites, remain relevant. The purpose of such research is to develop methods for ensuring the specified elastic and plastic deformability of concrete while maintaining the strength class. This makes it possible to increase the technical and economic efficiency of various building structures, especially slab and beam constructions.

In practice, compressive strength norm and control are implemented everywhere, while the main indicator of concrete deformability, the modulus of elasticity (deformation), is not controlled in any way. Therefore, designers and technologists have nothing in service except its relations with the strength of the normative documentation. However, with the modern expansion of monolithic concreting, their values vary in a fairly wide range. The concrete modulus of elasticity and plastic deformations norming would greatly facilitate the task of providing calculated deflections of slab and beam constructions. To do this, it's necessary to create a model that combines simple technological techniques and trends in managing the elasticity of concrete. This makes possible to think about the concrete elastic modulus or deformation norm implementation, both instantaneous and long-term. However, when setting standards for the modulus of elasticity (deformation) of concrete, it is necessary to provide manufacturers with recommendations for managing the module when calculating and selecting the composition of concrete mixtures, as well as materials for their manufacture. Among the mentioned techniques and trends for improving elastic properties, we can distinguish:

1) increasing the compressive strength of concrete by increasing the compressive strength/modulus of elasticity of hydrating cement paste in the composite [1–10]

2) increasing the compressive strength/modulus of elasticity of the aggregate [11–13]

3) increasing the volume content of a more elastic component-aggregate (heavy) or hydrating cement paste (with light aggregates) [14–16]

4) increasing the largest aggregate size and reducing the relative surface area of the aggregate [17–20]

A careful examination of the concrete elasticity modulus research results using the above techniques shows the absence of either a direct proportion or a direct connection between the module and each of the factors – strength concrete, modulus of elasticity of the aggregate, its maximum size and the content. It tells about the interaction of factors and the need to account for this interaction.

The greatest development of the theory of elasticity of composites was in the middle of the last century. Itskovich, Sheikin, Gansen, and others proposed computational models of the elasticity modulus from the main factors: the modulus of elasticity of components, the volume contents of components. Some models are based on the equal deformability of elements, others on their equal strength. I.N. Akhverdov [21] proposed a model that takes into account both the different deformations and different stresses of components.

$$E_c = \cfrac{1}{\dfrac{V_{agg}}{E_{agg}}k_{agg} + \dfrac{V_{c\,max}}{E_{cem}}k_{c\,max} + \dfrac{V_{c\,min}}{E_{cem}}k_{c\,min}} \tag{1}$$

where V_{agg} is the relative content of aggregate;

$V_{c\,max}$ is the relative content of the part of the hydrating cement paste with the maximum stress;

$V_{c\,min}$ is the relative content of the part of the hydrating cement paste with the maximum stress;

E_{agg} is the elastic modulus of the aggregate;

E_{cem} is the modulus of elasticity of hydrating cement paste;

k_{agg}, $k_{c\,max}$, $k_{c\,min}$ are the coefficients that take into account the proportion of tangent stresses during loading.

The given model takes into account different levels of tension of the composite elements during loading, and does not take into account the influence of the contact zone of the hydrated cement paste with the aggregate (ITZ).

If we try to summarize past and current research, we can highlight the following principles and postulates in the formation of elastic properties of cement composites:

1) cement composite is a three-phase structure, basic elements of which are hydrated cement paste, aggregate, and the contact area between them or interfacial transition zone (ITZ), these components have different elasticity and their different elasticity determines the overall deformation properties of the composite [15–20], spherulitic model is shown in Fig. 1, the contact area ITZ is more porous due to the water demand of the aggregate surface, so ITZ is more deformative in comparison to other elements;

2) the stress-strain state of the cement composite does not under the principle of additivity, each element in the overall structure has different stresses and deformations, so the elastic modules of elements, the volume content of elements, the degree of their involvement in the work, which depends on their geometric distribution and their differ-elasticity [3, 4, 10, 15, 20–21] are used as factors in creating mathematical models of elasticity or "stress-strain" dependencies.

Thus, when considering the operation of concrete under instantaneous loading without taking into account plastics, we can assume the validity of a layer design model with equal strength of elements, consisting of 3 consecutive continuous layers: cement paste, the contact zone with the aggregate ITZ and the aggregate. To simplify the calculation, consider a flat layer model in which there are no discrete elements, all elements are continuous within the surface area of the ITZ (Fig. 1).

In this paper, an attempt will be made to confirm the performance of this model and link it to the indicators of the composition of the concrete mix.
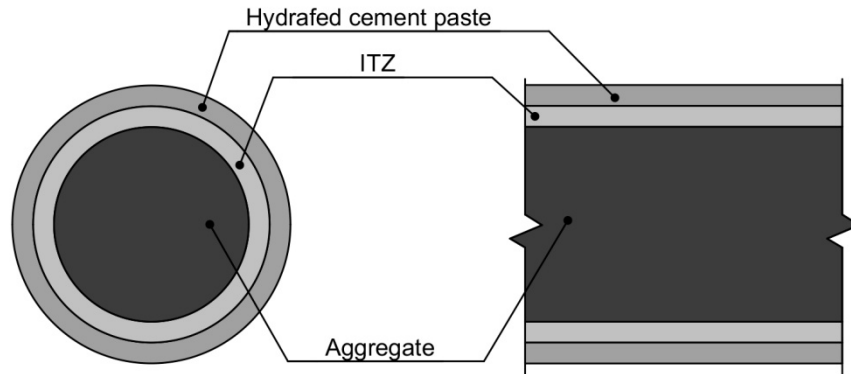
Figure 1. Spherical and layer calculation models of cement composite structure base element elastic and plastic properties.

2. *Materials and Methods*

The analytical method was used to select and evaluate the composites layer model calculation method.

Standard methods of Russian State Standards GOST 24452-80 "Concretes. Methods of prismatic, compressive strength, modulus of elasticity and Poisson's ratio determination" and GOST 22690-2015 "Concretes. Determination of strength by mechanical methods of nondestructive testing" were used to determine the modulus of elasticity and compressive strength of concrete of various classes. Each classes series of 3 samples were tested under compression on Matest press with determination of longitudinal elastic and plastic deformation using digital deformation sencors on every sides of sample. Compression was made by 10% of cracking stress stages to the 40% of cracking stress (Fig.2). Elasticity modulus has been determined as a relation of 30% cracking stress to the sum of elastic relative deformation except plastic on stages delay by standard. Compressive strength was determined on 6 samples series by standard.

Figure 2. Concrete sample modulus of elasticity under compression testing.

In our experiment to define fact concrete elasticity modulus, we used local producers materials: granite coarse aggregate and quartz sand with a strength of R_{agg} = 1000 MPa and an elastic modulus of E_{agg}=50*10⁴ MPa, Portland cement B42.5 CEM I with a water requirement of normal density cement paste 25 % and the strength of cement paste with a with water/cement ratio (W/C) of normal density in the standard age R_{cem} = 100 MPa and an elastic modulus of E_{cem} = 50*10⁴ MPa. Content of various classes mixture components presented in Table 1.

3. *Results and Discussion*

Considering experimental data of cement concrete deformation under compression (Fig. 3) goes to following conclusions:

1) when compressive loading of samples according to the standard method in steps of 10 % with a delay at each stage, after reaching 10...20% of the destructive load, there are well-known incoming plastic deformations, which continue to develop at the next loading stages, when bending plastic deformations are not observed;

2) as the load increases, the increase in elastic deformations is expected to remain constant, the increase in plastic deformations with loading increases in an arithmetic progression over the load according to the proposed model (Eq.2), in this regard, the modulus of concrete deformation is not constant and depends on the load.

$$\varepsilon_s = \varepsilon_{0.3} \frac{\sigma_s}{\sigma_{0.3}}.$$ (2)

ε_s is the relative deformation of the composite at a given loading stage;

$\varepsilon_{0.3}$ is the relative deformation of the composite at a given loading stage;

σ_s is the compression stress of the composite at a given loading stage;

$\sigma_{0.3}$ is the compression stress of the composite at a given loading stage.

3) compression failure is classically gradual as micro- and macro-cracks form and accumulate, and bending failure is instantaneous after initial cracking.
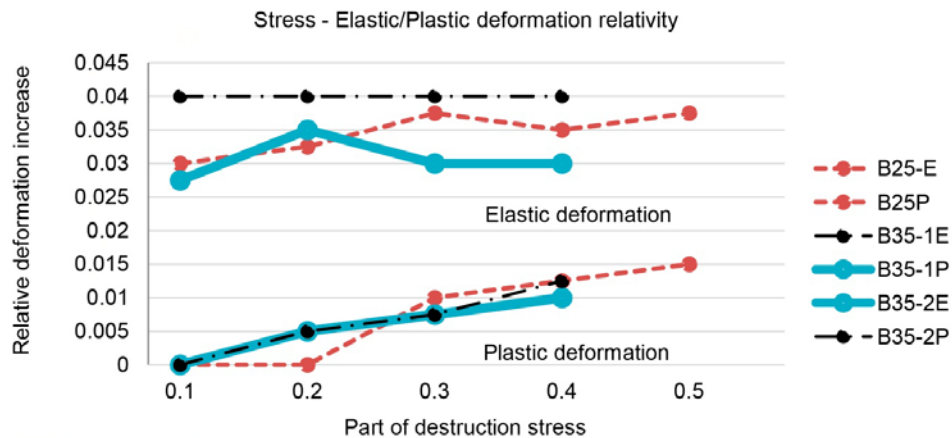
Figure 3. Concrete elastic and plastic deformations under compression by stages.

It is characteristic that concretes of the same strength class can differ significantly in elastic and plastic deformations. In this regard, we can offer the following model for the operation of cement composites under compressive loads. As the stress-strain state is loaded, it goes through the following stages:

1. 0 ... 10% of the destructive load is a zone of pure elasticity, joint elastic work of all components, only elastic deformations are observed. When stretching and bending, cement composites work only in this zone.

2. 10 ... 80% of the destructive load. Reaching the tensile strength of the cement paste shells, their primary fault in places of maximum tension (Fig. 4) and the development of microcracking, forming a zone of elastoplastic deformation. In this zone the cement paste and aggregate work is elastic, and highly porous contact zone, having the greatest deformation, is plastically squeezed due to transverse strains like compressible fluid. The total deformation includes instantaneous elastic and plastic deformations, because during instant loading, the contact area working elastically as the compressed fluid, which over time of transverse deformation coming to the accumulation of plastic deformations.

3. From 80% to destructive load is plastic zone, accumulated micro-cracking passes into macro-cracking, there are significant transverse cracks, visible cracks, and destruction.

Elastic deformation

Elastic-plastic deformation

Plastic deformation

Figure 4. Three stages of deformation of concrete at failure.

In this model, under instantaneous loading, all components of a cement composite, even in the elastic-plastic zone, are equally stressed, work together, and are elastic. Microplastic deformations can be considered as a sum of deformations along the contact zones, after complete compression beginning the stage of macro-cracking and destruction occurs.
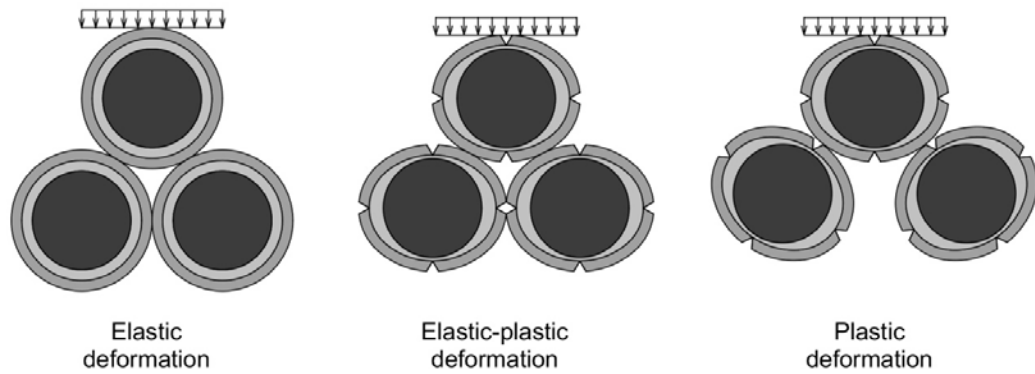
Differently from another models that all are spherulitic [15–20], the layer model in case of deformativity presenting the composite structure as a structure where all components non-discrete and continuous so modelled like layers.

According to the principle of equal stress of elements, to determine the elastic modulus of the composite, it is necessary to determine the sum of partial deformations of each micro-volume, which includes all 3 elements/layers of the concrete structure.

$$\varepsilon_c = \frac{\sigma_c}{E_c} = \frac{\dfrac{\sigma}{E_{cem}}\delta_{cem} + \dfrac{\sigma}{E_{itz}}\delta_{itz} + \dfrac{\sigma}{E_{agg}}\delta_{agg}}{\delta_{mv}} \tag{3}$$

σ_c is the stress in the composite structure;

E_c is the elastic modulus of the composite;

E_{cem} is the elastic modulus of the layer of the contact zone of hydrating cement paste and aggregate;

E_{itz} is the elastic modulus of the layer of the contact zone of hydrating cement paste and aggregate;

E_{agg} is the modulus of elasticity of the filler layer;

δ_{mv} is the thickness of the selected micro-volume that combines all the structural layers;

δ_{cem} is the thickness of the hydrating cement paste layer;

δ_{itz} is the layer thickness of the contact zone of hydrating cement paste and aggregate;

δ_{agg} is the thickness of the aggregate layer.

Converting the equation, we get the elastic modulus of the composite

$$E_c = \frac{\delta_{mv}}{\dfrac{\delta_{cem}}{E_{cem}} + \dfrac{\delta_{itz}}{E_{itz}} + \dfrac{\delta_{agg}}{E_{agg}}} \tag{4}$$

In its final form, the expression takes the form

$$E_c = \frac{E_{cem}E_{itz}E_{agg}}{cemE_{itz}E_{agg} + itzE_{cem}E_{agg} + aggE_{itz}E_{cem}}, \tag{5}$$

where $cem = \dfrac{\delta_{cem}}{\delta_{mv}}$; $itz = \dfrac{\delta_{itz}}{\delta_{mv}}$; $agg = \dfrac{\delta_{agg}}{\delta_{mv}}$.

In the resulting equation, the assumption is made that the elastic modulus of the aggregate particles (both large and small) is equal. if there is a significant difference, this expression should be used to determine the elastic modulus of the mortar and calculate the elasticity of the structure with a large aggregate using a 2-layer model [22].

If the elastic modulus of hydrating cement paste and aggregate can be quantified, then the elastic modulus of the contact zone, as well as the relative thicknesses of all layers, require approaches in determining.

The relative thicknesses of the "hydrating cement paste+contact zone" and "aggregate" layers can be calculated based on the composite layer model, in which the weighted average particle size is replaced by the weighted average size of the layers with a conditional specific surface area of the components. Accordingly, the relative thickness of "hydrating cement paste+contact zone" is determined

$$cem_0 = \frac{\delta_{cem0}}{\delta_{mv}} = \frac{S_{itz}\delta_{cem0}}{S_{itz}(\delta_{cem0} + \delta_{agg})} = \frac{V_{cem0}}{V_{cem0} + V_{agg}} \tag{6}$$

and the relative thickness of a layer of "aggregate"

$$agg = \frac{\delta_{agg}}{\delta_{mv}} = \frac{S_{itz}\delta_{agg}}{S_{itz}(\delta_{cem0} + \delta_{agg})} = \frac{V_{agg}}{V_{cem0} + V_{agg}}, \tag{7}$$

where δ_{cem0} is the absolute thickness of a layer of "hydrating cement paste+contact zone";

S_{itz} is the related surface area of the contact zone;

V_{cem0} is the volume concentration of the "hydrating cement paste+contact zone" layer;

V_{agg} is the volume concentration of the "aggregate" layer.

$$V_{agg} = \frac{A}{\rho_{agg}} = \frac{\rho_{con} - C - W}{\rho_{agg}}, \tag{8}$$

where A is the aggregate consumption per cubic meter of the mix;

C is the cement consumption per cubic meter of the mix;

ρ_{con} is the average density of the mixture;

ρ_{agg} is the true density of the aggregate;

total water consumption

$W=C*W/C$

W/C is the water-cement ratio.

For develop further approaches to calculating layer thicknesses, we suggest the following assumption: under the condition of not exceeding the water consumption sum water demand components of the mixture water content in the central layer of cement paste corresponds to the standard normal density W/C_{cem} = 0.22…0.28, the volume of the layer, the contact area is formed by water adsorbed by the aggregate and the corresponding water demand aggregate, which is calculated as the residual water after deduction of water requirement of cement

$$V_{itz} = W_{itz} = C(\frac{W}{C} - \frac{W}{C_{cem}}) = 0.15...0.7 \tag{9}$$

$$V_{cem0} = \frac{C(1 + W / C_{cem})}{\rho_{cp}} + W_{itz} \tag{10}$$

Then the volume of the hydrating cement paste layer is

$$V_{cem} = \frac{C(1 + W / C_{cem})}{\rho_{cp}}, \tag{11}$$

where ρ_{cp} is the density of cement paste with normal density

The relative thickness of the "hydrating cement paste" layer

$$cem = cem_0 \frac{V_{cem}}{V_{cem0}} = \frac{1}{1 + \dfrac{W_{itz}\rho_{cp}}{C(1 + W / C_{cem})}} \tag{12}$$

at the relative thickness of the layer "hydrating cement paste + aggregate"

$$cem_0 = \frac{1}{1 + \dfrac{(\rho_{con} - C - W)\rho_{cp}}{C(1 + \dfrac{W}{C_{cem}}) + W_{itz}\rho_{cp}}} \tag{13}$$

The relative thickness of a layer of "aggregate"

$$agg = \frac{1}{1 + \dfrac{C(1 + \dfrac{W}{C_{cem}}) + W_{itz}\rho_{cp}}{(\rho_{con} - C - W)\rho_{cp}}} \tag{14}$$

The relative thickness of a layer of "contact zone"

$$itz = \frac{\delta_{itz}}{\delta_{mv}} = \frac{S_{itz}\delta_{itz}}{S_{itz}(\delta_{cem} + \delta_{itz} + \delta_{agg})} = \frac{V_{itz}}{V_{cem} + V_{itz} + V_{agg}} = 1 - cem - agg \tag{15}$$

For further testing in the experiment with cement concretes, we will use the basic equation of module (5) using the equation (13), (14), (15). Working compositions of commercial concrete mixes of our own concrete mixing plant were used for testing. Thus, all data is available for calculation except the elastic modulus of the contact zone, which will be determined by the correlation method. Table 1 shows data for the sequential calculation of the elastic modulus of commercial concrete of classes B7.5…B60 for the layer model based on the parameters of the modulus of components and composition of the concrete mix: relative thicknesses cem, agg, itz. To assess the accuracy, the standard values of the elastic modulus for classes according to Russian Building Norms SNiP 2.03.01-84*(1996) "Concrete and reinforced concrete structures" were used.

As a result of correlation, the elastic modulus of the contact zone was determined as $E_{itz} = 7*10^4$ MPa. As can be seen from the data in table 1, the method, starting from class B20, gives a good convergence in the prediction of the elastic modulus, deviations do not exceed 5%. From class B15 and below, the calculation data is significantly overstated, obviously due to the large amount of free water and the hydration of the aggregate particles, the elastic modulus of the contact zone of low classes decreases, the convergence of the calculation at low classes reaches at $E_{itz} = 4*10^4$ MPa.

If we analyze the significance of the factors in the design model, we can conclude that a decrease or increase in the relative thickness and modulus of one of the layers leads to a disproportionate decrease or increase in the elastic modulus of concrete as a whole. Therefore, the increase in particle size of the aggregate is not accompanied by a reduction in water and cement can only lead to the increase in the ratio of the relative thickness of the flowable layer, the contact area and not only increase the modulus of the concrete, but lead to its reduction. To verify this proposal, the calculation model was tested by manufacturing concrete images from concrete of classes B25 (compositions 0, 3, 13) and B35 (compositions 1, 2, 4, 12, 14). In the compositions of class B25, the sand size modulus (MK) and cement consumption (C) varied: $0 - MK = 2.0$, $C = 360$ kg/m³; $3 - MK = 2.5$, $C = 340$ kg/m³; $13 - MK = 2.5$, $C = 290$ kg/m³. In the compositions of class B35, the largest aggregate size (NC), sand size modulus and cement consumption varied: $1 - MK = 2.0$, $NC = 20$ mm, $C = 350$ kg/m³; $2 - MK = 2.0$, $NC = 30$ mm, $C = 350$ kg/m³; $4 - MK = 2.5$, $NC = 30$ mm, $C = 350$ kg /m³ ; $12 - MK = 2.0$, $NC = 30$ mm, $C = 305$ kg/m³; $14 - MK = 2.5$, $NC = 30$ mm, $S = 300$ kg/m³.

Testing of the model showed that the thickness and elasticity of the weakest element disproportionately reduces the elasticity and increases the plastic properties of the cement composite as a whole. The contact zone ITZ is determined not only by the relative surface of the aggregate, but also by the water/cement and water/aggregate ratio subject to cement and aggregate water demand. So, increasing cement composite elastic properties requires complex solutions. The most effective of which, while maintaining the strength class of concrete, is simultaneously increasing the size of the aggregate and reducing cement consumption, provided by reducing the water demand of the aggregate and plasticizing the mixture through the use of additives. The elastic properties of the predominant aggregate element are also crucial, a 10% decrease in the elastic modulus of the aggregate can lead to a 15–20% decrease in the elastic modulus.

Reducing the relative surface of the aggregate without reducing the consumption of cement leads to an increase in the thickness of the layers of cement paste and the contact zone, which negates the effect of increasing the modulus of elasticity. Meanwhile, reducing the consumption of cement with strength maintaining, the modulus of elasticity can be increased by 10% or more.

It should also be noted the tendency (Table 2, last column) to significantly reduce (by 15–20%) plastic deformations when creating conditions for increasing the modulus of elasticity. According to the proposed model of concrete deformation, the main potential for the development of plastic deformations is the contact zone ITZ. An attempt was made to correlate the level of plastic deformation at 30% loading. As a result, a directly proportional relationship between the relative thickness of the contact zone and the relative plastic deformation of concrete is determined

$$\varepsilon_{pl0.3} = k_{pl0.3} itz \tag{16}$$

$k_{pl0.3}$ =0.08 is the coefficient of plastic deformation.

Table 1 shows the calculated data of relative plastic deformation at 30% loading, and the equation 2 can be converted to other loading levels. In prospective it makes possible to determine the modulus of concrete deformations under prolonged load action. The modulus of deformations standard calculation (Russian Building Rules SP 63/13330/2018 "Concrete and reinforced concrete constructions") is

$$E_{b,\tau} = \frac{E_b}{1 + \varphi_{b,cr}} = \frac{1.1E_b}{1 + 0.8\varphi_{b,cr}} \tag{17}$$

$\varphi_{b,cr}$ is the coefficient of creep of concrete is taken on the recommendations.

Taking into account that modulus of elasticity increasing goes to plastic deformation decrease, the coefficient of creep of concrete $\varphi_{b,ct}$ could be corrected in correlation with $\varepsilon_{pl0.3}$.

Table 1. Calculated and standard characteristics of the concrete elasticity modulus.

B	C, kg/m³	W/C	W, kg/m³	W_{cp}, kg/m³	W_{itz}, kg/m³	V_{cem0}, m³/m³	ρ_{con}, kg/m³	V_{agg}, m³/m³	cem	itz	agg	E_c, 10³, MPa	E_{st}, 10³, MPa	Δ, %	$\varepsilon_{el0.3}$, 10⁻²
5	180	1.40	252	45.0	207.0	313.2	2200	631.4	0.112	0.219	0.668	21.3	13.0	-63.9	1.75
10	210	1.00	210	52.5	157.5	281.4	2250	653.6	0.133	0.168	0.699	24.6	18.0	-36.5	1.35
15	260	0.80	208	65.0	143.0	296.4	2330	665	0.160	0.149	0.692	26.1	23.0	-13.6	1.19
20	290	0.70	203	72.5	130.5	301.6	2350	663.2	0.177	0.135	0.687	27.3	27.0	-1.1	1.08
25	320	0.60	192	80.0	112.0	300.8	2450	692.1	0.190	0.113	0.697	29.5	30.0	1.5	0.09
30	360	0.54	194	90.0	104.4	316.8	2450	677	0.214	0.105	0.681	30.4	32.5	6.5	0.84
35	380	0.46	175	95.0	79.8	304.0	2450	676.9	0.229	0.081	0.69	33.3	34.5	3.4	0.65
40	410	0.42	172	103.0	69.7	311.6	2480	677.8	0.244	0.070	0.685	34.9	36.0	3.1	0.56
45	440	0.38	167	110.0	57.2	316.8	2480	668.9	0.263	0.058	0.679	36.9	37.5	1.7	0.46
50	470	0.35	165	118.0	47.0	324.3	2500	666.3	0.280	0.047	0.673	38.7	39.0	0.7	0.38
55	480	0.34	163	120.0	43.2	326.4	2450	645.3	0.291	0.044	0.664	39.3	39.5	0.6	0.36
60	520	0.32	166	130.0	36.4	343.2	2430	622.7	0.318	0.038	0.645	40.6	40.0	-1.5	0.30

Table 2. Calculated and experimental characteristics of the concrete elasticity modulus and plastic deformations.

No.	B	C, kg/m³	W/C	W, kg/m³	W_{cp}, kg/m³	W_{itz}, kg/m³	V_{cem0}, m³/m³	ρ_{con}, kg/m³	V_{agg}, m³/m³	cem	itz	agg	E_c, 10³, MPa	E_{exp}, 10³, MPa	Δ, %	$\varepsilon_{el0.3}$, 10⁻²	$\varepsilon_{el0.3exp}$, 10⁻²
0	25	360	0.61	220	90	129.6	354.6	2430	755	0.20	0.12	0.68	29.1	29	-0.4	0.93	1.00
3	25	340	0.62	211	85	125.8	338.3	2470	783	0.19	0.11	0.70	29.6	33	10.3	0.90	0.80
13	25	290	0.63	183	72.5	110.2	291.5	2470	815	0.16	0.1	0.74	31.0	33	6.0	0.80	0.25
1	35	350	0.54	189	87.5	101.5	320.3	2500	800	0.20	0.09	0.71	32.1	35	8.2	0.72	0.80
2	35	350	0.54	189	87.5	101.5	320.3	2510	804	0.19	0.09	0.72	32.2	38	15.3	0.72	0.80
4	35	350	0.54	189	87.5	101.5	320.3	2500	800	0.20	0.09	0.71	32.1	34	5.5	0.72	0.80
12	35	305	0.53	162	76.3	85.4	276.0	2540	846	0.17	0.08	0.75	34.1	38	10.3	0.61	0.50
14	35	300	0.53	159	75.0	84.0	271.5	2490	829	0.17	0.08	0.75	34.0	36	5.4	0.61	1.00

4. *Conclusion*

As a result of analytical and experimental work, first the suitability of the layer model for evaluating the instant elastic modulus and deformative properties of cement composites was confirmed. It made in development of all basic and last researches in this area for available technological calculation support.

First the cement composite elasticity modulus calculation model based on the layer model operates on 6 factors: elastic modules and relative thicknesses of structural layers "aggregate", "contact zone of cement paste-aggregate", "hydrated cement paste". Cause the model is operating by easy definable factors in difference from other solutions first it made possible to receive the "step-by-step" method of cement composites elasticity modulus calculation depending on concrete mix components properties and proportions. Calculation is determining the relative thicknesses of layers with known separate elasticity modulus and finally defines whole composite structure elasticity modulus. So with components elasticity modulus data the calculation of composite elasticity modulus making of Eq. 5. The method allows to solve two basic technological problems: 1) to ensure the normative deformability of the given class concrete; 2) to identify ways to increase elastic properties within a given composition and raw materials.

Separately, it should be noted that method makes possible to norm the modulus of elasticity of commercial concrete because making available to predict elastic properties on the stage of the concrete mix composition design. The development of methods for simple and rapid control of the modulus of elasticity of concrete will make able to norm the deformative properties of concrete in projects and ensure compliance with these standards, which in turn will ensure minimum costs already at the design stage.

5. *Acknowledgment*

References

1. Alsalman, A., Dang, C.N., Prinz, G.S., Hale, W.M. Evaluation of modulus of elasticity of ultra-high performance concrete. Construction and Building Materials. 2017. DOI: 10.1016/j.conbuildmat.2017.07.158

2. Fládr, J., Bílý, P., Trtík, T. Analysis of the influence of supplementary cementitious materials used in UHPC on modulus of elasticity. IOP Conference Series: Materials Science and Engineering. 2019. 522. Pp. 012010. DOI: 10.1088/1757-899X/522/1/012010.

3. Bahr, O., Schaumann, P., Bollen, B., Bracke, J. Young's modulus and Poisson's ratio of concrete at high temperatures: Experimental investigations. Materials and Design. 2013. DOI: 10.1016/j.matdes.2012.07.070

4. Brooks, J.J. Elasticity of Concrete. Concrete and Masonry Movements 2015.

5. Kurugöl, S., Tanaçan, L., Ersoy, H.Y. Young's modulus of fiber-reinforced and polymer-modified lightweight concrete composites. Construction and Building Materials. 2008. DOI: 10.1016/j.conbuildmat.2007.03.017

6. Klyuev, S.V., Khezhev, T.A., Pukharenko, Y.V., Klyuev, A.V. Experimental study of fiber-reinforced concrete structures. Materials Science Forum. 2018. Pp. 115–119. DOI: 10.4028/MSF.945.115

7. Noguchi, T., Nemati, K.M. Relationship between compressive strength and modulus of elasticity of high-strength concrete. Proceedings of the 6th International Conference on Fracture Mechanics of Concrete and Concrete Structures. 2007.

8. Sideris, K.K., Manita, P., Sideris, K. Estimation of ultimate modulus of elasticity and Poisson ratio of normal concrete. Cement and Concrete Composites. 2004. 26(6). Pp. 623–631. DOI: 10.1016/S0958-9465(03)00084-2

9. Wongpa, J., Kiattikomol, K., Jaturapitakkul, C., Chindaprasirt, P. Compressive strength, modulus of elasticity, and water permeability of inorganic polymer concrete. Materials and Design. 2010. DOI: 10.1016/j.matdes.2010.05.012

10. Yildirim, H., Sengul, O. Modulus of elasticity of substandard and normal concretes. Construction and Building Materials. 2011. DOI: 10.1016/j.conbuildmat.2010.10.009

11. Odelson, J.B., Kerr, E.A., Vichit-Vadakan, W. Young's modulus of cement paste at elevated temperatures. Cement and Concrete Research. 2007. DOI: 10.1016/j.cemconres.2006.11.006

12. Sprince, A., Pakrastins, L., Gailitis, R. Long-Term Parameters of New Cement Composites 2020. Pp. 85–94.

13. Sanahuja, J., Dormieux, L., Chanvillard, G. Modelling elasticity of a hydrating cement paste. Cement and Concrete Research. 2007. DOI: 10.1016/j.cemconres.2007.07.003

14. Silva, R.V., De Brito, J., Dhir, R.K. Establishing a relationship between modulus of elasticity and compressive strength of recycled aggregate concrete 2016.

15. Topçu, I.B., Bilir, T., Boğa, A.R. Estimation of the modulus of elasticity of slag concrete by using composite material models. Construction and Building Materials. 2010. DOI: 10.1016/j.conbuildmat.2009.10.034

16. Usanova, K. Properties of Cold-Bonded Fly Ash Lightweight Aggregate Concretes. Lecture Notes in Civil Engineering. 2020. Pp. 507–516. DOI: 10.1007/978-3-030-42351-3_44

17. Jurowski, K., Grzeszczyk, S. The influence of concrete composition on Young's modulus. Procedia Engineering. 2015. DOI: 10.1016/j.proeng.2015.06.181

18. Li, G., Zhao, Y., Pang, S.S. Four-phase sphere modeling of effective bulk modulus of concrete. Cement and Concrete Research. 1999. DOI: 10.1016/S0008-8846(99)00040-X

19. Zhu, X., Gao, Y., Dai, Z., Corr, D.J., Shah, S.P. Effect of interfacial transition zone on the Young's modulus of carbon nanofiber reinforced cement concrete. Cement and Concrete Research. 2018. DOI: 10.1016/j.cemconres.2018.02.014

20. Varlamov, A.A., Rimshin, V.I., Tverskoi, S.Y. The modulus of elasticity in the theory of degradation. IOP Conference Series: Materials Science and Engineering. 2018. 463. Pp. 022029. DOI: 10.1088/1757-899X/463/2/022029. URL: https://iopscience.iop.org/article/10.1088/1757-899X/463/2/022029

21. Akhverdov, I.N. Osnovy fiziki betona. Moskva, Strojizdat, 1981.

22. Korolev, A.S., Zyrianov, F.A. Layer model of the cement composites deformation in the reinforced masonry structures. Construction of Unique Buildings and Structures. 2020. 92. DOI: 10.18720/CUBS.92.2

Contacts:

Alexander Korolev, korolev@sc74.ru

Nikolai Vatin, vatin@mail.ru

DOI: 10.34910/MCE.104.14

Stress level in beams with sinusoidal perforation

A.I. Pritykin[a,b], A.S. Lavrova[a,b]*
[a] Kaliningrad State Technical University, Kaliningrad, Russia
[b] Immanuel Kant Baltic Federal University, Kaliningrad, Russia
*E-mail: anna-gaide@bk.ru

Abstract. The problem of determining of stress state in beams with sinusoidal perforation under concentrated force was considered. An empirical expression has been obtained for the stress distribution in dependence on parameters of perforation and force factors – bending moment and shear force. Von Mises equivalent stresses near the edge of openings is presented by the sum of two items caused by two types of deformations – shear and bending. The numerical coefficients of this dependence were determined with help of the finite element method calculations. The obtained empirical relation was verified by FEM calculations using the ANSYS software. It was studied effect of the fillet radius in corners of openings on stress state of beams with sinusoidal perforation in wide range of relative height of openings. Obtained results allow to conclude that calculation of equivalent stresses in beams with sinusoidal perforation bring to divergence not exceeding 5%.

1. *Introduction*

In perforated beams there are the most common circular and hexagonal openings. Such beams differ from each other in level of stress concentration and manufacturing cost. The stress concentration in beams with hexagonal openings is much higher than in beams with circular openings. But they are cheaper due to significant reduction in volume of cutting. The desire of designers to reduce the stress level in beams with hexagonal openings led to production of beams with sinusoidal perforation. In fact, these are the same beams with hexagonal openings obtained by non-waste technology, but with fillet corner radius extended. The beams with sinusoidal openings are using in frameworks of different constructions (Figure 1). The range of design conceptions of such beams is wide.

Figure 1. Framework with sinusoidal perforated beams.

The strength and optimum design of perforated beams were studied in many works of foreign [1–21] and Russian [22–28] authors. In most of them, the stress distribution is considered near of hexagonal openings of regular shape using finite element method [1, 3, 8, 9, 11, 12, 14–24]. In researches [4–7, 10, 13, 26, 27] it was studied beams with sinusoidal perforation and in researches [2,25,28] beams with circular openings are investigated.

Budi et al. [1] performed the optimization analysis using FEM and laboratory tests on 225 mm height castellated steel beams with 3 m length for verification. All tested models have 150 mm height holes with various opening angles in range 45°–70° and different distances between holes. A summary analysis of castellated beams showed that maximum stress concentration in models with 45° opening angle is located in the weld joint area of web-post, but in all other models maximum stresses take place at the corner area of hexagonal holes. Strength analysis in [1] allow to conclude that optimum angle size is 60° with distance between holes (0.186 – 0.286) mm. Durif et al. [4-7] research load capacity of cellular beams with sinusoidal perforation. The study is focused on the experimental and numerical analyses of isolated web-posts specimens with four opening quarters taken from whole cellular beams. The stress measurements near contours of openings were also made using resistance wire strain gauges. Chhapkhane at al. [15] deals with finding the elastic stress distribution in castellated beams by FEM and experimentally on steel models. Strain gauge location was determined using the initial finite element models. The tests were carried out on simply supported short castellated beams containing only 4 openings with central concentrated loading. The stress level obtained with the any strain gauges located around the interior cells was the same. No stress concentration was fixed. Wakchaure at al. [18] observed from the finite element analysis that as the depth of hexagonal opening increases, stress concentrations increases at the hole corners. So by taking corrective measures, i.e. by rounding hole corners, the strength of castellated beams can be improved in practice. Wang et al. [21] investigated by FEM the failure of castellated beams with fillet corner web openings. Compared to beams with traditional hexagonal openings the proposed beams with fillet corner enjoy a higher load bearing capacity. Pritykin et al. [23, 25] conducted series of studies of the stress distribution in beams near hexagonal openings of regular shape, stress concentration in cellular beams with circular opening and obtained some empirical relations for estimating of the stress values. Later Pritykin et al. [26, 27] studied and obtained relations for deformations and stress concentration in castellated beams with sinusoidal perforation but only for one size of fillet radius. Dobrachev et al. [24] try to describe stress distribution in the web-post of castellated beam analytically by approximate function.

The purpose of the study is to obtain an empirical relation for evaluating of von Mises equivalent stress in beams with sinusoidal web perforation. A simply supported beams loaded with concentrated force in the middle of span were considered.

2. Methods

2.1. Dependence for Equivalent Stresses in the Zone of T-shaped Flanges

According to the geometry of perforations the highest stress level can be either in area of reentering angle of openings on neutral axis, where maximum shearing stresses act, or near an opening corners, where stress level is determined by action of bending moment and shear force. We derive an empirical dependence for the definition of the stresses in the region of openings in the zone of T-section.

When deriving dependences for stresses, we consider dimensions of hexagonal openings with a fillet radius of the corner $r = 0$ as basic values (Figure 2a). In general, web perforation of a beam with sinusoidal openings is determined by three linear parameters (Figure 2b): openings height $h_0 = 2a\sin\theta$, web-post width $c = \gamma a$, representing minimum distance between edges of two neighbor openings and fillet radius of the corner r. For beam with sinusoidal perforation the width of web-post is always equal to the horizontal side of opening. One more parameter is angle θ of inclination of hexagon sides to neutral axis of beam. It can vary within $45^\circ \leq \theta \leq 70^\circ$, but in the research it will be equal $\theta = 60^\circ$.
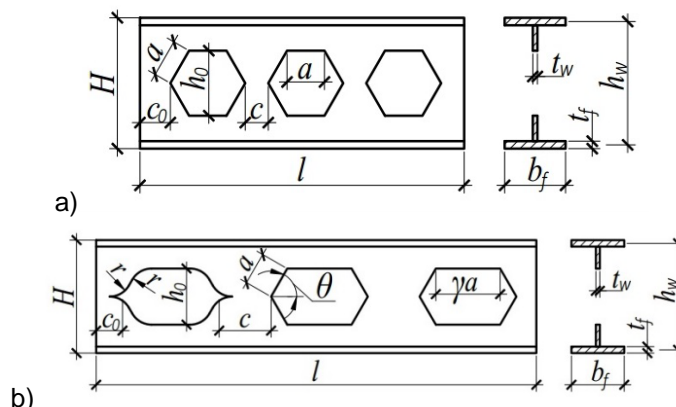

Figure 2. Perforated beam geometry:
a) basic perforation; b) perforation with sinusoidal openings.

As well known, in calculations for different beams comparing, relative parameters are convenient to use. Therefore, a relative height of openings is denoted as $\beta = h_0 / h_w$ (h_w is height of the beam web, $h_w = H - t_f$). To indicate the dimensions of beam the following abbreviated form of notation $l - h_w - t_w - b_f - t_f - \beta - \gamma - \rho$ was used in research. It completely determines the beam geometry. The interpretations are: l – length of beam, h_w and t_w – height and thickness of web, b_f and t_f are width and thickness of flanges; $\rho = r / a$ is relative fillet radius (a is inclined side of opening). The dimensions of the beam are indicated in centimeters.

In lateral bending, both bending moment M and shear force V play an important role in magnitude of $\sigma_{\max}^{eqv}$. Taking into account the above notation, we can approximately represent stresses $\sigma_{\max}^{eqv}$ near of edge n^{th} opening of beam with two components: from action of shear force V and bending moment M_n

$$\sigma_{\max}^{eqw} = \alpha_V \frac{V}{h_w t_w} + \alpha_M \frac{M_n}{W}, \tag{1}$$

where α_V and α_M are force and moment coefficients unknown here yet and determining by using the FEM calculations; modulus of section W is calculated approximately as

$$W = b_f t_f h_w + h_w^2 t_w / 6. \tag{2}$$

Assume that contour of the first opening is located at a distance c from the support. Then bending moment M_n in region of nth opening, where von Mises equivalent stress $\sigma_{\max}^{eqv}$ is determined, can be represented in the form

$$M_n = V x_n = V(2n-1)(\cos\theta + \gamma)a. \tag{3}$$

Substitution of (2) and (3) into (1) taking into account accepted notation $a = h_0 / 2\sin\theta$ and $\beta = h_0 / h_w$ leads to the expression

$$\sigma_{\max}^{eqv} \approx \left(\alpha_V + \alpha_M^* \frac{(n-0.5)(\cos\theta + \gamma)\beta}{\sin\theta(b_f t_f / h_w t_w + 0.167)} \right) \frac{V}{h_w t_w} \tag{4}$$

Relation (4) in general form is valid for any angle of inclination angle but in particular case, when $\theta = 60^\circ$ it is simplified to view

$$\sigma_{\max}^{eqv} \approx \left(\alpha_V + \alpha_M \frac{(n-0.5)(0.5 + \gamma)\beta}{6 b_f t_f / h_w t_w + 1} \right) \frac{V}{h_w t_w}. \tag{5}$$

The influence of fillet radius is taken into account using the coefficients α_V and α_M. The value $b_f t_f / h_w t_w$ represents ratio of areas of flanges and web. For practical application of relation (5), it remains to determine coefficients of force α_V and moment α_M.

2.2. Coefficient of Stress Concentration

To compare efficiency of different designs, it is convenient to use stress concentration factor α_σ, which in the study was defined as ratio of maximum equivalent stresses in the opening zone $\sigma_{\max}^{eqv}$ to the level of maximum stresses in beam with a solid web $\sigma_{\max}^{TT}$ under action of external load. The value α_σ was estimated by formula

$$\alpha_\sigma = \sigma_{\max}^{eqw} / \sigma_{\max}^{TT}, \tag{6}$$

where $\sigma_{\max}^{TT}$ is stresses in flange, determined according to the technical theory of beam as

$$\sigma_{\max}^{TT} = M_{\max} / W .$$
(7)

Here $M_{\max}$ is the maximum bending moment, W is the section modulus of beam without openings in web, determined by (2).

For possibility of practical application of relations (5) and (6) first of all is necessary to determine coefficients of force α_V and moment α_M with help of FEM calculations.

As known the accuracy of FEM calculations is largely determined by size of FE: smaller finite elements lead to more accurate calculation as a rule. However, it is impractical to use a small size FE mesh for entire structure because of calculation time. For example, on a computer with 4 GB of RAM, calculating of a system of equations with 400000 unknowns takes about a minute. To reduce the size of equations system and, relatively, calculation time, different approaches can be used: the method of superelements; accounting for symmetry of structure, allowing only half of beam to be considered; the use of irregular mesh of FEs and others. The last two approaches turn out to be the simplest and quite effective. However, the question arises what the size of finite elements would be sufficient to obtain the required calculation accuracy. It is quite difficult to theoretically justify the optimal sizes of FEs, so in the most cases this is done on the basis of successive analysis with a decrease in size of elements until difference in results becomes negligible (for example, 0.1% – 0.2%).

In study a fine mesh was used at the edge of openings through one and only on that part where the level of maximum stresses was estimated (Figure 3). It was considered one part of beam to the section where concentrated force is applied The resulting system of equations turned out to be optimal in terms of calculation time. It is clear that the size of the FE should be linked to fillet radius of corners of hexagonal opening. After all, the smaller radius, the smaller finite elements should be, otherwise calculation of average stresses within FE reduce accuracy. In the calculations below, the radius r was taken equal to $r = 0.25a$, $r = 0.5a$ and $r = 0.75a$, where a – inclined side of opening. The analysis showed that satisfactory accuracy is achieved with FE sizes of $(0.02 - 0.03)r$, therefore, in the calculations, FE sizes near edge of opening were equal to $\Delta_{FE} = 2$ mm, and in the rest of beam – $\Delta_{FE} = 20$ mm, with overall opening height $h = 500 - 600$ mm.

The simply supported beams loaded with concentrated force applied at an arbitrary point of span were initially considered.

3. Results and Discussion

3.1. Dependence for Equivalent Stresses in the Zone of T-section

The series of calculations of perforated beams made from №60 rolled section with different opening parameters were carried out. The values of relative fillet radius of openings ρ in range $0.25 \leq \rho \leq 0.75$, the relative height of openings in the range $0.667 \leq \beta \leq 0.73$ with a fixed relative width of web-post $\gamma = 1.5$ and the angle of inclination of sides $\theta = 60°$, were varied.

Under manufacturing a perforated beam using non-waste technology there is a relationship between the initial height of beam with a solid web H_0 and height of the perforated beam H, depending on the relative height of openings β

$$H = H_0 / (1 - 0.5\beta) .$$
(8)

Below it is considering beams manufacturing of pattern beam with height $H_0 = 600$ mm as the initial one, then for values of $\beta = 0.667$; $\beta = 0.7$ and $\beta = 0.73$ in accordance with (8) the height of perforated beams will be $H = 900$ mm; $H = 923$ mm and $H = 945$ mm respectively.

The FEM calculations of the simply supported beam loaded with force $F = 10$ kN in the middle of span, according to the program developed by the authors using the ANSYS software solution, lead to the values shown in Figure 3.

The analysis of results revealed that for beams with the above parameters, acceptable values of coefficients α_V and α_M correspond to the expressions:

$$\alpha_V = 60(2.17\beta - 1)(1.25 - \rho) ; \tag{9}$$

$$\alpha_M = 3.8(5.15\beta - 1) . \tag{10}$$

As can be seen from (9) and (10), the coefficient α_V can be approximately considered linearly dependent on ρ and β, and the coefficient α_M – linearly dependent only on β. The stress distributions in the beams with parameters $l - h_w - 1.2 - 19 - 1.78\text{cm} - \beta - 1.5 - 0.75$ shown in Figure 3 are linear, i.e., the values of von Mises equivalent stress $\sigma_{\max}^{eqv}$ near the edge of openings are proportional to magnitude of the bending moment. The given empirical dependence (5), taking into account the relations (9) and (10), allows us to compare the maximum equivalent stresses in the region of sinusoidal openings with an arbitrary number n, obtained by the FEM and analytically (Table 1).

Figure 3. Stress state of simply supported beams $l - h_w - 1.2 - 19 - 1.78\text{cm} - \beta - 1.5 - 0.75$ **with different opening height:**

a) $h_w = 88.22$ **cm;** $\beta = 0.667$; **b)** $h_w = 90.52$ **cm;** $\beta = 0.7$; **c)** $h_w = 92.72$ **cm;** $\beta = 0.73$

Table 1. Comparative analysis value of stresses $\sigma_{\max}^{eqv}$ *in beams* $l–h_w–1.2–19–1.78cm–\beta–1.5–0.75$ *at different relative height of openings.*

	Opening number, n		5	7	9
β	0.667	FEM	15.1	19.0	22.7
		by (5)	15.3	19.3	23.3
	Divergence δ, %		1.3	1.6	2.6
	Beam		l–88.22–1.2–19–1.78 cm–0.667–1.5–0.75		
β	0.7	FEM	17.4	21.7	25.9
		by (5)	17.2	21.6	26.1
	Divergence δ, %		1.1	0.5	0.8
	Beam		l–90.52–1.2–19–1.78 cm –0.7–1.5–0.75		
β	0.73	FEM	19.9	24.6	29.2
		by (5)	18.9	23.7	28.6
	Divergence δ, %		5.0	3.7	2.1
	Beam		l–92.72–1.2–19–1.78 cm –0.73–1.5–0.75		

As can be seen from the results presented in Table 1, the divergence of stresses calculated on (5) and by FEM does not exceed 5%.

The similar calculations performed by the FEM for perforated beams made from the initial profile №50 (Russian State Standard GOST 8239-89) are presented in Figure 4. The divergence according to (5) in this case is also less than 5% (Table 2).
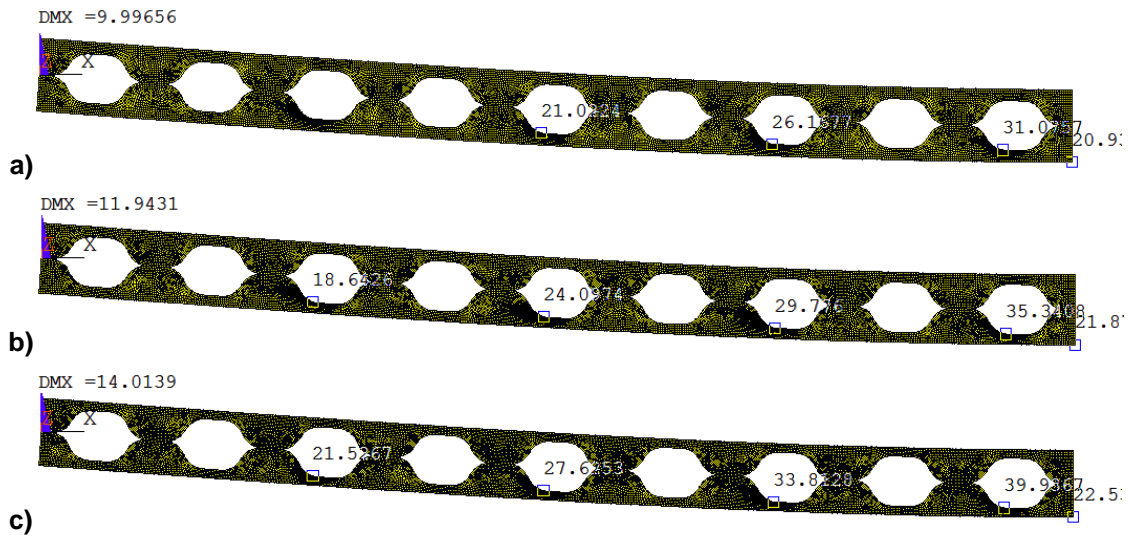

Figure 4. Stress state of simply supported beams $l - h_w - 1.0 - 17 - 1.52\text{cm} - \beta - 1.5 - 0.75$ **with different opening height:**

a) $h_w = 73.48$ **cm;** $\beta = 0.667$ **; b)** $h_w = 75.38$ **cm;** $\beta = 0.7$ **; c)** $h_w = 77.22$ **cm;** $\beta = 0.73$

Table 2. Comparative analysis value of stresses $\sigma_{\max}^{eqv}$ **in beams** $l–h_w–1.0–17–1.52cm–\beta–1.5–0.75$ **at different relative height of openings.**

	Opening number, n		5	7	9
β	0.667	FEM	21.0	26.1	31.1
		by (5)	21.3	26.7	32.1
	Divergence δ, %		1.4	2.3	3.2
	Beam		l–73.48–1.0–17–1.52 cm –0.667–1.5–0.75		
β	0.7	FEM	24.0	29.8	35.3
		by (5)	23.9	29.9	35.9
	Divergence δ, %		0.4	0.3	1.7
	Beam		l–75.38–1.0–17–1.52 cm –0.7–1.5–0.75		
β	0.73	FEM	27.6	33.8	39.9
		by (5)	26.2	32.8	39.4
	Divergence δ, %		5	3.0	1.3
	Beam		l–77.22–1.0–17–1.52 cm –0.73–1.5–0.75		

3.2. Stress concentration factor

The strength calculation of any structures, including beams, is estimated by the level of maximum stresses arising in it. Considering the data presented in Figure 3 with a constant fillet radius of corner, the value α_σ calculated on (6) varies linearly depending on the relative height of openings β (Figure 5).
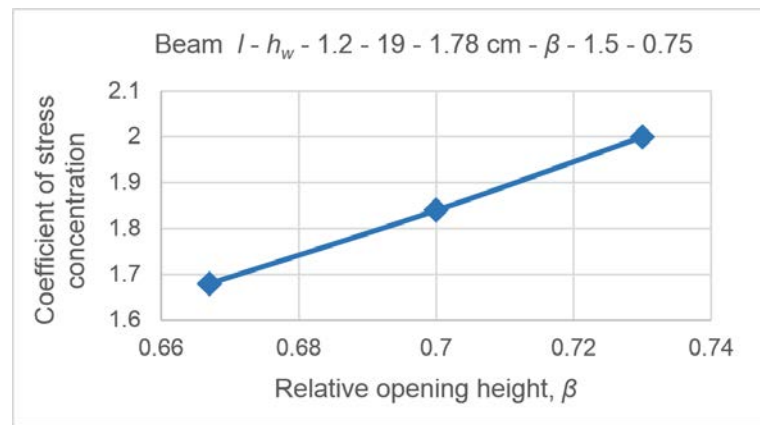
Figure 5. Dependence value α_σ on relative height of openings β.

The stress concentration level is significantly affected not only by the relative height of the openings β, but also by the fillet radius of their corners. In practice, openings with relative fillet radius of corners from $\rho = 0.25$ (Figure 6a) to $\rho = 0.75$ (Figure 6b) are used. Therefore, beams with different fillet radius were investigated.

a)

b)

Figure 6. Perforated beams with different fillet radius of corner: a) $r = 0.25a$; b) $r = 0.75a$.

At relative fillet radius of corner $\rho = 0.25$ and $\rho = 0.5$ for beams made from $H_0 = 600$ mm profile, at $\beta = 0.667$, the stress distribution pattern shown in Figure 7 indicates that a decrease of ρ lead to an increase of stress concentration. So, when the radius decreases from $r = 0.75a$ (Figure 3a) to $r = 0.5a$ (Figure 7a), the stress level increases by about 10%, and additional reducing of radius from $r = 0.5a$ (Figure 7a) to $r = 0.25a$ (Figure 7b), lead to augmentation of stresses by another 20%. For radius $r = 0.25a$ and $\beta = 0.667$, the value of $\alpha_\sigma = 2.15$, while for $r = 0.75a$ the coefficient $\alpha_\sigma = 1.65$.
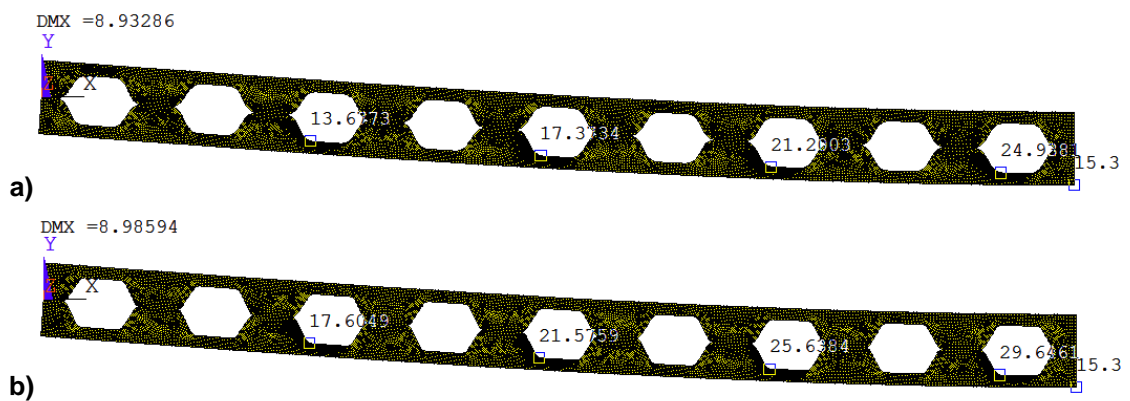

a)

b)

Figure 7. Stress level in beams $l - 88.22 - 1.2 - 19 - 1.78 \text{cm} - 0.667 - 1.5 - \rho$ with:

a) $\rho = 0.5$; b) $\rho = 0.25$.

Similar calculations by FEM of beam $l-92.72-1.2-19-1.78\text{cm}-0.73-1.5-\rho$ with the fillet radius $r=0.5a$ and $r=0.25a$ lead to a picture of the stress distribution shown in Figure 8. The value of α_σ for beam with $\rho=0.5$ (Figure 8a) does not exceed value $\alpha_\sigma=2.17$, and with a further decrease of radius to $\rho=0.25$ (Figure 8b), the stress concentration level increases to $\alpha_\sigma=2.56$.

For beam shown in Figure 8b, the stress level calculated according to (5) gives a value of $\sigma_{\max}^{eqv}=36.5$ MPa in the 9th opening, which indicates divergence with calculation by FEM of 3.7%.
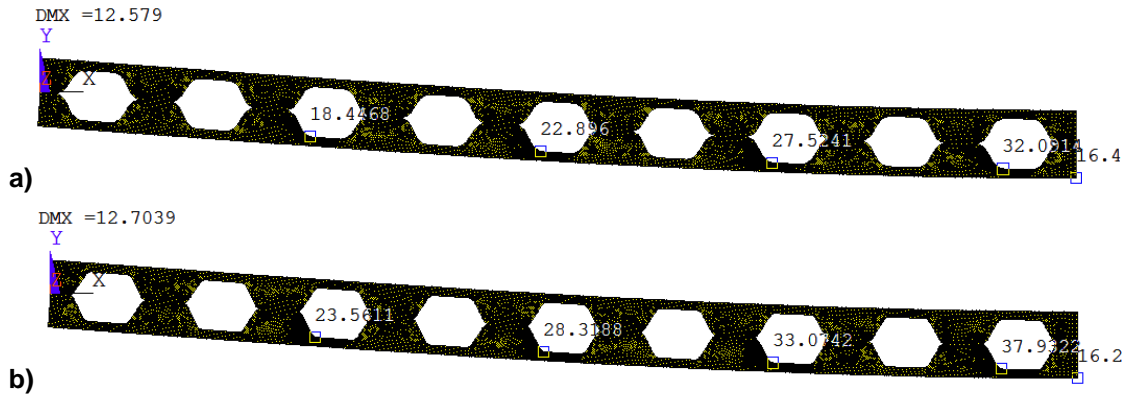
DMX =12.579

18.4468 22.896 27.5241 32.0914 16.4

a)

DMX =12.7039

23.5611 28.3188 33.0742 37.9522 16.2

b)

Figure 8. Stress level in beams $l-92.72-1.2-19-1.78\text{cm}-0.73-1.5-\rho$ with:

a) $\rho=0.5$; b) $\rho=0.25$.

The obtained results are applicable for case of loading a simply supported beam with a force F in an arbitrary section of span, taking as the shear force V the reaction of support in corresponding section of beam. Applying the superposition principle, it is possible to determine the stress concentration under action of a few concentrated forces.

Since in beams with sinusoidal openings, potentially dangerous zones can also be the welded zones of the perforated teeth at the level of neutral axis, where the reentering angles are located, these zones were also studied.

3.3. Equivalent stress in web-post zone

Consider a simply supported beam $15.4H-73.48-0.6-17-1.52\text{cm}-0.667-1.5-0.5$ loaded with concentrated force in the middle of span. Calculation of stress level by FEM using ANSYS software (Figure 9a) shows stress state of the web-post zones at the level of neutral axis.

As can be seen from Figure 9b, the danger zone of stress state is the entering acute angle in web-post: maximum stresses in this zone near axis of 2nd hole reach value $\sigma_{\max}^{eqv}=31.453$ MPa, while the maximum stress in area of rounded zone of 3rd hole is only $\sigma_{\max}^{eqv}=27.711$ MPa (Figure 9c), i.e. near neutral axis a stress level is higher. In flanges at a stated load the maximum stresses are $\sigma_{flange}=12.6$ MPa (Figure 9a). Thus, the stresses near neutral axis are more than 2.5 times higher than stresses in flanges. Based on this it can be concluded that decreasing the stress concentration in the region of opening corners lead to augmentation of stresses near the neutral axis (Figure 9b).
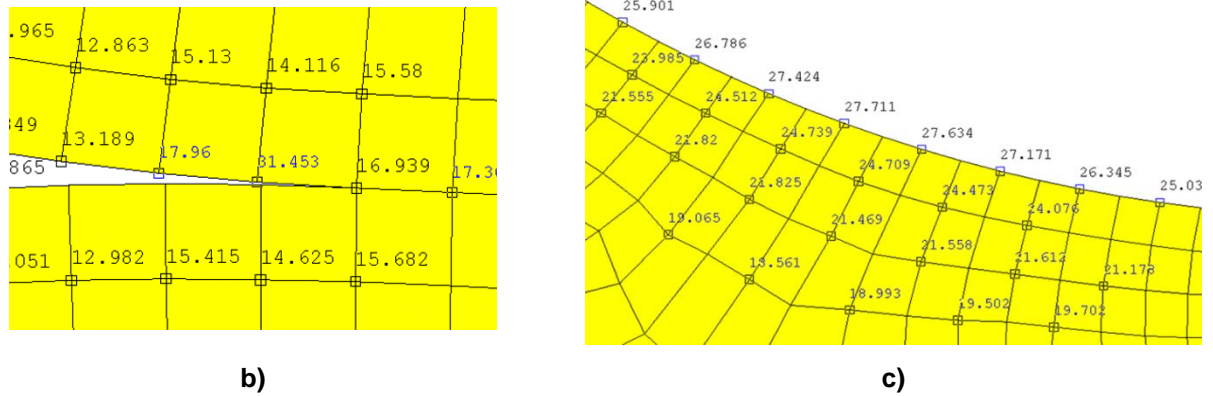
DMX =2.373

9.34 9.387 9.654 9.598 12.47

19.269 27.711 12.6

a)

b)

c)
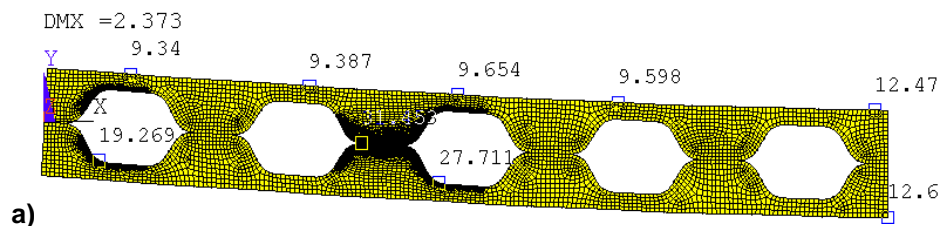
Figure 9. Stress state of beam $15.4H - 73.48 - 0.6 - 17 - 1.52\text{cm} - 0.667 - 1.5 - 0.5$ **under force** $F = 10$ **kN applied in mid-span: a) general picture of stress distribution; b) near axis of 2nd hole; c) in rounded zone of 3rd hole.**

Stress state near axis of 4th hole (Figure 10a) show level $\sigma_{\max}^{eqv} = 36.916$ MPa, while maximum stresses at contour of 5th hole (Figure 10b) is only $\sigma_{\max}^{eqv} = 32.62$ MPa.
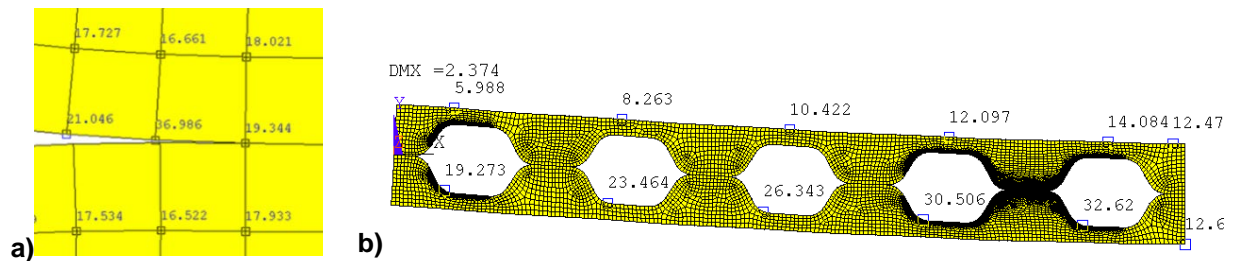

a)

b)

Figure 10. Stress state of beam $15.4H - 73.48 - 0.6 - 17 - 1.52\text{cm} - 0.667 - 1.5 - 0.5$ **under force** $F = 10$ **kN applied in mid-span: a) near axis of 4th hole; b) general picture of stress distribution.**

As can be seen from Figure 10, at a constant shear force, the stresses at the reentering edge of opening increase with expansion of bending moment from 31.5 MPa at the second web-post to 36.916 MPa at the fourth web-post (Figure 10a). The stress concentration factor at edge of opening in the region of the 4th web-post take a value $\alpha_\sigma = 36.916 / 11.9 \approx 3.11$.

Let us now consider a beam with an increased fillet radius up to $r = 0.75a$. From Figure 11 it follows that growth of the fillet radius of corner practically does not affect the stress level in the beam flange near of application of concentrated force. But the level of maximum equivalent stresses $\sigma_{\max}^{eqv}$ decreases from 32.62 MPa (Figure 10b) to 27.64 MPa in the region of the 5th openings (Figure 11b). At the same time, the level $\sigma_{\max}^{eqv}$ in the zone of reentering angles increases almost 1.3 times from 37 MPa to 47.3 MPa (Figure 11a). Thus, the level of stress concentration increases to $\alpha_\sigma = 47.3 / 11.9 \approx 3.97$.
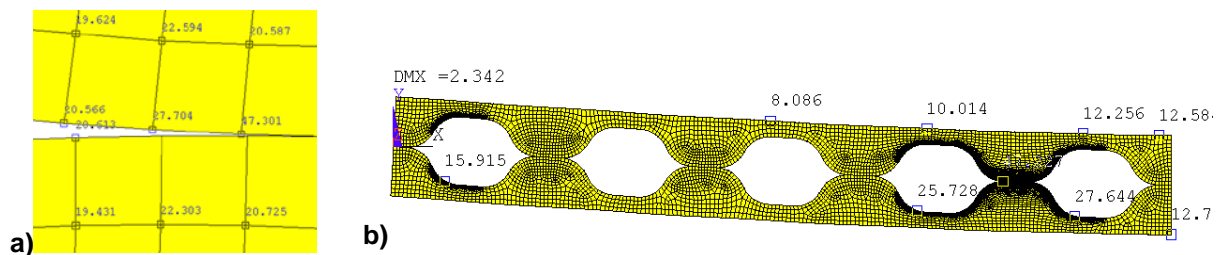

a)

b)

Figure 11. Stress state of beam $15.4H - 73.48 - 0.6 - 17 - 1.52cm - 0.667 - 1.5 - 0.75$ **under force** $F = 10$ **kN applied in mid-span: a) near axis of 4th hole; b) general picture of stress distribution.**

In fact, the level of stresses in the region of the reentering angles at the level of the neutral axis is much lower due to the presence of welds, which somewhat smooth the sharp reentering angles (Figure 6b).

Note that in case of sinusoidal perforation the zone of increased stresses includes only one node in the zone of the reentering angle at the level of neutral axis (see, for example, Figure 10a or Figure 11a). At the same time, in the region of neighboring nodes, the stress level decreases by 1.7–2 times, but in the zone of the T-shaped of flanges, the region of increased stresses is quite extensive, covering several nodes (Figure 9c). Hence, It can be concluded that using of beams with sinusoidal perforation allows to reduce the stress level approximately 1.7–2.3 times compare with regular hexagon perforation. As for the reentering nodes, as can be seen from Figure 6b, the presence of welds decrease sharpness of corners and thereby reduce the actual level of maximum stresses to an acceptable value. In study of Durif at al. [4] it is noted the formation of four plastic hinges takes place at the opening corners. Our research confirms that namely at corners level of stresses is highest. In addition to results of work [26] this study allows estimate level of stresses depending on radius of fillet. In work of Wakchaure [17] from the finite element analysis results, it is also concluded that the castellated steel beam corners of openings should be rounded to reduce the stress level.

4.   *Conclusions*

1. An empirical dependence is obtained for stresses $\sigma_{\max}^{eqv}$ near the edge of openings in the form of the sum of two items which makes it possible to differentiate the role of shear force and bending moment.

2. With a constant shear force, the maximum von Mises stresses $\sigma_{\max}^{eqv}$ near the edge of the hexagonal openings are linearly distributed in proportion to the magnitude of the bending moment.

3. For perforated beams, the value of α_σ should be calculated as the ratio of the maximum equivalent stresses at the edge of openings to the maximum stresses in the flange, determined by the technical theory of beam bending.

4. With a fixed fillet radius of the corners, the stress concentration at the openings increases in proportion to their relative height. The value α_σ with a relative fillet radius $\rho = 0.75$ does not exceed 2, decreasing with diminishing height of openings.

5. Although the level of stress concentration in the regions of the reentering angles in the web-posts exceeds the level α_σ in regions of the rounding of openings, the presence of welds reduces this concentration.

References

1. Budi, L., Sukamta, Partono, W. Optimization analysis of size and distance of hexagonal hole in castellated steel beams. Procedia Engineering. 2017. 171. Pp. 1092–1099. DOI: 10.1016/j.proeng.2017.01.465

2. Chung, K.F., Liu, T.C.H., Ko, A.C.H. Investigation on vierendeel mechanism in steel beams with circular web openings. Journal of Constructional Steel Research. 2001. 57(5). Pp 467–490. DOI: 10.1016/S0143-974X(00)00035-3

3. Dervinis, B., Kvedaras, A.K. Investigation of Rational Depth of Castellated Steel I-Beam. Journal of Civil Engineering and Management. 2008. 149(3). Pp. 163–168. DOI: 10.3846/1392-3730.2008.14.12

4. Durif, S., Bouchair, A. Behavior of cellular beams with sinusoidal openings. Procedia Engineering. 2012. 40. Pp.108–113. DOI: 10.1016/j.proeng.2012.07.064

5. Durif, S., Bouchair, A., Vassart, O. Experimental tests and numerical modeling of cellular beams with sinusoidal openings. Journal of Constructional Steel Research. 2013. 82. Pp.72–87. DOI: 10.1016/j.jcsr.2012.12.010

6. Durif, S., Bouchair, A., Vassart, O. Experimental and numerical investigation on web-post specimen from cellular beams with sinusoidal openings. Engineering Structures. 2014. 59. Pp. 587–598. DOI: 10.1016/j.engstruct.2013.11.021

7. Durif, S., Bouchair, A. Analytical model to predict the resistance of cellular beams with sinusoidal openings. Journal of Constructional Steel Research. 2016. 121. Pp 80–96. DOI: 10.1016/j.jcsr.2016.01.015

8. Frans, R., Parung, H., Sandy, D., Tonapa, S. Numerical modelling of hexagonal castellated beam under monotonic loading. Procedia Engineering. 2017. 171. Pp. 781–788. DOI: 10.1016/j.proeng.2017.01.449

9. Gandomi, A.H., Tabatabaei, S.M., Moradian, M.H., Radfar, A., Alavi, A.H. A new prediction model for the load capacity of castellated steel beams. Journal of Constructional Steel Research. 2011. 67(7). Pp 1096–1105. DOI: 10.1016/j.jcsr.2011.01.014

10. Kumbhar, P. D. Jamadar, A. M., Optimization of opening size for castellated beam with sinusoidal openings. International Journal OF Optimization in Civil Engineering. 2015. 5(3). Pp. 301–313.

11. Lagaros, N.D., Psarras, L.D., Papadrakakis, M., Panagiotou, G. Optimum design of steel structures with web opening. Engineering Structure. 2008. 30 (9). Pp. 2528–2537. DOI: 10.1016/j.engstruct.2008.02.002

12. Liu, T.C.H., Chung, K.F. Steel beam with large web opening of various shapes and sizes: Finite element Investigation// Journal of Constructional Steel Research. 59(9). 2003. Pp. 1159–1176. DOI: 10.1016/S0143-974X(03)00030-0

13. Martin, P.O., Couchaux, M., Vassart, O., Bureau, A. An analytical method for the resistance of cellular beams with sinusoidal openings. Engineering Structures. 2017. 143. Pp 113–126. DOI: 10.1016/j.engstruct.2017.03.048

14. Oliveira, J.P., Cardoso, D., Sotelino, E.D. Elastic flexural local buckling of Litzka castellated beams: Explicit equations and FE parametric study. Engineering Structures. 2019. 186. Pp. 436–445. DOI: 10.1016/j.engstruct.2019.02.034

15. Chhapkhane, N.K., Shashikant, R.K. Analysis of stress distribution in castellated beam using finite element method and experimental techniques. International Journal of Mechanical Engineering Applications Research. 2012. 3(3). Pp. 190–197.

16. Tsavdaridis, K.D., Mello, C.D. Optimisation of novel elliptically-based web opening shapes of perforated steel beams. Journal of Constructional Steel Research. 2012. 76. Pp. 39–53. DOL: 10.1016/j.jcsr.2012.03.026

17. Wakchaure, M.R., Sagade, A.V. Finite Element Analysis of Castellated Steel Beam. International Journal of Engineering and Innovative Technology. 2012. 2(1). Pp. 365–372.

18. Wakchaure, M.R., Sagade, A.V., Auti, V.A. Parametric study of castellated beam with varying depth of web opening [Online]. International Journal of Scientific and Research Publications. 2012. 2(8). URL: http://www.ijsrp.org/research-paper-0812/ijsrp-p0880.pdf

19. Wang, P., Wang, X., Ma, N. Vertical shear buckling capacity of web-posts in castellated steel beams with fillet corner hexagonal web openings. Engineering Structures. 2014. 75. Pp. 315–326. DOI: 10.1016/j.engstruct.2014.06.019

20. Wang, P., Ma, Q., Wang, X. Investigation on Vierendeel mechanism failure of castellated steel beams with fillet corner web openings. Engineering Structures. 2014. 74. Pp. 44–51. DOI: 10.1016/j.engstruct.2014.05.008

21. Wang, P., Guo, K., Liu, M., Zhang, L. Shear buckling strengths of web-posts in a castellated steel beam with hexagonal web openings. Journal of Constructional Steel Research. 2016. 121. Pp. 173–184. DOI: 10.1016/j.jcsr.2016.02.012

22. Dobrachev, V.M., Litvinov, Ye.V. Analiticheskoye opredeleniye napryazhenno-deformirovannogo sostoyaniya stenki-peremychki perforirovannoy balki [Analytical determination of the stress-strain state of the web-post of a perforated beam]. Izvestiya vuzov. Stroitelstvo. 2003. No. 5. Pp.128-133. (rus)

23. Pritykin, A. Stress concentration in castellated I-beams under transverse bending. Mechanika. 2016. 22(6). Pp. 466–473. DOI: 10.5755/j01.mech.22.6.13590

24. Pritykin, A.I. Kontsentratsiya napryazheniy v balkakh s odnim ryadom shestiugolnykh vyrezov [Stress concentration in beams with one line of hexagonal openings]. Vestnik MGSU. 2009. No. 1. Pp. 118–121. (rus)

25. Pritykin, A.I., Lavrova A.S. Prediction of the stress level and stress concentration in cellular beams with circular opening. Mechanika. 2017. 23(4). Pp. 488–494. DOI: 10.5755/j01.mech.23.4.15136

26. Pritykin, A.I., Misnik, A.V. Stress distribution and concentration in castellated beams with sinusoidal wall perforation [Raspredeleniye i kontsentratsiya napryazheniy v balkakh s sinusoidalnoy perforatsiyey stenki]. Vestnik MGSU. 2017. Vol. 12. No. 8(107). Pp. 876-884. DOI: 10.22227/1997-0935.2017.8.876-884

27. Pritykin, A.I. Deflection of beams with sinusoidal perforation. IOP Conf. Series: Materials Science and Engineering. 2020. Vol. 913. 022062. DOI:10.1088/1757-899X/913/2/022062

28. Solovyev, A.V., Vasyukov, I.A. Stiffness value analyses of perforated I-beams with circular web perforation [Analiz zhestkostnykh kharakteristik perforirovannykh balok s krugloy perforatsiyey stenki]. Promyshlennoye i grazhdanskoye stroitelstvo. 2014. No. 3. Pp. 36–38. (rus)

Contacts:

Aleksey Pritykin, prit_alex@mail.ru

Anna Lavrova, anna-gaide@bk.ru

ПОЛИТЕХ
Санкт-Петербургский
политехнический университет
Петра Великого

Инженерно-строительный институт
Центр дополнительных профессиональных программ

195251, г. Санкт-Петербург, Политехническая ул., 29,
тел/факс: 552-94-60, www.stroikursi.spbstu.ru,
stroikursi@mail.ru

Приглашает специалистов проектных и строительных организаций, не имеющих базового профильного высшего образования на курсы профессиональной переподготовки (от 500 часов) по направлению «Строительство» по программам:

П-01 «Промышленное и гражданское строительство»
Программа включает учебные разделы:

- *Основы строительного дела*
- *Инженерное оборудование зданий и сооружений*
- *Технология и контроль качества строительства*
- *Основы проектирования зданий и сооружений*
- *Автоматизация проектных работ с использованием AutoCAD*
- *Автоматизация сметного дела в строительстве*
- *Управление строительной организацией*
- *Управление инвестиционно-строительными проектами. Выполнение функций технического заказчика*

П-02 «Экономика и управление в строительстве»
Программа включает учебные разделы:

- *Основы строительного дела*
- *Инженерное оборудование зданий и сооружений*
- *Технология и контроль качества строительства*
- *Управление инвестиционно-строительными проектами. Выполнение функций технического заказчика и генерального подрядчика*
- *Управление строительной организацией*
- *Экономика и ценообразование в строительстве*
- *Управление строительной организацией*
- *Организация, управление и планирование в строительстве*
- *Автоматизация сметного дела в строительстве*

П-03 «Инженерные системы зданий и сооружений»
Программа включает учебные разделы:

- *Основы механики жидкости и газа*
- *Инженерное оборудование зданий и сооружений*
- *Проектирование, монтаж и эксплуатация систем вентиляции и кондиционирования*
- *Проектирование, монтаж и эксплуатация систем отопления и теплоснабжения*
- *Проектирование, монтаж и эксплуатация систем водоснабжения и водоотведения*
- *Автоматизация проектных работ с использованием AutoCAD*
- *Электроснабжение и электрооборудование объектов*

П-04 «Проектирование и конструирование зданий и сооружений»
Программа включает учебные разделы:

- *Основы сопротивления материалов и механики стержневых систем*
- *Проектирование и расчет оснований и фундаментов зданий и сооружений*
- *Проектирование и расчет железобетонных конструкций*
- *Проектирование и расчет металлических конструкций*
- *Проектирование зданий и сооружений с использованием AutoCAD*
- *Расчет строительных конструкций с использованием SCAD Office*

П-05 «Контроль качества строительства»
Программа включает учебные разделы:

- *Основы строительного дела*
- *Инженерное оборудование зданий и сооружений*
- *Технология и контроль качества строительства*
- *Проектирование и расчет железобетонных конструкций*
- *Проектирование и расчет металлических конструкций*
- *Обследование строительных конструкций зданий и сооружений*
- *Выполнение функций технического заказчика и генерального подрядчика*

По окончании курса слушателю выдается диплом о профессиональной переподготовке установленного образца, дающий право на ведение профессиональной деятельности